Shaping the cell: theories of active membranes

Hervé Turlier

To cite this version:

Hervé Turlier. Shaping the cell: theories of active membranes. Physics [physics]. Université Pierre & Marie Curie - Paris 6, 2013. English. NNT : 2013PA066685 . tel-01424097

HAL Id: tel-01424097
https://hal.science/tel-01424097v1

Submitted on 2 Jan 2017

THÈSE

PRÉSENTÉE A

L'UNIVERSITÉ PIERRE ET MARIE CURIE

ÉCOLE DOCTORALE : Physique de la Région Parisienne - ED107

Par Hervé TURLIER

POUR OBTENIR LE GRADE DE

DOCTEUR

SPÉCIALITÉ : Physique Théorique

Shaping the cell
Theories of active membranes

Directeur de recherche : Jean-François JOANNY
Co-directeur de recherche : Jacques PROST

Soutenue publiquement le : 10 décembre 2013

Devant la commission d'examen formée de :

Mme Martine BEN-AMAR	Présidente du Jury
M. Arezki BOUDAOUD	Rapporteur
M. Matthew TURNER	Rapporteur
M. Jean-François JOANNY	Directeur de thèse
M. Karsten KRUSE	Examinateur
M. François NEDELEC	Examinateur
M. Jacques PROST	Co-directeur de thèse, membre invité
M. Basile AUDOLY	Membre invité

UNIVERSITE PIERRE ET MARIE CURIE
DOCTORAL SCHOOL ED107
PHYSIQUE DE LA REGION PARISIENNE

PHD THESIS

to obtain the title of

PhD in Science

of the Université Pierre et Marie Curie
Specialty : Theoretical physics

Defended by
Hervé Turlier

Shaping the cell: theories of active membranes

Thesis Advisors: Jean-François Joanny, Jacques Prost

prepared at Institut Curie

defended on December 10, 2013

Jury :

President :	Martine Ben Amar	-	LPS - ENS Paris
Reviewers :	Arezki Boudaoud	-	LJC - ENS Lyon
	Matthew Turner	-	University of Warwick
Examiners :	François Nédélec	-	European Molecular Biology Laboratory
	Karsten Kruse	-	Universität des Saarlandes
Advisor :	Jean-François Joanny	-	Institut Curie
Co-advisor :	Jacques Prost	-	ESPCI and Institut Curie
Invited member:	Basile Audoly	-	IJLRDA - UPMC

Acknowledgments

La thèse est très certainement l'une des étapes les plus marquantes de ma scolarité, et non pas uniquement car elle en signe l'achèvement. Certes, on a toujours un petit pincement au coeur à rendre sa carte étudiante, mais en réalité la thèse de doctorat n'a plus grand chose à voir avec les études supérieures, et, comme aiment à vous le rappeller vos amis qui se sont engoufrés dans le monde de l'entreprise, elle ne constitue pas non plus encore un véritable métier, au regard du monde économique. La thèse est un peu à mi-chemin, un sas progressif entre les études et le monde du travail, qui permet tout à la fois de goûter encore au plaisir d'apprendre mais aussi de commencer à produire par soi-même, l'occasion unique d'être à la fois encadré dans son travail mais aussi de jouir d'une extraordinaire liberté. Cette grande liberté a fait que mon expérience du doctorat fut loin se limiter à sa seule réalité académique. La thèse a constitué pour moi un réel moment de découverte et de construction personnelle, moment qui m'avait certainement un peu manqué pendant les précédentes années peut-être un peu trop studieuses, en prépa à Ginette puis à l'Ecole Polytechnique. Ce sont donc à la fois mes encadrants, collaborateurs et collègues que je veux prendre le temps de remercier un à un, mais aussi toutes les personnes avec qui j'ai partagé ces moments forts et intenses qui m'ont forgé en dehors du labo.

La thèse pour moi a commencé par une rencontre, celle de mon futur directeur, Jean-François Joanny, dont l'agilité à manier les équations et l'habileté à nous les expliquer physiquement a marqué toute la promotion du master de physique des liquides. Faire ma thèse avec Jean-François fut une évidence, au point que j'ai abandonné toute idée de thèse expérimentale pour me mettre à la théorie, malgré une première expérience expérimentale plutôt concluante au laboratoire de Sid Nagel à Chicago, une année auparavant. Quelle ne fut pas alors ma surprise de me rendre compte, qu'après 7 ans d'études de physique, mon ignorance puisse être si grande... Je pense avoir appris trois fois plus en physique pendant ma thèse que pendant tout le reste de mes études. Jean-François m'a toujours laissé toute la liberté pour étudier et travailler sur ce que je voulais, peut-être même parfois trop ! Les échéances ont bien fini par rattraper ma propension naturelle à m'éparpiller, mais je ne regrette pas d'avoir pu élargir mon sujet initial, et par là même d'apprendre autant. Merci Jean-François ! Jacques Prost fut la seconde pièce maîtresse de ma construction académique, et chacune de nos réunions, bien que toujours trop courtes, furent d'une telle intensité que l'on en oubliait souvent le sujet de départ. Jacques a toujours réussi à trouver le temps, dans son réel agenda de ministre, pour m'aider à progresser dans ma réflexion et je lui en suis très reconnaissant. Mais, faire une thèse sous la direction de Jean-François et Jacques n'est pas uniquement une expérience scientifique de haut niveau, c'est aussi un relation empreinte d'humanité, d'humilité et de bienveillance, créant les conditions idéales pour la réussite de leur étudiant. Ma thèse n'aurait sûrement pas pris un tournant aussi positif et décisif sans l'aide précieuse de Basile Audoly. Basile fut est un peu mon troisième directeur de thèse, complétant le brillant duo de Jean-François et Jacques, en y apportant une expertise numérique et mécanique indispensable. Mon projet sur la cytocinèse a pris un véritable tournant grâce à Basile, et je lui dois tout ce que je sais en C++ et en théorie des membranes mécaniques. Le chemin est encore long pour un jour, peut-être, maîtriser le numérique comme il le fait. Son aide et sa disponibilité à toute épreuve ont très largement contribué à la réussite du projet.

La thèse c'est aussi bien-sûr les collègues de labo, qui deviennent souvent des amis. Comment ne pas pouvoir ignorer que l'ambiance de "travail" a largement bénéficié d'une grande complicité avec Edouard, avec qui nous nous sommes rencontrés dès le master, mais aussi Jonas et Alexandre, sans oublier nos chers post-docs, Pierre et Christoph, fraîchement arrivés et avec qui je regrette déjà de ne pas avoir pu passer plus de temps. Je n'oublie pas, bien-sûr, Philippe et Thomas, toujours disponibles et ne tenant jamais rigueur de mes mauvaises blagues. Je les remercie tous pour leur bonne humeur, surtout quand la mienne n'était pas au rendez-vous, notamment parfois ces derniers mois...

La thèse ce sont aussi des collaborateurs, avec qui j'ai eu beaucoup de plaisir à discuter et travailler. J'ai énormément apprécié les longues heures passées à réfléchir avec Timo Betz, dont la capacité à se mettre dans la peau d'un théoricien m'a toujours impressioné, au delà de son expertise expérimentale incontestable. Je le remercie de m'avoir fait confiance, et j'espère un jour pouvoir commencer une nouvelle aventure ensemble. Ma deuxième pensée va à Chantal Roubinet, dont le grand sens physique n'est pas courant pour une biologiste. Nos discussions et projets m'ont beaucoup appris sur la biologie expérimentale, et j'espère que cette complicité continuera encore longtemps. Je ne saurais oublier Philippe Bun, avec qui j'ai découvert un système expérimental extrêmement prometteur, et passé de passionnantes heures de travail. J'espère que ce projet n'est que le début d'une longue histoire, et je remercie Maïté Coppey-Moisan pour avoir accepté de m'y intégrer. Je remercie enfin Cécile Sykes et Charles Baroud pour avoir accepté de former mon comité de thèse, ainsi que l'ensemble des membres du jury que je n'ai pas encore cités d'avoir accepté de lire et évaluer ma thèse: Martine Ben-Amar, Matthew Turner, Arezki Boudaoud, Karsten Kruse et François Nédélec.

Comme je le disais plus haut, la thèse fut également une réelle période de découverte personnelle, et les conditions de travail enviables et la liberté dans lesquelles j'ai eu la chance d'évoluer n'y sont sûrement pas pour rien. Je n'en serai sans aucun doute pas là si ma route n'avait pas croisé celle de Marie, mon rayon de soleil quotidien. Une si belle rencontre, sur une drop-zone, lieu de pratique du parachutisme sportif, ça n'est pas des plus courants ! Tout comme les amis que nous nous y sommes faits. Une toute autre vie a commencé pour moi là-bas en première année de thèse, et je ne compte pas y renoncer. Comment oublier les premiers sauts d'avion et premières chutes libres avec Christophe, Wandrille, Maya... Le parachutisme n'était qu'un début, et me voilà vite embarqué dans l'aventure du speedriding, vous savez ces minivoiles avec des skis qui dévalent les pentes. Voilà la désormais classique semaine à Valfréjus que l'on attend chaque année avec impatience, pour ne pas dire fébrilité, avec Alexandre, Marine et Pierre-Arnaud ! Mais qui dit skis hors-piste, dit ski de rando, et nous voilà embarqués pour de longs week-ends au club-alpin français. C'est une véritable passion pour la montagne à l'état pur que je me suis découvert, avec l'alpinisme et le parapente estivaux et la cascade de glace hivernale. C'est malheureusement le décès accidentel de mon ami Antoine en début d'année sous une avalanche, qui me rappelle désormais tous les jours combien cette irresistible attraction pour la montagne est exigeante.

Je remercie enfin mes parents et mes frères, qui ont toujours cru en moi et ont toujours été à mes côtés, leur amour me suit à chacune des étapes de ma vie.

Contents

General introduction

The surface of animal cells is composed of a lipid bilayer associated with a cytoskeleton. The lipid bilayer constitutes a physical barrier between the intra and extracellular media, thereby controlling selectively the molecular exchanges of the cell with the outside world. The cytoskeleton lies under the lipid-bilayer and gives to the cell its shape and mechanical strength. It is tightly, but dynamically, connected with the lipid bilayer to hold it firm against the intracellular pressure. Despite the connotations of the word *skeleton*, the cytoskeleton is not a fixed structure, but rather a highly dynamic and adaptive network. It is principally composed of polymeric filaments and regulatory proteins.

In this thesis we consider the lipid bilayer and associated cytoskeleton as a single layer, that we call a membrane. In its very broad meaning, a membrane is a thin, film-like structure. In mechanics, a membrane is defined systematically as an elastic or viscous shell that can sustain tangential stress but not flexural moments: it has vanishing bending modulus. In biophysics, on the contrary, the term membrane describes generally the lipid bilayer, which is essentially characterized by a bending modulus.

Membranes, in this thesis, are furthermore called *active*, in reference to the steady consumption of free energy required to sustain their dynamical behavior. One strong feature of cells is indeed the constant production and supply of ATP molecules, that make them "living". ATP is the molecule that provides, through its hydrolysis, the free energy required for the metabolism of cells. This molecular unit of intracellular energy can be converted into mechanical work, for example by molecular motors, or used to assemble and disassemble elements of the cytoskeleton.

The thesis is divided into two parts.

In the first part, we consider the actomyosin cortex, which exists in the vast majority of animal cell types. The cortex is a thin layer of cross-linked filamentous actin polymers steered by molecular motors. The local motors activity, driven by ATP, results essentially in a contractile stress. Integrated over the thickness of the thin cortical layer, this leads to a tension. The cortex provides therefore the surface tension that shapes the cell: the local and time-dependent adjustment of this tension allows the cell to deform and to move.

In this thesis, we study the role of the cortex in cell shape, during cytokinesis and for a polarization process. We propose a viscous-active membrane theory of the cortical layer, using either Eulerian or Lagrangian coordinates. A perturbation approach of the Eulerian equations is used to describe a cell polarization process. Then we implement numerically the Lagrangian formulation to study the large deformations of a cell during cytokinesis. Cytokinesis is the last step of cell division, and corresponds to the physical cleavage of one cell into two. Our model takes into account the mechanics of the whole cell surface, which allows us to study quantitatively the conditions for cytokinesis success.

In the second part of the thesis, we consider the surface of red-blood cells. Deprived of a cortical layer, their membrane is made of a lipid bilayer associated with a hexagonal network of elastic polymers, called spectrin filaments. In this system, the constant supply of ATP is thought to weaken the anchoring of the filaments into the lipid bilayer. Our study is motivated by experimental data showing a violation of the fluctuation-dissipation relation in this system. We propose a theory of active fluctuations of the composite red-blood cell membrane, that takes into account the intrinsic fluctuations of the chemical reaction of filament attachment and detachment. We present preliminary arguments for the origin of the active noise, which is a strong evidence of the living and dynamic nature of human red-blood cell membranes.

Part I

The cell cortex as an active membrane

CHAPTER 1

Introduction: cell shape and cytoskeleton

Contents

1.1 The cell cytoskeleton

The cytoskeleton in eukaryotic cells carries three main functions

- It organizes spatially and transport cell components.
- It connects physically and biochemically the cell to the external environment.
- It controls cell shape and deformation.

Principally composed of interconnected filamentous proteins and regulatory proteins (cross-linkers, motors, nucleators, deconstructors, etc...) it can create very diverse and adaptive structures, which are highly dynamic. We detail below its main components and focus our attention on the mechanical properties of the actomyosin cortex in relation to cell shape control.

1.1.1 Principal components

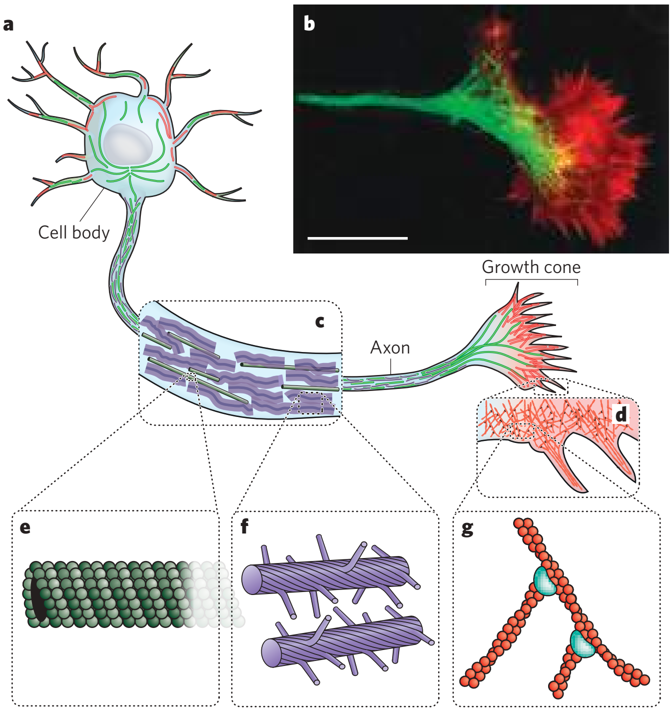

Figure 1.1: Main components of the cytoskelton. (a) Neurons are specialized eukaryotic cells of the nervous system and typically consist of three main skeletal polymers: microtubules (green), intermediate filaments (green) and actin filaments (red). (b) Fluorescence micrograph of the neuronal growth cone where microtubules and actin filaments have been labeled respectively in green and red. (c) The axon is made of intermediate neurofilaments (f) and microtubules (e), whereas the growth cone (d) is a dendritic network of actin filaments. (Adapted from [Fletcher 2010])

Three main types of cytoskeletal polymer are traditionnaly distinguished: actin filaments, microtubules and a family of polymers denoted collectively as intermediate filaments (see fig. 1.1). Despite various structures and mechanical properties at the scale of single polymer filaments, all three cytoskeleton components share common concepts in their organisation and structure. They first self-assemble and interact, giving rise to long-range order. Second their architectural structure, more than their composition, is the key parameter that controls the mechanical properties of the cell. Finally, all three turn over permanently, but within very different time scales, thereby mediating different cellular behaviours at short and long times. We also mention other building blocks associated with cell shape maintainance (septins and plasma membrane.)

1.1.1.1 Actin and myosin

Actin

Actin is a small protein ($43\,kDa$) which spontaneously self-assemble into filaments. Monomeric actin is therefore usually denoted by *G-actin* to differentiate it from filamentous actin, denote *F-actin*. Very abundant (10% of the total mass of cell proteins) and interacting with a high number of other proteins, G-actin is a highly conserved protein among mammalians, presumably because any mutation would affect many of its functions.

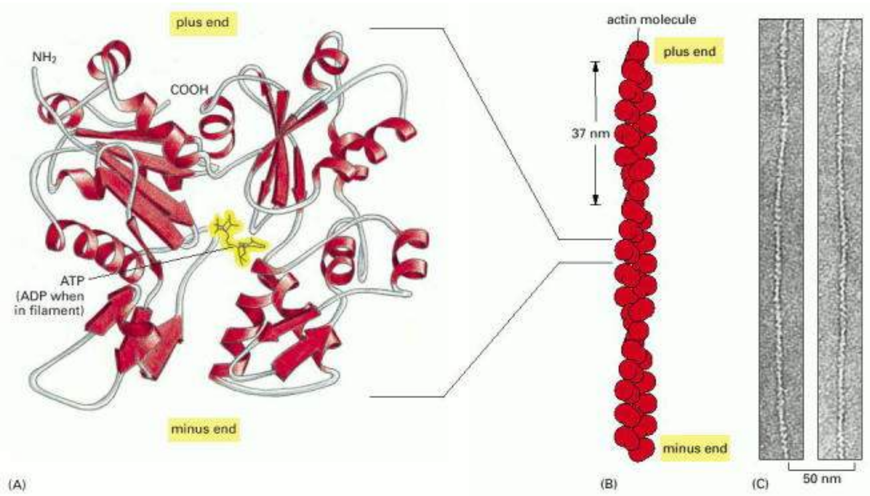

Figure 1.2: Structures of monomeric and polymeric actin. (A) A monomer or G-actin. (B) The filamentous actin, or F-actin, is arranged in a double helix, with a twist of period $37\,nm$, which makes it a polar structure with a plus and a minus end. (C) Electron micrograph of negatively stained actin filaments. (Adapted from [Alberts 2007])

Actin filaments can reach lengths of a few μm and are relatively flexible. Their persistance length [1] is about $17\,\mu m$. They have a double helix structure, composed of two parallel protofilaments (see fig. 1.2 (B)), which makes them polar objects. The

---

[1] The persistance length is the characteristic length over which the angular correlations of the polymer are lost.

two ends of the filaments are usually denoted plus end (or barbed end) and minus end (or pointed end) and are not equivalent in terms of filament growth dynamics.

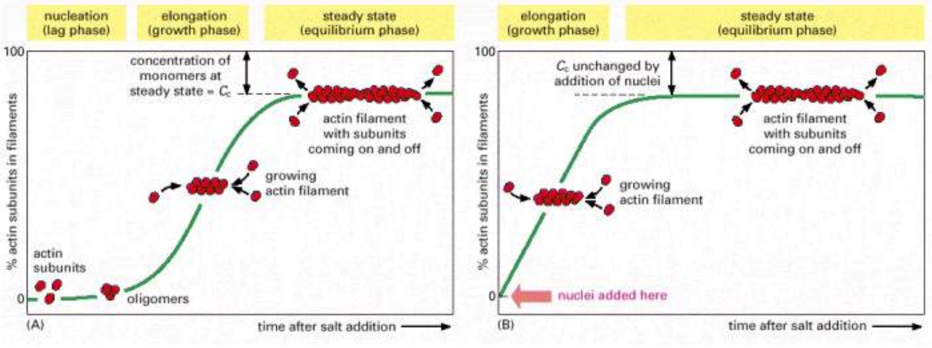

Figure 1.3: Actin nucleation and polymerisation (A) Starting with monomers, growth of filaments is kinetically limited by nucleation of oligomers. (B) Starting from preexisting nuclei suppresses the nucleation lag phase. (Adapted from [Alberts 2007])

Actin polymerisation and depolymerisation The polymerisation of actin *in vitro* is made of three phases: (1) nucleation of an oligomer, made of 3 or 4 monomers, (2) growth of a filament from this nucleation seed, (3) dynamic steady-state with both polymerisation and depolymerisation. The nucleation process is the limiting kinetic factor. This lag phase in filament growth cancels out if pre-polymerized nuclei are added to the solution. The cell takes advantage of this nucleation process to control precisely the localization and the dynamic of actin growth via proteins catalysing actin nucleation, such as Arp2/3 or formins.

Actin filaments preferentially polymerises at it their barbed end. A steady-state is reached for a critical concentration of monomers C_c at which depolymerisation at the pointed end compensates exactly – on average – the polymerisation at barbed end. This process is called treadmilling. ATP promotes the polymerisation at barbed end by hydrolysing actin monomers. It leads to a broad range $[C_c(T), C_c(D)]$ of monomer concentration where treadmilling can arise (see fig. 1.4 A).

In vivo the polymerization and depolymerization of actin filaments is not only controled by nucleation proteins, but also by sequestering, capping and severing proteins.

- Thymosin, which is very abundant in cells, prevent the actin filaments to polymerize byy sequestering actin monomers. To polymerize actin, a second sequestering protein called profilin is activated and competes with thymosin: on the contrary to thymosin, it catalyses actin monomer hydrolysis by ATP, thereby promoting the growth of the barbed end.

- Certain proteins cap specifically pointed ends (tropomodulin) or barbed ends (Cap Z, gelsolin). Cap Z (or simply "capping protein") has a very high affinity to barbed ends and can inhibits its polymerization.

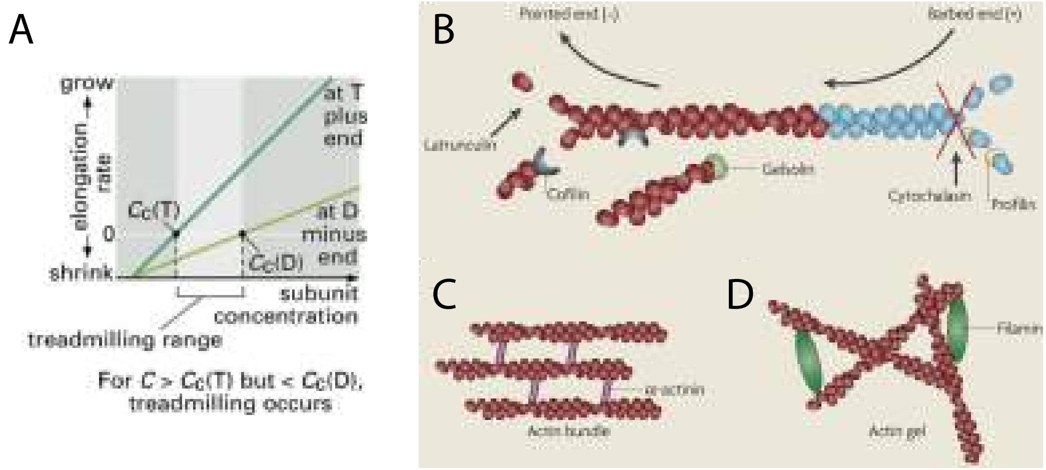

Figure 1.4: Actin treadmilling and actin binding proteins (A) Treadmilling occurs at intermediate concentrations of free subunits, between the critical concentrations at the plus $C_c(T)$ and the minus ends $C_c(D)$. (B) Actin binding proteins can promote depolymerization by severing (ADF/cofilin and gelsolin), or polymerization by sequestering (profilin). Drugs can also block polymerization like cytochalasin (B and D) or promote depolymerization (Latrunculin). (C) Cross-linkers such as α-actinin lead to actin bundles. (D) Filamin, on the contrary, arrange F-actin in a gel. (Adapted from [Alberts 2007] and [Cingolani 2008])

- Severing proteins can sever filaments, as indicated by their names. The most common is ADF-cofilin which can exert torsional stress to the filament, thereby promoting its spontaneous breakage, otherwise very unlikely. Gelsolin can simulatneously cap the barbed end and sever filaments, both effects contributing to reduce the typical filament size.

Drugs can also influence the polymerization dynamics of actin. Cytochalasin B and D are capping proteins for the barbed end, and block polymerization. Filaments that are not stabilized (by tropomodulin for example) have no choice but to depolymerize. Latranculin A sequesters on the contrary G-actin, thereby shifting the equilibrium between F-actin and G-actin toward depolymerization.

Actin filaments organisation Actin filaments self-organize in cells under the mediated action of cross-linkers and motors. Depending on the cross-linker, filaments can organize into bundles, branched networks or randomly, forming a gel-like structure. Resulting reticulated networks have viscoelastic properties that differs strongly from pure actin gels. The cross-linkers are therefore generally classified into three types, depending on the organisation of the resulting network

- Cross-linkers such as α-actinin, fimbrin, fascin or scruin lead to bundles of actin (see fig. 1.4 C).

- Arp2/3 but also α-actinin at low concentration lead to branched actin networks, found for example in the lamellipodia.

- Filamin and spectrin lead to gel-like organisation, where the branching angle is random in the network (see fig. 1.4 D).

Note that the network structure does not depend only on the cross-linker type, but also on its concentration [Lieleg 2010, Cyron 2013].

Furthermore, cross-linker attachment to actin is generally dynamic, with a broad range of attachment times, depending on the cross-linker type [Lieleg 2008]. Some cross-linkers (or motors) have catch-bond-like response to stress, such as α-actinin 4 [Yao 2013]. The various actin structures can therefore display very distinct viscoelastic [Tharmann 2007] and/or non-linear mechanical behaviors [Gardel 2004], depending on the type, the concentration and the dynamics of cross-linkers that generate them. The filament organisation can furthermore lead to strong anisotropies in the mechanical response.

Myosin

Muscle myosin, which is responsible for generating the force for muscle contraction, was the first motor protein identified. Called myosin II, it is the member of a superfamily of actin binding molecular motors that has diversified during evolution to allow the proteins to interact with different cargoes. It comprises at least 18 subfamilies of molecules, numbered from I to XVIII, and composed of one- or two-headed motors.

Myosin II structure and power-stroke Here we focus on the non-muscle Myosin II motor family (Myosin II A and B), which is composed of two heavy chains, each possessing an actin-binding domain (head) and a long α-helix (tail), and two pairs of light chains. The heads contain the binding sites to ATP, that allow the motor to walk on actin filaments by using the energy of ATP hydrolysis to create a power stroke. One of the two pairs of light chains is the substrate of different kinases that regulate the myosin II activity and are hence called regulatory light chains (RLC). The interaction of actin and Myosin II goes through the following cycle:

1. Attached configuration: the myosin head is tightly bound to the actin filament when neither linked to ATP or ADP.

2. Released configuration: when an ATP molecule binds to the myosin head, it detaches from actin by conformational change.

3. Cocked configuration: the myosin closes around the ATP molecule, which causes the head to be displaced along the filament by a distance of about $5\,nm$. Hydrolysis of ATP occurs but ADP and Pi stay tightly bound to the protein.

4. Power stroke: the release of Pi allows the head to bind again tightly to actin. The release of ADP corresponds to the conversion of hydrolysis energy into a

movement: a conformation change triggers the power stroke that moves the actin filament.

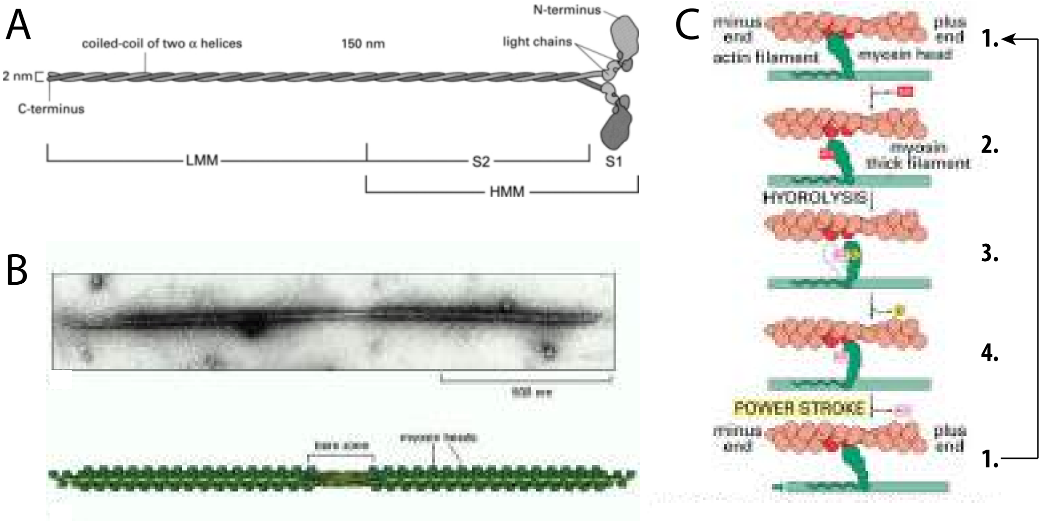

Figure 1.5: Myosin II motor structure, self-assembly and power stroke mechanism (A) Myosin II molecule is composed of two globular heads that can bind to actin and hydrolyse ATP, a regulatory neck domain, forming the myosin light chains (MLC) and a tail of two coil-coiled α-helices, that forms an extended rod in solution. (B) Micrograph and sketch of an isolated myosin II bipolar thick filament: myosin II molecules aggregate by means of their tail ragions, while their heads are exposed to the outside of the filament. (C) Cycle of changes by which a myosin II molecule walks along an actin filament by a power stroke mechanism. (Adapted from [Alberts 2007])

Thus, the association of myosin motors with the actin filament is regulated by the ATPase cycle. The different myosin motors vary in the time they spend in the tightly bound state per ATPase cycle: this fraction is measure by the duty ratio. Myosin II motors have a low duty ratio: myosin head spends little time in association with actin, its motion is called non-processive. On the contrary, others myosin motors, such as Myosin V, move processively for many steps before detaching [Howard 1997].

Myosin II proteins self-assemble into particles of two sizes, named mini-filaments (or thin filaments) and thick filaments [Pollard 1982]. The mini-filament is composed of about 16 motors, whereas thick filaments contain about 300 motors. In muscles, the contractile unit containing myosin II thick filaments are called sarcomeres (see fig. 1.5 B)

Non-muscle myosin II regulation Myosin II interaction with actin can create contractile stress within a gel (see section 1.1.2.3). The activity of Myosin II in non-muscle cells controls migration and deformation, and needs therefore to be tightly regulated. In eukaryotic cells, this regulation is mediated essentially by the phosphorylation of myosin light chains (MLC). When the light chains are not phosphorylated, Myosin molecules adopt an inactive folded conformation, which prevents them to bind to actin or to interact to form bipolar thick filaments. We describe the effect of a few major kinases, responsible for the phosphoryation of these light chains. The Myosin Light Chain Kinase (MLCK) phosphorylates the regulatory light chain (RLC). It induces a conformation change which unfolds the myosin tail, thereby making binding sites accessible. Myosin II is active and can self-assemble into thick filaments (see fig. 1.6). Note that MLCK phosphorylation is effective only in the presence of Ca^{2+}, but other kinases like the Rho-kinase or ROCK can phosphorylate the regulatory light chains independently of calcium. ROCK is the effector of the small GTPase Rho[2] (see section 1.2.2.1). ROCK furthermore inhibits myosin phosphatases, which dephosphorylate the RLC [Kimura 1996], thereby contributing in two different manners to myosin II activation.

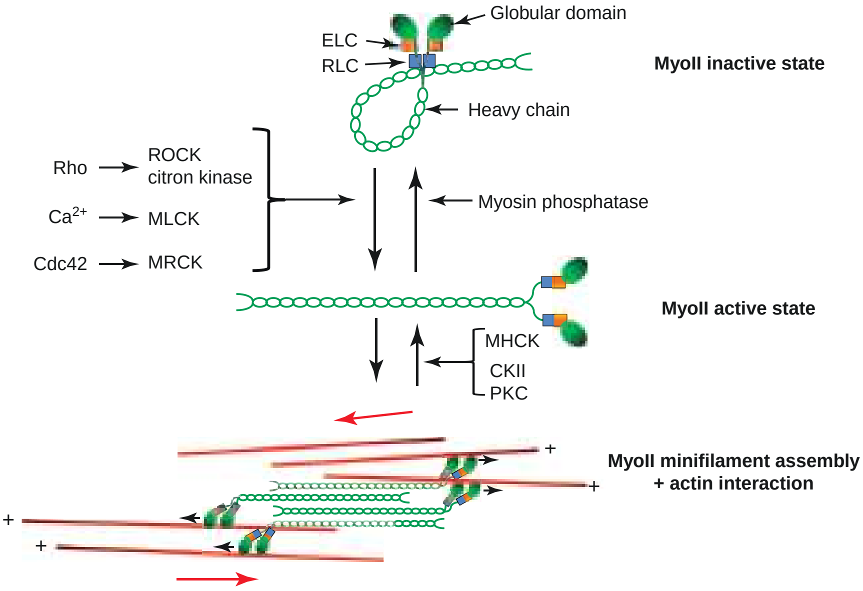

Figure 1.6: Biochemical pathways controlling Myosin II activation and minifilament assembly. Myosin conformation changes upon phosphorylation of its regulatory light chain (RLC) by multiple kinases. The assembly into minifilaments is controlled by the phosphorylation of the heavy chain. (Adapted from [Levayer 2012])

The myosin II heavy chains (MHC) also have phosphorylation sites. The protein kinase C (PKC) inhibits the formation of bipolar filaments of Myosin II B, whereas the small GTPase Rac antagonize Rho by regulating phosphorylation of the myosin II heavy chain [van Leeuwen 1999].

The myosin II activity can finally be affected by drugs. We mention two major ones:

- Blebbistatin is a spectific inhibitor of non-muscle Myosin II [Straight 2003]. It blocks the Myosin II in its detached state (see fig. 1.5 C state 3.), thereby preventing the powerstroke of the motor.

---

[2] Rho means "Ras-homologous": small Rho GTPases are members of the super-family of GTPases Ras.

- Y27632 is an inhibitor specific of the Rho-kinase (ROCK). Cells treated with this drug have therefore a very low level of RLC phosphorylation, but the action of the drug is not specific to myosin II.

1.1.1.2 Microtubules

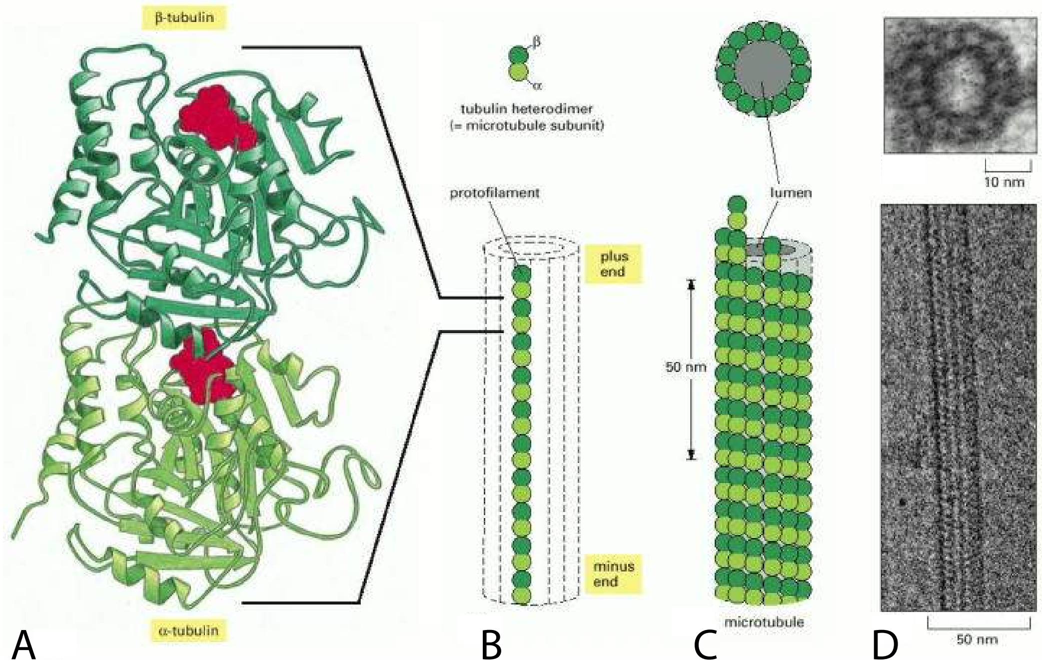

Figure 1.7: Microtubule structure. (A) Subunit formed from a pair of α- and β-tubulin. (B) Protofilament composed by the association of several subunits. (C) 13 protofilament can assemble in parrallel into a hollow cylindrical microtubule filament. (D) Electron micrograph of the cross-section and a segment of microtubule. (Adapted from [Alberts 2007])

Microtubules are polymers formed from protofilaments of tubulin. Tubulin protofilaments are made of heterodimers formed from α-tubulin and β-tubulin, tightly bound together. 13 protofilaments can assemble in parallel into a hollow cylindrical structure called a microtubule (MT). The nucleation of MTs is mediated by the Microtubule Organizing Center (MTOC), which comprised in particular the centrosomes. Microtubules are highly dynamic structures that display successive periods of growth and shrinkage (called catastrophes). More rigid than actin filaments, their persistence length is of the order of the mm [Gittes 1993]. Microtubules are polar structures and have also their specific molecular motors, composed of two main families: the kinesins that walk toward the plus end of the filament, and the dyneins that walk toward the minus end. Microtubules have various roles in cytoplasmic transport, signalling, polarisation and mitosis, but we focus only on their role in cytokinesis, detailed in the next section (see section 1.2).

1.1.1.3 Intermediate filaments

Intermediate filaments (IFs) have been less studied by physicists than the two previous cytoskeleton components, possibly because they do not have specific molecular motors because of their apolar structure. However the family of genes that encode functional intermediate filaments proteins in human cells, with 67 genes, is one of the largest in the human genome [Chang 2004]. Intermediate filaments have been classified into five distinct types: keratins (types I and II), type III (vimentin, desmin), type IV (neurofilaments) and the nuclear IFs forming the type V (lamins). The assembly of IFs takes place in three steps: tetramers first associate to form unit-length filaments; these unit-length filaments then anneal end-to-end to form loosely packed filaments of a few of *nm*; finally these filaments compact to produce mature IFs (see fig. 1.8). Intermediate filaments have been shown to turn over in cells on long time scales (several minutes to one hour), this property being furthemore highly dependent on microtubules. Intermediate filaments have indeed been shown to interact with microtubules very early, forming for example closely associated parallel arrays throughout the cytoplasm in fibroblasts [Goldman 1971], and are also thought to interact with actin filaments: treatment of epithelial cells with cytochalasin D has been shown to disrupt the organization of keratin intermediate-filaments networks [Green 1987] and half of the total actin motor Myosin Va is associated to IFs in neurons. Relatively little is however known on the contribution of intermediate filaments on the cell mechanics. Recent studies suggest that they participate in the mechanical integrity of cells and in the cellular localization of organelles by increasing the overall cell stiffness [Guo 2013].

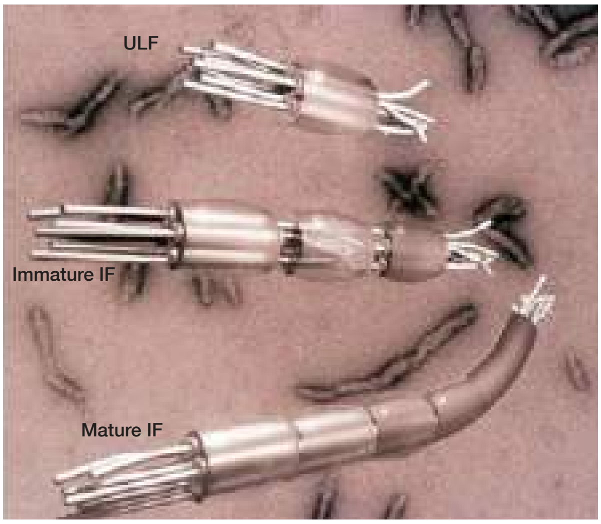

Figure 1.8: Intermediate filaments assembly *in vitro*. Unit-length filaments anneal end-to-end to form immature intermediate filaments, that further compact to form mature filaments. (Adapted from [Chang 2004])

1.1.1.4 Septins

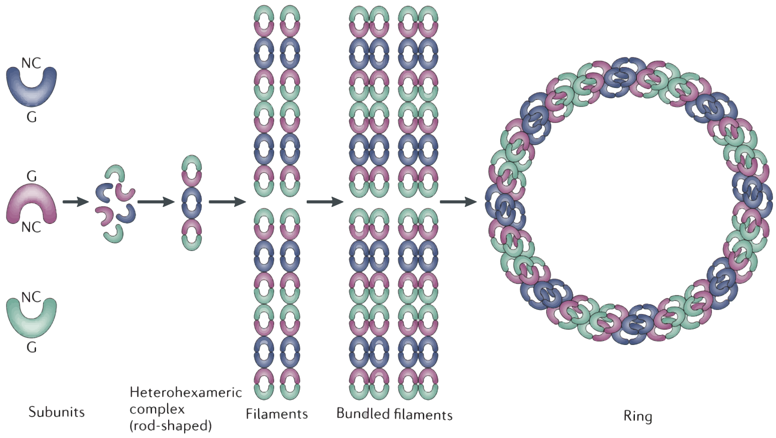

Figure 1.9: Septins assembly *in vitro*. Septin subunits interact via their GTP-binding domain denoted G-domain and their amino and carboxy-terminal regions, denoted NC interface, to form complexes. Joining end-to-end these complexes assemble into filaments. The different colours depict different groups of septins. The resulting filaments are apolar and can further assemble inot bundles or high-order structures such as rings. (Adapted from [Mostowy 2012])

Septin proteins form a highly conserve family in eukaryotes and have been recently proposed to be a fourth component of the cell cytoskeleton [Mostowy 2012]. Septins are classified into four homology groups, denoted SEPT2, SEPT3, SEPT6 and SEPT7. All septins can form heteromeric complexes, which associate to form high-order structures like filaments, bundles and rings. Septin-septin interactions are regulated by GTP hydrolysis, which induces conformational changes in the phosphorylation site, called G-domain, and in the NC interface, for amino and carboxy-terminal regions (see fig. 1.9). The different high-order structures of septin have been reported to been involved in an expanding number of key cellular processes, in particular in late cytokinesis [Joo 2007]. They have indeed been shown to interact with actin [Kinoshita 2002], Myosin II [Joo 2007], microtubules [Bowen 2011], as well as phospholipid membranes [Bertin 2010]. A recent study identified a role of septins in the contractility of the actomyosin ring [Founounou 2013], but their mechanical and biochemical functions remain still unclear.

1.1.2 The actomyosin cortex controls the cell shape

The cell cortex is a thin, crosslinked network of actin filaments lying immediately beneath the plasma membrane in animal cells (see fig. 1.10). It is the key regulator of the cell shape. We first detail its structure and dynamical properties, which are the basis for understanding its mechanical properties, explained in a second step. Finally we expose briefly the active-gel framework that has been recently proposed to account for actomyosin rheology.

1.1.2.1 Structure and dynamics

Structure and composition
The cell cortex is composed mainly of actin filament and non-muscle myosin II motors as shown in fig. 1.10. It contains also cross-linkers, mainly α-actinin [Mukhina 2007], and many regulatory proteins of actin and myosin activity (for a more exhaustive list of the cell cortex molecular components see [Biro 2013]). Electron microscopy studies have revealed a dense crosslinked network of actin filaments where filaments are preferentially parallel to the plasma membrane [Medalia 2002] and isotropically oriented in the membrane plane [Morone 2006] (see fig. 1.11 A). Due to the uncertainty of sample preparation in electron microscopy, the precise 3-dimensional organization and polarity of the filaments has however not been clearly established. The network mesh size has been measure by electron microscopy to be about a few tens of nanometers [Morone 2006] and the cortex thickness was evaluated in the range of $200 - 300\,nm$ in Dictyostelium discoideum cells [Medalia 2002] (see fig. 1.11 B). Recently a new experimental technique based on simultaneous fluorescence imaging of the plasma membrane and actin cortex was proposed to measure the cortex thickness in living cells [Clark 2013]. The distance Δ between the two fluorescence peaks is shown to be essentially half of the cortex thickness h, and the average cortex thickness in mitotic HeLa cells is evaluated to be about $200nm$.

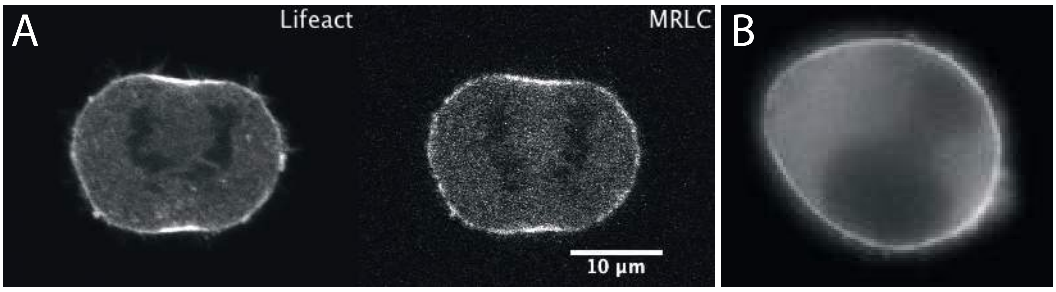

Figure 1.10: Cell cortex. (A) Dividing L929 mouse fibroblast cell. F-actin and myosin II are visualized by fluorescence using Lifeact-GFP and MRLC-tdRFP respectively (Adapted from [Sedzinski 2011]). (B) Swiss 3T3 polarized fibroblast. Myosin II A is visualized by fluorescence using eGFP-MyoIIA. (Courtesy of P. Bun)

The attachment of the cortex to the plasma membrane is regulated by the family of ERM proteins (Ezrin, Radixin, Moesin), but nucleators of actin like formins and Arp2/3 may also associate actin to the membrane. The plasma membrane can however detach locally from the underlying cortex in a bulge called a bleb. Blebbing reveals that membrane-to-cortex attachment is essential to maintain the integrity of the cortex: a few tens of seconds after membrane detachment, the remaining cortex depolymerizes and repolymerizes on the detached membrane, as shown on fig. 1.12. Blebbing reveal hence that the actomyosin cortex is a highly dynamic structure that turns over permanently.

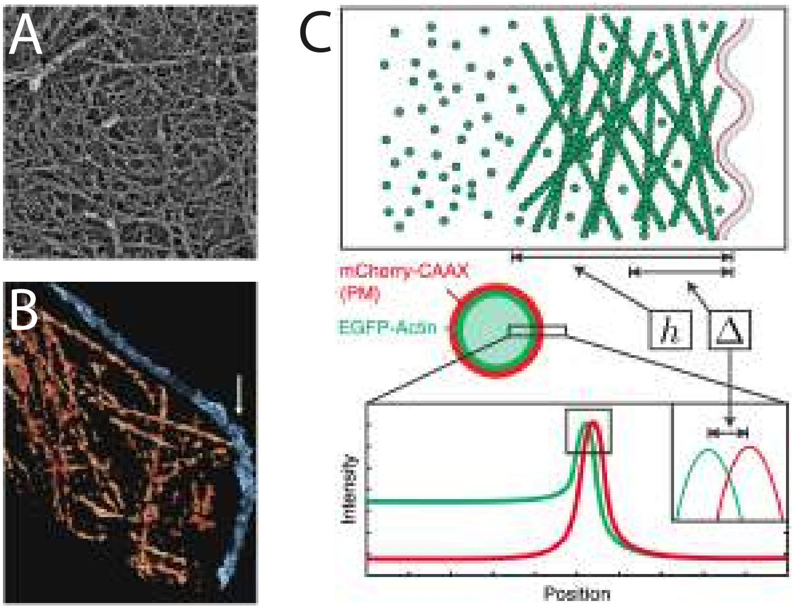

Figure 1.11: Cell cortex structure and thickness. (A) Electron micrograph of the actin network beneath the plasma membrane of normal rat kidney fibroblast (NRK) (Adapted from [Morone 2006]). (B) 3-dimensional reconstruction from a $500\,nm$ by $300\,nm$ micrograph of the cortical region of a Dictyostelium cell, showing membrane-associated actin filaments (in red, the membrane in blue)(Adapted from [Medalia 2002]). (C) Schematic representation of the cortex and its thickness (Adapted from [Clark 2013]).

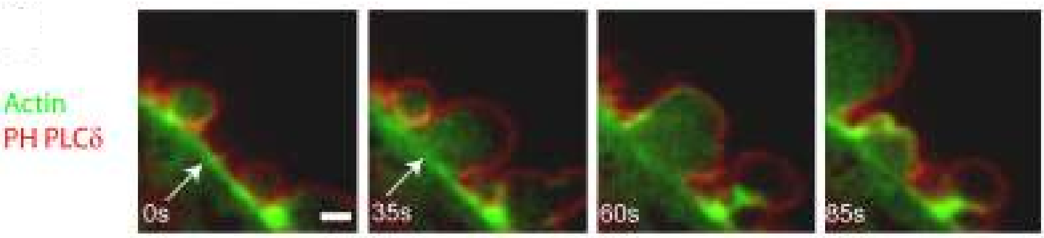

Figure 1.12: Localization and dynamics of actin during bleb expansion and retraction in confocal microscopy. The plasma membrane is marked in red and actin in green. (Adapted from [Charras 2006]).

Turnover of actin and myosin

The molecular components of the cortex are highly dynamic and their turnover time has been measured in various cell types by fluorescence recovery after photobleaching technique (FRAP). The whole cortex is generally entirely renewed in about $1\,min$. The dynamics of myosin and cortical cross-linking proteins (α-actinin, dynacortin, and fimbrin) is the fastest, with typical recovery half-times of a few seconds [Uehara 2010, Mukhina 2007, Reichl 2008].

The turnover of actin has been measured during mitosis in animal cells [Guha 2005, Murthy 2005] (LLCPK1 and NK1 cells) and was shown to be of the order of a few tens of seconds, or even faster in the furrow region during telophase[3]. Recent measurements in blebbing M2 melanoma cells by FRAP and fluorescence loss after photoactivation (FLAP) have been compared to first-order reaction kinetics and suggest the presence of two subpopulations of actin filaments with different turnover rates [Fritzsche 2013]. A first population, the most abundant, has a turnover half time of less than $1\,s$, whereas the second population turns over with a half time of $25s$. The turnover was also found to be in average four time faster in fresh cortices that newly forms in blebs.

1.1.2.2 Mechanical properties

Viscoelasticity

The turnover results suggest that in response to any deformation applied on time-scales longer than the minute, the cortex should behave like a fluid because elastic stresses are necessarily relaxed in the renewing process. The attachment/detachment kinetics of a single cross-linker is enough to fluidize a polymer network on time scales much longer than its turnover time [Heussinger 2012], but it leads to a broad spectrum of macroscopic relaxation times due to the abscence of correlations between unbinding events [Broedersz 2010]. Cross-linkers have also been shown to influence actin turnover by hindering depolymerization *in vitro* [Schmoller 2011]. Myosin motors activity on the contrary enhances actin filament turnover *in vitro* by a severing process mediated by filaments buckling [Murrell 2012, Vogel 2013], as suggested by *in vivo* studies [Guha 2005, Haviv 2008]. If most theoretical and experimental studies show that the cortex behaves like a fluid at long time scales, the precise interplay between cross-linkers dynamics, actin dynamics and motor contractility that generate the complex viscoelastic rheology of the cortex remains far from being understood [Wen 2011].

Actomyosin contractility

The ability of actomyosin gels to contract under the concerted action of myosin motors has been characterized experimentally for many years. The traditional picture of contraction is the muscle sarcomere arrangment of antiparallel actin filaments connected by myosin filaments, which leads intuitively to contraction when myosin motors walk toward the plus end of actin filaments (see fig. 1.13 A). But in isotropic disordered actomyosin gels (see fig. 1.13 B), the microscopic mechanism that generates contractility remains poorly understood. It has been recently argued that 1-dimensional structures like actin bundles, which do not have a sarcomere-like organisation of their filaments, require a non-linear elastic response of filaments to generate contractility [Lenz 2012a]. From a theoretical point of view, there is no reason *a priori* that myosin activity would produce rather contraction than expansion of the network. A possible mechanism to break this symmetry, and to lead effectively to contraction in disordered network, has been proposed to emerge from the asymmetric load response of actin filaments: if they can support large tension, they will easily

---

[3] See section 1.2 for a definition of the telophase.

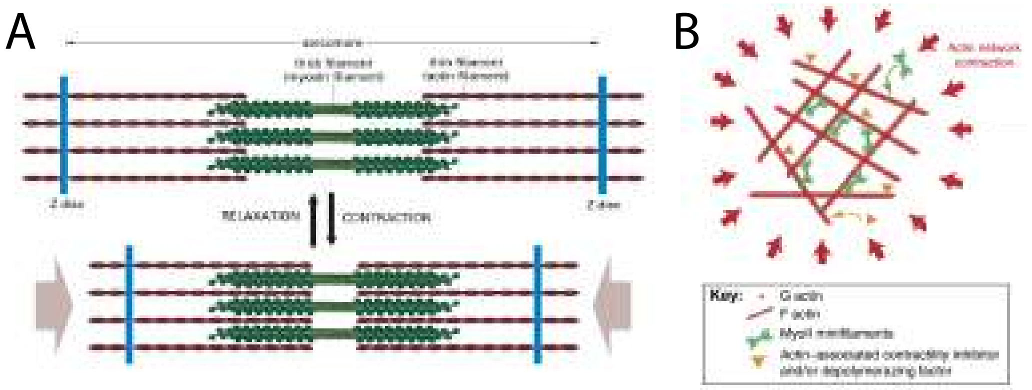

Figure 1.13: Force generation in actin structures. (A) Sarcomeric organization of actin filaments and myosin thick filaments: the motors walk toward the plus end of actin filaments, thereby contractin the sarcomer (Adapted from [Alberts 2007]). (B) Sketch of the contraction of a disordered actomyosin network (Adapted from [Levayer 2012]).

buckle under compression [Soares E Silva 2011]. This non-linear buckling response of filaments has been recently characterized *in vitro* [Lenz 2012b, Murrell 2012].

Cortex tension and cell shape

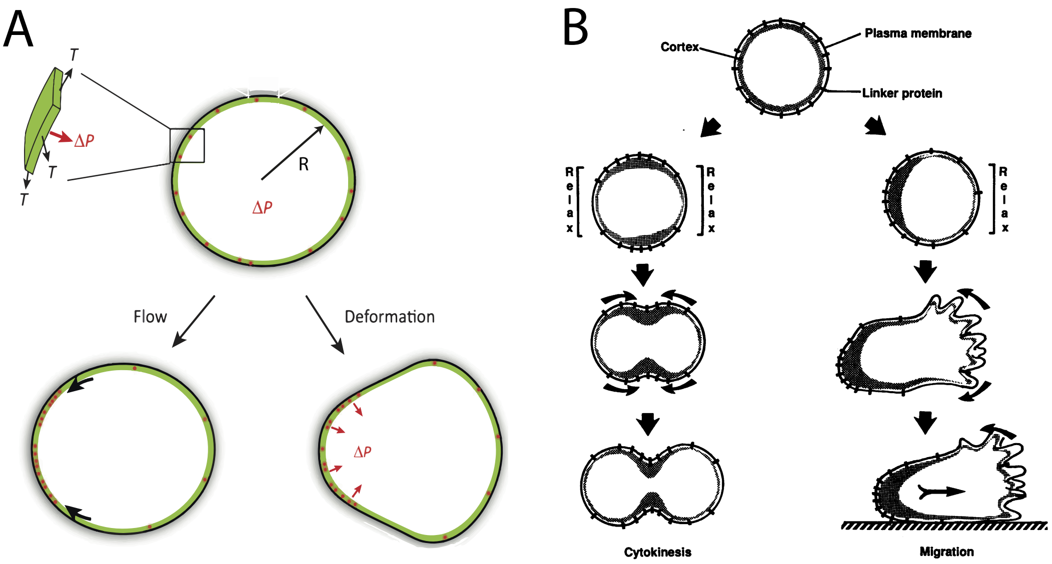

Figure 1.14: Cortex tension and cell shape. (A) The membrane is described by the thin black line, the cortex by the green layer and the local motor contractility by red dots. (top) Cortical tension gives rise to an hydrostatic pressure ΔP in the cytoplasm. (bottom left) Gradients of contractility give rise to tangential cortical flow along the cortex on long time-scales. (bottom right) On short time scales, local contraction can give rise to shape deformation with net cytoplasm displacement (non-uniform cytoplasmic pressure) (Adapted from [Salbreux 2012]). (B) Sketch of analogous cortical flow movements in cytokinesis and cell polarization/migration (Adapted from [Bray 1988]).

The internal stress within the actomyosin layer, when integrated over the thin cortex layer thickness leads to an effective tension [Salbreux 2007]. Cortical tension is the key determinant of the morphology of an isolated cell: a uniform tension T gives rise to an hydrostatic pressure ΔP and to a spherical shape of radius R, according to normal force balance given by Laplace's law $\Delta P = \frac{2T}{R}$. The tension is mostly regulated by contractility generated by myosin motors, and local imbalance of contractility leads to cortical flows along the cortex at long time scales, as proposed by Bray and White in their seminal review [Bray 1988]. Drastic cell deformations like cytokinesis or amoeboid cell migration are proposed to be driven by the same mechanism of cortical flows that pulls cortical components from regions of relaxation toward regions of contraction. Cortical flows have also been shown experimentally to be a key determinant for the segregation of polarity determinants during the fertilization of C. Elegans zygote [Munro 2004, Goehring 2010]. The cortical tension is however not simply the result of its contractility and the viscoelastic resistance of the actomyosin gel upon elastic or viscous deformation, can also contribute, positively or negatively, to the total cortex tension [Salbreux 2009, Mayer 2010]. The cortical tension has been evaluated by different techniques. The cortical tension can be measured through the pressure required to aspirate a cell inside a micropipette [Evans 1989, Tinevez 2009] (see fig. 1.15 A), or can be inferred from the force necessary to compress a cell between two plates [Yoneda 1972] or with the tip of an atomic force microscope (AFM)[4] [Lomakina 2004] (see fig. 1.15 B). Cortical tension measurements can vary by two orders of magnitude between cell types, ranging from a few tens of $pN\mu m^{-1}$ to several thousands of $pN\mu m^{-1}$. All these tension measurement techniques are however strongly dependent on the underlying model assumption, especially on the elastic or viscous feature of the cortex at the time scale of experiment. An important parameter, sometimes neglected, is the contribution

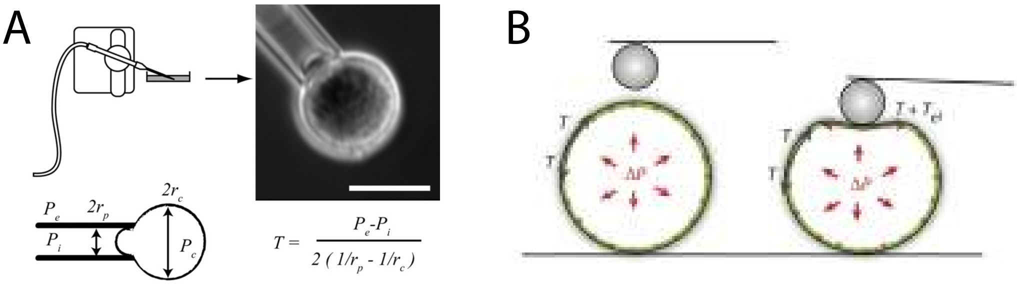

Figure 1.15: Cortex tension measurement. (A) Micropipette aspiration technique. Microscope image of a L929 cell aspirated into a micropipette (scale bar, 10 μm) and corresponding description. The tension T is given by the formula, as a function of the difference of pressure between the micropipette P_i and the exterior P_e and of the pipette and cell curvature radii r_p and r_c (Adapted from [Tinevez 2009]). (B) Schematic description of the atomic force microscopy indentation technique. A bead replaces the AFM tip pushes on the cell, which responds by a force that depends on the tension, elastic deformation of the cortex and on hydrostatic pressure (Adapted from [Salbreux 2012]).

---

[4] The AFM tip is often replaced by a bead in these experiments.

of the hydrostatic and osmotic pressures to the cell response.

Volume and pressure regulation

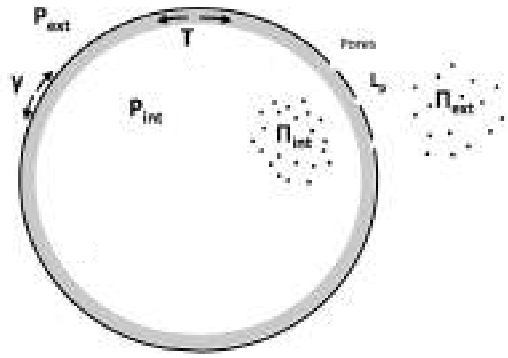

Figure 1.16: Cell volume and pressure regulation. The cortical (and membrane) tension $T + \gamma$ create a normal force that balances the hydrostatic pressure $\Delta P = P_{\text{int}} - P_{\text{int}}$. The osmotic pressure $\Delta\Pi = \Pi_{\text{int}} - \Pi_{\text{ext}}$ comes from an imbalance of osmolytes (ions and small molecules) accross the cell. Ions and water molecules can cross the plasma membrane via pores, mechano-sensitive channels or active pumps.

When the cortex is curved, its tension results in a normal force that is balanced by hydrostatic pressure. The osmotic pressure comes from the imbalance of ions and small molecules between the cytosol and the external medium (see fig. 1.16) and is typically of the order of $\sim 10^2 - 10^3\, Pa$ in animal cells. The osmotic pressure is therefore actively regulated by ion-pumps and mechano-sensitive channels that wrap the plasma membrane and allow ions to respectively enter or escape the cytosol. Mechano-sensitive channels are sensitive to the plasme membrane tension γ, that we ignored up to now because it is generally one order of magnitude lower than the cortical tension. The plasma membrane is furthemore partially permeable to water molecules, a property enhanced by the presence of aquaporins [Karlsson 2013]. An imbalance between osmotic and hydrostatic pressure differences accross the cell boundary (respectively $\Delta\Pi = \Pi_{\text{int}} - \Pi_{\text{ext}}$ and $\Delta P = P_{\text{int}} - P_{\text{ext}}$) can therfore lead to cell volume variations, according to a permeation dynamics of the form

$$\frac{dV}{dt} = n_p\, L_p \,(\Delta\Pi - \Delta P)\ . \tag{1.1}$$

where n_p is the total number of water pores in the membrane and L_p is the permeability of a pore. The cell volume is thus the result of a complex interplay between ion dynamics, plasma membrane tension and cortical mechanics and activity [Jiang 2013]. Experimentally, the cortex tension has only a small influence on volume, because resulting hydrostatic pressure variations are weak. Shape changes associated with cell swelling are therefore likely to be mainly directed by ion pump dynamics. Depolymerizing the actin cortex in a round cell leads thus only to a 10%

cell size increase; on the contrary, the metaphase cell rounding is thought to be mainly driven by osmotic changes [Stewart 2011].

1.1.2.3 Coarse-grained modeling of the cell cortex

Microscopic modeling of cortical actomyosin gels requires to know in details the molecular components and mechanisms at work. We have seen above (see section 1.1.2.2) that the origin of contractility itself in polymer networks was not fully understood. Stochastic molecular simulations may at some point reproduce accurately the mechanical properties of the cortical layer, but coarse-grained approach prove to be efficient to describe the mechanics of the cortex at the whole cell scale. Coarse-grained approaches do not require detailed knowledge of the microscopic interactions between filaments, motors and cross-linker, but rather describe the network as a continuous viscoelastic gel, where a contribution to the internal stress comes from active processes. Coarse-grained models however require the introduction of phenomenological coefficients, which need to be matched *a posteriori* to experimental molecular properties.

The polar active gel theory

The terminology of *gels* is used here to describe the visco-elastic properties of the actomyosion cortex, characterized by a typical Maxwell visco-elatic relaxation time $\tau_{\text{Maxwell}} = \frac{\eta}{E}$, where η is the viscosity of the gel and E its elastic Young modulus. The word *active* refers to the permanent local consumption of energy, in the form of ATP molecules, by myosin molecular motors. Finally the word *polar* refers to the description of the filament polarity.

The one-component active-gel theory [Kruse 2005] has proven to describe successfuly cortical flow anisotropies in the C. Elegans zygote [Mayer 2010], filament orientation patterns during the formation of the contractile ring in cytokinesis [Salbreux 2009], or cell migration in a 3-dimensional matrix [Hawkins 2011].

Active-gels are hydrodynamic theories. They consist in keeping only the physical slow variables, i.e. that relax slowly in time and on large length scales, the other variables being supposed at thermodynamic equilibrium [Chaikin 2000]. Such theories have been successful in describing liquid crystals, polymers, gels etc... The active-gel theory is an extension of the hydrodynamic theory for liquid crystals to active systems.

The derivation of the continuous dynamics equation for the hydrodynamic variables can be systematically carried out following the general scheme established in [De Groot 1962] and [Martin 1972]. After identifying generalized fluxes and conjugate forces in the system, fluxes are written as a function of the forces at the linear order of approximation, following Onsager relations [Onsager 1931] and the symmetries of the system:

$$flux \leftrightarrow force \;\|\; \sigma_{\alpha\beta} \leftrightarrow v_{\alpha\beta} \;\|\; p_\alpha \leftrightarrow h_\alpha \;\|\; r \leftrightarrow \Delta\mu$$

$\sigma_{\alpha\beta}$ is the stress tensor in the active gel, $v_{\alpha\beta}$ is the strain rate tensor. p_α is the local filament polarity (or order parameter) and h_α is called the molecular field [de Gennes 1995]. r is the rate of ATP consumption and $\Delta\mu$ is the chemical potential difference between ATP and its hydrolysis products, ADP and inorganic phosphate, specifically[5] $\Delta\mu = \mu_{\mathrm{ADP}} + \mu_{\mathrm{Pi}} - \mu_{\mathrm{ATP}} \geq 0$.

The activity comes from the steady consumption of ATP, driven by a strictly negative chemical potential $\Delta\mu < 0$. When $\Delta\mu$ vanishes the chemical reaction is therefore at equilibrium and there is no energy production.

We do not detail her the derivation for polar active gels, which can be found in [Kruse 2005], but rather present below directly its results in the viscous limit ($t \gg \tau_{\mathrm{Maxwell}}$)

$$2\eta v_{\alpha\beta} = \sigma_{\alpha\beta} - \left(\zeta\Delta\mu p_\alpha p_\beta + \zeta'\Delta\mu p_\gamma p_\gamma \delta_{\alpha\beta} + \bar{\zeta}\Delta\mu\delta_{\alpha\beta}\right) - \frac{\nu_1}{2}\left(p_\alpha h_\beta + p_\beta h_\alpha\right) - \bar{\nu_1} p_\gamma h_\gamma \delta_{\alpha\beta}\,, \tag{1.2a}$$

$$\frac{Dp_\alpha}{Dt} = \left(\frac{1}{\gamma_1} h_\alpha + \lambda_1 p_\alpha \Delta\mu\right) - \left(\nu_1 v_{\alpha\beta} p_\beta + \bar{\nu_1} v_{\beta\beta} p_\alpha\right), \tag{1.2b}$$

$$r = -\zeta p_\alpha p_\beta v_{\alpha\beta} - \bar{\zeta} v_{\alpha\alpha} - \zeta' p_\alpha p_\alpha v_{\beta\beta} + \Lambda\Delta\mu + \lambda_1 p_\alpha h_\alpha\,. \tag{1.2c}$$

The first equation (1.2a) generalizes the expression of the stress tensor $\sigma_{\alpha\beta}$ for Stokesian viscous fluids to active polar systems. The active terms are proportional to $\Delta\mu$. We remark that even in absence of external load $\sigma_{\alpha\beta} = 0$, internal active terms, measured by the coefficients ζ, ζ' and $\bar{\zeta}$ can lead to flows ($v_{\alpha\beta} \neq 0$). The terms ζ' and $\bar{\zeta}$ contributes isotropically to the stress tensor. The sign of these coefficients is given by experiments, which show that such systems are contractile, rather than expansile. To lead to contractility, they are chosen positive[6], consistently with our convention $\Delta\mu > 0$.

The second equation (1.2b) describes the dynamics of the polar order parameter **p**. The active term, proportional to the coefficient λ_1, tends to align filaments parallel to each other. Other terms are traditional liquid crystals coupling terms between the order parameter and the flow (ν_1 and $\bar{\nu_1}$) or dissipating term proportional to the rotational viscosity γ_1.

The third equation (1.2c) is specific to active gels and describes the rate of ATP consumption r, essentialy driven by the coefficient Λ but also modulated by the myosin activities (terms proportional to ζ, ζ' and $\bar{\zeta}$) and by the coupling between the gel and the molecular field h

The molecular field is defined as the opposite of the functional derivative of the

---

[5] Note that the convention for $\Delta\mu$ here is the same as in the original paper [Kruse 2005], but inversed compared to the second part of the thesis, related to red-blood cell membrane fluctuations, where we defined $\Delta\mu_{\mathrm{ATP}} = \mu_{\mathrm{ADP}} + \mu_{\mathrm{Pi}} - \mu_{\mathrm{ATP}} \leq 0$.

[6] Note that, in comparison to the original paper [Kruse 2005], we have chosen ζ, ζ' and $\bar{\zeta}$ positive and inversed their signs in the active-gel equations.

free elastic energy with respect to the parameter order **p** [de Gennes 1995]

$$\mathbf{h} = -\frac{\delta \mathcal{F}}{\delta \mathbf{p}}\,, \tag{1.3}$$

where $\mathcal{F}$ is the polar Frank-Oseen free energy [Frank 1958, de Gennes 1995]

$$\mathcal{F} = \int d^2r \left[\frac{K_1}{2}(\nabla.\mathbf{p})^2 + \frac{K_2}{2}(\mathbf{p}.\nabla \times \mathbf{p})^2 + \frac{K_3}{2}(\mathbf{p} \times \nabla \times \mathbf{p})^2 + k\nabla \cdot \mathbf{p} \right]\,. \tag{1.4}$$

K_1, K_2 and K_3 are the bend, splay and twist elastic moduli of the gel. The three Frank constants are sometimes considered of the same order of magnitude for small molecules $K_1 \sim K_2 \sim K_3 \sim K$.

Note that generalizations of the previous 1-component equations have been proposed to take into account permeation effects of the fluid within the network [Joanny 2007, Callan-Jones 2011].

The interplay of actin turnover and active contractility was also recently studied in the framework of the active-gel theory [Joanny 2013]. The cortical actomyosin layer is described as an active wetting film, whereby actin condenses on the membrane driven by myosin contractility.

1.2 Cytokinesis in animal cells, a brief overview

1.2.1 The final step of cell division

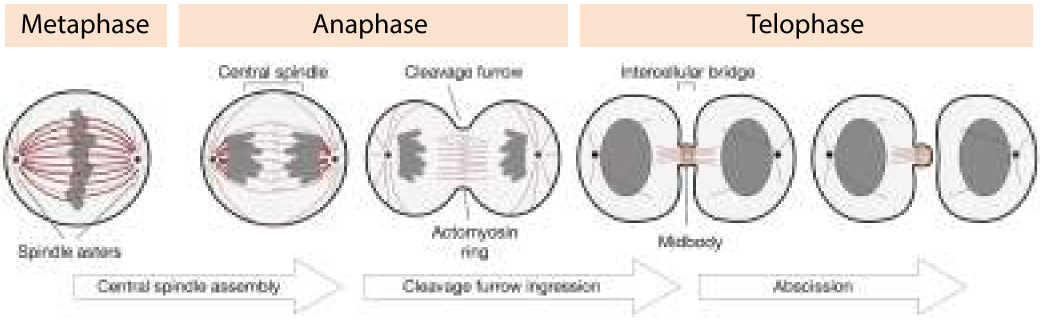

Figure 1.17: Overview of animal cell cytokinesis: schematic representation of the cell surface (in black), microtubules (MTs) (in red) and chromatids (in grey) reorganization stages. Cytokinesis begins at early anaphase: the MTs from the mitotic spindle (asters and/or central spindle) signal to the cell cortex to induce the assembly of an actomyosin contractile ring at the cell division plane. The constriction of the actomyosin ring leads to the invagination of the cell membrane and to the ingression of this cleavage furrow until a narrow intercellular bridge remains, called the midbody. The midbody is the organizing center for the recruitment of the abscission machinery (Adapted from [Fededa 2012]).

Cytokinesis is the process of physical cleavage at the end of cell division that partitions the content of a cell into two daughter cells. In animal cells the physical separation occurs in two major stages: the formation and the ingression of a cleavage furrow and the abcission, which corresponds to the final cut (see fig. 1.17). From the point of view of the separation of chromosomes[7], biologists traditionally distinguish the anaphase from the telophase, two phases that do not necessarily overlap with the two previous cell surface deformation stages (see fig. 1.17). Starting from a round cell in metaphase, where chromosomes are aligned along the future plane of division, the anaphase corresponds to the break of chromosomes into chromatids, which are dragged by shortening of kinetochore microtubules to spindle poles. In telophase the kinetochore microtubules disappear and chromatids decondense, before the nuclear envelop begins to reform.

Central spindle assembly The assembly at the cell equator of the microtubules spindle is the key event of cytokinesis initiation, as it contributes to specify the the division plane and constitutes the template for future abscission. The spindle midzone is built from two arrays of interdigitated microtubules, organized in an antiparallel way, with their minus end facing the cell poles [Euteneuer 1980]. The microtubules are bundled with motor-associated proteins and kinesin motors (MKLP1), which allow the sliding of these two groups of microtubules away from one another: the overlap goes from $\sim 2.5\mu m$ in early anaphase to $\sim 0.5\mu m$ in late

---

[7] A chromosome is formed from a pair of chromatids, each containing the same genetic information.

anaphase in PtK1 cells [Mastronarde 1993]. This narrow region forms the central spindle [Glotzer 2009], which regulates the cleavage furrow formation by recruiting signalling molecules (see section 1.2.2.1).

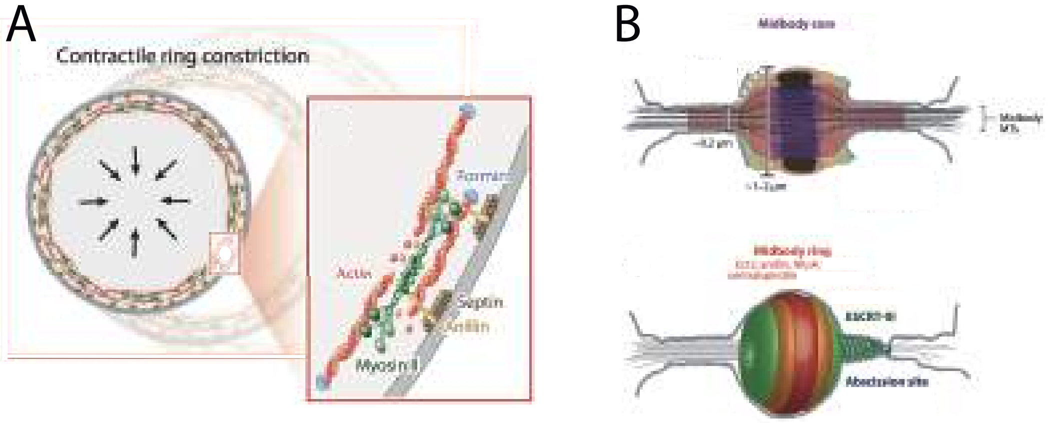

Figure 1.18: Constriction and abscission. (A) Schematic representation of the contractile ring constriction and principal molecular components. The ring is composed of three types of filaments: actin filaments nucleated by formins, myosin minifilaments and septin filaments. Annilin is thought to be the scaffold that link these three filament types. The constriction is proposed to result from the contraction of filaments by myosin motors. (B) Organization of the midbody: central plane (top) and surface view (bottom) of the intracellular bridge, with the principal molecular components. (Adapted from [Green 2012]).

Cleavage furrow assembly and ingression The spindle midzone promotes the assembly of a – so-called – contractile ring (see sections 1.2.2.1 and 1.2.2.2). The contractile ring is traditionally represented as broad band of filamentous actin and Myosin II motors, organized on a ring along with additional structural (anillin, septin) and regulatory proteins (formin, profilin, ADF-cofilin etc...) [Miller 2011]. The contractile ring is linked to the plasma membrane such that, when it constricts by the means of Myosin II motors force generation, it creates a cleavage furrow. The ingression of the cleavage furrow finally gather the interzonal spindle microtubules into the midbody, which is the targeting platform for abscission.

Midbody formation and abscission The abscission is the final cut that splits the mother cell into two topological distinct cells. When the actomyosin ring closes, it compacts the spindle zone into a thin and dense cytoplasmic bridge of about 1 to 2 μm thick. A remodeling of the contractile ring and the spindle, called midbody formation and maturation, lasts for one to two hours before abcission occurs. If the precise composition of the midbody remains partially unknown, its assembly requires successful furrow ingression, as indicated by blebbistatin treatments [Hu 2012]. The stables microtubules that overlap to form the midbody core (see fig. 1.18 B) are thought to provide mechanical stability to the intercellular bridge and to be both the platform and the tracks for recruiting the abcission machinery, composed of hundreds of different proteins [Guizetti 2010]. Notably, several contractile ring components are retained in the midbody ring, including anillin, septins and RhoA, and are thought to anchor the midbody ring to the plasma membrane (see fig. 1.18 A) [Echard 2004]. The main abscission machinery has been recently identified as the Endosomal Sorting Complex Required for Transport III complex, which are known for their role in membrane scission during viral budding [Morita 2007]. ESCRT-III proteins polymerize to form a spiral polymer associated to the membrane [Henne 2012] and are disassembled in an energy-consuming process. Although computational models have been proposed to explain ESCRT-III mediated abcission [Fabrikant 2009, Elia 2012], its precise mechanism remains unclear. It was thus shown recently that a tension exerted on the intercellular bridge counter-intuitively delays abscission, while its release induces abscission [Lafaurie-Janvore 2013].

1.2.2 Molecular regulation of cytokinesis

1.2.2.1 Division plane specification

Spindle and dynamic astral microtubules specify the division plane

In animal cells, the division plane is positioned through signalling between the spindle and the cortex. Rappaport, in his seminal work on cytokinesis in marine eggs [Rappaport 1996] showed that this molecular communication is highly dynamic: by shifting the mitotic spindle by micromanipulation in a sand dollar egg he could induce reversible furrow regression at the former division site and the appearance of a new furrow at the new spindle position [Rappaport 1985]. Years later, two groups

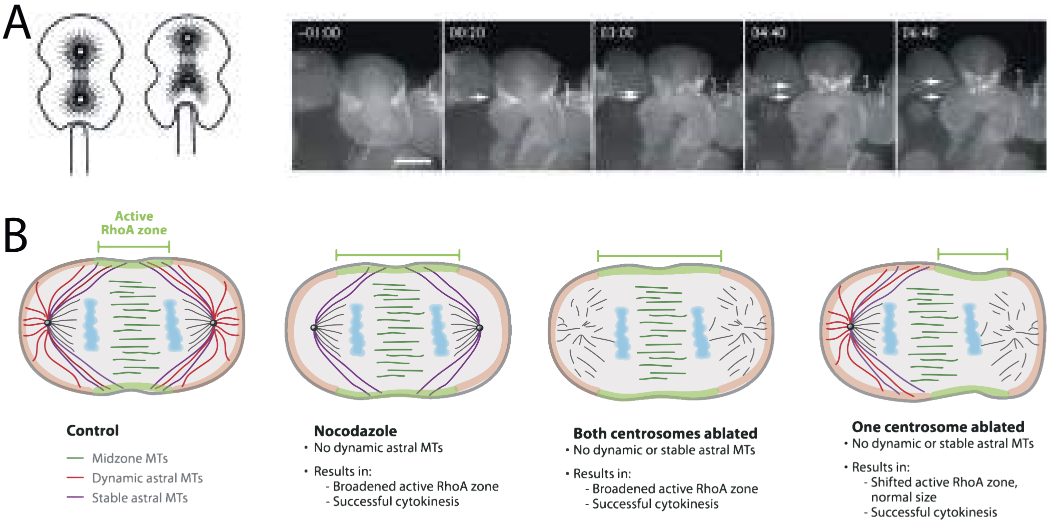

Figure 1.19: The spindle and the dynamic astral microtubules specify the division plane by confining RhoA at the cell equator. (A) Physical displacement of the cortex relative to the spindle shifts the RhoA zone and the furrow in a green urchin embryo. (Times are in min and scale bar is $25\mu m$. Adapted from [Bement 2005]). (B) Dynamic astral microtubules confine active RhoA to the cell equator (Adapted from [Green 2012], experiments originally performed on sea-urchin eggs by [von Dassow 2009b]).

clearly identified this division signal to be a spatially restricted RhoA activation zone in the cortex [Bement 2005, Yüce 2005]. Importantly, RhoA accumulates before furrow ingression and this accumulation arises independently of actin or myosin II (see fig. 1.18 A). Rappaport's experiment was repeated by [Bement 2005] in an urchin embryo blastomere expressing a fluorescent probe of active RhoA, showing clearly the shift of the RhoA zone concomitantly with the spindle (see fig. 1.18 A).

Rappaport showed furthermore, in his toroidal cell experiment, that two adjacent microtubules asters are sufficient to induce furrowing without the central spindle [Rappaport 1996, Oegema 1997], thereby suggesting another pathway for furrow induction. By separating the spindle from an aster with a laser, the authors of [Bringmann 2005] show that the asters and the midzone indeed provide two superimposed signals that position the furrow. However, instead of inducing a positive signal, the asters rather prevent the accumulation of actomyosin in their vicinity, leading therefore to a relative enrichment at the cell equator. This mechanism was then confirmed in grasshopper spermatocytes [Chen 2008] and in sea uchin embryos, where the elimination of astral microtubules by laser ablation leads to a broader zone of active RhoA (and consequently of Myosin II). This is consistent with the idea that astral microtubules refine the division plane specification by inhibition of a positive signal outside the midzone [Foe 2008, von Dassow 2009b] (see fig. 1.19). It is interesting to note that the total amount of active RhoA remains constant when asters are ablated, suggesting that asters in fact cage a total fixed amount of active RhoA, to prevent it from expanding outside the cell equator.

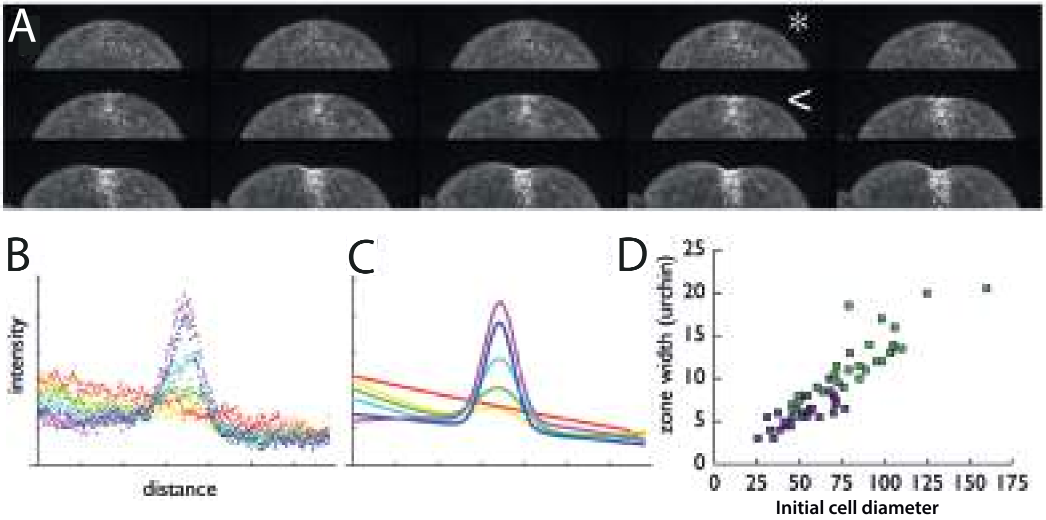

Figure 1.20: Characteristics of the active RhoA zone. (A) Serie of active RhoA fluorescence images in a purple urchin embryo. The RhoA accumulation (*) precedes furrowing (<). (Frames are 20s apart). (B) Active RhoA signal intensity measured along the cortex during division in a green urchin embryo. The different curves are 2min apart with time points ordered along the rainbow from red to violet. (C) Curves obtained by fitting the previous signal intensities by the weighted sum of a Gaussian and a quadratic polynomial. (D) Scatter plot of RhoA activity zone width versus the initial cell diameter in various green and purple urchin embryos, showing their proportionality. (Adapted from [Bement 2005]).

Characteristics of the active RhoA zone

The RhoA zone was further characterized in [Bement 2005]: the authors measured the intensity of the active RhoA signal along the cortex of sea urchin eggs, as shown in fig. 1.18 A and B. Activity signals were recorded at different times in the course of furrowing and could be nicely fitted by Gaussian functions (see fig. 1.18 C). The width of the Gaussians does not vary appreciably as the furrow ingresses, whereas their amplitudes increase rapidly to reach a plateau. Measuring the width of this RhoA zone as a function of the cell diameter, at various stages of embryonic development and for several organisms, they could further show a reproducible proportionality between active RhoA zone width and initial cell size (fig. 1.20 D).

Filling the gap between microtubules and RhoA

The demonstration that active RhoA dynamically senses microtubule perturbations, implies that the RhoA molecule is the key link between microtubules geometry and stimulation of cytokinetic furrowing. Like most other small GTPases, RhoA is regulated by guanine-nucleotide exchange factors (GEFs), which enhances its activity, and a GTPase-Activating Protein (GAP), that has an opposite function (see fig. 1.21). Activation of equatorial RhoA critically depends on the Rho GEF Ect2, which associates with a complex of proteins called the centralspindlin [Kamijo 2006, Nishimura 2006].

The centralspindlin is composed of two units of the kinesin MKLP1 and two units of the Rho-family GAP MgcRacGAP and concentrates at the central spindle, where it recruits directly the Rho-GEF Ect2 as sketched on fig. 1.21. The centralspindlin has been observed on the tips of microtubules near the furrow region in [Nishimura 2006], and it has recently been shown that the centralspindlin subunit MgcRacGAP associates with the plasma membrane by interacting with polyanionic phosphoinositide lipids [Lekomtsev 2012]. Yet, how exactly Ect-2 reaches the cell cortex from the central spindle to induce local Rho activation remains unknown. A simple diffusion process has been proposed [Salmon 1990, von Dassow 2009b], yet in order to achieve dynamic and spatially confined Rho GTPase zones, cells must restrict diffusion in a narrow zone. Alternatively MKLP1-mediated transport along stable microtubules [Inoue 2004] could also lead to accumulation of the centralspindlin and therefore Ect2 at equator, as it was confirmed recently by a stochastic computational model [Atilgan 2012].

1.2.2.2 Contractile ring formation and ingression

Assembly of the actomyosin ring

The small GTPase RhoA is the key regulator of the contractile ring assembly. Upon activation by its GEF Ect2, RhoA acts through two main effectors, as shown on fig. 1.21:

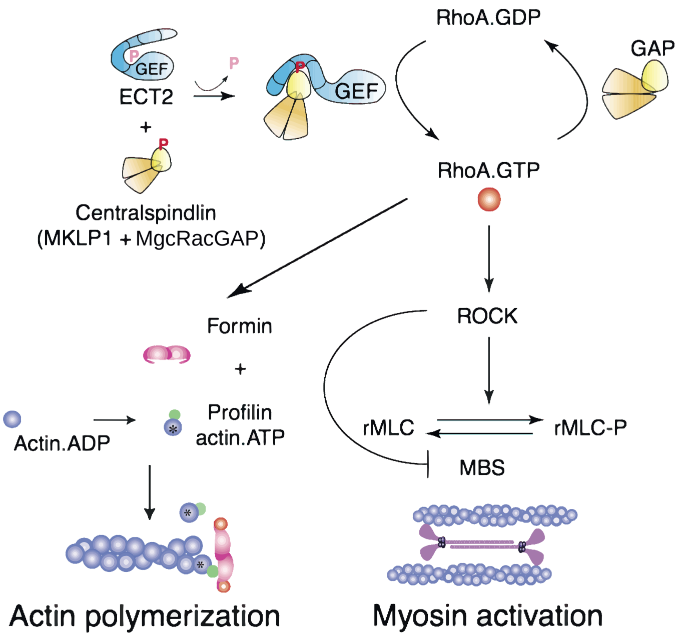

Figure 1.21: Activation of RhoA is controled by the GEF ECT2, which depends on the centralspindlin complex assembly. Active RhoA triggers myosin phosphorylation via its effector ROCK and the polymerization of actin by formins. (Adapted from [Piekny 2005])

1. the Rho-kinase (ROCK), which phosphorylates the myosin-light chain of Myosin II motors and therefore triggers contractile activity;
2. the formin Diaphanous, which nucleates unbranched actin filaments.

In addition to *de novo* assembly [Cao 1990b], it has been shown that about half of the accumulation of actin in the contractile ring is due to the transport of filaments from the cell cortex to the division plane by cortical flows [Cao 1990a]. The fact that the contractile ring in dividing animal cells is formed primarily through the reorganization of existing actin filaments may question the relevance of the classical picture where the contractile ring is presented as isolated from the rest of the cortex.

Two steps are generally distinguished in the assembly of the contractile ring: the accumulation of contractile ring proteins in a broad band, and the compaction in a condensed structure characterized by the alignment of the filaments along the perimeter [Fishkind 1993]. Again this distinction may simply be two limits of a continuous process in time, where actomyosin flows driven by the gradients of contractility between the furrow region and the poles, result in the alignment of actin filaments, and therefore the compaction of the equatorial region, as suggested by active-gel modeling [Salbreux 2009].

Anchoring to the plasma membrane

Tight anchorage of the contractile ring into the plasma membrane is essential to drive proper physical separation of the mother cell into two. PtdIns(4,5)P2 (or PIP2) is a phosphoinositide[8] which has been shown to play a determinant role in cytokinesis [Echard 2012]. Sequestration of PIP2 in mouse fibroblasts leads to the separation of the contractile ring from the plasma membrane [Field 2005] and cytokinesis failure, suggesting that PIP2 is involved in the anchorage of the plasma membrane to the cortex. PIP2 has indeed been shown to accumulate in the equatorial region [Emoto 2005] concomitantly with the contractile ring assembly. Ezrin-Radixin-Moesin (ERM) proteins are good candidates for connecting the actomyosin ring to the plasma membrane. Activated ERM proteins indeed link cortical F-actin with PIP2 [Fehon 2010]. However depletion of moesin in Drosophila, where it is the unique family member, only results in reduced penetrance cytokinesis defects [Kunda 2008, Roubinet 2011]. This suggests that redundant mechanisms cooperate with ERM for linking the actin cytoskeleton during furrow ingression, possibly annilin and/or septins.

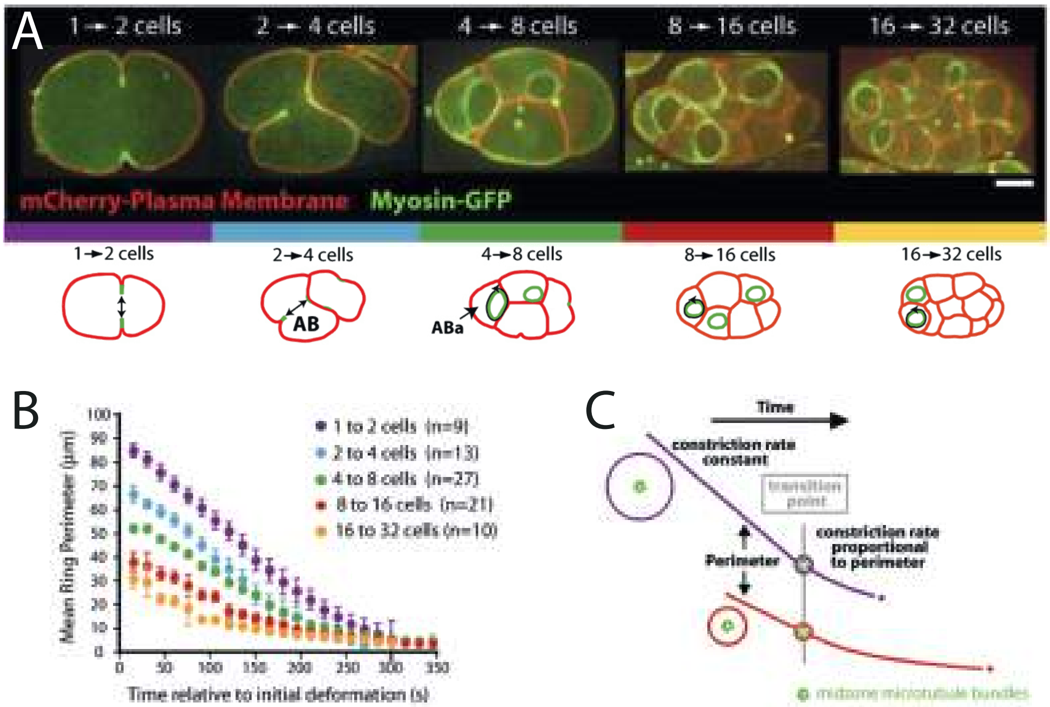

Figure 1.22: Contractile ring closure during the first five divisions of the C. elegans embryo. (A) Confocal images of embryos coexpressing non-muscle Myosin-II-GFP and mCherry plasma membrane probe (scale bar 10 μm. (B) Mean contractile perimeter versus time. (C) The contractile ring constrics in two phases. During the first phase, the constriction rate is roughly constant; during the second phase the perimeter decreases exponentially. (Adapted from [Carvalho 2009])

---

[8] Phosphoinositides are phospholipids of the plasma membrane

Constriction and influence of the polar cortex

The ring constriction has been shown to occur at a roughly constant rate in several organisms [Carvalho 2009, Calvert 2011, Ma 2012]. In C. Elegans embryos the actomyosin ring constriction displays two phases, a first phase of mean constriction rate roughly proportional to the initial perimeter of the ring, and a second phase of exponential decrease of the ring perimeter (see fig. 1.22). The authors of [Carvalho 2009] postulate the exponential decrease to happen when the ring starts to contact the spindle and show that the proportionality between constriction rate and initial cell size enables cells with different sizes to divide in the same amount of time. They further show that main contractile ring components (actin, myosin II, anillin and septins) are lost in proportion to the decrease in perimeter during constriction, consistently with pioneering Schroeder's work measuring the actin network volume in electron micrographs [Schroeder 1972].

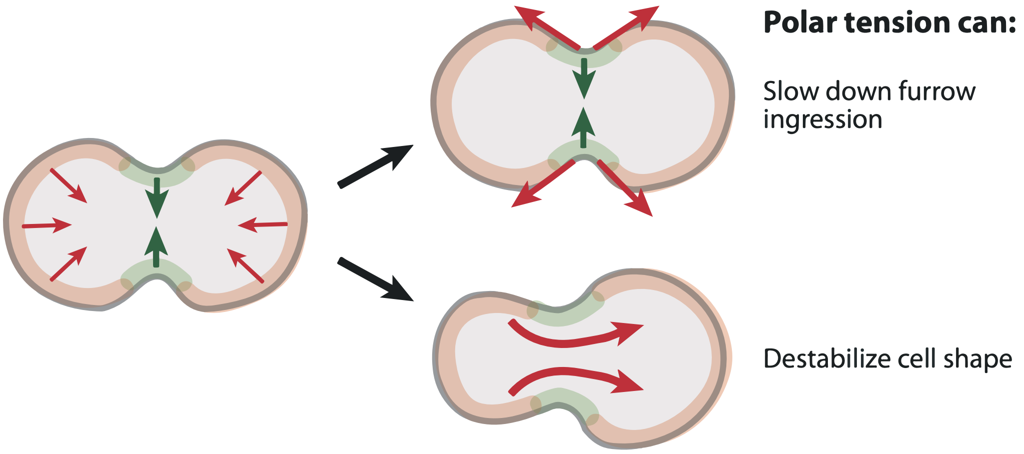

Figure 1.23: Influence of the polar cortex on cytokinesis. The polar tension (red arrows) can slow down furrow ingression (green arrows), or destabilize the cell shape if left and right poles tensions and/or volumes are not balanced precisely. (Adapted from [Green 2012])

As we mentioned earlier, the contractile ring may have specific filament arrangment and composition, it still remains a region of the continuous actomyosin cortex. The cortex at the cell poles, in particular, remains contractile, eventhough its "stiffness", measured by AFM, was shown to be much lower than in the furrow region [Matzke 2001]. The contractile tension at the poles has been proposed to slow down constriction [Yoneda 1972] and leads theoretically to an intrinsically unstable cell shape. If left and right contractile forces do not compensate precisely, an instability may develop [Piekny 2008, Sedzinski 2011], in which on pole contracts at the expense of the other, as illustrated in fig. 1.23.

1.2.3 Modeling of constriction

Mechanical engineers and physicists tried early to address the drastic cell deformation occuring during cytokinesis. Continuous elastic or viscous models of the entire cell surface have been proposed in the 1980-90's [Greenspan 1977, Akkas 1980, White 1983, Zinemanas 1987, Zinemanas 1990, He 1997] to account for early experimental observations and force measurements performed on sea-urchin eggs [Hiramoto 1958, Hiramoto 1971]. By contrast, most of the recent theoretical work is focused on the contractile ring, based on coarse-grained descriptions [Zhang 2005, Zumdieck 2005, Salbreux 2009] or microscopic models for motor-filament interactions [Biron 2005, Zumdieck 2007, Mendes Pinto 2012]. We also only mention a recent work [Koyama 2012], that attempts to model the cortex deformation in C. Elegans cytokinesis with a pure elastic bending energy, of Helfrich type[9]. Finally in [Prothero 1967, Yoneda 1972, Sedzinski 2011], the polar cortices are approximated as two portions of sphere under tension, which resist to ring constriction.

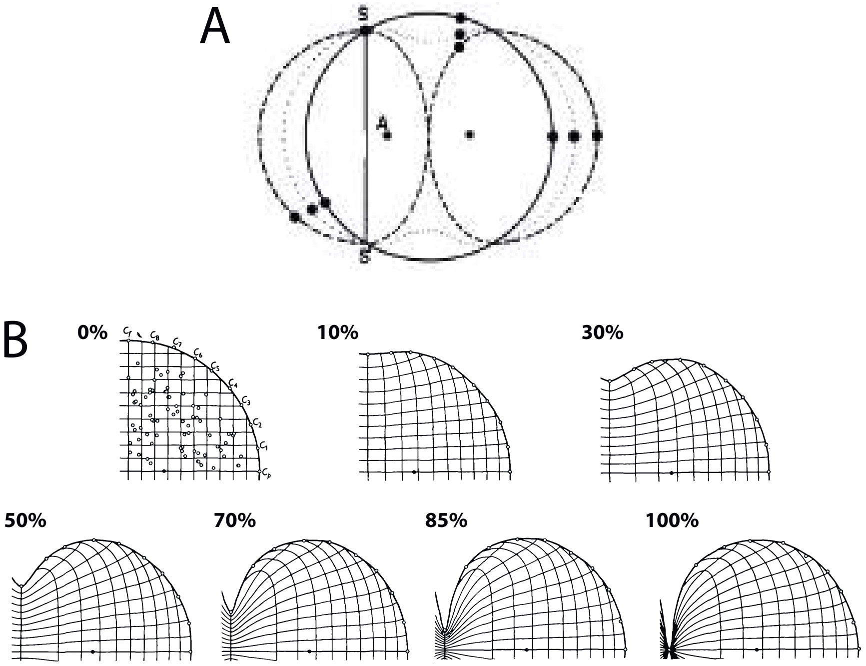

Figure 1.24: Surface movement in sea-urchin eggs. (A) Three successive contours of a cleaving sea-urchin egg illustrating the stationary surface rings S-S'. *A* is the original center of the asters and the black circles represent carbon particles attached to the surface (From [Wolpert 1960], after [Ishizaka 1957]). (B) Diagram indicating movement of the cell surface for successive cleavage stages of *Clypeaster* egg. A quarter of the egg is shown. The stages are indicated in percentage of furrow ingression. White particles from the poles to the furrow (C_f to C_p) represent carbon particles attached to the surface (Adapted from [Hiramoto 1958]).

---

[9] Helfrich energy for lipid bilayer membranes is defined in section 3.2.2.1.

1.2.3.1 Early experimental observations and geometrical arguments

A number of experimental investigations have been done in the 1940-50's in sea-urching eggs to determine if the cell poles are stretched, or if the furrow is the only region of surface increase [Dan 1938, Dan 1940]. The method consists in tracking the movement of carbon particles, randomly attached to the cell surface. The cell surface increase is found to arise from the stretching of preexisting cell surface in a wave of expansion from the poles toward the furrow region. Ishizaka and K. Dan show, using the same method, that an annular surface region on each side of the furrow neither changes in diameter, nor moves relative to the cell equator and they name this region "stationary surface rings" [Ishizaka 1957] (see fig. 1.24 A). Refining the method of K. Dan, Hiramoto constructs a map of cell-surface deformation (see fig. 1.24 B) in sea-urchin eggs, indicating that the "stationary ring" of Ishizaka demarcates two surfaces behaving relatively differently [Hiramoto 1958]. The cell volume is shown to be almost perfectly constant during constriction, which implies a cell surface increase of about 25%. The new surface comes mainly (80%) from the expansion of the region comprised between the stationary rings and the poles [Wolpert 1960]. The region between the rings and the equator, mostly contractile, contributes to the 20% remaining surface increase. The furrow surface therefore shrinks in circumference while it stretches in the direction from equator to pole.

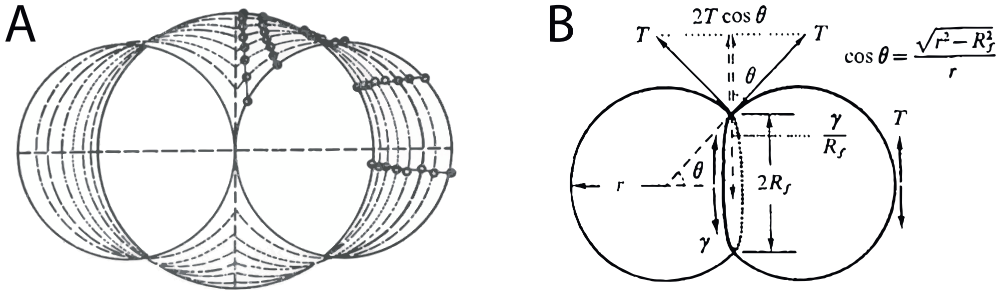

Figure 1.25: Spherical geometry hypothesis. (A) Dividing grasshopper spermatocyte successive contours and movement of surface markers (open circles) (Reproduced from [Ishizaka 1966]). Solid lines through the open circles represent trajectories calculated in [Prothero 1967]. (B) Balance of forces in a dividing cell with spherical poles. T is the polar tension, γ the constricting force and R_f the furrow radius. (Adapted from [Yoneda 1972]).

Ishizaka then applies the same marking technique to the cleaveage of grasshopper spermatocyte [Ishizaka 1966]. The surface is shown to expand approximately uniformly during division, in contrary to sea-urchin eggs, and the successive cell contours can be fitted with portion of spheres, which suggests an isotropic and uniform tension along the cell surface. Prothero and Rockafeller have proposed a model to account for Ishizaka's observation: it postulates that the constraints governing the cell cleavage are minimum surface area and cell volume conservation, as in bubbles, [Prothero 1967], which leads naturally to the union of two spheres. Using simple geometrical arguments, they fit nicely the movement of carbon markers recorded by Ishizaka fig. 1.25. Yoneda and K. Dan have used the same spherical approximation as [Ishizaka 1966] for the division of sea-urching eggs [Yoneda 1972], although the shape of their polar regions is not spherical (see fig. 1.24 A). Assuming the constancy of the cell volume, and inserting the tension at poles T and the furrow radius R_f in the course of division, they evaluate the minimum necessary force of constriction γ from simple force balance

$$\frac{\gamma}{R_f} = \frac{2\sqrt{r^2 - R_f^2}}{r} T \,. \tag{1.5}$$

Their simple approach quantifies therefore for the first time the resisting influence of the poles on constriction.

1.2.3.2 Continuous formulations

Several rigorous formulations of the cell surface mechanics have been proposed at the end of the last century to model cell cleavage. These studies do not seem to have been much examined by the biological community, presumably because of their technical nature. A few computational models were later proposed and received more attention. We attempt to give below a short and comprehensive overview of these various investigations, in a relatively chronological order.

Mechanical models of the cell surface

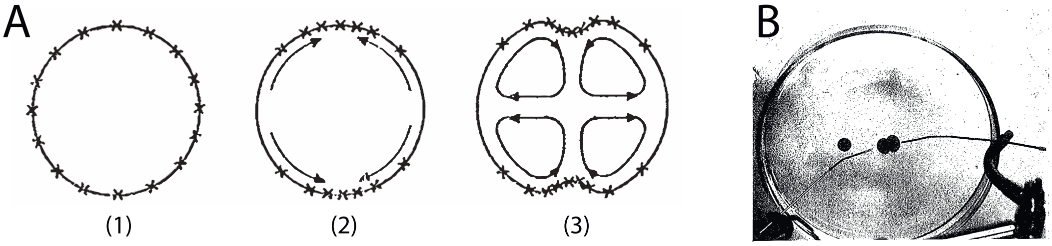

Figure 1.26: Fluid model of cleavage. (A) Schematic representation of the instability induced by the movement of surface tension elements: (1) initial state of uniform surface tension; (2) a gradient of distribution of the tension elements triggers a surface contraction toward the equator, which tends to concentrate the elements; (3) surface elements flow induces a circulation of the cytoplasm. (Adapted from [Greenspan 1977]). (B) A droplet of cod liver and olive oil suspended in water distorts in response to an efflux of caustic solution from two opposite serynges. (Reproduced from [Greenspan 1978]).

Greenspan proposes in 1977 a completely fluid model of the cleavage dynamics, where the forces exerted within the cell surface layer are approximated by an effective surface tension [Greenspan 1977]. The magnitude of the effective surface tension is assumed to depend on the local concentration of *tension elements*[10]. These tension elements can move along the cell surface and their position is

---

[10] The precise molecular origin of contractility in the cell cortex was not yet clearly established at that time.

randomized by a surface diffusion coefficient D. The cell surface movements are supposed to be balanced mainly by the shear stress within the cytoplasm, as in a droplet. The axisymmetric cell, initially spherical and under uniform tension, is asymptotically perturbed[11] by lowering the tension at the poles. The tension gradient produces a surface flow from the poles toward the equator, reminiscent of the Gibbs-Marangoni effect in fluid droplest. The surface flow causes an accumulation of tension elements at the equator, given that the gradient exceeds diffusion, thereby further increasing the tension there. The resulting instability spontaneously develop into cleavage, and induces a circulation of the cytoplasm (see fig. 1.27 A). Greenspan points out that this dynamical behavior depends only on the relative difference in tension between equator and pole. In this regard the two biological competing theories, polar relaxation and equatorial constriction, are not mutually exclusive. This theoretical process was elegantly illustrated on a neutrally buoyant oil drop in water where the surface tension is dropped symmetrically at the poles by means of an active substance [Greenspan 1978] (see fig. 1.27 B).

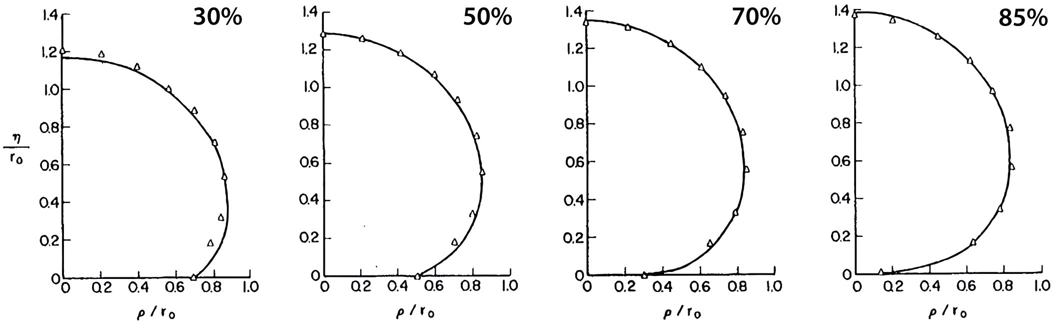

Figure 1.27: Elastic membrane model: comparison of numerical profiles of a deformed membrane (STZC material) and experimental results of [Hiramoto 1963] at successives stages of ring constriction (in percentage). (Reproduced from [Pujara 1979]).

Two mathematical models, treating the cell surface as a non-linear, elastic material have been proposed almost simultaneously [Pujara 1979, Akkas 1980].

Pujara and Lardner examine the deformation pattern of an initially spherical membrane[12] for a prescribed displacement at the equator, subject to the constraint of constant enclosed volume. The membrane is modeled as an elastic non-linear material and two different materials are compared: a moonley-rivlin material, usually used to model the deformation of rubber-like objects [Rivlin 1948], and a Skalak-Tozeren-Zarda-Chien (STZC) material [Skalak 1973], that was proposed to describe the mechanics of the red-blood cell membrane. The model is therefore passive, in that it does not take into account the formation of a contractile ring, nor the active driving mechanism. Yet numerical predictions for cell shapes are found to agree satisfactorily with experimental data in [Hiramoto 1963].

---

[11] This approach is formally very similar to the one we adopt in section 2.1.2.2.

[12] Note that a membrane in mechanics (see chapter 2) is different from the plasma membrane, generally described by an Helfrich energy (see section 3.2.2.1).

The model proposed by Akkas is very similar, but the cell volume is allowed to vary and the cell is supposed initially slightly inflated. The division process is again considered as a large deformation, quasi-static problem and the problem is solved numerically. Akkas comes to the conclusion that numerical predictions can indeed agree with experimental results of Hiramoto, but only if the material stiffness is not constant over time, but first increases and then decreases during the course of constriction, thereby displaying a maximum. Akkas makes the interesting point that this maximum delimitates a critical stage of cleavage, where the constricting force has to increase to overcome the membrane elastic resistance, from a *"deteriorating"* stage of cleavage, where the force does not need to increase further for division to complete. Akkas therefore conjectures the possibility of cleavage failure, if the critical stage is not passed, and suggests that a consistent description of the cell membrane, that does not suppose material constant variations, would require a new visco-elastic material description, that he named a *"deteriorating material"*.

A numerical calculation for large deformations indicates that the hydrodynamic model of Greenspan does not lead to complete cleavage [Sapir 1985]. Greenspan has however conjectured that the contractile filaments should rotate and reoriente themselves parrallel to the cleavage plane during their motion toward equator, thereby leading to anisotropic surface tension. Zinemanas and Nir propose therefore a new fluid-mechanical approach ten years later that combines macroscopic equations of motion with microscopic local balances for filament concentration and orientation distribution [Zinemanas 1987]. The filament orientation dynamics is coupled to the surface flow and to the rate of filament production, very similarly to the recent active-gel theory [Kruse 2005]. Conversely, surface motions can be induced by concentration gradients, as in [Greenspan 1977], but also by filament orientation gradients. The problem is formulated as a boundary-integral equation, which consists in formulating partial differential equations in a domain as an integral on its boundary [Pozrikidis 1992], and solved numerically for large deformations. To be tractable numerically, the model is however simplified by neglecting diffusion effects and passive contributions to the tension, originating from surface deformations. A biochemical stimulus furthermore controls the production of active filaments, and is assumed to diffuse toward the surface from two point sources located at the asters of the mitotic apparatus.

The authors find that the resulting concentration gradient induces a tangential surface flow toward the equator represented in fig. 1.28 A. This profile exhibits a region of negative velocity gradient around the equator and two zones of positive gradient near the poles. This flow pattern orient the filaments parallel to the cleavage plane near the equator, as shown on fig. 1.28 B. The filament reorientation leads to an anisotropy of the surface tension in the equatorial region, that allows the furrow to constrict further than in the isotropic case. However only the adding of a muscle-like contractile activity of the filaments can drive the process to complete constriction (see fig. 1.28 C). The authors suggest that the simultaneous concentration increase and filaments reorientation at the equator provides a mechanism for the contractile

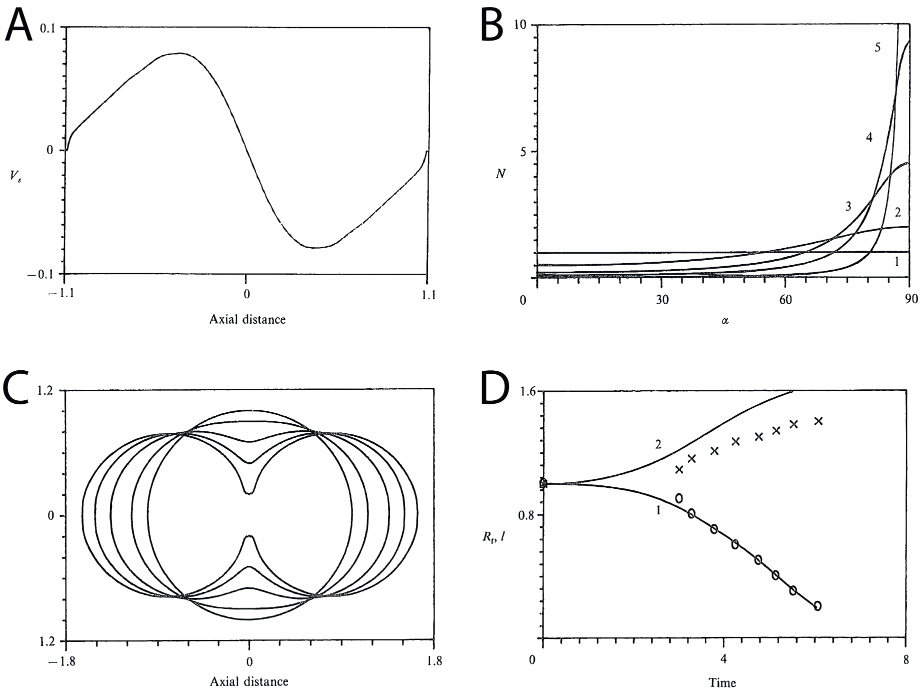

Figure 1.28: Hydrodynamic model with filament orientation. (A) Typical pattern of the tangential velocity along the meridional contour. (B) Orientation distribution for successive times (N=1 corresponds to an isotropic distribution). (C) Evolution of the furrow radius R_f and polar distance l compared to experimental results of [Hiramoto 1958]. (D) Consecutive numerical surface shapes of the dividing cell. (Reproduced from [Zinemanas 1987]).

ring formation. This idea was recently reformulated in the framework of active-gel theory and led to very similar results at first order in perturbation [Salbreux 2009] (see section 1.2.3.3).

Computational models of the cell surface

In 1983, White and Borisy present the first purely computational model of cytokinesis [White 1983]. They distinguish the basal contractility of the cortex that leads to a surface tension, from the modulation of this surface tension by the mitotic apparatus to create a gradient with the highest value at the equator. The surface deformations are supposed to be limited by viscosity and the hydrostatic pressure resulting from cortical tension and volume conservation is supposed uniform throughout the cytoplasm. The cortical elements are assumed to be free to move in the cortex plane, and therefore accumulate as an equatorial belt as a result of the tension gradient, thereby reproducing the formation of the contractile ring, as proposed by [Greenspan 1977]. The tension elements are furthermore supposed to have an orientational order, so that their contraction results in their partial orientation. The model results in realistic shape profiles (see fig. 1.29), and is even generalized satisfactorily to asymmetric divisions. However the numerical methods,

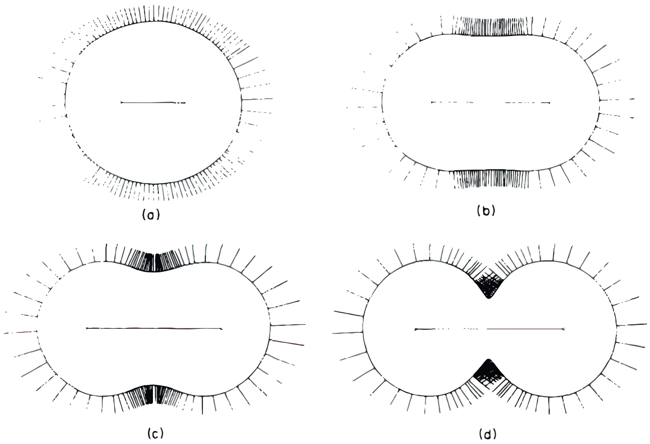

Figure 1.29: Computational fluid model of cleavage. (a) and (b) initial redistributions of tension elements for form a broad belt that pinches the equator into a cylindrical shape. (c) and (d) the broad furrow rapidly sharpens as it progresses. (Reproduced from [White 1983]).

the typical numerical values and the couplings between parameters are not, or not clearly specified in the paper (notably the coupling between filament orientation and flow). It prevents the reader to repeat their computational prodecure, as pointed out later in [Zinemanas 1987].

Previous fluid models, that suppose that the tension elements free to move within the surface plane, result to a self-amplifying contraction mechanism that only needs to be initiated to eventually lead to complete cleavage. In [Harris 1990], the author proposes a computational fluid surface model of the cell cortex with volume conservation, where, on the contrary, the anisotropic surface tension is prescribed and does not reorganizes via mobile elements. He shows that cleavage completion then requires the ratio of two tensions along and accross the furrow to be at least 18 : 1, thereby implying a threshold for cytokinesis success.

The computational model proposed by He and Dembo is also hydrodynamic, but somewhat different from the previous studies, since it considers the cytoplasm and the cortex as two fluids that can interpenetrate [He 1997]. The two phases, called *"cytoskeletal"* and *"solvent"* phases, can therefore be present at every location of the cell. The cytoskeletal phase is furthermore supposed to be continuously recycled from material in the solvent phase, on a fast time scale fast compared to the constriction time scale. This process mimicks therefore the fast turnover of cytoskeletal components. The contractility is however approximated as isotropic, in contrast to the latter models [White 1983, Zinemanas 1987]. Numerical results for the dynamics of constriction are in relatively good agreement with experimental data of [Hiramoto 1963]. In particular they reproduce the slowdown of constriction at the end of furrowing, that they attribute to an increase of density due to compaction of the furrow region (see fig. 1.30 C). By considering a balance of mechanical power

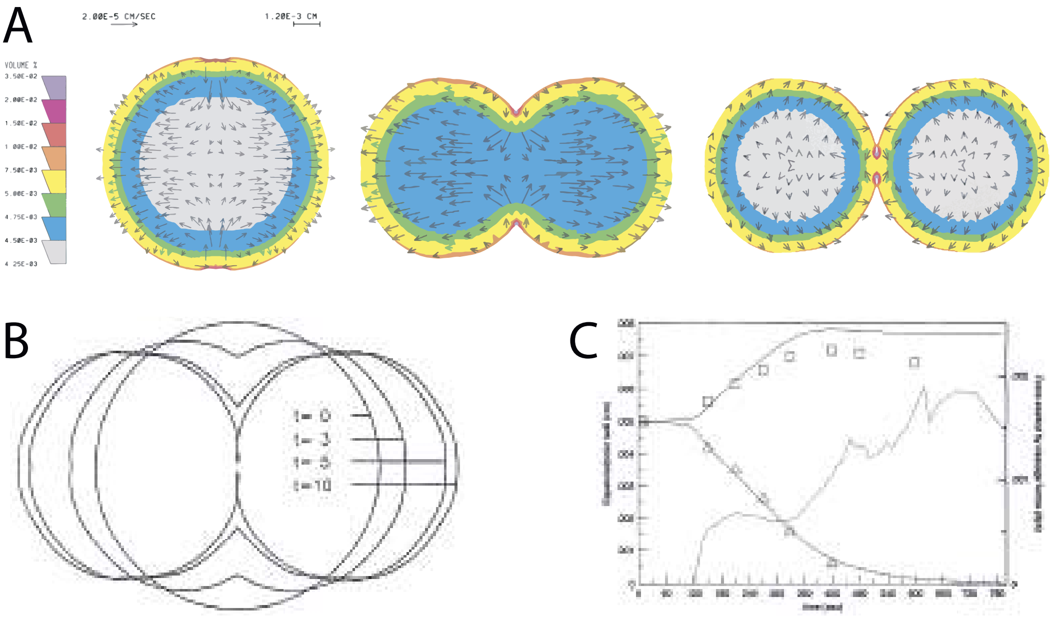

Figure 1.30: Computational two components fluid model of cleavage. (A) Network density and flow at the start, at middle stage and at the end of cleavage. The color code represents the density of the cytoskeletal phase, and arrows the direction and magnitude of the solvent flow. (B) Superimposed outlines of the cell shape at successive stages of cleavage. (C) Time evolution of the pole-to-pole distance (top) and furrow radius (bottom), compared to experimental data of [Hiramoto 1963] (triangles for furrow radius, squares for pole-to-pole distance). The dashed line represents the time course of the force exerted by the cleavage furrow. (Adapted from [He 1997])

supply and dissipation, the authors determine an upper bound for the rate of constriction. It shows that at high density, the internal ring viscosity grows faster than the contractile stress with density. As a consequence, the inhibition of cytoskeletal depolymerization increases the network density and leads to a decrease of the rate of contraction[13]. The flow patterns of the solvent and network (see fig. 1.30 A) are in very good qualitative agreements with experimental data [Hiramoto 1971]. The agreement of shape profiles is less satisfactory, owing presumably to the omission of contractile anisotropy, and the final pole-to-pole distance is notably over-estimated (see fig. 1.30 B and C).

---

[13] We note that our one-component cortical model in chapter 2, does takes into account material turnover but not density variations, which would require a two-component active gel theory [Callan-Jones 2011]. Our results on the influence of depolymerization may therefore be in contradiction to high density predictions of [He 1997].

1.2.3.3 Models of the contractile ring

Coarse-grained models of the contractile ring formation

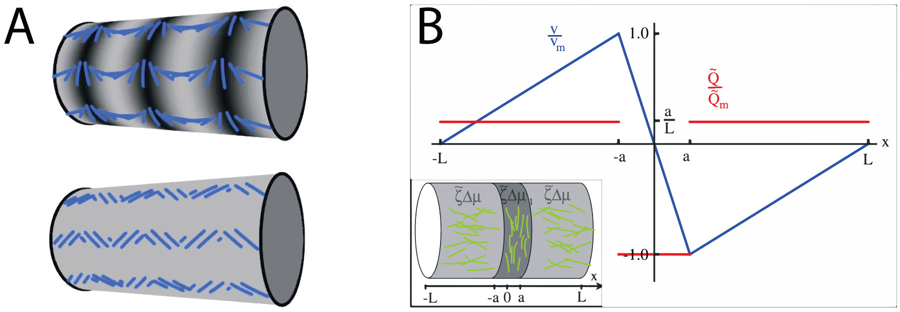

Figure 1.31: Contractile ring formation in cylindrical geometry. (A) Examples of stationary solutions: chevrons (top) and multiple rings pattern (bottom) (Adapted from [Zumdieck 2005]). (B) Axial velocity and nematic order parameter along the cylinder submitted to an excess of myosin activity in a central band $\zeta\Delta\mu_1 > \zeta\Delta\mu$. (Inset) Schematic representation of the equatorial belt with filaments aligned along a ring. (Reproduced from [Salbreux 2009])

In [Zumdieck 2005], the authors propose a continuum description of a cylindrical layer of cytoskeletal filaments and motor proteins. The layer of cortical filaments is modeled as an active material with a nematic order and variable density. The density of contractile filaments obeys a conservation law with turnover and the 2-dimensional stress is coupled to the density and to the nematic order by symmetry arguments. The layer is furthemore supposed to move on a fixed cylinder against a background fluid that creates an effective friction. A linear stability analysis shows that a great variety of instabilities can arise in the system depending on the relative value of the parameters: stationnary patterns like chevrons and multiple rings (see fig. 1.31 A), and oscillating patterns of one or multiple rings. The paper, however, does not consider mechanical deformation of the cylinder, and does not relate the many phenomenological coefficients introduced to experimentally measurable parameters.

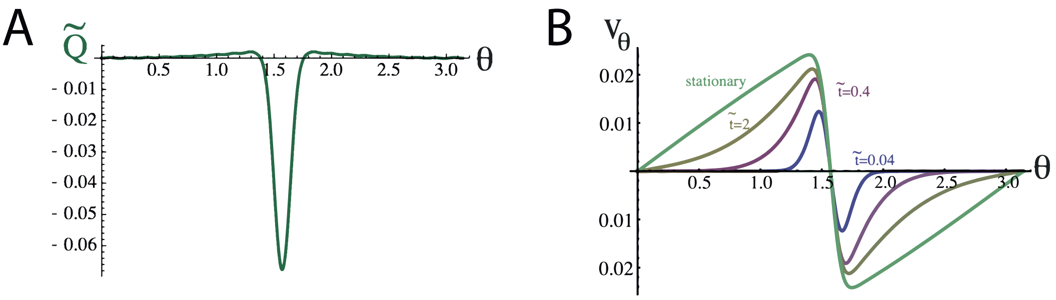

Figure 1.32: Contractile ring formation in spherical geometry. (A) Stationary profile of filament orientational order along an axisymmetric contour of the cortex; zero corresponds to an isotropic distribution, negative values indicate an alignement along the equator. (B) Dimensionless tangential flow profiles along an axisymmetric contour of the cortex for different times.(Adapted from [Salbreux 2008])

A slightly more recent study [Salbreux 2009] considers a similar situation where 2-dimensional layer of active viscous filamentous fluid has a nematic order coupled to its flow. In contrast to the former work, the density is assumed constant and turnover is neglected, and the equations are derived from the active-gel theory [Kruse 2005] (see section 1.1.2.3). A linear perturbation approach shows that increasing the contractiliy in a central region of the cylinder triggers a flow from the less contractile region toward the more contractile region, that reorients the filaments along a ring in the central region, as shown on fig. 1.31 B. Contractile ring formation is calculated with realistic values of the phenomenological parameters, taken from the literature. The same process is extended to a spherical geometry where the surface is allowed to deform against an uniform pressure [Salbreux 2008]. Upon small increase of the contractile activity in an equatorial band, the filaments, initially isotropically distributed, are shown to similarly realign along an equatorial belt, as a result of the tangential flow profile reproduced in fig. 1.32. These results are qualitatively similar to the former study of [Zinemanas 1987] in large deformations.

Models of the contractile ring ingression

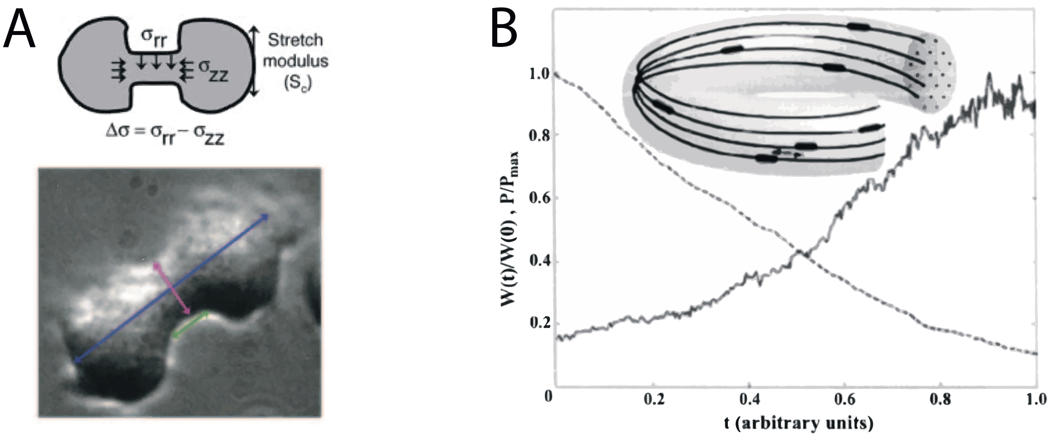

Figure 1.33: Contractile ring models in *D. Discoideum.* (A) The contractile stress σ_{rr} opposes to viscous flow of the cytoplasm σ_{zz} and extension of the poles of tension S_c. (Adapted from [Zhang 2005]). (B) Results from the simulation of the actomyosin contractile ring, schematically represented with actin filaments moving along the ring perimeter. The dashed line represent the dimensionless ring radius $w(t)/w(0)$ as a function of time. The solid line is the time evolution of the normalized power provided by the motors. (Adapted from [Biron 2005])

Two concomittant studies of cytokinesis in *Dictyostelium discoideum*[14] start from similar basic hypotheses: the contractile ring is seen as a cylinder of constant width, and the main process that limits constriction is considered as the dissipation associated to the flow of cytoplasm driven out the furrow region. The authors in [Biron 2005] simulate the constriction of the ring resulting from filament sliding.

---

[14] Note that *Dictyostelium discoideum* is not an animal organism.

To obtain a linear decrease of the ring in time, consistent with experiments, they suppose that the motors provide more and more power as longs as the contractile ring shrinks, because the cytoplasmic viscous dissipation scales as the inverse of the ring perimeter (see fig. 1.33 B).

In [Zhang 2005], the furrow region is submitted to a constant radial stress σ_{rr} mediated by myosin motors (see fig. 1.33 A). The cylindrical ring is furthermore supposed to have a lower pressure than the spherical poles[15], which can help the furrow thinning process at late stages of constriction (see fig. 1.33 A). The dynamics of constriction is first exponential, due to viscous dissipation, and then linear in time, owing to the pressure difference process.

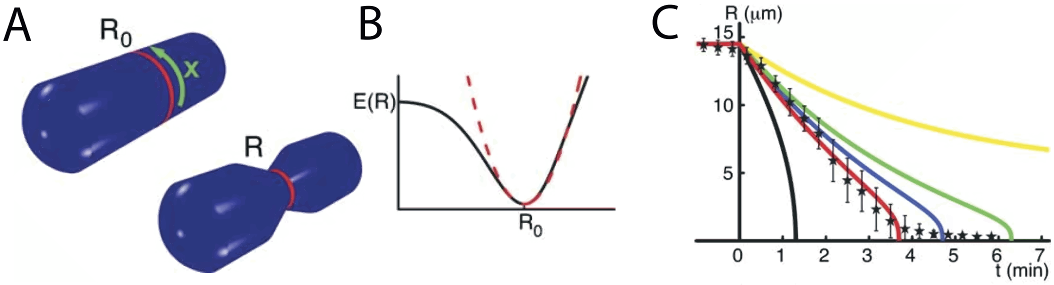

Figure 1.34: Contractile ring ingression with turnover. (A) Schematic representation of the cylindrical elastic cell surface of initial radius R_0 and in a contracted state $R < R_0$. (B) Typical profile of the elastic energy of cell deformation (black line) and the quadratic approximation used (dashed red line). (C) Time evolution of the contractile ring radius for various values of the filament turnover and ratio of contractile force and elastic force: the ring fails to constrict fully if the contractile force is too low (yellow line); decreasing the contractile force (blue line) or the polymerization (green line) leads to a reduced constriction rate, compared to the red line; in the absence of turnover, the constriction rate increases over time (black line). Stars are experimental data from *C. Elegans*. (Adapted from [Zumdieck 2007])

In [Zumdieck 2007], the authors propose that the contractile stress in the ring results not only from the action of motors, but also from treadmilling of the filaments at the microscopic level, in the presence of end-tracking cross-linkers. The ring is formed of several actin filament bundles and wrapped around a cylindrical surface representing the cell surface of *C. Elegans*, which is assumed to be elastic[16]. The elastic deformation opposes the contractile force, and is slowed down by an effective friction. The contractile force is moreover taken proportional to the number of filaments in a bundle and to the square density of filaments in a bundle. The density obeys a mass balance with polymerization and depolymerization. Solving for the coupled dynamics for contractile ring ingression and filament turnover, the authors show that the ring constriction rate is mainly determined by the ratio of contractile

---

[15] The tension S_c is supposed the be same at poles and in the furrow region, the Law of Laplace gives therefore a pressure in the cylinder $P = S_c/a > 2S_c/R$ for a cylinder radius $a < R/2$, where R is the pole radius.

[16] No assumption is however made on the cell volume, and this model is therefore essentially local.

force and elastic resistance. They also clarify the role of turnover: in the absence of filament disassembly, the contraction rate increases because the rise of filaments density leads to a higher contractile force; if, on the contrary, filament treadmilling is fast enough, the density remains fairly constant throughout constriction.

1.2.3.4 Shape instabilities

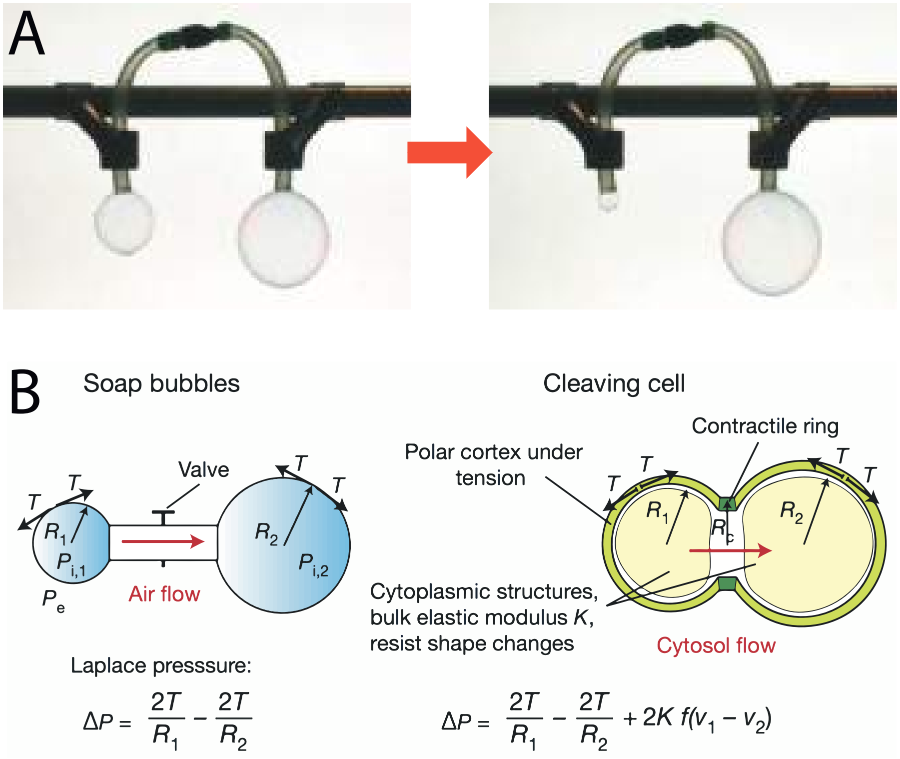

Figure 1.35: Shape instability. (A) The small bubble empties itself into the big bubble because of Laplace pressure instability. (Reproduced from [de Gennes 2004]). (B) Analogy between two bubbles and a cell during cytokinesis. (Adapted from [Sedzinski 2011])

As I have suggested in my Master thesis, if the cortical mechanics can be modeled by an effective surface tension, the cell shape during cytokinesis should be intrinsically unstable. An analogy can be drawn with bubbles: we consider two bubbles of two initial different radii and connected via a valve. The pressures in the small bubble, denoted 1, and the larger bubble, denoted 2, relative to the outer pressure are given by the law of Laplace $P_1 = \frac{2T_1}{R_1}$ and $P_2 = \frac{2T_2}{R_2}$. Assuming that the two bubbles have the same surface tension $T_1 = T_2$, the pressure is higher in the small than in the bigger bubble: $R_1 < R_2 \iff P_1 > P_2$. The situation is intrinsically unstable, and the small bubble empties itself in the big bubble as illustrated experimentally in fig. 1.35 A. Approximating a dividing cell as two portions of spheres under tension separated by a cylindrical contractile ring, leads to the exact same unstable situation, owing to a slightly imperfect left-right symmetry, as I proposed in my Master thesis. Assuming a bulk elasticity of the cytoplasm may however stabilize the dividing state, as sketched in fig. 1.35 B.

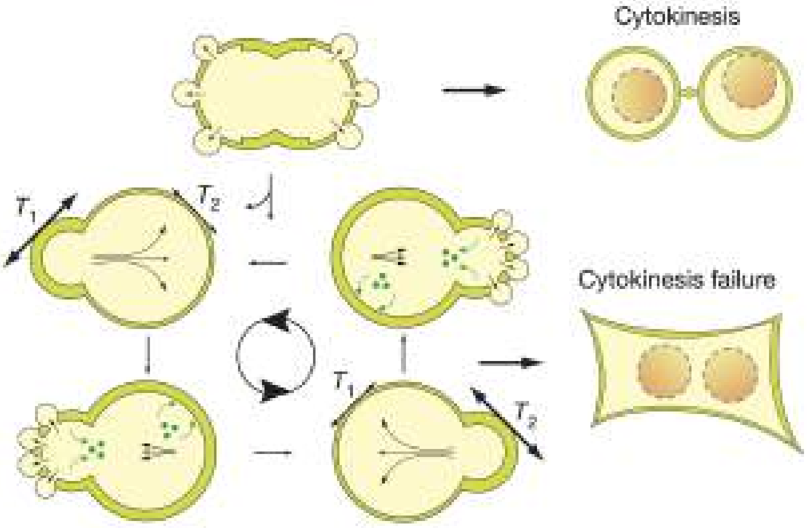

Figure 1.36: Cell shape oscillations in cytokinesis. High polar tension or pressure imbalance between the poles triggers shape oscillations. (Reproduced from [Sedzinski 2011])

This idea has been developed further in a recent combined experimental and theoretical study [Sedzinski 2011]. Blebbing HeLa and L929 cells are shown to display a similar instability in certain drug conditions or upon destabilization by laser ablation of the cortex, or asymmetric depolymerizing treatment by cytochalasin D. Blebs are local bulges of plasma membrane, that form upon detachment from the cortex and retract when a new cortex repolymerizes on the lipid-bilayer [Charras 2008]. A bleb is suggested by the authors to relax locally the hydrostatic pressure.

Unexpectedly, all unstable cells display furthermore an oscillating behavior, attributed by the authors to the asymmetric and contraction-synchronized blebbing (see fig. 1.36). They ultimately fail to constrict. The mechanism is depicted schematically on fig. 1.36 and is the following: starting from a slightly asymmetric state of the cell, the smaller pole decreases its volume at the expense of the other, until an elastic process (presumably asymmetric blebbing, releasing the pressure locally, or a non-identified bulk cytoplasmic elasticity) stops the contraction; the cytoplasmic flow then reverses, presumably again by continuous local release of pressure in the smaller cell. A theoretical model, approximating the dividing cell to a spherical geometry similar to [Yoneda 1972], can reproduce the experimental oscillations when turnover is added and supposed slower than active contraction. A linear perturbation approach shows the existence of a Hopf bifurcation, leading to oscillations, in a well-defined range of cortical tension, elasticity and turnover parameters. Intriguingly, the model does not adress the possible role of the blebs in this process.

Chapter 2

A visco-active membrane theory of the cell cortex

Contents

In our approach, the cell surface is viewed as a fluid continuum, in the spirit of earlier work [Greenspan 1977, Zinemanas 1987], but turnover of the cortex components prevents the cortical layer to become unstable, as suggested in [Zumdieck 2007]. The cortical actomyosin is furthermore treated using recent active-gel rheologies [Kruse 2005]. The cortex is approximated as one single fluid phase, distinct from the cytoplasm, and we neglect therefore possible local density variations, which may affect the cortex viscosity, as pointed out in [He 1997]. Identifying the mechanical work and dissipated power in the system, we can interpret the numerical results for cytokinesis by scaling arguments in the simplified geometry of [Yoneda 1972] (see section 2.3.2).

2.1 Eulerian continuous formulation

As discussed in section 1.1.2, the actomyosin cortex is a contractile active gel, which is essentially viscous at times longer than the Maxwellian relaxation time. We want therefore to develop a viscous active theory of the cortex mechanics, based on the active-gel theory [Kruse 2005] (see section 1.1.2.3).

The cortical layer remains generally thin compared to cell size, which prompts to use the theory of thin shells to describe its mechanical equilibrium. Thin shell theory is based on the integration of the stresses over the layer thickness, thereby eliminating any explicit dependence of the relevant fields on the transverse direction of the shell. This coarse-graining process leads to effective 2D equilibrium equations of the shell, described in terms of tensions and moments acting tangentially to the shell mid-surface. The mechanical equilibrium is thus given by the balance of forces normal and tangential to the shell mid-surface, and the balances of torques acting on this surface. There exists a very dense literature on thin shells mechanics since the development of the theory of thin plates[1] by Love in 1927 [Love 1927], using the following kinematic assumptions proposed by Kirchhoff [Kirchhoff 1859]: *straight lines normal to the mid-surface remain straight and normal to the mid-surface after deformation, and the thickness of the plate does not change during a deformation.*

Most of the literature deals with elastic thin shells [Timoshenko 1959, Goldenveizer 1961, Novozhilov 1964]. In these studies, the shell thickness is generally considered as constant, consistently with Kirchhoff's hypothesis. The first formal derivations of thin viscous *sheets* theory, with variable thickness, is much more recent [Howell 1996, Ribe 2002].

As noticed by Rayleigh in his study of vibrations of shells in 1877 [Rayleigh 1976], *deformation* [of a thin elastic shell of thickness e] *includes in general, both stretching and bending, and any expression for the* [elastic] *energy will be of the form*:

$$A\,e(\text{extension})^2 + B\,e^3(\text{bending})^2\,. \tag{2.1}$$

In viscous sheets, the dissipation is similarly composed of an extensional term, associated with tensions, proportional to the thickness and a bending term, associated

---

[1] A plate is flat at rest, whereas a shell mid-surface can be naturally curved.

with moments, proportional to the thickness to the power 3. In the limit of vanishing thickness, the dissipation associated with bending is therefore two orders of magnitude lower. This formal consideration is the starting point for deriving a mechanical membrane theory. A membrane is a thin shell where the contribution of bending moments and the transverse shear component are neglected compared to in-plane tensions. By formally expanding the equilibrium equations for axisymmetric thin shells, with the small shell thickness used as an expansion parameter, we derive in the following the equations of motion of a visco-active membrane with cylindrical symmetry in curvilinear coordinates.

2.1.1 Derivation of the axisymmetric visco-active membrane equations

To derive the Eulerian equations of motion for a visco-active membrane, we start from the equilibrium equations for a thin shell (2.6) in axisymmetric curvilinear geometry. We write the constitutive relations and volume conservation equation in bulk for a viscous actomyosin gel and take advantage of the fact that the thickness e of the actomyosin layer is much smaller than the longitudinal size L of the cell to expand the expressions of the shell tensions and moments up to leading order in e/L. We finally show that the resulting equilibrium membrane equations can be integrated analytically along the curvilinear length s into a system of two coupled equations in the membrane local radius r and thickness e.

2.1.1.1 Mechanical equilibrium of an axisymmetric thin shell

Geometrical relations

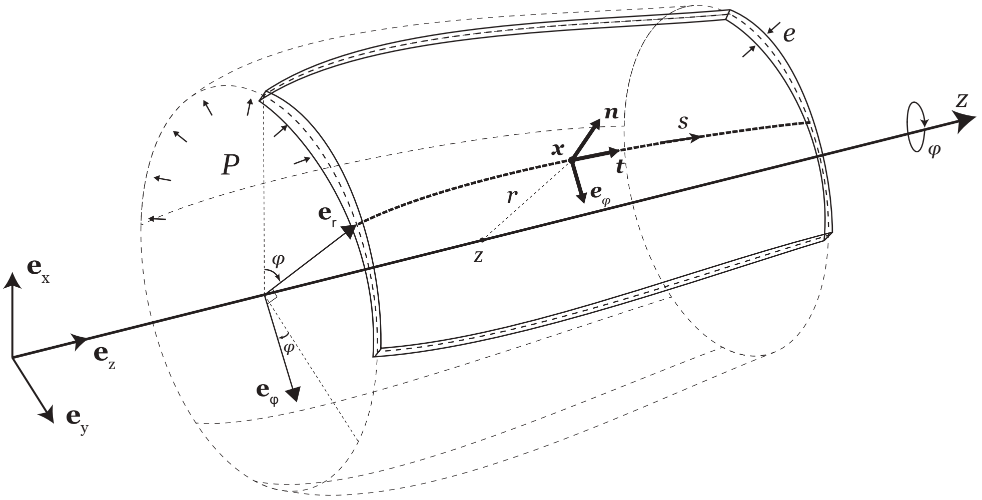

Figure 2.1: Thin shell of revolution: definition of the geometrical parameters

We consider an axisymmetric thin shell. Its shape in 3 dimensions can therefore be reconstructed by revolving a base curve — that we call the mid-line — about the z-axis, as shown on fig. 2.1. The azimuthal angle is called φ and we consider therefore only a section plane $(\mathbf{e}_z, \mathbf{e}_r)$ perpendicular to the azimuthal direction $\mathbf{e}_\varphi$ as shown on fig. 2.2. The cylindrical frame unit vectors depend on the azimuthal angle ϕ: $\mathbf{e}_r(\varphi) = \cos\phi\,\mathbf{e}_x + \sin\phi\,\mathbf{e}_y$ and $\mathbf{e}_\varphi(\varphi) = \frac{d\mathbf{e}_r}{d\phi}$.

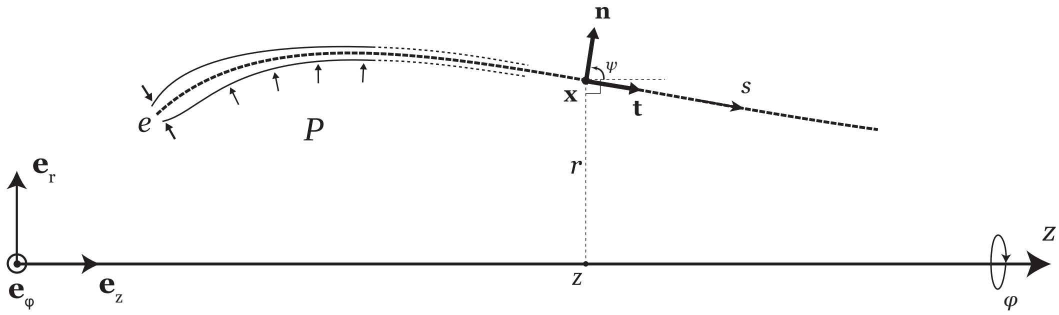

Figure 2.2: Section plane $(\mathbf{e}_z, \mathbf{e}_r(\varphi))$ of the shell of revolution

We define the local Frenet frame $(\mathbf{t}, \mathbf{n}, \mathbf{e}_\varphi)$ such that $\mathbf{t}$ is the unit vector tangent to the mid-line, pointing in the direction s, $\mathbf{n}$ is the unit vector normal to the mid-surface and $\mathbf{e}_\varphi$ the unit vector pointing in the azimuthal direction, cross product of $\mathbf{t}$ and $\mathbf{n}$. We define the intrinsic angle $\psi = \widehat{(\mathbf{e}_z, \mathbf{n})}$. The Frenet frame is fully determined by the intrinsic angle ψ and azimuthal angle ϕ

$$\mathbf{t} = -\cos\psi\cos\varphi\,\mathbf{e}_x - \cos\psi\sin\varphi\,\mathbf{e}_y + \sin\psi\,\mathbf{e}_z\,, \tag{2.2a}$$

$$\mathbf{n} = \sin\psi\cos\varphi\,\mathbf{e}_x + \sin\psi\sin\varphi\,\mathbf{e}_y + \cos\psi\,\mathbf{e}_z\,, \tag{2.2b}$$

$$\mathbf{e}_\varphi = -\sin\varphi\,\mathbf{e}_x + \cos\varphi\,\mathbf{e}_y\,. \tag{2.2c}$$

The unit vectors of the Frenet frame also verify the following classical Frenet-Serret relations (no torsion because of axisymmetry)

$$\frac{\partial \mathbf{t}}{\partial s} = \frac{\partial \psi}{\partial s}\left[\sin\psi\left(\cos\phi\,\mathbf{e}_x + \sin\phi\,\mathbf{e}_y\right) + \cos\psi\,\mathbf{e}_z\right] = \frac{\partial \psi}{\partial s}\,\mathbf{n}\,, \tag{2.3a}$$

$$\frac{\partial \mathbf{n}}{\partial s} = \frac{\partial \psi}{\partial s}\left[\cos\psi\left(\cos\phi\,\mathbf{e}_x + \sin\phi\,\mathbf{e}_y\right) - \sin\psi\,\mathbf{e}_z\right] = -\frac{\partial \psi}{\partial s}\,\mathbf{t}\,, \tag{2.3b}$$

where $\frac{\partial \psi}{\partial s}$ is the local radius of curvature of the mid-line contour in the section plane $(\mathbf{e}_r, \mathbf{e}_\varphi)$ and the following derivatives with respect to the azimuthal angle φ

$$\frac{\partial \mathbf{t}}{\partial \varphi} = -\cos\psi\,\mathbf{e}_\varphi\,, \quad (2.4a) \qquad \frac{\partial \mathbf{n}}{\partial \varphi} = \sin\psi\,\mathbf{e}_\varphi\,, \quad (2.4b) \qquad \frac{\partial \mathbf{e}_\varphi}{\partial \varphi} = -\mathbf{e}_r\,. \quad (2.4c)$$

The midline contour is described by its intrisic coordinates (s, ψ), or alternately by the spatial coordinates (z, r).

They are related by the following geometrical equations

$$\frac{\partial r}{\partial s} = \cos\psi\,, \qquad (2.5a) \qquad\qquad \frac{\partial z}{\partial s} = \sin\psi\,. \qquad (2.5b)$$

Force and moment balance in an axisymmetric thin shell

We summarize below the effective 2-dimensional equilibrium equations for an axisymmetric viscous thin shell, projected onto the local Frenet frame $(\mathbf{t}, \mathbf{n}, \mathbf{e}_\varphi)$. Our thin shell representing the cortical layer, it is submitted to the pressure difference across the cell $-\Delta p_n = P_{\text{int}} - P_{\text{ext}} \equiv \Delta P$ and we neglect the friction of the cortex on the underlying cytosol and on the plasma membrane $\Delta p_t = 0$. The interested reader can find the full derivation in section 2.A.

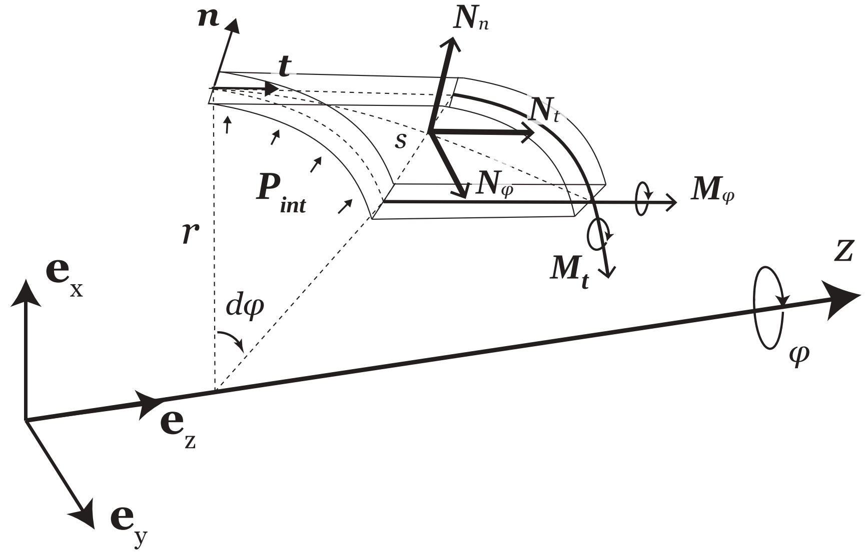

Figure 2.3: Tensions and moments acting an element of an axisymmetric thin shell projected on the local Frenet frame $(\mathbf{t}, \mathbf{n}, \mathbf{e}_\varphi)$.

$$\boxed{\begin{aligned} 0 &= \frac{\partial N_t}{\partial s} + \frac{N_t - N_\varphi}{r}\frac{\partial r}{\partial s} + N_n\frac{\partial \psi}{\partial s} && \textit{Tangential force balance} \\ \Delta P &= N_t\frac{\partial \psi}{\partial s} + N_\varphi\frac{\sin\psi}{r} - \frac{1}{r}\frac{\partial\, r N_n}{\partial s} && \textit{Normal force balance} \\ N_n &= g_\varphi\frac{\partial r}{\partial s} + \frac{1}{r}\frac{\partial\, r g_t}{\partial s} && \textit{Moment balance} \end{aligned}}$$

(2.132a)
(2.132b)
(2.135)

where we defined (see section 2.A)

$$N_t = \int_{-e/2}^{e/2} \sigma_{tt} \left(1 + \xi \frac{\sin\psi}{r}\right) d\xi \qquad \textit{Axial tension} \tag{2.127}$$

$$N_n = \int_{-e/2}^{e/2} \sigma_{nt} \left(1 + \xi \frac{\sin\psi}{r}\right) d\xi \qquad \textit{Transverse shear force} \tag{2.128}$$

$$N_\varphi = \int_{-e/2}^{e/2} \sigma_{\varphi\varphi} \left(1 + \xi \frac{\partial\psi}{\partial s}\right) d\xi \qquad \textit{Azimuthal tension} \tag{2.129}$$

$$g_t = \int_{-e/2}^{e/2} \sigma_{tt}\, \xi \left(1 + \xi \frac{\sin\psi}{r}\right) d\xi \qquad \textit{Axial moment} \tag{2.133}$$

$$g_\varphi = \int_{-e/2}^{e/2} \sigma_{\varphi\varphi}\, \xi \left(1 + \xi \frac{\partial\psi}{\partial s}\right) d\xi \qquad \textit{Azimuthal moment} \tag{2.134}$$

2.1.1.2 Constitutive relation

To evaluate the tensions an moments in the thin shell, we specify below the form of the bulk stress tensor in the cortex. It is the sum of a viscous and an active term $\sigma_{\alpha\beta} = \sigma^v_{\alpha\beta} + \sigma^a_{\alpha\beta}$ (Einstein notation convention).

Isotropic active stress

Here we start from the active-gel formulation, but we consider only the nematic —and not the polar– order of the filaments, as in [Salbreux 2008, Salbreux 2009].

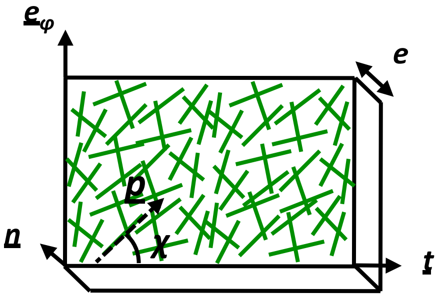

Figure 2.4: Orientation of filaments in the plane of the membrane.

We suppose that the director $\mathbf{p}$ of the filaments is parallel to the midsurface plane, as illustrated in fig. 2.4. It is decomposed as $\mathbf{p}\big(\chi(s), s\big) = \cos\left[\chi(s)\right] \mathbf{t}(s) + \sin\left[\chi(s)\right] \mathbf{e}_\varphi(s)$. The average orientation of a collection of filaments can be described by a nematic tensor $\underline{\underline{\mathbf{Q}}}$ of vanishing trace in 3-dimensions. $Q_{mn} \equiv \left\langle p_m p_n - \frac{1}{3}\delta_{mn}\right\rangle$ is diagonal in the Frenet frame:

$$\underline{\underline{\mathbf{Q}}} = Q_s\, \mathbf{t} \otimes \mathbf{t} + Q_\varphi\, \mathbf{e}_\varphi \otimes \mathbf{e}_\varphi + Q_n \mathbf{n} \otimes \mathbf{n}\,, \tag{2.8}$$

We define $\tilde{Q} = \left\langle \cos^2\chi \right\rangle - \frac{1}{2} = \frac{1}{2} - \left\langle \sin^2\chi \right\rangle$. This scalar measures the deviation from an isotropic orientation of filaments $\langle \cos^2\chi\rangle_{\text{iso}} = \langle \sin^2\chi\rangle_{\text{iso}} = \frac{1}{2}$. The 3-dimensional nematic tensor $Q_{\alpha\beta}$ can therefore be written

$$Q_{\alpha\beta} = \begin{pmatrix} 1/6+\tilde{Q} & 0 & 0 \\ 0 & -1/3 & 0 \\ 0 & 0 & 1/6-\tilde{Q} \end{pmatrix} \tag{2.9}$$

Note that the off-diagonal term $Q_{\varphi t} = Q_{t\varphi} = \langle \sin\chi \cos\chi\rangle$ vanishes for 2-dimensional nematics, as required by axisymmetry. A polar theory of the cortex could, on the contrary, break this symmetry.

From this point we could develop a nematic active membrane theory, but to simplify the problem we suppose here that the filaments remain isotropic: $\tilde{Q} = 0$. No dynamics is therefore associated with filament orientation, and the active part of the stress tensor reduces then to a single term

$$\sigma^a_{\alpha\beta}(s) = \zeta(s)\Delta\mu \begin{pmatrix} 1/6 & 0 & 0 \\ 0 & -1/3 & 0 \\ 0 & 0 & 1/6 \end{pmatrix} \qquad \text{in the Frenet frame } (\mathbf{t}, \mathbf{n}, \mathbf{e}_\varphi). \tag{2.10}$$

Stokean viscous stress

The cortex can be viewed as viscous on the time scale of this study (larger than a minute) and inertial effects are completely negligible at the μm cellular scale. The rheology corresponds therefore to a Stokean fluid, the constitutive relation of which in 3 dimensions reads [Happel 1983]

$$\sigma^v_{\alpha\beta} = 2\eta\, v_{\alpha\beta} - p\delta_{\alpha\beta} \tag{2.11}$$

where p the bulk pressure in the fluid and $v_{\alpha\beta}$ the strain rate tensor, which is the symmetric part of the velocity gradient that we need to evaluate.

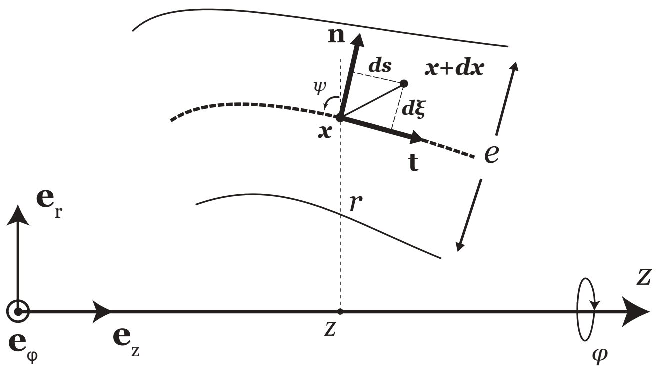

Figure 2.5: Small displacement $d\mathbf{x}$ of a point $\mathbf{x}$ within the layer, in a section plane $(\mathbf{e}_z, \mathbf{e}_r(\varphi))$ of the shell of revolution. The displacement is decomposed into tangential and transverse components, respectively ds and $d\xi$.

A small displacement of a point $\mathbf{x}$ in the cortical layer is given by

$$\begin{aligned} d\mathbf{x} &= dr\,\mathbf{e}_r + dz\,\mathbf{e}_z + rd\phi\,\mathbf{e}_\varphi \\ &= (-ds\cos\psi + d\xi\sin\psi)\;\mathbf{e}_r + (ds\sin\psi d\xi\cos\psi)\;\mathbf{e}_z + rd\phi\,\mathbf{e}_\varphi \\ &= ds\,\mathbf{t} + d\xi\,\mathbf{n} + rd\phi\,\mathbf{e}_\varphi\,, \end{aligned}$$

where ξ is the coordinate in the transverse direction $\mathbf{n}$ as defined on fig. 2.5. Its velocity $\mathbf{v}$ is therefore given by

$$\mathbf{v} = \frac{d\mathbf{x}}{dt} = \frac{ds}{dt}\,\mathbf{t} + \frac{d\xi}{dt}\,\mathbf{n} + r\frac{d\varphi}{dt}\,\mathbf{e}_\varphi \equiv v_t(s,\xi)\,\mathbf{t}(s) + v_n(s,\xi)\,\mathbf{n}(s)\,. \tag{2.12}$$

where v_t and v_φ do not depend on φ because of the symmetry of revolution.

From the previous decomposition of the velocity (2.12) we deduce the formal expression of its gradient in the Frenet frame $(\mathbf{t}, \mathbf{n}, \mathbf{e}_\varphi)$

$$\boldsymbol{\nabla}\mathbf{v} = \underset{\textcircled{1}}{\mathbf{t} \otimes \left(\frac{\partial \mathbf{v}}{\partial s}\right)} + \underset{\textcircled{2}}{\mathbf{n} \otimes \left(\frac{\partial \mathbf{v}}{\partial \xi}\right)} + \underset{\textcircled{3}}{\mathbf{e}_\varphi \otimes \left(\frac{1}{r}\frac{\partial \mathbf{v}}{\partial \varphi}\right)}\,.$$

We evaluate each term separately, using the geometrical relations (2.3)

$$\begin{aligned} &\textcircled{1} = \mathbf{t}\otimes\mathbf{t}\left\{\frac{\partial v_t}{\partial s} + v_n\frac{\partial \psi}{\partial s}\right\} + \mathbf{t}\otimes\mathbf{n}\left\{\frac{\partial v_n}{\partial s} - v_t\frac{\partial \psi}{\partial s}\right\}\,, \\ &\textcircled{2} = \mathbf{n}\otimes\mathbf{n}\,\frac{\partial v_n}{\partial \xi} + \mathbf{n}\otimes\mathbf{t}\,\frac{\partial v_t}{\partial \xi}\,, \\ &\textcircled{3} = \mathbf{e}_\varphi\otimes\mathbf{e}_\varphi\left\{\frac{1}{r}\left(-v_t\cos\psi + v_n\sin\psi\right)\right\}\,. \end{aligned}$$

The symmetric viscous stress tensor reads therefore

$$\sigma^v_{\alpha\beta} = 2\eta\frac{\boldsymbol{\nabla}\mathbf{v}^\top + \boldsymbol{\nabla}\mathbf{v}}{2} - p\mathbb{1} = 2\eta\begin{pmatrix} v_{tt} & v_{tn} & 0 \\ v_{nt} & v_{nn} & 0 \\ 0 & 0 & v_{\varphi\varphi} \end{pmatrix} - p\mathbb{1} \tag{2.14}$$

where

$$v_{tt} = \mathbf{t}\cdot\frac{\partial \mathbf{v}}{\partial s} = \frac{\partial v_t}{\partial s} + v_n\,\frac{\partial \psi}{\partial s}\,, \tag{2.15a}$$

$$v_{nn} = \mathbf{n}\cdot\frac{\partial \mathbf{v}}{\partial \xi} = \frac{\partial v_n}{\partial \xi}\,, \tag{2.15b}$$

$$v_{\varphi\varphi} = \mathbf{e}_\varphi\cdot\frac{1}{r}\frac{\partial \mathbf{v}}{\partial \varphi} = \frac{\mathbf{e}_r\cdot\mathbf{v}}{r} = \frac{-v_t\,\cos\psi + v_n\,\sin\psi}{r}\,, \tag{2.15c}$$

$$v_{tn} = v_{nt} = \frac{1}{2}\left(\frac{\partial v_t}{\partial \xi} + \frac{\partial v_n}{\partial s} - v_t\,\frac{\partial \psi}{\partial s}\right)\,. \tag{2.15d}$$

Note that the off-diagonal terms involving φ ($v_{t\varphi}$ and $v_{n\varphi}$) are zero because of axisymmetry, but the diagonal term $v_{\varphi\varphi}$, that corresponds to a cylindrical inflation or compression, respects the symmetry of revolution.

2.1.1.3 Volume conservation

Local mass conservation, reads in its most general form $\frac{\partial \rho}{\partial t} + \boldsymbol{\nabla} \cdot (\rho \mathbf{v}) = 0$ where ρ is the local gel density, that we suppose constant and uniform here, which leads immediately to

$$
\begin{aligned}
0 &= \boldsymbol{\nabla} \cdot \mathbf{v} = \mathrm{Tr}\left[\boldsymbol{\nabla} \mathbf{v}\right] \\
&= v_{tt} + v_{nn} + v_{\varphi\varphi} \qquad \Big(\text{from } (2.14)\Big)\,, \qquad (2.16) \\
&= \frac{\partial v_t}{\partial s} + v_n \frac{\partial \psi}{\partial s} + \frac{\partial v_n}{\partial \xi} + \frac{-v_t \cos\psi + v_n \sin\psi}{r} \qquad \Big(\text{using } (2.15)\Big)\,. \qquad (2.17)
\end{aligned}
$$

We find the same equation by the direct calculation (2.137), which confirms that our formulation for the strain rate tensor is correct.

2.1.1.4 Expansion of the equations

We follow here a similar approach as [Howell 1994, Howell 1996], used to derive the equations for viscous sheets, but we keep only the leading order to obtain membranes equations. We suppose that typical lengths and velocities are L and U in the longitudinal directions (t, $\mathbf{e}_\varphi$), and εL and εU in the transverse direction $\mathbf{n}$, where the small parameter $\varepsilon \ll 1$ is defined as

$$\varepsilon \equiv \frac{e}{L}\,. \qquad (2.18)$$

The velocity $\mathbf{v}$ of a particle in the shell is the sum of the mid-line velocity $\mathbf{v}^{(0)}(s) = \frac{Dr}{Dt}$ that depends only on s and a component within the layer $\mathbf{v}^{(1)}(s,\xi)$ that depends on s and on the transverse coordinate ξ.

$$\mathbf{v}(s,\xi) = \mathbf{v}^{(0)}(s) + \mathbf{v}^{(1)}(s,\xi)\,. \qquad (2.19)$$

The time-scale associated with flows in the longitudinal direction is L/U, we rescale therefore time as $t = (L/U)\,t'$. Other quantities are non-dimensionalized as follows

$$
\begin{aligned}
r &= L\,r'\,, & e &= \varepsilon L\,e'\,, \\
\mathbf{v}^{(0)} &= U\,\mathbf{v}'^{(0)}\,, & \mathbf{v}^{(1)} &= \varepsilon U\,\mathbf{v}'^{(1)}\,, \\
s &= L\,s'\,, & \xi &= \varepsilon L\,\xi'\,, \\
\sigma &= (\eta U/L)\sigma'\,,
\end{aligned}
$$

The pressure p and the active stress $\zeta\Delta\mu$ are adimensionalized in the same way as the stress σ.

The solutions are sought in the form of asymptotic expansions in powers of the slenderness parameter ε, typically

$$f \sim f^{(0)} + \varepsilon\,f^{(1)} + \varepsilon^2\,f^{(2)}\,\cdots\,. \qquad (2.20)$$

We first evaluate the shear and normal components of the stress tensor up to first-order in ε

$$\sigma_{tn}(s,\xi) = \frac{\eta U}{L}\left[\sigma'^{(0)}_{tn}(s',\xi') + \varepsilon\,\sigma'^{(1)}_{tn}(s',\xi') + \mathcal{O}(\varepsilon^2)\right]$$

and $$\sigma_{nn}(s,\xi) = \frac{\eta U}{L}\left[\sigma'^{(0)}_{nn}(s',\xi') + \varepsilon\,\sigma'^{(1)}_{nn}(s',\xi') + \mathcal{O}(\varepsilon^2)\right]$$

Their first derivatives relative to the transverse coordinate ξ read therefore

$$\frac{\partial\sigma_{tn}}{\partial\xi} \sim \frac{\eta U}{L}\left[\frac{1}{\varepsilon}\frac{\partial\sigma'^{(0)}_{tn}(s',\xi')}{\partial\xi'} + \frac{\partial\sigma'^{(1)}_{tn}(s',\xi')}{\partial\xi'}\right] \tag{2.22a}$$

$$\frac{\partial\sigma_{nn}}{\partial\xi} \sim \frac{\eta U}{L}\left[\frac{1}{\varepsilon}\frac{\partial\sigma'^{(0)}_{nn}(s',\xi')}{\partial\xi'} + \frac{\partial\sigma'^{(1)}_{nn}(s',\xi')}{\partial\xi'}\right] \tag{2.22b}$$

We insert the previous expanded expressions of $\frac{\partial\sigma_{tn}}{\partial\xi}$ and $\frac{\partial\sigma_{tn}}{\partial\xi}$ (2.22), in the local force balance $\boldsymbol{\nabla}\cdot\sigma = 0$, calculated in section 2.C. Dropping primes, the local tangential and normal force balance (2.140a) and (2.140b) lead respectively to

$$\frac{\partial\sigma^{(0)}_{tn}}{\partial\xi} \sim -\varepsilon\left[\frac{\partial\sigma^{(1)}_{tn}}{\partial\xi} + \frac{\partial\sigma_{tt}}{\partial s} + \cos\psi\frac{\sigma_{\varphi\varphi}-\sigma_{tt}}{r} + \frac{\sin\psi}{r}\sigma_{tn}\right].$$

$$\frac{\partial\sigma^{(0)}_{nn}}{\partial\xi} \sim -\varepsilon\left[\frac{\partial\sigma^{(1)}_{nn}}{\partial\xi} + (\sigma_{tt}-\sigma_{nn})\frac{\partial\psi}{\partial s} + \sin\psi\frac{\sigma_{nn}-\sigma_{\varphi\varphi}}{r} + \frac{\partial\sigma_{tn}}{\partial s} - \frac{\cos\psi}{r}\sigma_{tn}\right].$$

$\frac{\partial\sigma^{(0)}_{tn}}{\partial\xi}$ and $\frac{\partial\sigma^{(0)}_{nn}}{\partial\xi}$ are therefore of minimum order ε, which is impossible by definition. They are therefore necessarily zero, and $\sigma^{(0)}_{nn}$ and $\sigma^{(0)}_{tn}$ are independent of ξ:

$$\sigma_{tn}(s,\xi) = \sigma^{(0)}_{tn}(s) + \sigma^{(1)}_{nn}(s,\xi)\,,$$
$$\sigma_{nn}(s,\xi) = \sigma^{(0)}_{nn}(s) + \sigma^{(1)}_{nn}(s,\xi)\,.$$

The boundary conditions on the upper and lower surfaces of the membrane read

$$\sigma_{tn}(s,e/2) = \sigma_{tn}(s,-e/2) = 0 \qquad \text{(no tangential friction)}\,,$$
$$\sigma_{nn}(s,e/2) - \sigma_{nn}(s,-e/2) = \int_{-e/2}^{e/2}\frac{\partial\sigma_{nn}}{\partial\xi}\,d\xi = -\Delta P\,.$$

We deduce immediately that

$$\sigma^{(0)}_{tn}(s) = \sigma^{(0)}_{nn}(s) = 0 \tag{2.26}$$

Let us evaluate now the leading-order components of the strain-rate tensor $v_{\alpha\beta}$

$$v_{tt}^{(0)} = \frac{\partial v_t^{(0)}}{\partial s} + v_n^{(0)} \frac{\partial \psi}{\partial s} \tag{2.27a}$$

$$v_{\varphi\varphi}^{(0)} = \frac{-v_t^{(0)} \cos\psi + v_n^{(0)} \sin\psi}{r} \tag{2.27b}$$

$$v_{nn}^{(0)} = \frac{\partial v_n^{(1)}}{\partial \xi} \tag{2.27c}$$

$$v_{tn}^{(0)} = \frac{1}{2}\left(\frac{\partial v_t^{(1)}}{\partial \xi} + \frac{\partial v_n^{(0)}}{\partial \xi} - v_t^{(0)} \frac{\partial \psi}{\partial s}\right) \tag{2.27d}$$

We deduce the leading-order components of the dimensionless bulk stress tensor $\sigma_{\alpha\beta}$ from the constitutive relations (2.10) and (2.14):

$$\sigma_{tt}^{(0)} = \frac{\zeta\Delta\mu}{6} + 2\left(\frac{\partial v_t^{(0)}}{\partial s} + v_n(0)\frac{\partial \psi}{\partial s}\right) - p^{(0)}\,, \tag{2.28a}$$

$$\sigma_{nn}^{(0)} = 0 = -\frac{\zeta\Delta\mu}{3} + 2v_{nn}^{(0)} - p^{(0)}\,, \tag{2.28b}$$

$$\sigma_{nt}^{(0)} = 0 = v_{tn}^{(0)}\,, \tag{2.28c}$$

$$\sigma_{\varphi\varphi}^{(0)} = \frac{\zeta\Delta\mu}{6} + 2v_{\varphi\varphi}^{(0)} - p^{(0)}\,. \tag{2.28d}$$

In addition, equation (2.16) for volume conservation yields

$$0 = v_{tt}^{(0)} + v_{\varphi\varphi}^{(0)} + v_{nn}^{(0)} + \mathcal{O}(\varepsilon) \tag{2.29}$$

We use the condition of vanishing normal stress $\sigma_{nn}^{(0)} = 0$ (2.26) to express the dimensionless pressure at leading order

$$\begin{aligned} p^{(0)} &= -\frac{\zeta\Delta\mu}{3} + 2v_{nn}^{(0)} \\ &= -\frac{\zeta\Delta\mu}{3} - 2\left(v_{tt}^{(0)} + v_{\varphi\varphi}^{(0)}\right)\,, \end{aligned}$$

where we eliminated $v_{nn}^{(0)}$ via the previous equation for volume conservation (2.29).

Replacing the pressure term from the expression above in the stress tensor and integrating over the membrane thickness leads to the following expression for the dimensionless tensions and moments evaluated from (2.7) at leading order

$$\begin{aligned} N_t &\sim \frac{\zeta\Delta\mu\, e}{2} + 2e\left(2v_{tt}^{(0)} + v_{\varphi\varphi}^{(0)}\right) + \mathcal{O}(\varepsilon) \\ N_\varphi &\sim \frac{\zeta\Delta\mu\, e}{2} + 2e\left(2v_{\varphi\varphi}^{(0)} + v_{tt}^{(0)}\right) + \mathcal{O}(\varepsilon) \\ N_n &\sim \mathcal{O}(\varepsilon^2) \\ g_t &\sim \mathcal{O}(\varepsilon^2) \\ g_\varphi &\sim \mathcal{O}(\varepsilon^2) \end{aligned}$$

In a membrane theory we keep only the leading order quantities. This leads us to neglect the terms of moments, g_t and g_φ, and the shear force N_n, which are of minimum order ε. A more detailed analysis would show that they are in fact of order $\mathcal{O}(\varepsilon^2)$ and therefore largely negligible for $\varepsilon \to 0$ compared to the zeroth-order tension terms.

The equilibrium of a membrane is finally described by the tangential and normal force balance only

$$\Delta P = N_t \frac{\partial \psi}{\partial s} + N_\varphi \frac{\sin \psi}{r} \,, \tag{2.31a}$$

$$0 = \frac{\partial N_t}{\partial s} + \frac{N_t - N_\varphi}{r} \frac{dr}{ds} \,, \tag{2.31b}$$

involving the following membrane tensions, that we redimensionalized

$$N_t = \frac{\zeta \Delta\mu \, e}{2} + 2\eta \, e \left(2 v_{tt}^{(0)} + v_{\varphi\varphi}^{(0)} \right) \,, \tag{2.32a}$$

$$N_\varphi = \frac{\zeta \Delta\mu \, e}{2} + 2\eta \, e \left(2 v_{\varphi\varphi}^{(0)} + v_{tt}^{(0)} \right) \,, \tag{2.32b}$$

2.1.1.5 Actin turnover

The cortical actomyosin is under permanent turnover. The source term, due to actin polymerization, is proportional to the membrane surface since polymerization nucleators are located near the plasma membrane. We describe this effect via a polymerization velocity v_p from the shell upper surface $\xi = e/2$. By contrast depolymerization acts in volume and leads to a depolymerization rate k_d. We integrate polymerization/depolymerization effects by defining a total transverse strain rate $u_{\alpha\alpha}$ (at zeroth order in ε) in the membrane as the sum of the previous viscous contribution $v_{\alpha\alpha}$ and an transverse uniform polymerization term.

$$u_{nn} = v_{nn}^{(0)} - v_\text{p} \, \delta\left(\xi - \frac{e}{2}\right) , \qquad u_{tt} = v_{tt}^{(0)} , \qquad u_{\varphi\varphi} = v_{\varphi\varphi}^{(0)} , \tag{2.33}$$

where $\delta(x)$ is a Delta function of x.

The boundary form of the polymerization term is justified if we consider the normal velocity within the layer with the effect of turnover

$$u_n = \int_{-e/2}^{e/2} u_{nn} \, d\xi = \int_{-e/2}^{e/2} d\xi \left[v_{nn}^{(0)} + v_\text{p} \, \delta\left(\xi - \frac{e}{2}\right) \right] = v_n^{(0)} - v_\text{p} . \tag{2.34}$$

Local volume conservation (2.136) becomes therefore

$$u_{tt} + u_{nn} + u_{\varphi\varphi} = -k_\text{d} \tag{2.35}$$

By averaging this local volume conservation equation across the membrane thickness, we obtain an evolution equation for the thin shell thickness

$$\frac{1}{e} \frac{De}{Dt} + u_{tt} + u_{\varphi\varphi} = -k_\text{d} + \frac{v_\text{p}}{e} \,, \tag{2.36}$$

where $\frac{De}{Dt} \equiv v_n^{(1)}(s,e/2) - v_n^{(1)}(s,-e/2) = \int_{-e/2}^{e/2} d\xi \, \frac{\partial v_n^{(1)}}{\partial \xi}$ is the Lagrangian rate of membrane thickness change; the material time derivative operator reads $\frac{D}{Dt} \equiv \frac{\partial}{\partial t} + \mathbf{v}^{(0)} \cdot \boldsymbol{\nabla}$.

Note that the sum of the tangential and azimuthal strain rates corresponds to the Lagrangian rate of membrane local surface stretch $u_{tt} + u_{\varphi\varphi} = \frac{1}{\delta a}\frac{D\delta a}{Dt}$. If the membrane is not stretched the stationary solution of the equation for volume conservation is

$$e = e_0 \equiv \frac{v_\mathrm{p}}{k_\mathrm{d}} \,, \tag{2.37}$$

which allows us to rewrite the mean volume conservation equation as follows

$$\delta a \frac{De}{Dt} + e\delta a \left(u_{tt} + u_{\varphi\varphi}\right) = \delta a \frac{De}{Dt} + e\frac{D\delta a}{Dt} = \frac{D(e\delta a)}{Dt} = -k_\mathrm{d}\delta a \left(e - e_0\right) \,, \tag{2.38}$$

2.1.1.6 Integration of the equations of motion

Here we show that, for zero tangential friction, the equations for membrane equilibrium can be integrated in the curvilinear coordinate s, independently from the constitutive relation. We use then this compact formulation to reduce our problem to a system of only two coupled equations in membrane radius r and thickness e.

We start from the membrane equilibrium equations

$$\Delta P = N_t \, \kappa_t + N_\varphi \kappa_\varphi \,, \tag{2.31a}$$

$$0 = \frac{\partial N_t}{\partial s} + \frac{N_t - N_\varphi}{r}\frac{\partial r}{\partial s} \,, \tag{2.31b}$$

where κ_t and κ_φ are the principal curvature radii that we can express as a function of r and s only

$$\kappa_t = -\frac{\partial^2 r}{\partial s^2}\frac{1}{\sqrt{1 - \left(\frac{\partial r}{\partial s}\right)^2}} \,, \tag{2.40a}$$

$$\kappa_\varphi = \frac{\sqrt{1 - \left(\frac{\partial r}{\partial s}\right)^2}}{r} \,. \tag{2.40b}$$

From the normal force balance equation (2.39) we extract the azimuthal tension $N_\varphi = \frac{\Delta P}{\kappa_\varphi} - N_t \frac{\kappa_t}{\kappa_\varphi}$, expression that we inject in the tangential force balance (2.39) multiplied by r to obtain

$$\begin{aligned}
\frac{\partial r \, N_t}{\partial s} &= N_\varphi \frac{\partial r}{\partial s} \\
&= -N_t \frac{r \frac{\partial r}{\partial s}\frac{\partial^2 r}{\partial s^2}}{1 - \left(\frac{\partial r}{\partial s}\right)^2} + \frac{\Delta P \, r \frac{\partial r}{\partial s}}{\sqrt{1 - \left(\frac{\partial r}{\partial s}\right)^2}} \\
&= -r \, N_t \, \frac{\partial}{\partial s} \log \sqrt{1 - \left(\frac{\partial r}{\partial s}\right)^2} + \frac{\Delta P \, r \frac{\partial r}{\partial s}}{\sqrt{1 - \left(\frac{\partial r}{\partial s}\right)^2}}
\end{aligned}$$

We therefore need to solve the following first order differential equation in the quantity rN_t

$$\frac{\partial r N_t}{\partial s} + r N_t \frac{\partial}{\partial s} \log \sqrt{1 - \left(\frac{\partial r}{\partial s}\right)^2} = \frac{\Delta P \, r \frac{\partial r}{\partial s}}{\sqrt{1 - \left(\frac{\partial r}{\partial s}\right)^2}} \, .$$

The homogeneous equation can be solved as $rN_t = \frac{A}{\sqrt{1-\left(\frac{\partial r}{\partial s}\right)^2}}$, where A is a constant. We then apply the constant variation method to find the solution of the equation with a second member. It yields $\frac{dA}{ds} = \Delta P \, r \frac{\partial r}{\partial s}$, which can be integrated as $A(s) = B + \Delta P \, r^2/2$ with B a constant (ΔP is uniform). The general solution of the differential equation reads finally

$$rN_t = \frac{B + \Delta P \, r^2/2}{\sqrt{1 - \left(\frac{\partial r}{\partial s}\right)^2}} \, . \tag{2.41}$$

Here we consider a closed membrane surface, which implies the following boundary conditions $r(s) = r(L) = 0$ and $\frac{\partial r}{\partial s}\big|_{s=0} = -\frac{\partial r}{\partial s}\big|_{s=L} = 1$, where L is the membrane contour total length. This yields necessarily $B = 0$ to avoid a singularity at $s = 0$ and $s = L$.

We end up with the following general formula for the membrane tensions, independently from the constitutive equation of the material

$$N_t = \frac{\Delta P}{2} \frac{r}{\sqrt{1 - \left(\frac{\partial r}{\partial s}\right)^2}} = \frac{\Delta P}{2} \frac{1}{\kappa_\varphi} \, , \tag{2.42a}$$

$$N_\varphi = \frac{\Delta P}{2} \frac{1}{\kappa_\varphi} \left(2 - \frac{\kappa_t}{\kappa_\varphi}\right) \, . \tag{2.42b}$$

This formulation is very useful, since we can easily deduce that an isotropic tension $N_t = N_\varphi$ leads necessarily to a spherical shape $\kappa_t = \kappa_\varphi$.

Combining eq. (2.32) and eq. (2.36) and remarking that $u_{\varphi\varphi} = v^{(0)}_{\varphi\varphi}(s) = \frac{\mathbf{e}_r \cdot \mathbf{v}^{(0)}}{r} = \frac{1}{r}\frac{Dr}{Dt}$, we can obtain a system of two coupled equations for e and r :

$$\boxed{\begin{aligned} \frac{De}{Dt} &= -k_\mathrm{d}\left(e - e_0\right) + \frac{\zeta \Delta\mu \, e}{6\eta} - \frac{\Delta P}{12\eta} \frac{1}{\kappa_\varphi} \left[3 - \frac{\kappa_t}{\kappa_\varphi}\right] \, , & \text{(2.43a)} \\ \frac{Dr}{Dt} &= -\frac{\zeta \Delta\mu \, r}{12\eta} + \frac{\Delta P}{12\eta e} \frac{r}{\kappa_\varphi} \left[3 + \frac{2\kappa_t}{\kappa_\varphi}\right] \, . & \text{(2.43b)} \end{aligned}}$$

This formulation of the problem has the advantage to be very compact and to show directly the main effects at work:

- We identify the typical time-scale of the problem that we denote $T_a = \frac{2\eta}{\zeta \Delta\mu}$: it measures the viscous flow time-scale of the gel in response to an active stress $\zeta \Delta\mu$.

- The local membrane thickness e (2.43a) emerges as a competition between turnover effects (proportional to k_{d}) and active flows (term proportional to $\zeta\Delta\mu/\eta$), but also depends on the local membrane geometry and cell pressure (term proportional to ΔP).

- The local cell azimuthal radius r (2.43b) emerges as a competition between active contraction (term proportional to $\zeta\Delta\mu$) and inner pressure resistance (term proportional to ΔP and positive for $\kappa_t \geq -\frac{3}{2}\kappa_\varphi$, where $\kappa_\varphi = \frac{\sin\psi}{r}$ is positive by construction)

If we assume conservation of the inner volume delimited by the closed membrane, ΔP becomes a non-local variable that depends on the whole membrane configuration $\big(r(s), e(s)\big)_{s\in[0,L]}$. The system of coupled equations in the local variables e and r (2.43) becomes then very hard to solve numerically. We can however perturb the equilibrium from a reference state, and solve analytically the linearized equations. This is the approach we adopt for the study of a cell polarization process in the next subsection. In the next section we present a Lagrangian equivalent formulation that can be more easily implemented numerically and allows for solving extensively the non-linear problem.

Summary of the Eulerian theory of visco-active axisymmetric membranes

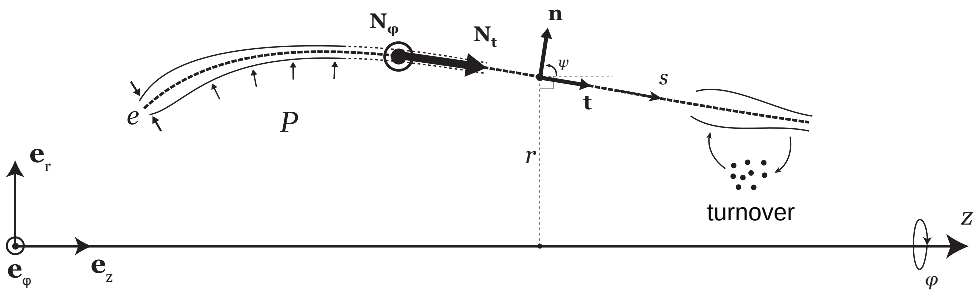

Figure 2.6: Plane section $(\mathbf{e}_z, \mathbf{e}_r(\varphi))$ of the axisymmetric membrane with tangential and azimuthal tensions N_t and N_φ and inner pressure P.

$$\Delta P = N_t\,\kappa_t + N_\varphi\,\kappa_\varphi \qquad \textit{Normal force balance} \tag{2.31a}$$

$$0 = \frac{\partial N_t}{\partial s} + \frac{N_t - N_\varphi}{r}\frac{dr}{ds} \qquad \textit{Tangential force balance} \tag{2.31b}$$

$$\kappa_t = \frac{\partial \psi}{\partial s} \tag{2.40a}$$

$$\kappa_\varphi = \frac{\sin\psi}{r} \qquad \textit{Geometrical relations} \tag{2.40b}$$

$$\frac{dr}{ds} = \cos\psi \tag{2.5a}$$

$$N_t = N^a + N_t^v = \frac{e}{2}\zeta\Delta\mu + 2\eta e\,(2u_{tt} + u_{\varphi\varphi}) \qquad \textit{Axial tension} \tag{2.32a}$$

$$N_\varphi = N^a + N_\varphi^v = \frac{e}{2}\zeta\Delta\mu + 2\eta e\,(u_{tt} + 2u_{\varphi\varphi}) \qquad \textit{Azimuthal tension} \tag{2.32b}$$

$$0 = u_{tt} + u_{\varphi\varphi} + \frac{1}{e}\frac{De}{Dt} + k_d - \frac{v_p}{e} \qquad \textit{Volume conservation} \tag{2.36}$$

Summary 2.1: Eulerian visco-active axisymmetric membrane theory. (2.31a): normal force balance is a generalized version of the original law of Laplace $\Delta P = \frac{2N}{R}$ when the surface tension is anisotropic, i.e. when the two tensions in the principal directions N_t and N_φ are not the same. (2.31b): tangential force balance relates the tension anisotropy $N_t - N_\varphi$ and the gradient of axial tension $\frac{\partial N_t}{\partial s}$: an anisotropic membrane tension implies a non-zero gradient of axial tension, and conversely, unless the membrane is purely cylindrical $\frac{\partial r}{\partial s} = 0$. Eqs. (2.40a), (2.40b) and (2.5a): the three geometrical relations are measures of the membrane shape. Eqs. (2.32a) and (2.32b): the membrane tensions N_t and N_φ are the sum of an isotropic active term $N^a = \frac{e}{2}\zeta\Delta\mu$ and an anisotropic viscous term $N^v_{t,\,\varphi}$. The tension anisotropy is therefore due to an anisotropy of membrane stretching $N_{tt} - N_{\varphi\varphi} = 2\eta e\,(u_{tt} - u_{\varphi\varphi})$, which reveals a tangential cortical flow along the membrane. eq. (2.36): the variation of membrane thickness is due to membrane stretching and flow but also to turnover terms.

2.1.2 Study of a cell polarization mechanism by an analytical perturbation approach

2.1.2.1 Experimental observations

Introduction

Cell polarization is a fundamental biological process that has implications in many stages of embryonic and tissue development. The cell polarity can be defined, in a very general way, as a morphological asymmetry of cellular components along a well-defined axis that drives a functional asymmetry in the cell [Drubin 1996]. Cell migration on 2D surfaces is one long-studied typical example of cellular components asymmetry (PIP_2, Rac, Cdc42, Myosin II, actin etc...) that drives a functional symmetry breaking by triggering cell movement along the polarity axis [Ridley 2003]. Symmetry breaking can be spontaneous, like in cell motility [Yam 2007], but cell polarization can also be triggered by a localized cue, like the sperm entry in *C. Elegans* embryo [Munro 2004]. Notably, the interaction of the cell with the extracellular matrix (ECM), via the complex integrin-fibronectin, drives spreading and motility in 2 dimensions and is mechanosensitive (durotaxis [Lo 2000]). An experimental setup was developed by P. Bun in the group of M. Coppey-Moisan to study a polarization process in 3D of a suspended 3T3 fibroblast (unpublished work). As shown schematically on fig. 2.7 the cell lies on a poly(L-lysine)-graft-poly(ethylen glycol) (Pll-PEG) treated cover slip, that prevents the formation of adhesion sites to the glass surface but maintains the center of mass of the cell at a fixed position. A bead coated with fibronectin (Fn) is manipulated with an optical tweezer which allows for measuring forces exerted on the bead by the cell. It also permits to exert a counteraction force on the displaced bead that scales linearly with the trap stiffness. A DIC microscope (differential interference contrast) images the cell in 3D. Fluorescent labels allows furthermore to quantify the geometrical and molecular cell response to the adhesion cue. Various bead coatings and trap stiffness are tested.

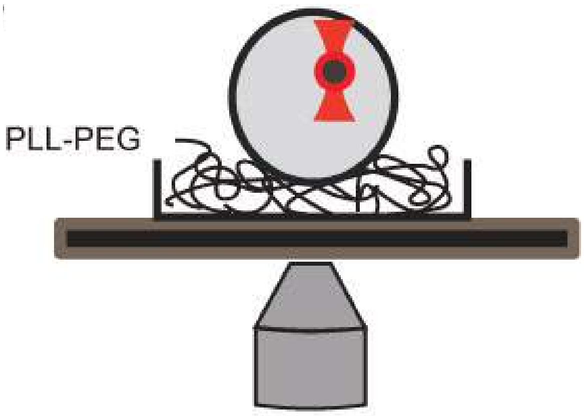

Figure 2.7: Sketch of the experimental setup used to study the response of a suspended cell to a mechanochemical adhesion cue (Credits: P. Bun, unpublished work).

Results

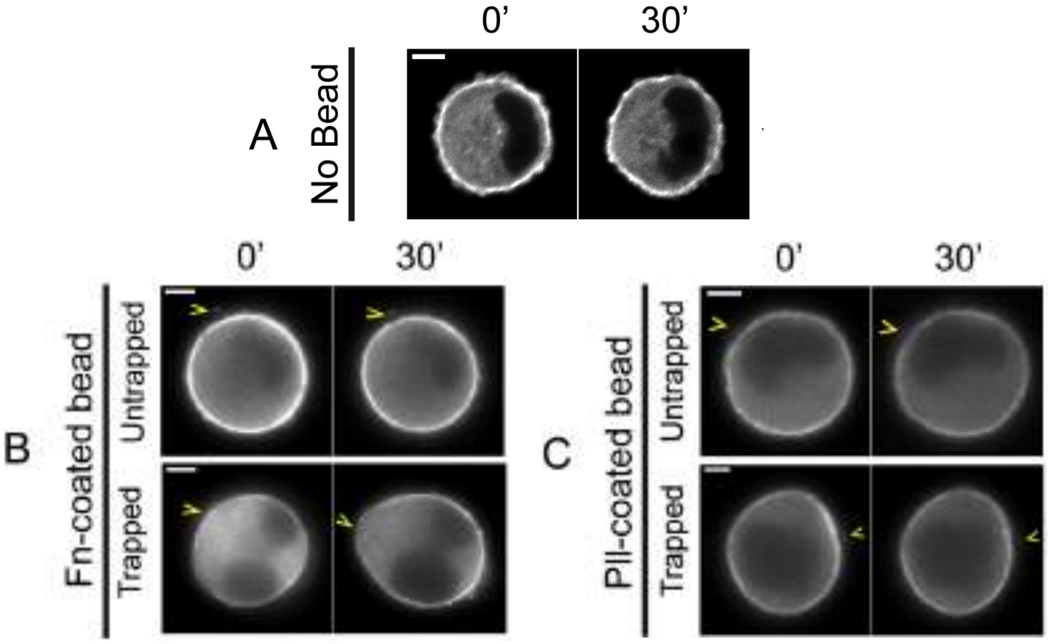

Figure 2.8: Cell shape polarization. Fluorescence images of single unadhered cells expressing eGFP-myosin IIA at 0min and 30min, for five different conditions: (A) *No bead*, (B) *Fn-coated untrapped bead* and *Fn-coated trapped bead*, (C) *Pll-coated untrapped bead* and *Pll-coated untrapped bead*. The yellow arrow indicates the position of the bead. (Credits: P. Bun, unpublished work).

Five different conditions are compared:

(A) No bead: The unadhered fibroblast displays continuous shape oscillations at a well-defined principal frequency of $0.013 \pm 0.003\,\text{Hz}$. This spontaneous oscillation of fibroblasts upon de-adhesion has been already described in [Salbreux 2007] and modeled using an visco-active thin shell theory with analogous ingredients, but with a coupling to mechanosensitive calcium channels.

(B) Fn-coated untrapped bead and *Fn-coated trapped bead*: When a Fn-coated bead adheres to the cell, shape oscillations stop and the cells adopt a nice spherical shape a time $t = 0$. For the untrapped bead, the cell shape does not evolve further as shown on fig. 2.8 *(B)*, whereas the cell polarizes within a few tens of minutes in response to the adhesion to a Fn-coated bead trapped by a non-zero tweezer stiffness. The cell polarization is characterized by the formation of an actomyosin-enriched pole opposite to the adhesive trapped bead and by the concomitant slow deformation of the cell into a pear-like shape, along a well-defined polarization axis crossing the bead center. The polarization process is actomyosin dependent, since addition of blebbistatin, a drug that inhibits myosin II ATPase activity, prevents systematically polarization. These results show that a single Fn adhesion cue with non-zero trap stiffness can induce a actomyosin-dependent polarization of a cell in 3D along an axis crossing the center of the cue.

(C) Pll-coated untrapped bead and *Pll-coated untrapped bead*: To show the chemical specificity of the cell polarization to the complex fibronectin-integrin, the same experiment is repeated with Pll-coated beads, trapped and untrapped. The adhesion cue induces again a stop of cell oscillations, but no spontaneous polarization appears in either of the two cases.

We summarize schematically these experimental results in fig. 2.9 below.

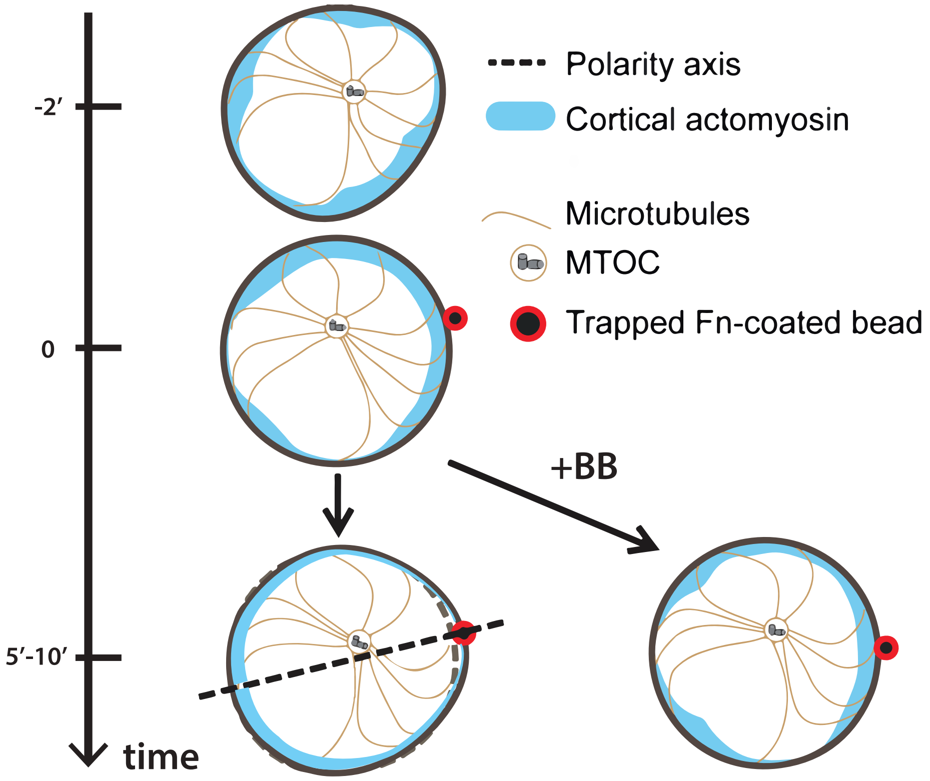

Figure 2.9: Illustration of the actomyosin-dependent polarization process upon adhesion of a Fn-coated trapped bead (Credits: P. Bun, unpublished work).

2.1.2.2 A perturbation model to account for the polarization process

Model hypothesis

We use here the Eulerian membrane theory of the cell cortex, previously derived, to describe the cell polarization process. We assume that the mechanical equilibrium within the cytosol is very rapid compared to the slow deformation of the cortex (about $20min$). We therefore consider the internal hydrostatic cell pressure P_{int} as uniform. This is justified experimentally by the absence of visible cytosolic flow within the cell on the observation time-scale.

The model predicts the cell shape and the actomyosin distribution along the cell surface, given the myosin motor activity and polymerization within the cortex. These parameters are indeed actively and locally tightly regulated by the cell, and are used as prescribed inputs in the model. We linearize the mechanical equations and only consider small perturbations of the different variables from a given reference state chosen as a spherical cell. The results remain hence limited to small amplitudes, but they reveal the fundamental physical principles at work. We therefore do not intend to obtain quantitatively accurate results, but rather to bring out and rationalize the essential mechanisms involved in the cortical redistribution and cell shape change upon the adhesion-cue trigger.

Linearization of the membrane equations around the sphere

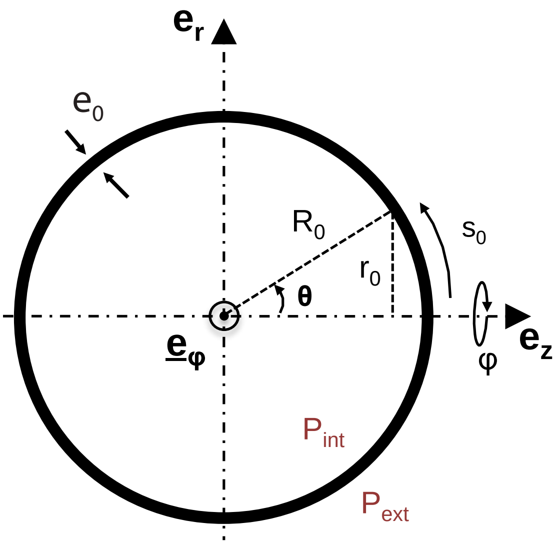

Figure 2.10: Sketch of the initial spherical configuration of the membrane.

We perturb the variables in section 2.2.2.4 around a spherical reference state of the membrane depicted in fig. 2.10, of radius R_0 and thickness $e_0 = \frac{v_\mathrm{p}}{k_\mathrm{d}}$ and subjected to a tension $N_0^a = \zeta_0 \Delta\mu\, e_0$ that satisfies Laplace's equilibrium: $\Delta P_0 = \frac{2N_0^a}{R_0}$. We choose the polar angle $\theta \equiv \frac{s_0}{R_0}$ as the main coordinate here

$$\begin{aligned}
&\psi(\theta) = \theta + \delta\psi(\theta)\,, && R(\theta) = R_0 + \delta R(\theta)\,,\\
&e(\theta) = e_0 + \delta e(\theta)\,, && r(\theta) = r_0(\theta) + \delta r(\theta)\,,\\
&v_p(\theta) = e_0\, k_d + \delta v_p(\theta)\,, && \kappa_t(\theta) = \frac{1}{R_0} + \delta\kappa_t(\theta)\,,\\
&\zeta(\theta) = \zeta_0 + \delta\zeta(\theta)\,, && \kappa_\varphi(\theta) = \frac{1}{R_0} + \delta\kappa_\varphi(\theta)\,,\\
&P = P_{\mathrm{int}0} + \delta P_{\mathrm{int}}\,. &&
\end{aligned}$$

We rescale the variables as follows to makes them dimensionless

$$\begin{aligned}
\bar{R} &= R/R_0\,, & \bar{t} &= t\,\tfrac{\zeta_0\Delta\mu}{2\eta}\,,\\
\bar{\kappa}_t &= R_0\,\kappa_t\,, & \bar{v}_{\mathrm{p}} &= \tfrac{v_{\mathrm{p}}}{e_0\,k_d}\,,\\
\bar{\kappa}_\varphi &= R_0\,\kappa_\varphi\,, & \bar{k}_{\mathrm{d}} &= k_{\mathrm{d}}\,\tfrac{2\eta}{\zeta_0\Delta\mu}\,,\\
\bar{e} &= e/e_0\,, & \bar{u}_{\alpha\alpha} &= u_{\alpha\alpha}\,\tfrac{2\eta}{\zeta_0\Delta\mu}\,,\\
\bar{\zeta} &= \zeta/\zeta_0\,, & \bar{P} &= \tfrac{P}{\zeta_0\Delta\mu}\,\tfrac{R_0}{e_0}\,.
\end{aligned}$$

From curvilinear force balance and turnover dynamics (eqs. (2.31a) and (2.31b) and eq. (2.36)) we get three coupled linearized and dimensionless equations describing the quasi-static mechanical equilibrium of the membrane shell. We omit the upper-bar from here on for sake of readability.

$$\delta P_{\mathrm{int}} = \delta e + \delta\zeta + 3\left(u_{tt} + u_{\varphi\varphi}\right) + \frac{1}{2}\left(\delta\kappa_t + \delta\kappa_\varphi\right), \tag{2.45a}$$

$$0 = \partial_\theta\,\delta e + \partial_\theta\,\delta\zeta + 2\left[\partial_\theta\left(2u_{tt} + u_{\varphi\varphi}\right) + \cot\theta\left(v_{tt} - v_{\varphi\varphi}\right)\right], \tag{2.45b}$$

$$0 = k_{\mathrm{d}}\left[\delta e - \delta v_{\mathrm{p}}\right] + u_{tt} + u_{\varphi\varphi} + \frac{d\delta e}{dt}. \tag{2.45c}$$

The geometric variables are not independent from each others and one can easily show that

$$\delta\kappa_t = -\left\{\partial_\theta^2 + 1\right\}\,\delta R\,, \tag{2.46a}$$

$$\delta\kappa_\varphi = -\left\{\cot\theta\,\partial_\theta - 1\right\}\,\delta R\,. \tag{2.46b}$$

We can also express the strain rates as a function of the velocities (v_θ, v_R) along the radial and polar directions $(\mathbf{e}_\theta, \mathbf{e}_R)$ at first order in perturbation:

$$u_{tt} = \partial_\theta v_\theta + v_R\,, \tag{2.47a}$$

$$u_{\varphi\varphi} = \cot\theta\,v_\theta + v_R\,. \tag{2.47b}$$

Local perturbation of activity or/and turnover in the bead region

We look at the response of the cell to the combined effect of a prescribed decrease of polymerization and myosin activity in the region of the bead (B). We suppose that these perturbations are of Gaussian form:

$$\delta v_{\mathrm{p}}(\theta) = -\delta v_{\mathrm{p}}^{\mathrm{B}}\,e^{-\left(\frac{\theta}{\theta_B}\right)^2}\,, \tag{2.48a}$$

$$\delta\zeta(\theta) = -\delta\zeta_{\mathrm{B}}\,e^{-\left(\frac{\theta}{\theta_B}\right)^2}\,. \tag{2.48b}$$

where $\theta_B \equiv \arcsin\left(\frac{a}{R_0}\right)$. a is the size of the perturbation region, $\delta v_p^B > 0$ and $\delta\zeta_B$ are the amplitude of, respectively, the polymerization and activity decrease in the cue region.

We seek for a stationary equilibrium solution of eqs. (2.45) to (2.47), which imposes $v_R \equiv \frac{1}{R}\frac{DR}{dt} = 0$ and $\frac{De}{Dt} = 0$. We therefore infer

$$\frac{1}{2}\left\{\partial_\theta^2 + \cot\theta\,\partial_\theta + 2\right\}\,\delta R = 3\left\{\partial_\theta + \cot\theta\right\}\,v_\theta + \delta e + \delta\zeta\,, \tag{2.49a}$$

$$4\left\{\partial_\theta^2 + \cot\theta\,\partial_\theta - \cot^2\theta - \frac{1}{2}\right\}\,v_\theta = -\partial_\theta\,\delta e - \partial_\theta\,\delta\zeta\,, \tag{2.49b}$$

$$-k_\mathrm{d}\,\left[\delta e - \delta v_\mathrm{p}\right] = \left\{\partial_\theta + \cot\theta\right\}\,v_\theta. \tag{2.49c}$$

We can check that we have three variables v_θ, δe and δR and three coupled differential equations. We therefore only need to precise the boundary conditions at $\theta = 0$ and $\theta = \pi$ to fully determine the solution of the problem subject to the external perturbations $\delta\zeta(\theta)$ and $\delta v_p(\theta)$ (2.48):

$$v_\theta(0) = v_\theta(\pi) = 0\,, \tag{2.50a}$$

$$\partial_\theta R(0) = \partial_\theta R(\pi) = 0\,, \tag{2.50b}$$

$$\partial_\theta e(0) = \partial_\theta e(\pi) = 0\,. \tag{2.50c}$$

We decompose the variables in series of Legendre or Gegenbauer polynomials since these functions constitute a orthogonal basis which is well-adapted to problems close to circular geometries:

$$v_\theta(\theta) = \sum_{n=1}^{+\infty} V^{(n)}\,\frac{\mathcal{I}_{n+1}(\cos\theta)}{\sin\theta}\,,$$

$$\delta e(\theta) = \sum_{n=0}^{+\infty} E^{(n)}\,\mathcal{P}_n(\cos\theta)\,,$$

$$\delta R(\theta) = \sum_{n=0}^{+\infty} R^{(n)}\,\mathcal{P}_n(\cos\theta)\,,$$

$$\delta\zeta(\theta) = \sum_{n=0}^{+\infty} Z^{(n)}\,\mathcal{P}_n(\cos\theta)\,,$$

$$\delta P_\mathrm{int} = \sum_{n=0}^{+\infty} P_\mathrm{int}^{(n)}\,\mathcal{P}_n(\cos\theta) = P_\mathrm{int}^{(0)}\,.$$

where $\mathcal{P}_n$ is the Legendre polynomial of order n and $\mathcal{I}_{n+1} \equiv \frac{\mathcal{P}_{n-1}-\mathcal{P}_{n+1}}{2n+1}$ is the Gegenbauer polynomial of order $n+1$. The choice to decompose a quantity into Legendre or Gegenbauer polynomials depends on the order of the derivatives at which the variable appears in the equation: the two polynomials are first derivative functions of one another up to a factor $\sin\theta$ (see section 2.D.2) and we want to end up with equations of Legendre polynomials of the same order only.

We insert the previous decompositions into the stationary mechanical membrane equations (2.49). Using classical properties of Legendre polynomials (eq. (2.153) in section 2.D.2) we get the following recursion relations the decomposition coefficients: $\forall\, n \geq 1$

$$\frac{1}{2}\left[2 - n\,(n+1)\right]\, R^{(n)} = 3V^{(n)} + E^{(n)} + Z^{(n)}, \tag{2.52a}$$

$$2\left[1 - 2\,n\,(n+1)\right]\, V^{(n)} = n\,(n+1)\left[E^{(n)} + Z^{(n)}\right], \tag{2.52b}$$

$$V^{(n)} = -k_{\mathrm{d}}\left[E^{(n)} - V_p^{(n)}\right]. \tag{2.52c}$$

Mode $n = 0$ The mode $n = 0$ corresponds to an isotropic expansion of the cell, so $V^{(0)} = 0$. Because we consider that the cell volume does not vary we impose $R^{(0)} = 0$. Therefore only internal pressure has to increase to compensate the activity variation. Higher modes, on the contrary, conserve volume at first-order and do not contribute to pressure variation.

$$R^{(0)} = 0\,, \qquad V^{(0)} = 0\,,$$
$$E^{(0)} = 0\,, \qquad P_{\mathrm{int}}^{(0)} = Z^{(0)}\,.$$

Mode $n = 1$ The mode $n = 1$ is treated separately since eqs. (2.52a) and (2.52b) become degenerate which leaves $R^{(1)}$ undefined. This mode corresponds to a cell translation along the z axis and we impose here that the cell does not move along the z-axis according to experiments, so $R^{(1)} = 0$.

$$R^{(1)} = 0\,, \qquad V^{(1)} = \frac{k_d\,V_p^{(1)}}{1-3k_d}\,, \qquad E^{(1)} = \frac{3k_d\,V_p^{(1)}}{3k_d-1}\,,$$

Modes $n > 1$ For modes $n > 1$ the determinant of the system of equations (2.52) is non-zero and we can solve it:

$$R^{(n)} = \frac{2\,k_{\mathrm{d}}\left\{V_p^{(n)} + Z^{(n)}\right\}}{2\,k_{\mathrm{d}}\left[1 - 2n\,(n+1)\right] + n\,(n+1)}, \tag{2.53a}$$

$$V^{(n)} = \frac{k_{\mathrm{d}}\,n\,(n+1)\left\{V_p^{(n)} + Z^{(n)}\right\}}{2\,k_{\mathrm{d}}\left[1 - 2n\,(n+1)\right] + n\,(n+1)}, \tag{2.53b}$$

$$E^{(n)} = \frac{2\,k_{\mathrm{d}}\left[1 - 2n\,(n+1)\right]\,V_p^{(n)} - n\,(n+1)\;Z^{(n)}}{2\,k_{\mathrm{d}}\left[1 - 2n\,(n+1)\right] + n\,(n+1)}. \tag{2.53c}$$

We calculate numerically the coefficients $Z^{(n)}$ and $V^{(n)}$ from the expression of motor activity and polymerization perturbation (2.48) up to a certain order n:

$$Z^{(n)} = \frac{2n+1}{2}\int_0^{\pi} d\theta\,\delta\zeta(\theta)\,\mathcal{P}_n(\theta)\sin\theta\,, \tag{2.54a}$$

$$V_p^{(n)} = \frac{2n+1}{2}\int_0^{\pi} d\theta\,\delta v_p(\theta)\,\mathcal{P}_n(\theta)\sin\theta\,. \tag{2.54b}$$

We can then reconstruct numerically the functions $\delta v_\theta(\theta)$, $\delta e(\theta)$ and $\delta R(\theta)$, solutions of the problem by means of the Eqs. (2.1.2.2), (2.1.2.2) and (2.53).

Note that the effects of the two perturbations, motor activity and polymerization, add up linearly (2.53), as expected for linearized equations.

Results of the model

Local decrease of active tension at the bead pole triggers cell cortex and shape polarization We impose successively in the bead region:

1. a decrease of motor activity ζ plotted in fig. 2.11, while maintaining the polymerization v_p uniform along the cortex;
2. a decrease of the polymerization plotted in fig. 2.12, while maintaining the motor activity ζ uniform along the cortex;
3. a simultaneous decrease of polymerization and myosin activity, which would correspond to a decrease of active RhoA, fig. 2.13 *(C)*.

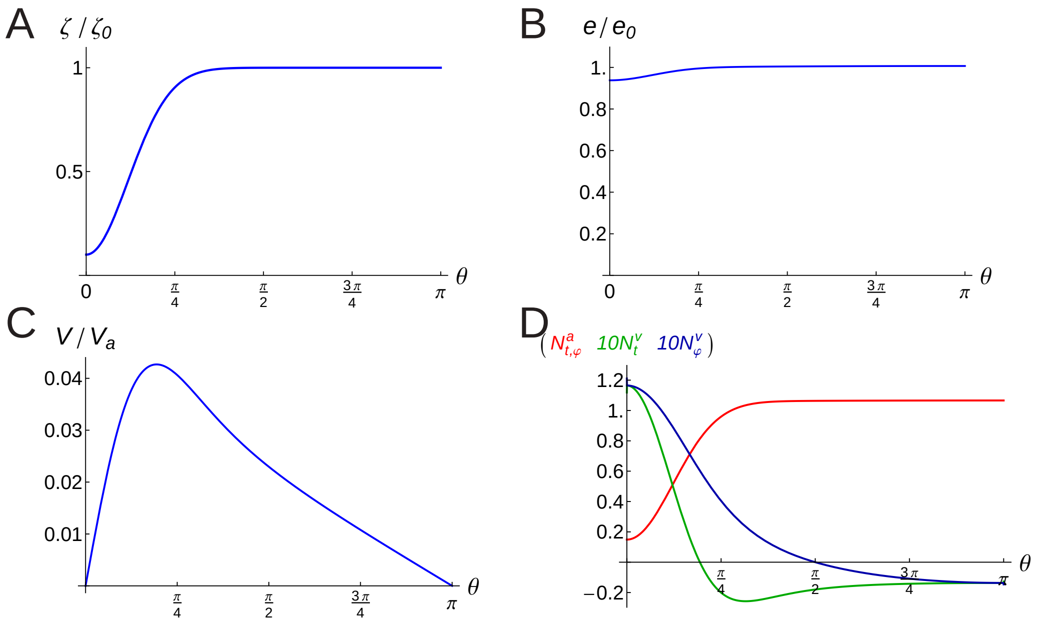

Figure 2.11: Results of the perturbation approach for a local decrease of the myosin activity in the region of the bead. *(A)* Form of the activity perturbation function ζ/ζ_0 imposed along the cortex as a function of the polar angle θ. *(B)* Distribution of the cortical thickness $e(\theta)$ along the cortex, normalized by the initial thickness e_0. *(C)* Amplitude of the cortical flow $V(\theta)$ generated by the perturbation, normalized by a typical active velocity $V_a = R_0\frac{\zeta_0\Delta\mu}{2\eta}$, along the cortex as a function of θ. *(D)* Cortical tensions as function of θ: isotropic active tension $N^a_{t,\varphi}(\theta)$ (*red*) and anisotropic viscous tensions $N^v_t(\theta) \neq N^v_\varphi(\theta)$ (*green, blue*), multiplied by a prefactor 10.

The three scenarios correspond to a decrease of the active tension — proportional to ζ and e — (eqs. (2.32a) and (2.32b)) in the region of the bead and lead to the same process of polarization. Th decrease of polymerization and myosin activity lead however to distinct preeminent effects. Both perturbations result in a decrease of active tension that triggers a longitudinal active flow propagating along the cortex away from the bead toward the opposite pole. The flow velocity V, normalized by a typical active velocity $V_a \equiv R_0 \frac{\zeta_0 \Delta\mu}{2\eta}$, is zero at the two poles and has a maximum around the region where the activity perturbation vanishes. This cortical flow tends to deplete actomyosin from the region of the bead and to accumulate it to the opposite pole, but this effect alone is pretty weak with a perturbation of the myosin activity alone, as shown on fig. 2.11*B*. The competition of this flow with turnover dynamics, which tends to maintain a uniform thickness e_0 along the cortex, leads to a stationary distribution of cortical thickness along the cortex. Therefore the decrease of thickness is more prominent when the polymerization is decreased in the bead region (see fig. 2.12*B*). The cortical flow leads in both cases to anisotropic viscous tensions along the cortex: $N_t^v(\theta) \neq N_\varphi^v(\theta)$. This anisotropy is responsible for the stationary non-spherical shape of the cell, as we explain further. However the shape deformation of the perturbed cell is pretty weak, unless we decrease simultaneously the polymerization and the myosin activity in the bead region. We summarize these results in fig. 2.13 with plots of the cell shape with thickness, where we outlined the amplitude of the cortical flow via a color gradient. The cell tends to elongate along the polarization axis to lead to a pear-like shape in fig. 2.13*C*, in good qualitative agreement with experimental observations of the polarized state of cells.

Cortical flows are necessary to account for non-spherical cell shapes

As we already mentioned in eq. (2.42), a purely isotropic cortical tension $N_t = N_\varphi$ leads necessarily to a spherical shape, which indeed minimizes optimally the surface for a given volume. Note that this is true only for an isolated cell, which is not submitted to any external force, apart from the inner and outer pressures. We neglect here the axial force exerted by the optical tweezer on the cell, as well as the frictional drag of the Pll-PEG layer. Since the active tension is isotropic by definition here (see eqs. (2.32a) and (2.32b)), anisotropic contributions to the cortical tensions have to be invoked to account mechanically for the non-spherical shapes of the polarized cells. They can only emerge from a sustained cortical flow, which is necessarily anisotropic on a closed surface and is triggered by a gradient of active tension along the cortex. This simple mechanical analysis predicts therefore that non-spherical stationary shape of the polarized cells is an evidence for persistent and longitudinal cortical flows along their surface.

Further analysis of the plots of tensions within the cortical shell (figs. 2.11 and 2.12*D*) reveal common mechanical properties:

- The viscous tension along the azimuthal direction $\mathbf{e}_\varphi$ is systematically higher than the viscous tension along the axial direction $\mathbf{t}$: $N_\varphi^v \geq N_t^v$. The cell is subject to a higher tension along its azimuthal direction and elongates therefore along the revolution axis $\mathbf{e}_z$.

- The viscous tensions are equal at the poles: $N_t^v(\theta = 0) = N_\varphi^v(\theta = \pi) \equiv N^v$ making cortical tension locally isotropic. The two poles extrema, that we denote 1 for $\theta = 0$ and 2 for $\theta = \pi$, are therefore the only physical points

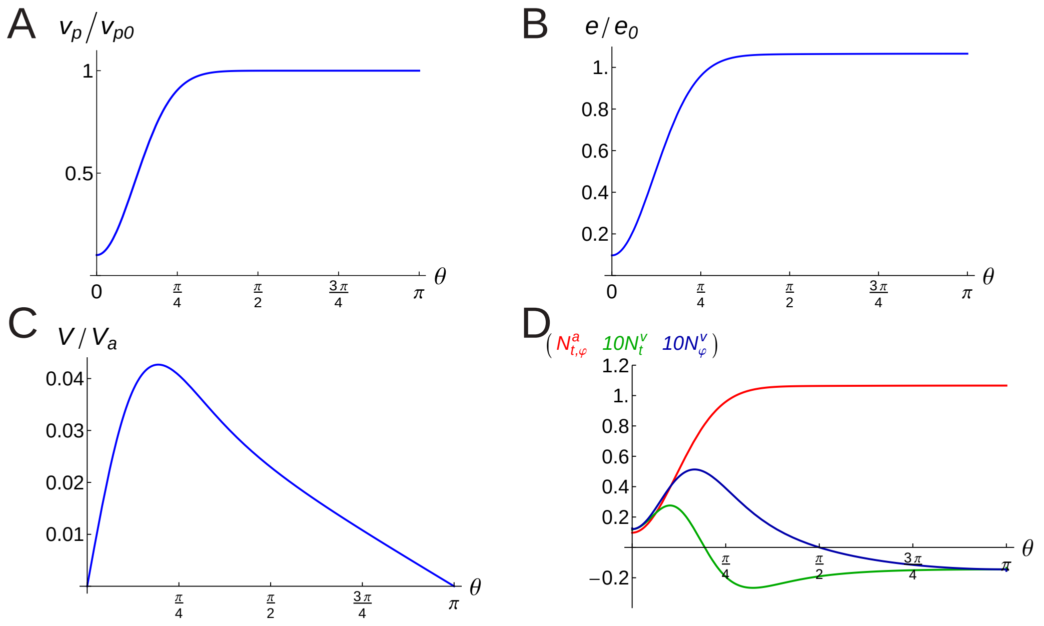

Figure 2.12: Results of the perturbation approach for a local decrease of the polymerization in the region of the bead. *(A)* Form of the polymerization function $v_\mathrm{p}/k_\mathrm{d}e_0$ imposed along the cortex as a function of the polar angle θ. *(B)* Distribution of the cortical thickness $e(\theta)$ along the cortex, normalized by the initial thickness e_0. *(C)* Amplitude of the cortical flow $V(\theta)$ generated by the perturbation, normalized by a typical active velocity $V_a = R_0\frac{\zeta_0\Delta\mu}{2\eta}$, along the cortex as a function of θ. *(D)* Cortical tensions as function of θ: isotropic active tension $N^a_{t,\varphi}(\theta)$ (*red*) and anisotropic viscous tensions $N^v_t(\theta) \neq N^v_\varphi(\theta)$ (*green, blue*), multiplied by a prefactor 10. *(E)* Cell shape, cortical thickness and cortical flow amplitude after perturbation; the arrows indicate the direction of the cortical flow and the color shading its local amplitude.

where the cell is purely spherical and where the original law of Laplace applies: $\Delta P = \frac{2\left(N^a_{1,2}+N^v_{1,2}\right)}{R_{1,2}}$. Since the active contribution dominates largely over the viscous contribution in the cortical tension here $N^a + N^v \approx N^a$ (note the multiplying factor 10 for viscous tensions in the plots), we can make a rough mechanical analysis of the curvature radius difference between these two points in experiments: the actomyosin has been depleted from region 1 (bead $\theta = 0$) and enriched in region 2 (opposite pole $\theta = \pi$), which leads to a stronger active tension, and therefore cortical tension in the region 2. Since the pressure is uniform within the cell at equilibrium, the law of Laplace reads $\frac{R_2}{R_1} \approx \frac{N^a_2}{N^a_1} > 1$. The radius of curvature in the region of the bead is indeed clearly lower than the one at the opposite pole. Because of the adhesion surface of the bead, one can remark nevertheless that the cell can not be perfectly spherical experimentally at this point.

2.1.2.3 Discussion

We propose a physically consistent scenario for the cell shape and cortex polarization by a local biomechanical trigger. The shape deformation and actomyosin redistribu-

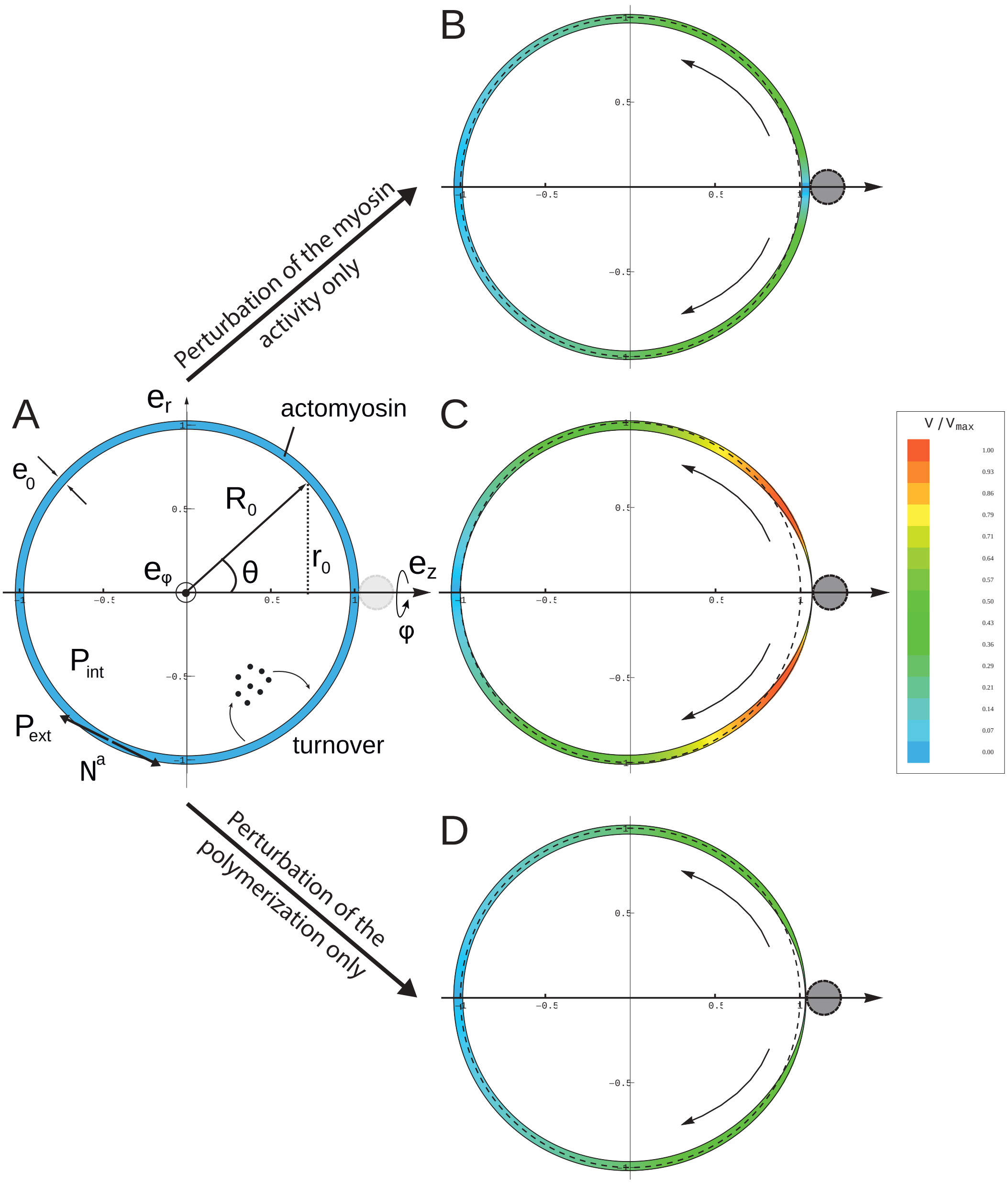

Figure 2.13: Cell shape, cortical thickness and cortical flow amplitude. *(A)* At spherical reference state: the myosin activity ζ generates an active tension N^a within the viscous cortex of initial thickness e_0 and radius R_0 under permanent turnover. The cortical tension balances the pressure difference across the cell according to Laplace's law: $P_{\text{int}} - P_{\text{ext}} = 2N_a/R_0$. *(A,B,C)* After perturbation in the bead region of myosin activity only *(B)*, polymerization only *(D)* and myosin activity and polymerization *(C)*. The arrows indicate the direction of the cortical flow and the color shading its local amplitude.

tion obtained theoretically are in very good qualitative agreement with experimental observations, even though they remain quite weak by their perturbative nature. We will see in the next section how we can go beyond the perturbation approach and solve numerically the non-linear problem. From the shape deformation, we infer the necessary presence of cortical flows along the cell cortex from the bead region to the opposite pole. It would be interesting to try to measure these cortical flows, for example by looking at the movement of very small beads adhering to the membrane surface (non-coated to avoid biochemical specific interaction), as it has been done in the context of cytokinesis [Hiramoto 1958]. The force exerted by the cell — that we neglected here — was furthermore measured as a function of time for varying trap stiffness. His results, shown on fig. 2.14, reveal two very interesting behaviors:

1. **There exists a force threshold, above which the cell sustains its polarization process even if the bead gets untrapped.** If the bead gets untrapped before the cell has reached this force threshold, it relaxes toward non-polarized spherical state. This behavior strongly suggests the existence of a positive feedback mechanism to sustain a gradient of active tension. A possible mechanism would be the advection of positive regulators of the myosin activity and/or actin polymerization by the cortical flow. Such a mechanism has already been proposed to account for the spontaneous polarization and migration of cells in 3D environments [Hawkins 2011] via advection of myosin motors directly, but also to explain the polarization of PAR proteins in *C.Elegans* upon sperm entry [Goehring 2011]. However in these two studies the cell deformation was not taken into account. It would be therefore interesting to add such a feedback mechanism to our cortical membrane framework to study this polarization process in a more general way. Experimentally it would require to measure and better characterize the signal induced by the cue, that we suspect to be a decrease of RhoA-GTP, but also to elucidate the feedback mechanism, that could involve proteins that act on the RhoA-pathway at a more upstream level (PIP_2, Ect2 etc...) (see section 1.1.1.1).

2. **The force exerted by the cell on the bead increases with time, and the loading rate increases with the trap stiffness.** It suggests that the cell response is mechanosensitive and that the biochemical signal transmitted at the cell level by the integrin-fibronectin complex depends on the force in a dose-dependent way. This system may have a self-amplifying feedback [Goehring 2013] that would explain the reinforcement of cell traction over time at fixed trap stiffness. There is a massive literature on the sensitivity of integrin-mediated cell adhesion upon 2-dimensional matrix rigidity, but little is known about the process in 3 dimensions. Notably, no formation of focal adhesion could be detected during the course of actomyosin-dependent cell polarization, in sharp contrast to cell adhesion on 2-dimensional matrices. The capacity of the cell to feel the trap stiffness may be linked of its ability to deform in 3 dimensions in order to exert a force. But the mechanosensitivity of the integrin-fibronectin complex could also be purely local and may not depend on cell deformation. To discriminate between these two scenarios, one could perform experiments involving several Fn-coated beads trapped at different locations on the cortex. To couple theoretically the trap force

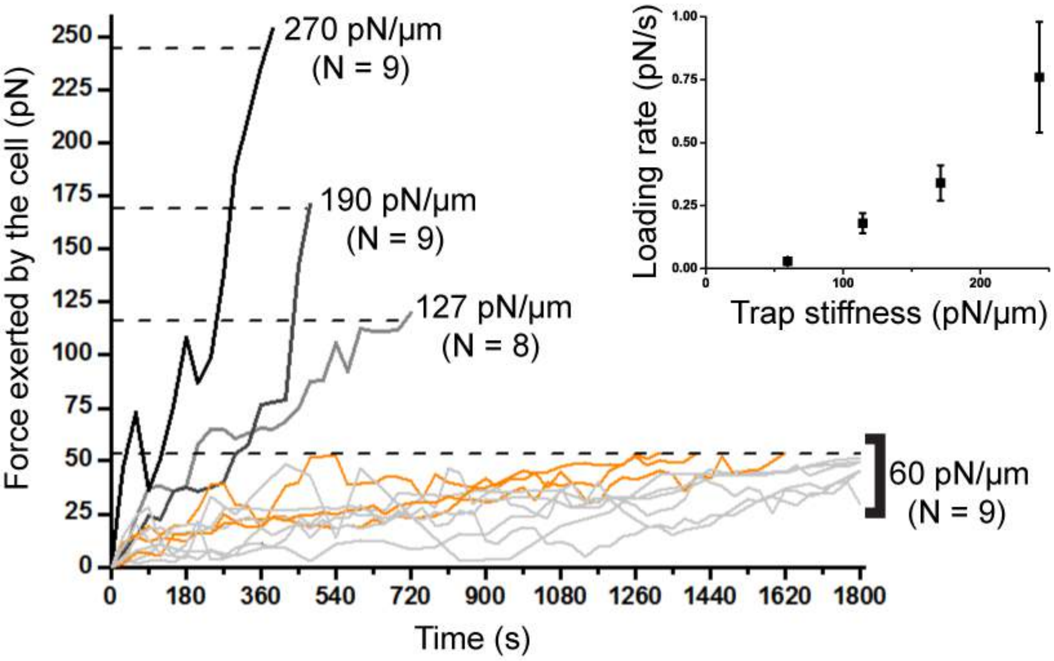

Figure 2.14: **Cellular forces developed by the cell in response to the trap stiffness.** Typical plots represent the time evolution of the force exerted by a polarizing cell to the Fn-coated bead trapped with different stiffness. Dashed lines indicate the maximum trapping force reached before the bead escapes from the trap. (N denotes the number of analyzed cells) *(Inset)* Cell loading rate as a function of the trap stiffness.

with the cell cortex response and test different modeling hypothesis we should add a realistic axial trap force along $\mathbf{e}_\varphi$ in our membrane model. We detail in section 2.E an extension of our membrane model to an unclosed surface subject to an axial force. We show that adding an axial force at one pole requires the exact opposite force on the cell to satisfy global force balance on the cell. In Bun's experiment this opposing force is mediated by a "solid" friction on the Pll-PEG cushion that we can hardly control and model. Our mechanical approach suggests to develop another setup to maintain the cell at a fixed position by a tunable axial opposite force like the suction force of a micropipette.

2.2 Lagrangian continuous and discrete formulations

We have seen that the Eulerian formulation of our visco-active membrane theory can be solved analytically in perturbation. Describing the furrow constriction dynamics during cytokinesis requires however to solve the equations of motion in the fully non-linear regime. We need therefore to use numerical tools, but as we mentioned previously the cytoplasmic pressure appears as a non-local term in the Eulerian partial diffential equations, making the problem difficult to solve by classical finite-difference schemes. We reformulate here the visco-active membrane theory in terms of Lagrangian variables. Although we do not insist on the formal equivalence between the Lagrangian and Eulerian formulations, the reader will easily appreciate their adequation. Hence we won't justify certain formula that result from exactly similar arguments, but we will insist on the geometrical aspects that differ from the Eulerian variables. The Lagrangian formulation provides a natural way to discretize smooth variables in space and the weak formulation of mechanical equilibrium allows to translate the equations of motion into a variational problem that can be solved by classical linear algebra and therefore easily implemented numerically. The Lagrangian approach and the solving method are direct extensions of the work of Basile Audoly and co-workers [Audoly 2013] on the dynamics viscous threads. Finally we adapted successfully to axisymmetric visco-active membranes the numerical code that they developed over the past years for simulating the dynamics viscous threads [Bergou 2010].

2.2.1 Derivation of the Lagrangian visco-active membrane equations

2.2.1.1 Continous formulation

The Lagrangian approach consists in following the movement of individual material points in the membrane. The current membrane configuration is therefore always defined relative to a reference state, that needs to be fully determined. It is chosen here to be spherical, corresponding to the metaphase cell shape, right before cytokinesis onset. We call S the Lagrangian curvilinear coordinate in the reference state of the membrane, to be distinguish from the Eulerian curvilinear or contour length s used in the previous section and redefined.

Spatial and temporal derivatives of any function $f(S,t)$ are defined by

$$f'(S,t) = \frac{\partial f(S,t)}{\partial S}\,, \tag{2.55a}$$

$$\dot{f}(S,t) = \frac{\partial f(S,t)}{\partial t}\,. \tag{2.55b}$$

Since S is a Lagrangian variable, the time derivative is a *material* derivative — often written $\dot{f}(S,t) = \frac{Df(s,t)}{Dt}$ in an Eulerian formulation — and describes the rate of change of f as one follows a given particle.

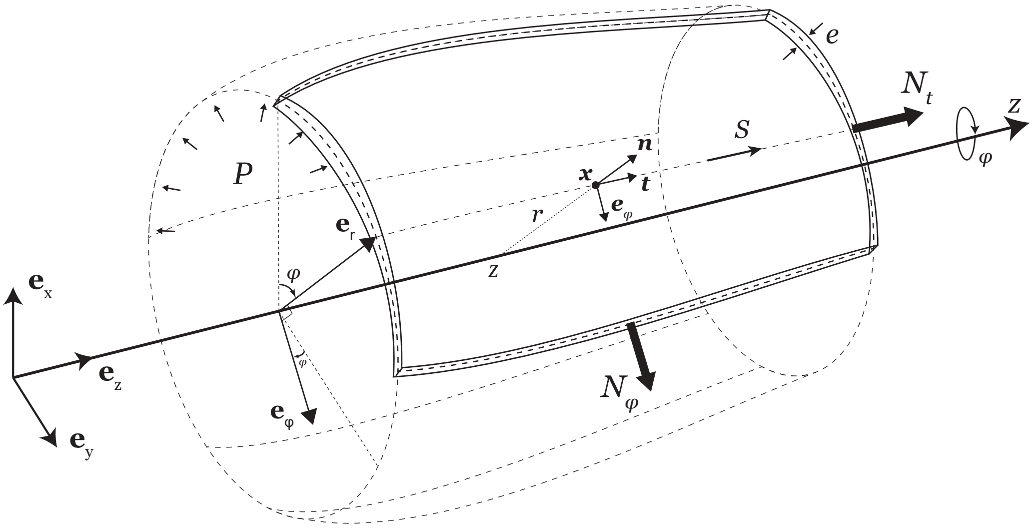

Figure 2.15: **Sketch of the continuous membrane shell:** Piece of the membrane layer of thickness e. The membrane mid-line is parametrized by $(r(S), z(S))$ in the plane $(\mathbf{e}_z, \mathbf{e}_r)$. In the local Frenet frame $\{\mathbf{t}(S), \mathbf{n}(S), \mathbf{e}_\varphi\}$, the membrane is subjected to a tension N_t in its tangential direction $\mathbf{t}$, to a tension N_φ in its azimuthal direction $\mathbf{e}_\varphi$ and to a uniform pressure P in its normal direction $\mathbf{n}$.

Membrane kinematics

In actual configuration at time t, the position of the membrane reads

$$\mathbf{x}(S,t) = z(S,t)\,\mathbf{e}_z + r(S,t)\,\mathbf{e}_r(\varphi)\,. \tag{2.56}$$

Its first and second time derivatives are the *material* velocity and acceleration:

$$\mathbf{u}(S,t) = \dot{\mathbf{x}}(S,t) = \Big(\dot{z}(S,t), \dot{r}(S,t)\Big)\,, \tag{2.57a}$$

$$\ddot{\mathbf{x}}(S,t) = \dot{\mathbf{u}}(S,t) = \Big(\ddot{z}(S,t), \ddot{r}(S,t)\Big)\,. \tag{2.57b}$$

The local Frenet frame $(\mathbf{t}, \mathbf{n}, \mathbf{e}_\varphi)$ is the same as in the Eulerian formulation. $\mathbf{t}$ and $\mathbf{n}$ are the unit vectors tangent and normal to the midline

$$\mathbf{t}(S,t) = \frac{\mathbf{x}'}{|\mathbf{x}'|} = \frac{\mathbf{x}'(S,t)}{\ell(S,t)}\,, \tag{2.58a}$$

$$\mathbf{n}(S,t) = \mathbf{e}_\varphi \times \mathbf{t}(S,t)\,. \tag{2.58b}$$

where $\ell(S,t) = |\mathbf{x}'(S,t)|$ measures the stretch of the mid-line curve, compared to the reference configuration.

The Eulerian curvilinear or contour length s is defined here using the equator as the origin: $s(S,t) = \int_{S_{\rm eq}}^{S} dS'\,\ell(S',t)$, where $S_{\rm eq}$ denotes the Lagrangian coordinate of the equator in the reference configuration.

The area of the membrane per unit dS and $d\varphi$ is given by

$$a = \left|\mathbf{x}' \times \mathbf{x}_{,\varphi}\right| = \left|\ell\,\mathbf{t} \times (-r\,\mathbf{e}_\varphi)\right| = \ell(S,t)\,r(S,t)\,. \tag{2.59}$$

where $f_{,\varphi} \equiv \frac{\partial f}{\partial \varphi}$

The rate of membrane stretching reads therefore

$$\frac{\dot a}{a} = \frac{\dot\ell}{\ell} + \frac{\dot r}{r}\,, \tag{2.60}$$

where $\dot\ell = \left|\frac{\partial^2 \mathbf{x}}{\partial S \partial t}\right| = \left|\frac{\partial \mathbf{u}}{\partial S}\right| = \mathbf{t}\cdot\frac{\partial \mathbf{u}}{\partial S}$.

By identification we deduce the two components $d_s + d_\varphi = \frac{\dot a}{a}$ of the membrane strain rate in the tangential direction $\mathbf{t}$ and in the azimuthal direction $\mathbf{e}_\varphi$

$$d_s(S,t) = \frac{\dot\ell}{\ell} = \mathbf{t}\cdot\left(\frac{1}{\ell}\frac{\partial \mathbf{u}}{\partial S}\right)\,, \tag{2.61a}$$

$$d_\varphi(S,t) = \frac{\dot r}{r} = \mathbf{e}_r \cdot \frac{\mathbf{u}}{r}\,. \tag{2.61b}$$

The membrane's strain rates in the tangential and azimuthal directions can be identified with the strain rates at the mid-surface at dominant order, $d_s = u_{tt}$ and $d_\varphi = u_{\varphi\varphi}$, similarly to the Eulerian formulation (2.33).

Membrane tensions

Exactly like in the Eulerian formulation (eqs. (2.32a) and (2.32b)), the membrane tensions are the sum of an isotropic active term and an anisotropic viscous contribution:

$$N_t = N^a + N^v_t = \frac{e}{2}\zeta\Delta\mu + 2\,\eta\,e\,(2\,d_s + d_\varphi)\,, \tag{2.62a}$$

$$N_\varphi = N^a + N^v_\varphi = \frac{e}{2}\zeta\Delta\mu + 2\,\eta\,e\,(d_s + 2\,d_\varphi)\,. \tag{2.62b}$$

Turnover dynamics

Similarly to the Eulerian formulation (2.36), gel incompressibility with turnover dynamics leads to

$$u_{tt} + u_{nn} + u_{\varphi\varphi} = \frac{v_\mathrm{p}}{e} - k_\mathrm{d}\,. \tag{2.63}$$

We consider an element of membrane of volume $a\,e = \ell(S,t)\,r(S,t)\,e(S,t)$ per unit dS and $d\varphi$, where the element of surface a is defined in eq. (2.59). We identify the rate of surface stretching $d_s + d_\varphi = u_{ss} + u_{\varphi\varphi} = \frac{\dot a}{a}$ and the rate of thickness variation $u_{nn} = \frac{\dot e}{e}$. We deduce the Lagrangian rate of variation of the element of membrane volume ae under both effects of incompressibility and turnover

$$\frac{d\,(a\,e)}{dt} = -k_\mathrm{d}\,ae + v_\mathrm{p}\,a\,. \tag{2.64}$$

Cytoplasm

Viscous dissipation in the cytoplasm Flows of the cytoplasm in cytokinesis are triggered by compression in the furrow region and by advection by cortical flows along the internal surface. Cytoplasmic flows are therefore passively driven by an active cortical flow of typical value v_{a}. The order of magnitude of the strain rate of cytoplasmic flows is therefore $\frac{v_{\mathrm{a}}}{R}$, where R is the mean curvature radius of the polar regions. Note that this scaling law also gives the strain rate of cortical flows from the poles toward the equator. Cytoplasmic flows operate on volumes of the order of cell volume R^3, whereas the typical cortical volume is $R^2 e_0$, where e_0 is the cortical thickness. We evaluate therefore the two sources of dissipation as follows

$$\mathcal{D}_{\text{cytoplasm}} \approx \eta_{\text{cytoplasm}} R^3 \left(\frac{v_{\mathrm{a}}}{R}\right)^2 , \tag{2.65a}$$

$$\mathcal{D}_{\text{cortex}} \approx \eta_{\text{actomyosin}} R^2 e_0 \left(\frac{v_{\mathrm{a}}}{R}\right)^2 . \tag{2.65b}$$

The ratio of the two sources of viscous dissipation, cytoplasmic and actomyosin cortical flows, scales finally as

$$\frac{\mathcal{D}_{\text{cytoplasm}}}{\mathcal{D}_{\text{cortex}}} \approx \frac{\eta_{\text{cytoplasm}}}{\eta_{\text{actomyosin}}} \frac{R}{e_0} . \tag{2.66}$$

which is identical to the formula derived by Yeung and Evans in a more detailed analysis [Yeung 1989]. The viscosity of the cortex is of the order of 10^5-10^6 $Pa.s$ (see table 2.1), whereas the cytoplasmic viscosity is of the order of 10^{-2}-10^1 $Pa.s$ [Daniels 2006, Charras 2009, Kalwarczyk 2011]. In spite of a high volume ratio $R/e_0 \approx 10^2$ (see table 2.1), the viscous dissipation in the cytoplasm remains therefore largely negligible compared to the dissipation in the cortex during cytokinesis: $\mathcal{D}_{\text{cytoplasm}} \ll \mathcal{D}_{\text{cortex}}$. Our model is based on the hypothesis opposite to that of [Zhang 2005], where authors assumed that cytoplasmic flows limit furrow constriction in Dictyostelium cells.

Cytoplasmic volume and pressure Measurements show that the cytoplasmic volume is nearly conserved throughout cytokinesis [Hiramoto 1958, Sedzinski 2011]. The cytoplasm is implemented here as a weakly compressible fluid with negligible viscosity. It applies therefore onto the membrane a uniform hydrostatic pressure P relative to the outer pressure given by

$$P = -K\left(\mathcal{V} - \mathcal{V}_0\right) , \tag{2.67}$$

where $\mathcal{V}_0 \equiv \frac{4}{3}\pi R_0^3$ is the initial cell volume. Using a large value of the bulk modulus K (see section 2.G) the cytoplasm becomes nearly incompressible and the volume $\mathcal{V}$ is nearly conserved (see fig. 2.23 A).

Force balance

Force balance of the 2-dimensional membrane reads in a very formal way

$$\boldsymbol{\nabla}^{2\mathrm{D}} \cdot \underline{\underline{\mathbf{N}}} + P\,\mathbf{n} = \mathbf{0}\,, \tag{2.68}$$

where the 2-dimensional divergence operator $\boldsymbol{\nabla}^{2\mathrm{D}}$ depends non-linearly on the actual configuration of the membrane. Its expression is made explicit further.

Alternatively to force balance we use the principle of virtual work for thin membranes, as it provides a natural way to obtain the equations of motion for discrete membranes. For any virtual motion of the membrane $\hat{\mathbf{u}}(S,t) = \hat{\dot{\mathbf{x}}}$ subject to the constraint of incompressibility, the balance of forces in weak form[2] reads (Einstein notation) [Libai 1998]

$$-\oint dA\, N_{\alpha\beta}\hat{d}_{\alpha\beta} - K\left(\mathcal{V}-\mathcal{V}_0\right)\hat{\dot{\mathcal{V}}} = 0\,. \tag{2.69}$$

where $\hat{d}_{\alpha\beta} = \hat{u}_{\alpha\beta} = \frac{1}{2}\left(\partial_\alpha \hat{u}_\beta + \partial_\beta \hat{u}_\alpha\right)$ is the virtual strain rate, $\hat{\dot{\mathcal{V}}} = \oint dA\, n_\beta \hat{u}_\beta$ is the virtual change of volume, and $\oint$ is the integral on the closed membrane surface.

The weak form allows us to calculate explicitely the divergence operator above. Although we don't use this explicit strong formulation of force balance, we prove the equivalence between the two approaches and illustrate the power of the weak formulation on this example. The divergence operator $\mathbf{div}\left(N_t, N_\varphi\right)$ is defined by the identity

$$\oint dA\, \mathbf{div}\left(N_t, N_\varphi\right)\cdot\hat{\mathbf{u}} = -\oint dA\,\left(N_s\hat{d}_s + N_\varphi\hat{d}_\varphi\right)$$

which must hold for any virtual displacement $\hat{\mathbf{u}}$ associated with the virtual strain rates $\hat{d}_s$ and $\hat{d}_\varphi$. Inserting the explicit expressions of the virtual strain rates, we find

$$\int 2\pi r\ell\, dS\, \mathbf{div}\left(N_t, N_\varphi\right)\cdot\left(\hat{\dot{z}}\mathbf{e}_z + \hat{\dot{r}}\mathbf{e}_r\right) \quad = \quad -\int 2\pi r\ell\, dS\left(N_t\frac{\mathbf{t}}{\ell}\cdot\frac{\partial\hat{\mathbf{u}}}{\partial S} + N_\varphi\frac{\hat{\dot{r}}}{r}\right)$$

$$= \int 2\pi r\ell\, dS\left\{\hat{\dot{z}}\left[-\frac{1}{r\ell}\frac{\partial}{\partial S}\left(r t_z N_t\right)\right] + \hat{\dot{r}}\left[\frac{N_\varphi}{r} - \frac{1}{r\ell}\frac{\partial}{\partial S}\left(r t_r N_t\right)\right]\right\},$$

Identifying both sides, we find an explicit expression of the divergence operator:

$$\mathbf{div}\left(N_t, N_\varphi\right) = -\frac{1}{r\ell}\frac{\partial}{\partial S}\left(r t_z N_t\right)\,\mathbf{e}_z + \left(\frac{N_\varphi}{r} - \frac{1}{r\ell}\frac{\partial}{\partial S}\left(r t_r N_t\right)\right)\cdot\mathbf{e}_r. \tag{2.70}$$

The principle of virtual work (2.69) yields therefore the force balance on a membrane.

---

[2] The weak formulation can be formally obtained by multiplying the force balance (2.68) by the virtual motion $\hat{\mathbf{u}}$ and integrating by parts.

2.2.1.2 Discrete formulation

We extend here the discretization approach proposed for viscous threads [Audoly 2013] to the case of axisymmetric membranes, based on the previous continuous equations.

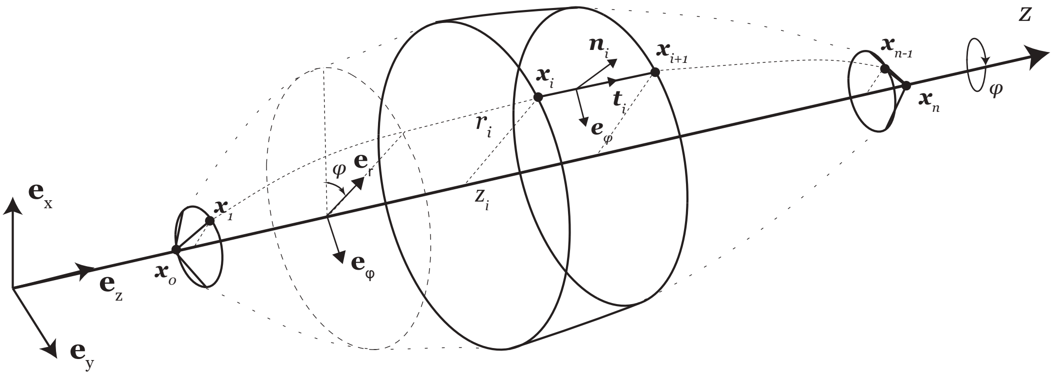

Figure 2.16: **Sketch of the discrete membrane shell:** Discrete axisymmetric membrane mid-surface reconstructed by revolving the discrete mid-line $\{\mathbf{x}_i = (z_i, r_i)\}_{0\leq i\leq n+1}$ defined in the section plane $(\mathbf{e}_r, \mathbf{e}_\varphi)$.

Geometrical relations

The axisymmetric membrane shell is represented by a collection of $n+1$ vertices $\{\mathbf{x}_i(t) = (r_i(t), z_i(t))\}_{0\leq i\leq n}$ living in the half-plane $r \geq 0$ as represented on fig. 2.16. Neighboring vertices are connected by segments enumerated from 1 to n. The vertices at the poles $\mathbf{x}_0$ and $\mathbf{x}_n$ are subjected to the constraint $r_0 = r_n = 0$, closing the membrane surface. The membrane motion is described by the vertex position, whereas the mass, surface, volume, stresses and strains are naturally segment based. Vertex based variables are numbered with a subscript as in v_i, whereas segment based variables are designated by a superscript as in s^i.

The volume enclosed by the membrane reads

$$\mathcal{V} = \sum_{i=1}^{n} V^i = \sum_{i=1}^{n} V(\mathbf{x}_{i-1}, \mathbf{x}_i)\,, \tag{2.71}$$

where the contribution associated with a segment is the volume enclosed by a truncated cone obtained by revolving the segment about the z-axis,

$$V(\mathbf{x}_{i-1}, \mathbf{x}_i) = \frac{\pi}{3}\left({r_{i-1}}^2 + r_{i-1}\, r_i + {r_i}^2\right)(z_i - z_{i-1})\,. \tag{2.72}$$

Let us call $\mathbf{g}_i$ the gradient of the enclosed volume with respect to vertex positions. It will be used to define a discrete pressure force:

$$\mathbf{g}_i = \nabla_{\mathbf{x}_i} \mathcal{V}\,. \tag{2.73}$$

It can be computed by summing contributions of the form

$$\mathbf{V}_{,i}(\mathbf{x}_{i-1}, \mathbf{x}_i) = \frac{\pi}{3}\left[(r_{i-1} + 2\, r_i)(z_i - z_{i-1})\,\mathbf{e}_r + ({r_{i-1}}^2 + r_{i-1}\, r_i + {r_i}^2)\,\mathbf{e}_z\right], \tag{2.74}$$

and the symetric formula for $V_{,i-1}(\mathbf{x}_{i-1},\mathbf{x}_i)$. Here, the comma in index denotes a gradient with respect to a vertex $\mathbf{x}_i$: $\nabla_{\mathbf{x}_i} f = f_{,\mathbf{x}_i}$.

The area of the membrane reads

$$\mathcal{A} = \sum_{i=1}^{n} A^i = \sum_{i=1}^{n} A(\mathbf{x}_{i-1},\mathbf{x}_i)\,, \tag{2.75}$$

where the contribution associated with a segment is the lateral area of a truncated cone,

$$A(\mathbf{x}_{i-1},\mathbf{x}_i) = 2\,\pi\,\frac{r_{i-1}+r_i}{2}\,\ell^i\,, \tag{2.76}$$

with

$$\ell^i = \sqrt{(r_i - r_{i-1})^2 + (z_i - z_{i-1})^2}\,, \tag{2.77}$$

denoting the segment length.

Membrane strain rates

From the continuous formulation (2.61), we deduce the discrete strain rates in the tangential and azimuthal directions

$$d_s^i = \frac{\dot{\ell}^i}{\ell^i} = \frac{\mathbf{t}^i\cdot(\mathbf{u}_i - \mathbf{u}_{i-1})}{\ell^i}\,. \tag{2.78a}$$

$$d_\varphi^i = \frac{\dot{r}_i + \dot{r}_{i-1}}{r_i + r_{i-1}} = \frac{\mathbf{e}_r\cdot(\mathbf{u}_{i-1}+\mathbf{u}_i)}{r_{i-1}+r_i}\,. \tag{2.78b}$$

Membrane tensions

From the continuous formulation in (2.62) the discrete membrane tensions read

$$N_t^{v\,i} = \frac{1}{2}\,e^i\,\zeta^i\Delta\mu + 2\,\eta\,e^i\,(2d_s^i + d_\varphi^i), \qquad N_\varphi^{v\,i} = \frac{1}{2}\,e^i\,\zeta^i\Delta\mu + 2\,\eta\,e^i\,(d_s^i + 2d_\varphi^i)\,. \tag{2.79}$$

Cytoplasmic pressure

From the continuous constitutive relation (2.67), we can express the uniform cytoplasmic pressure by summing discrete enclosed volume contributions in eq. (2.72)

$$P = -K\left(\sum_{i=1}^{n} V(\mathbf{x}_{i-1},\mathbf{x}_i) - \mathcal{V}_0\right)\,. \tag{2.80}$$

Balance of forces

The membrane stress (or tension) is described by a tensor living on segments

$$\mathbf{N}^i = N_t^i\,\mathbf{t}^i\otimes\mathbf{t}^i + N_\varphi^i\,\mathbf{e}_\varphi\otimes\mathbf{e}_\varphi\,, \tag{2.81}$$

where $\mathbf{t}^i$ is the unit tangent vector associated to the segment j.

The principle of virtual work (2.69) provides a natural way for discretizing the equations of motion: for any virtual motion of the vertices $(\hat{\dot{\mathbf{x}}}_i)_{0\leq i\leq n+1}$,

$$\sum_{\text{vert } i} P\,\mathbf{g}_i\cdot\hat{\dot{\mathbf{x}}}_i-\sum_{\text{seg } j}\left(N_t^j\,\hat{d}_s^j+N_\varphi^j\,\hat{d}_\varphi^j\right)A^j=0\,, \tag{2.82}$$

where P is the cytoplasmic pressure relative to the external medium. It is defined in (2.80) and its virtual work is derived from the continuous formulation (2.69): $P\,\hat{\dot{\mathcal{V}}}=P\,\nabla_{\mathbf{x}_i}\mathcal{V}\cdot\hat{\dot{\mathbf{x}}}_i=P\,\mathbf{g}_i\cdot\hat{\dot{\mathbf{x}}}_i$.

The virtual strain rates, in analogy with eq. (2.78), read

$$\hat{d}_s^j=\frac{\mathbf{t}^j\cdot(\hat{\dot{\mathbf{x}}}_j-\hat{\dot{\mathbf{x}}}_{j-1})}{\ell^j} \tag{2.83a}$$

$$\hat{d}_\varphi^j=\frac{\mathbf{e}_r\cdot(\hat{\dot{\mathbf{x}}}_{j-1}+\hat{\dot{\mathbf{x}}}_j)}{r_{j-1}+r_j} \tag{2.83b}$$

When the virtual velocities are eliminated, the discrete principle of virtual work (2.82) yields a set of $2n$ equations for the $2n$ degrees of freedom of the system. These equations depend on the velocities through the viscous constitutive law.

Membrane incompressibility with turnover dynamics

Each segment carries a volume $w^i(t)$, which evolves in analogy with the continuous formulation (2.64):

$$\dot{w}^i=-k_d\,w^i+v_p\,A^i\,, \tag{2.84}$$

where A^i is the lateral areal defined in (2.76).

This volume is used to reconstruct the thickness of a segment, based on the position of its end vertices:

$$e^i=\frac{w^i}{A^i}\,. \tag{2.85}$$

2.2.2 Numerical implementation

This section is a simplified version of the numerical approach developed by Basile Audoly and co-workers in [Audoly 2013] to solve the dynamics of viscous threads. For visco-active membranes, the solving method is identically based on a viscous time-step. We recapitulate its main ingredients to show the benefit of the discrete Lagrangian formulation for numerical implementation. Since our membrane remains axisymmetric, we only need to describe the discrete mid-line in a section plane $(\mathbf{e}_z,\mathbf{e}_r)$. This property allowed us to re-use the C++ code *DVR* (Discrete Viscous Rods) that Basile Audoly and co-workers developed to describe the dynamics of a viscous discrete rod in 3 dimensions [Bergou 2010]. We restricted its movement to a plane, we imposed to its two ends to stay attached to the z-axis $\mathbf{e}_z$ and we modified the geometrical framework to take into account the 2 dimensional axisymmetric surface features of our problem, as detailed above (segment surface, volume and strain rates).

2.2.2.1 Time discretization

Representation of the strain rates

Let us define the generalized position $\mathbf{X}$ and generalized velocity $\mathbf{U}$ of dimensions $2n+2$,

$$\mathbf{X} = \{r_0, z_0, r_1, z_1, \dots, r_n, z_n\}\,, \tag{2.86a}$$

$$\mathbf{U} = \{\dot{r}_0, \dot{z}_0, \dot{r}_1, \dot{z}_1, \dots, \dot{z}_n, \dot{z}_n\}\,. \tag{2.86b}$$

Then, the dependence of the strain rates on the velocities in eq. (2.78) is linear in the generalized velocity $\mathbf{U}$, and can be represented using sparse vectors, $\mathcal{L}_s^i$ and $\mathcal{L}_\varphi^i$:

$$d_s^i \equiv \boldsymbol{\mathcal{L}}_s^i(\mathbf{X}) \cdot \mathbf{U}\,, \qquad d_\varphi^i \equiv \boldsymbol{\mathcal{L}}_\varphi^i(\mathbf{X}) \cdot \mathbf{U}\,. \tag{2.87}$$

Definitions of $\boldsymbol{\mathcal{L}}_s^i$ and $\boldsymbol{\mathcal{L}}_\varphi^i$ are found directly by identification with eq. (2.78):

$$\boldsymbol{\mathcal{L}}_s^i(\mathbf{X}) = \frac{1}{l^i}\{0, \dots, -\underset{i-1}{\mathbf{t}^i}, \underset{i}{\mathbf{t}^i}, \dots, 0\}\,, \qquad \boldsymbol{\mathcal{L}}_\varphi^{\mathrm{i}}(\mathbf{X}) = \frac{1}{\mathrm{r_{i-1}} + \mathrm{r_i}}\{0, \dots, \underset{\mathrm{i-1}}{\mathbf{e}_{\mathrm{r}}}, \underset{\mathrm{i}}{\mathbf{e}_{\mathrm{r}}}, \dots, 0\}\,. \tag{2.88}$$

Note that the generalized velocity can also be virtual $\hat{\mathbf{U}} = \{\hat{\dot{r}}_0, \hat{\dot{z}}_0, \hat{\dot{r}}_1, \hat{\dot{z}}_1, \dots, \hat{\dot{z}}_n, \hat{\dot{z}}_n\}$..

Rayleigh potential

Helmotz in 1868 formulated the minimum dissipation theorem, which states that the unique flow solution of a Stokes problem is the velocity field that minimizes the rate of viscous dissipation, subject to the constraint of incompressibility and boundary conditions. Here we define a dissipation potential, or Rayleigh potential $\mathcal{D}$, function of the strain rate tensor $\underline{\underline{\mathbf{d}}}$[1] only, that we explicited in (2.87) for a given configuration $\big\{\mathbf{X}, \mathbf{U}\big\} = \big\{\{\mathbf{x}_i\}, \{\mathbf{u}_i\}\big\}$. The viscous Rayleigh potential plays a similar role to the potential elastic energy. It allows the equations of motion to be put in a variational form and provides a natural discretization of these equations, as noticed in [Batty 2008].

$$\mathcal{D}(\mathbf{X}, \hat{\mathbf{U}}) = \int_{\mathrm{mbr}} dS\ \underline{\underline{\mathbf{N}}}^v(\mathbf{X}, \hat{\mathbf{U}}) : \underline{\underline{\hat{\mathbf{d}}}}(\mathbf{X}, \hat{\mathbf{U}}) \tag{2.89}$$

The main property of the Rayleigh potential is that it yields the viscous force by simple derivation with respect to the velocity:

$$\mathbf{F}^v = -\left.\frac{\partial \mathcal{D}}{\partial \hat{\mathbf{U}}}\right|_{\hat{\mathbf{U}}=\mathbf{U}} = -\underline{\underline{\boldsymbol{\mathcal{D}}}}(\mathbf{X}) \cdot \mathbf{U}\,, \tag{2.90}$$

---

[1] For the sake of clarity we will add in this section a double underline to tensors, to distinguish them from vectors

where $\mathbf{F}^v$ is the viscous generalized force defined as $\mathbf{F}^v = \big(\mathbf{f}_0^v, \mathbf{f}_1^v, \ldots, \mathbf{f}_i^v, \ldots \mathbf{f}_{n+1}^v\big)$, with $\mathbf{x}_i$ the net viscous force acting on the vertex. It can also be directly calculated as

$$\mathbf{F}_i^v = -\left.\frac{\partial \mathcal{D}}{\partial \hat{\mathbf{u}}_i}\right|_{\hat{\mathbf{U}}=\mathbf{U}} \tag{2.91}$$

Although inertia is negligible in our problem, a small inertia term has been added in the *DVR* code to update easily the velocity. The segment mass m^i is set uniformly at reference state and fixed artificially constant, independently of the membrane volume update. The mass value is chosen arbitrarily small, and we check *a posteriori* the absence of detectable inertial effects in the system.

For the case of a purely viscous membrane, the discrete equations of motion for the vertex $\mathbf{x}_i$ read

$$\tilde{m}_i\, \dot{\mathbf{u}}_i(t) = \mathbf{f}_i^v(\mathbf{X}, \mathbf{U}) + \mathbf{f}_i^{\text{ext}} \tag{2.92}$$

where $\mathbf{F}_i^{\text{ext}}$ is the external loading, and $\tilde{m}_i$ is the vertex-based mass, defined as the sum of the adjacent segments masses $\tilde{m}_i = \sum_{j=i_1,i} \frac{m^j}{2}$ and at boundaries $\tilde{m}_0 = m^0$ and $\tilde{m}_{n+1} = m^n$. We define the mass matrix as $\underline{\underline{\mathbf{M}}} = \mathbf{Diag}\left(\tilde{m}_0 \underline{\underline{\mathbf{1}}}, ..., \tilde{m}_i \underline{\underline{\mathbf{1}}}, ...\right)$ and the generalized external loading $\mathbf{F}^{\text{ext}} = \big(\mathbf{f}_0^{\text{ext}}, \mathbf{f}_1^{\text{ext}}, \ldots, \mathbf{f}_i^{\text{ext}}, \ldots \mathbf{f}_{n+1}^{\text{ext}}\big)$.

The equations of motion can be rewritten in a very compact form using the generalized force

$$\underline{\underline{\mathbf{M}}} \cdot \dot{\mathbf{U}}(t) = \mathbf{F}^v\big(\mathbf{X}(t), \mathbf{U}(t)\big) + \mathbf{F}^{\text{ext}}(t)\,, \tag{2.93a}$$

$$\mathbf{F}^v\big(\mathbf{X}(t), \mathbf{U}(t)\big) = -\left.\frac{\partial \mathcal{D}(\mathbf{X}, \hat{\mathbf{U}})}{\partial \hat{\mathbf{U}}}\right|_{\hat{\mathbf{U}}=\mathbf{U}}\,. \tag{2.93b}$$

Using the discrete definition of the membrane stress (2.79) the dissipation potential can be written as a quadratic form of the generalized velocity

$$\mathcal{D}(\mathbf{X}, \hat{\mathbf{U}}) = \frac{1}{2} \hat{\mathbf{U}} \cdot \underline{\underline{\boldsymbol{\mathcal{D}}}}(\mathbf{X}) \cdot \hat{\mathbf{U}}\,. \tag{2.94}$$

where the dissipation matrix is defined as

$$\underline{\underline{\boldsymbol{\mathcal{D}}}}(\mathbf{X}) = \sum_{\text{seg}i}^{n} 2\,\eta\, e^i\, A^i \left[2\left(\boldsymbol{\mathcal{L}}_s^i \otimes \boldsymbol{\mathcal{L}}_s^i + \boldsymbol{\mathcal{L}}_\varphi^i \otimes \boldsymbol{\mathcal{L}}_\varphi^i\right) + \left(\boldsymbol{\mathcal{L}}_s^i \otimes \boldsymbol{\mathcal{L}}_\varphi^i + \boldsymbol{\mathcal{L}}_\varphi^i \otimes \boldsymbol{\mathcal{L}}_s^i\right)\right] \tag{2.95}$$

according to the definition of sparse operators $\boldsymbol{\mathcal{L}}^i$ (2.87).

We represent schematically below the dissipation matrix to illustrate its sparseness which eases its manipulation (inverse calculation)

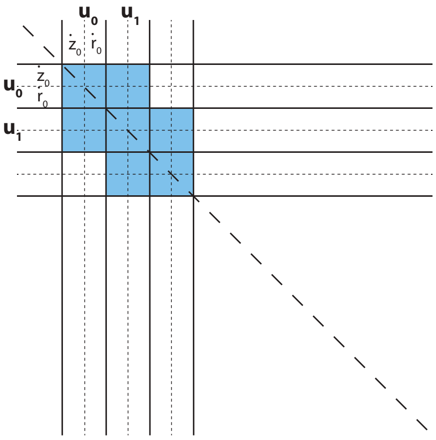

Figure 2.17: **Sparsity pattern for the viscous dissipation matrix $\underline{\underline{\mathbf{D}}}$.**

Viscous time step

The problem can now be expressed as follows: we start from a known membrane configuration $\{\mathbf{X}_t, \mathbf{U}_t\}$ at time t and we want to calculate the next membrane configuration at time $t+\varepsilon$ where ε is the numerical time step. In the discrete case this problem is described by the system

$$\underline{\underline{\mathbf{M}}} \cdot \frac{\mathbf{U}_{t+\varepsilon} - \mathbf{U}_t}{\varepsilon} = \mathbf{F}^v\big(\mathbf{X}_t, \mathbf{U}_{t+\varepsilon}\big) + \mathbf{F}^{\mathrm{ext}}(t)\,, \tag{2.96a}$$

$$\mathbf{F}^v\big(\mathbf{X}_t, \mathbf{U}_{t+\varepsilon}\big) = -\left.\frac{\partial \mathcal{D}(\mathbf{X}_t, \hat{\mathbf{U}})}{\partial \hat{\mathbf{U}}}\right|_{\hat{\mathbf{U}}=\mathbf{U}_{t+\varepsilon}} = -\underline{\underline{\boldsymbol{\mathcal{D}}}}(\mathbf{X}_t) \cdot \mathbf{U}_{t+\varepsilon}\,, \tag{2.96b}$$

$$\mathbf{X}_{t+1} = \mathbf{X}_t + \varepsilon\, \mathbf{U}_t\,, \tag{2.96c}$$

where we added an explicit position update rule (2.96c). The solution $\underline{U}_{t+\varepsilon}$ at step $t+\varepsilon$ is calculated implicitly from previous configuration t by simply inverting the dissipation and mass matrices $\underline{\underline{\boldsymbol{\mathcal{D}}}}$ and $\underline{\underline{\mathbf{M}}}$.

To complete the problem we need to enforce boundary conditions, and specifically here $r_0 = r_n = 0$. We allow therefore for the possibility to constrain generally some degrees of freedom. The generalized velocity $\mathbf{U}_{t+\varepsilon}$ at the end of a time step is determined by

$$\mathbf{U}_{t+\varepsilon} = \underline{\underline{\mathbf{B}}} \cdot \mathbf{W}_{t+\varepsilon}\,, \tag{2.97}$$

where $\mathbf{W}_{t+\varepsilon}$ is the reduced generalized velocity, collecting independent degrees of freedom; it is the principal unknown of the system (2.96). $\underline{\underline{\mathbf{B}}}$ is an orthogonal matrix $\big(\underline{\underline{\mathbf{B}}}^\top = \underline{\underline{\mathbf{B}}}^{-1}\big)$ that projects the equations of motion on "live" degrees of freedom. It is simply the identity matrix in the case of unconstrained membrane.

The equation of motion is therefore restricted to this sub-space of independent degrees of freedom:

$$\underline{\underline{\mathbf{B}}}^\top \cdot \underline{\underline{\mathbf{M}}} \cdot \frac{\mathbf{U}_{t+\varepsilon} - \mathbf{U}_t}{\varepsilon} = \underline{\underline{\mathbf{B}}}^\top \cdot \big(\mathbf{F}_t^{\mathrm{ext}} - \underline{\underline{\boldsymbol{\mathcal{D}}}}(\mathbf{X}_t) \cdot \mathbf{U}_{t+\varepsilon}\big) \tag{2.98}$$

Explicit update of the segment volume

The volume w^i of the segment i evolves according eq. (2.84). We implement the volume update explicitly

$$w^i(t+\varepsilon) = w^i(t) + \varepsilon\big(- k_\mathrm{d} w^i(t) + v_\mathrm{p} A^i(t)\big)\,. \tag{2.99}$$

2.2.2.2 Forces contributions

Generalized implementation of forces in the code *DVR*

We have seen the principle of time-discretization, based on a natural viscous time-step emerging from the Rayleigh potential quadratic structure. We need to add to the equation of motion (2.98) the contribution of active membrane stress and cytoplasmic pressure. Within the previous purely viscous framework we consider the active stress as an external force $\mathbf{F}^\mathrm{ext}$ without loss of generality.

We use the final velocity $\mathbf{U}_{t+\varepsilon} = \{\mathbf{u}_0^{t+\varepsilon}, \cdots, \mathbf{u}_n^{t+\varepsilon}\}$ as the main unknown and rewrite the dynamic update (2.98) as a sum on the forces f on the membrane:

$$\underline{\underline{\mathbf{0}}} = \underline{\underline{\mathbf{B}}}^\top \cdot \left\{ \sum_f \Big[\mathbf{F}_\mathrm{e}^f(\mathbf{X}_t, \mathbf{U}_t, t) + \underline{\underline{\mathbf{G}}}_X^f \cdot (\mathbf{X}_{t+\varepsilon} - \mathbf{X}_t) + \underline{\underline{\mathbf{G}}}_U^f \cdot (\mathbf{U}_{t+\varepsilon} - \mathbf{U}_t) \Big] \right\} \tag{2.100}$$

Combining this equation (2.100) with the position update (2.96c) we get the following very compact formulation as a function of the velocity time difference only

$$\underline{\underline{\mathbf{B}}}^\top \cdot \Big(\mathbf{e} - \underline{\underline{\mathbf{g}}} \cdot (\mathbf{U}_{t+\varepsilon} - \mathbf{U}_t) \Big) = \underline{0}, \tag{2.101}$$

where $\mathbf{e}$ and $\underline{\underline{\mathbf{g}}}$ depend only on actual configuration $\{\mathbf{X}_t, \mathbf{U}_t\}$.

$$\mathbf{e} = \varepsilon \sum_f \Big(\mathbf{F}_\mathrm{e}^f + \varepsilon\, \underline{\underline{\mathbf{G}}}_X^f \cdot \mathbf{U}_t \Big)\,, \tag{2.102a}$$

$$\underline{\underline{\mathbf{g}}} = -\varepsilon \sum_f \underline{\underline{\mathbf{G}}}_U^f\,. \tag{2.102b}$$

Implementation of a force[2] f is therefore done by calculating the corresponding contributions and $\mathbf{F}_\mathrm{e}^f$, $\underline{\underline{\mathbf{G}}}_X^f$ and $\underline{\underline{\mathbf{G}}}_U^f$ to the vector $\mathbf{e}$ and the matrix $\underline{\underline{\mathbf{g}}}$.

Inertia term

The inertial term, associated with the addition of an non-physical small mass, is implemented as

$$\mathbf{F}_\mathrm{e}^\mathrm{i} = 0, \quad \underline{\underline{\mathbf{G}}}_X^\mathrm{i} = \underline{\underline{\mathbf{0}}}, \quad \underline{\underline{\mathbf{G}}}_U^\mathrm{i} = -\frac{1}{\varepsilon}\, \underline{\underline{\mathbf{M}}}. \tag{2.103}$$

---

[2] We do not distinguish here the internal or external character of the force

Viscous stress

Here, we only consider the viscous contributions to the membrane stress, which are the terms proportional to $2\,\eta$ in eq. (2.79).

$$\mathbf{F}_{\mathrm{e}}^{\mathrm{v}} = \underline{\underline{\mathbf{G}}}_U^{\mathrm{v}} \cdot \mathbf{U}_t \tag{2.104a}$$

$$\underline{\underline{\mathbf{G}}}_X^{\mathrm{v}} = \underline{\underline{\mathbf{0}}} \tag{2.104b}$$

$$\underline{\underline{\mathbf{G}}}_U^{\mathrm{v}} = -\sum_{\mathrm{seg}i} 2\,\eta\, e^i\, A^i \left[2\,(\boldsymbol{\mathcal{L}}_s^i \otimes \boldsymbol{\mathcal{L}}_s^i + \boldsymbol{\mathcal{L}}_\varphi^i \otimes \boldsymbol{\mathcal{L}}_\varphi^i) + (\boldsymbol{\mathcal{L}}_s^i \otimes \boldsymbol{\mathcal{L}}_\varphi^i + \boldsymbol{\mathcal{L}}_\varphi^i \otimes \boldsymbol{\mathcal{L}}_s^i)\right] \tag{2.104c}$$

Note that the dissipation matrix $\underline{\underline{\boldsymbol{\mathcal{D}}}}$ defined in eq. (2.95) plays the role of $(-\underline{\underline{\mathbf{G}}}_U^{\mathrm{v}})$.

Pressure term

The compression modulus K being large to conserve cytoplasmic volume, we want to implement the pressure term in a (linear) implicit manner

$$\begin{aligned} p &\approx -K\,(\mathcal{V}_t - V_0) \\ &\approx -K \left(\sum_i \mathbf{g}_i \cdot (\mathbf{x}_i^{t+\varepsilon} - \mathbf{x}_i^t) - V_0 \right) \end{aligned} \tag{2.105}$$

Let us collect the volume gradients $\mathbf{g}_i$ into a generalized vector $\mathbf{G}$, such that

$$\sum_i \mathbf{g}_i \cdot \dot{\mathbf{x}}_i = \mathbf{G} \cdot \mathbf{U}\,. \tag{2.106}$$

Comparison of the discrete principle of virtual work (2.82) and (2.100), shows that the pressure is captured by

$$\mathbf{F}_{\mathrm{e}}^{\mathrm{p}} = -K\,(\mathcal{V}_t - V_0)\,\mathbf{G}, \quad \underline{\underline{\mathbf{G}}}_X^{\mathrm{p}} = -K\,\mathbf{G} \otimes \mathbf{G}, \quad \underline{\underline{\mathbf{G}}}_U^{\mathrm{p}} = \underline{\underline{\mathbf{0}}}\,. \tag{2.107}$$

This formula breaks unfortunately the sparseness of the linear system for a time step. The numerical code has been developed to take advantage of this sparseness feature of the viscous equations to solve the linear system with fast inversion algorithms. To keep the core structure of the code, we finally implemented pressure coarsely as an explicit force:

$$\mathbf{F}_{\mathrm{e}}^{\mathrm{p}} = -K\,(\mathcal{V}_t - V_0)\,\mathbf{G}, \quad \underline{\underline{\mathbf{G}}}_X^{\mathrm{p}} = 0, \quad \underline{\underline{\mathbf{G}}}_U^{\mathrm{p}} = 0\,. \tag{2.108}$$

A better alternative would be to use fast projection methods but it would require a profound revision of the original code.

Active stress

Here $N^{a\,i}$ denotes the active term in the membrane stress in eq. (2.79).

$$\mathbf{F}_{\mathrm{e}}^{\mathrm{a}} = -\sum_{\mathrm{seg}\,i} A^i\,(N^{a\,i}\,\boldsymbol{\mathcal{L}}_s^i + N^{a\,i}\,\boldsymbol{\mathcal{L}}_\varphi^i), \quad \underline{\underline{\mathbf{G}}}_X^{\mathrm{a}} = \underline{\underline{\mathbf{0}}}, \quad \underline{\underline{\mathbf{G}}}_U^{\mathrm{a}} = \underline{\underline{\mathbf{0}}}\,. \tag{2.109}$$

2.2.2.3 Adaptive mesh refinement and coarsening

Gradients of active tension trigger membrane flows and rapid accumulation of Lagrangian points toward the equatorial region (see fig. 2.21), where the contractile activity is maximum, and to the depletion from regions of lowest activity. Refinement is also needed due to the large curvature in the equatorial furrow. We implemented both mesh adaptation and coarsening as follows.

Adaptive mesh refinement
The procedure used for axisymmetric membranes is very similar to the original mesh refinement algorithm implemented in the *DVR* code [Audoly 2013]. Segments that need refinement are first identified at the end of a viscous time-step. The criterion is based on the comparison of the length of the segment to some prescribed maximal length, which has been chosen as $1.5\,\ell_0$ where $\ell_0 = 2\pi R_0/n_0$ is the initial length of segments (n_0 is the initial the number of segments). This refinement criterion has been adjusted manually to offer the best compromise between accuracy and efficiency. A new vertex is inserted in between the two vertices of each segment that have been marked, and two new segments are allocated to replace the former one. The new vertex is inserted, two new segments are allocated and the former segment is removed. The new vertex position and velocity are calculated by an interpolation of order 2 of position and velocity of its neighboring vertices. The stretching forces which depend on the derivatives of the positions and velocities to an order up to two, remain hence smooth upon subdivision. The volume of the two new segments is finally interpolated to globally conserve volume and to result in the same membrane thickness.

Adaptive mesh coarsening
The mesh coarsening procedure has been developed specifically for the present application. It follows the same lines as the previous conventional mesh refinement algorithm. At the end of a viscous time-step, the smallest segment is sought. Coarsening is applied to it when its length is below a prescribed threshold, or when the angle between its neighboring segments exceeds a threshold. This criterion triggers coarsening in the presence of large stretch, or when the curvature is large. Coarsening is applied by removing this segment and its two adjacent vertices, and replacing them by a single vertex. The position and velocity of this new vertex is interpolated again up to order 2, and the volume of the two adjacent segments are updated to conserve volume globally.

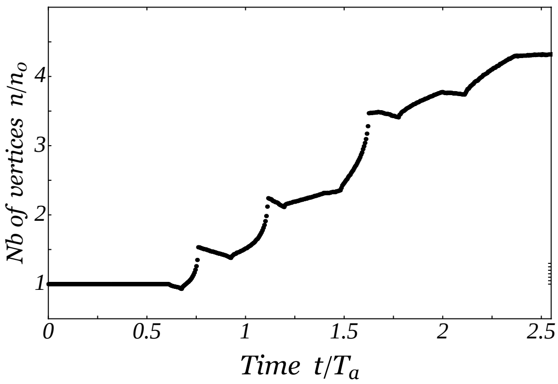

Figure 2.18: **Mesh refinement and coarsening process:** Example of the evolution of the number of vertices under the action of both adaptive mesh refinement and coarsening, corresponding to the simulation of furrow constriction in fig. 2.21

2.2.2.4 Time-stepping: summary

```
Require: $\varepsilon$   (time step)
Require: $\eta$, $K$, $v_\mathrm{p}$, $k_\mathrm{d}$   (Membrane constants)
Require: $\{m^i,\ w^i(t),\ \zeta^i(t)\}$   (current segments configuration)
Require: $\{\mathbf{x}_i(t),\ \mathbf{u}_i(t)\}$   (current vertices configuration)
Require: $\underline{\underline{\mathbf{B}}}$   (kinematical constraints eq. (2.97))
  set $l^i$, $A^i$, $e^i$, $\mathbf{g}_i$, $\tilde{m}_i$   (geometry section 2.2.1.2)
  assemble $\underline{\underline{\mathbf{M}}}$   (mass matrix)
  set $\boldsymbol{\mathcal{L}}^i_s$, $\boldsymbol{\mathcal{L}}^i_\varphi$   (discrete strain rates eq. (2.88))
  set $\underline{\underline{\boldsymbol{\mathcal{D}}}}$   (matrix dissipation eq. (2.95))
  assemble $\mathbf{X}_t$ and $\mathbf{U}_t$   eq. (2.86)
  assemble $\underline{\underline{\mathbf{G}}}^\mathrm{v}_U$, $\underline{\underline{\mathbf{G}}}^\mathrm{v}_X$, $\mathbf{F}^\mathrm{v}_\mathrm{e}$   (viscous stress contributions eq. (2.104))
  assemble $\underline{\underline{\mathbf{G}}}^\mathrm{i}_U$   (inertia term contribution eq. (2.103))
  assemble $\mathbf{F}^\mathrm{a}_\mathrm{e}$   (active stress contribution eq. (2.109))
  assemble $\mathbf{F}^\mathrm{p}_\mathrm{e}$   (pressure term contribution eq. (2.108))
  set $\mathbf{e}$ and $\underline{\underline{\mathbf{g}}}$   (eq. (2.102a))
  solve for $\mathbf{U}_{t+\varepsilon}$   (eq. (2.101))
  update $\mathbf{X}_{t+\varepsilon}$   (eq. (2.96c))
  update $w^i(t+\varepsilon)$   (eq. (2.99))
  refine and coarsen the mesh   (section 2.2.2.3)
```

2.2.2.5 Code validation: spherical contraction under uniform active tension

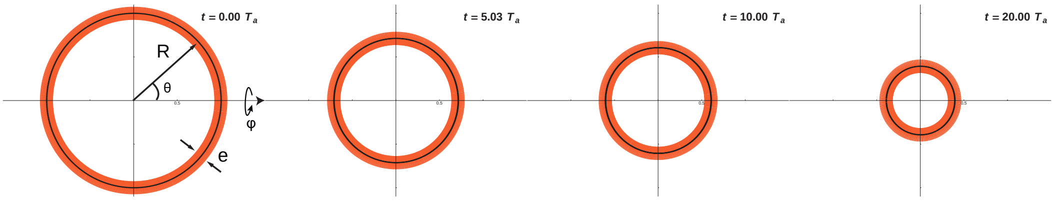

Figure 2.19: **Code validation: spherical contraction under uniform active tension.** The cell constricts under the action of the active stress $\zeta_0 \Delta\mu/2 = 100$, because the cytoplasmic bulk modulus $K = 10$ is low. On the contrary the cortex thickness e remains fairly constant ($e \approx e_0 = v_\mathrm{p}/k_\mathrm{d} = 0.1\, R_0$) because the turnover time-scale it high compared to the contraction time-scale: $k_\mathrm{d} T_a = 10$.

Analytical solution

We consider a spherical isotropic active membrane enclosing a compressible fluid. Its initial radius is R_0 and the membrane shell has an initial thickness e_0 as illustrated on section 2.2.2.5. At time $t = 0$ we apply an isotropic active tension N_0^a, and consider the spherical contraction, prescribed in spherical coordinates as

$$R(\theta_0, \varphi_0, t) = R(t), \qquad \theta(\theta_0, \varphi_0, t) = \theta_0, \qquad \varphi(\theta_0, \varphi_0, t) = \varphi_0.$$

Membrane volume dynamics with turnover (2.64) reads

$$2\frac{\dot{R}}{R} + \frac{\dot{e}}{e} = -k_d + \frac{v_p}{e}.$$

The strain rate tensor is locally isotropic, $\mathbf{d} = \frac{\dot{R}(t)}{R(t)} \left(\mathbf{e}_s \otimes \mathbf{e}_s + \mathbf{e}_\varphi \otimes \mathbf{e}_\varphi\right)$, and so is the membrane tension tensor $\mathbf{N} = (N^v + N^a)\left(\mathbf{e}_s \otimes \mathbf{e}_s + \mathbf{e}_\varphi \otimes \mathbf{e}_\varphi\right)$.

The viscous part is given by the constitutive law in (2.62) as $N^v = 6\,\eta\, e(t)\, \frac{\dot{R}(t)}{R(t)}$ and the active part is prescribed as a function $N^a(t)$.

The constitutive law for the inner compressible fluid reads $P = -K\left(\frac{4\pi}{3} R^3(t) - V_0\right)$. From the weak formulation of equilibrium (2.69), balance of forces reads then simply $P = \frac{2}{R(t)} N_0^a$

Combining the previous equations we get a system of two coupled ordinary differential equations (o.d.e.) governing the time evolution of the radius and the thickness

$$N_v + N_a^0 = 6\,\eta\, e(t)\,\frac{\dot{R}(t)}{R(t)} + N_0^a = -K\frac{R(t)}{2}\left(\frac{4\pi}{3} R^3(t) - V_0\right) \tag{2.110a}$$

$$2\frac{\dot{R}(t)}{R(t)} + \frac{\dot{e}(t)}{e(t)} = -k_\mathrm{d} + \frac{v_\mathrm{p}}{e(t)} \tag{2.110b}$$

Validation procedure

We validate our implementation of the compressible cytoplasm and of turnover by comparing a numerical solution to the ordinary differential equations in (2.110) obtained using Mathematica® 9.0.1., to the results of the simulation. We plot a comparison of numerical and analytical results for various values of K at fixed turnover in section 2.2.2.5 *A* and for various $k_\mathrm{d} > 0$ and $v_\mathrm{p} > 0$ at fixed K in section 2.2.2.5 *B*.

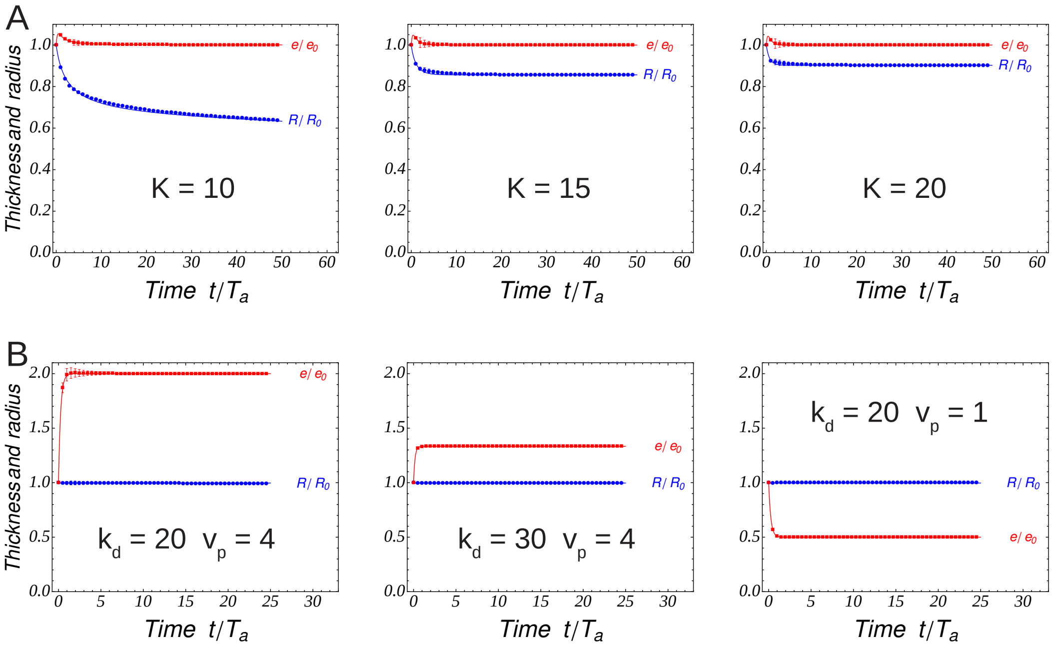

Figure 2.20: **Code validation: validation of cytoplasmic compressibility and cortex turnover.** Lines are solutions of the analytical equations for the cell radius R and membrane thickness e. Markers are solutions of the numerical model and error bars indicate maximum deviations along the membrane from the mean value. *(A)* Validation of the compressible cytoplasm implementation for three low values of the bulk modulus $K = 10$, 15 and 20 ($k_d = 40$ and $v_p = e_0\, k_d = 0.1$). The cell radius contracts correctly under the effect of active tension and shows little longitudinal error. The amplitude of the contraction decreases when K increases as expected. The membrane thickness reaches rapidly its stationary value v_p/k_d. *(B)* Validation of the turnover implementation for three values of the depolymerization rate k_d and polymerization velocity v_p, so that the initial membrane thickness $e_0 = 0.1$ is different from v_p/k_d. A high value of the bulk modulus $K = 250$ maintains the cell radius R at its initial value R_0 to conserve cytoplasmic volume. In each case, the membrane thickness e reaches its stationary value v_p/k_d according to the analytical prediction and shows little error along the membrane.

2.2.2.6 Numerical time-scales

A dimension analysis of the problem leads to three typical time-scales:

- An active time-scale $T_a = \frac{e_0 \eta}{N_0^a} = \frac{2\eta}{\zeta_0 \Delta\mu}$ that characterizes the typical time for viscous deformation of the actomyosin gel submitted to a basal active stress $\zeta_0 \Delta\mu/2$. For any activity ζ, one can define a corresponding active time scale $T_a(\zeta) = \eta/\zeta\Delta\mu$. T_a is therefore the longest active time-scale in our problem, since from Eq. 2 of the main text $\zeta(S,t) \geq \zeta_0$.
- A cytoplasmic compressibility time-scale $T_K = \frac{\eta\, e_0}{R_0 V_0 K}$ that compares the cortex deformation time scale to the cytoplasmic pressure response.
- A turnover time-scale $\frac{1}{k_d}$ that characterizes the typical time for the layer thickness relaxation.

Active layer intrinsic instability

We first compare the turnover and active time-scales. An active viscous layer with variable thickness is intrinsically unstable without turnover: any spatial difference in thickness creates a tension gradient that triggers an active flow toward the regions of higher thickness. The thickness increase enhances the gradient of tension and therefore amplifies itself via the cortical flow. Turnover stabilizes this effect if thicker regions depolymerize rapidly enough and thinner regions regrow rapidly enough. The active layer remains therefore stable if $T_a\, k_d \gg 1$.

Compressibility time-scale

We compare the compressibility time-scale T_K to the active time-scale T_a. The ratio $\frac{T_K}{T_a} = \frac{e_0}{R_0} \frac{\zeta_0 \Delta\mu}{V_0 K}$ compares active tension of the layer and cytoplasmic pressure. To avoid collapse of the membrane it has therefore to be lower than one.

Code general stability

The time-step has to be smaller than all other time-scales in the problem. Taking into account the previous stability requirements we end up with the following global requirement for code stability

$$dt \ll T_K < \frac{1}{k_d} \ll T_a \,. \tag{2.111}$$

2.3 Furrow constriction in animal cells cytokinesis

2.3.1 Numerical results

In the initial state of the simulation, the membrane is a sphere with radius R_0 and uniform stationary thickness $e_0 = v_\mathrm{p}/k_\mathrm{d}$. It is subject to a uniform contractile activity ζ_0. We note that the initial contractile stress ($\zeta_0\,\Delta\mu/2$) defines an active time-scale when balanced with the viscosity,

$$T_a \equiv \frac{2\eta}{\zeta_0 \Delta\mu}. \tag{2.112}$$

At cytokinesis onset, an Gaussian band of over-activity forms at the cell equator and causes cortical actin redistribution and furrowing [Bement 2005]. We therefore impose along the membrane a Gaussian distribution of contractility

$$\zeta(s,t) = \zeta_0 + \delta\zeta^\infty\, I(t)\, \exp\left(-\frac{1}{2}\left[\frac{s}{w}\right]^2\right), \tag{2.113}$$

where s is the curvilinear length defined from the equator, w is the band width, $\delta\zeta^\infty$ the amplitude of the over-activity. $I(t)$ is a sigmoidal function of time varying from 0 to 1, and plotted as inset of fig. 2.21, that reproduces the temporal increase of active RhoA at the cell equator [Bement 2005].

Typical numerical values for these parameters are picked from experimental references and summarized in the following table 2.1.

Notation	Quantity	Expmts	Simu	References
R_0	*Cell radius*	$10 - 100\ \mu m$	1	[Bement 2005, von Dassow 2009a]
e_0	*Cortical thickness*	$0.2 - 2\ \mu m$	0.02	[Salbreux 2012, Clark 2013]
w	*Ring width*	$1 - 10\ \mu m$	0.1	[Bement 2005, von Dassow 2009a]
$\frac{1}{2}\,\zeta_0\Delta\mu$	*Basal cortical active stress*	$10^3\ Pa$	1	[Tinevez 2009]
T_a	*Typical active time-scale*	$10^3\ s$	10	[Bement 2005, von Dassow 2009a]
$\eta = \frac{1}{2}\,\zeta_0\Delta\mu\, T_a$	*Actomyosin viscosity*	$10^6\ Pa\, s$	10	/
$k_\mathrm{d} = \frac{\log 2}{\tau_\mathrm{FRAP}}$	*Depolym. rate*	$0.04\ s^{-1}$	4	[Guha 2005, Murthy 2005, Fritzsche 2013]
$v_\mathrm{p} = e_0\, k_\mathrm{d}$	*Polym. velocity*	$8 - 80\ nm\, s^{-1}$	0.08	/

Table 2.1: Notations and typical experimental and numerical value(s) with reference(s). Numerical values have been chosen so that $R_0 = 1$ and $T_a = 10$ are the length and time-scales of reference.

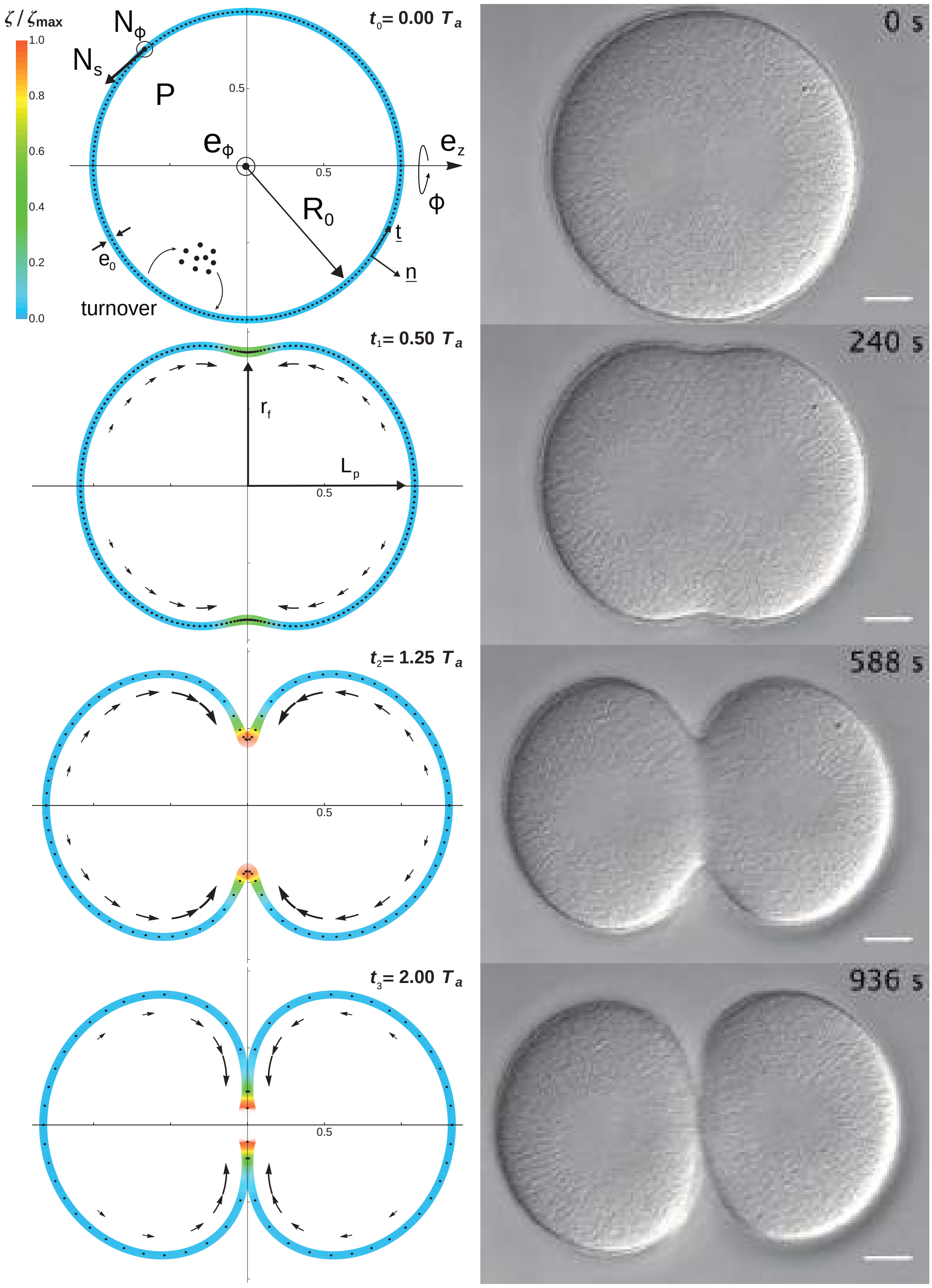

Figure 2.21: *(Left)* Numerical cell shape and cortex thickness evolution: (t_0) Initial spherical cortex of radius R_0 and main ingredients of the model. The membrane is axisymmetric around the axis $\mathbf{e}_z$ and is subjected to internal tensions N_s and N_φ in its axial $\mathbf{t}$ and azimuthal $\mathbf{e}_\varphi$ principal directions, and to the cytoplasmic pressure P along its normal $\mathbf{n}$. The actomyosin layer of initial thickness e_0 undergoes permanent turnover. About hundred Lagrangian nodes are represented to follow the tangential membrane deformation over time (not all simulations nodes are shown). (t_1, t_2 and t_3) Cell cortex snapshots at successive times of constriction, in response to the rescaled myosin activity signal $\zeta/\zeta_{\max}$ illustrated by the color shading. r_f is the furrow radius and L_p is the half pole-to-pole distance. Cortical flows along the membrane are represented by arrows of size proportional to the local tangent velocity. *(Right)* DIC microscopy images of a sand-dollar zygote (dendraster) deprived of its hyaline layer and jelly coat at four equivalent times of furrow constriction. The cell is not flattened and scale bar is $20\mu m$. (Credits: G. Von Dassow)

2.3.1.1 Four phases of furrow constriction

An equatorial gaussian band of overactivity $\delta\zeta^{\infty} = 75$ is progressively established according to the time profile $I(t)$ plotted in fig. 2.22 *(Inset)*. The evolution of the shape and thickness of the cell cortex is shown in fig. 2.21 *(left)*: the four snapshots illustrate four distinct phases of constriction.

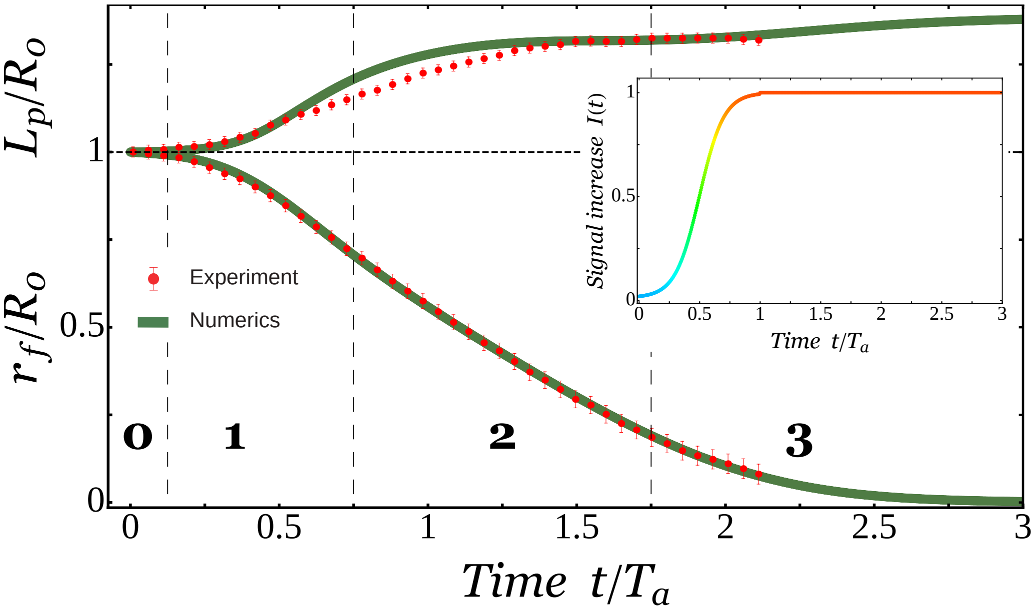

Figure 2.22: Furrow constriction dynamics: Time evolution of the furrow radius (r_f/R_0), and pole-to-pole half distance (L_p/R_0). Numerical results (line) are compared to experimental measurements of a sand dollar zygote (points, data from the same DIC microscopy images of fig. 2.21). Vertical dashed lines delimit the four phases of constriction described in the text and numbered from 0 to 3. *(Inset)* Equatorial signal $I(t)$ applied as a function of time.

The time evolution of the furrow radius r_f/R_0 and pole-to-pole distance L_p/R_0 (see definition in fig. 2.21) are qualitatively different during each of the four phases, as shown in fig. 2.22 Numerical results are compared in fig. 2.21 to DIC microscopy images of a sand-dollar zygote under cytokinesis and show very good agreement. The experimental time is rescaled by an active time-scale T_a of value $468s \approx 8min$, to match successfully experimental furrow radius and pole-to-pole distance evolutions with numerical results in fig. 2.22. This time-scale is perfectly consistent with the model, approximations, notably $k_{\mathrm{d}}T_a \gg 1$.

Phase 0: No overactivity The initial spherical cell, shown at time $t_0 = 0$ in fig. 2.21, is a stable equilibrium and verifies Laplace's law $P = e_0\zeta_0\Delta\mu/R_0$.

Phase 1: Activity increase at the equator Following the increase of myosin activity (*Inset* in fig. 2.22 and color shading in fig. 2.21), the equatorial region becomes more contractile. It triggers a cortical flow toward the equator, as shown by the arrows at time $t_1 = 0.50\,T_a$ in fig. 2.21. This actin accumulation forms an annular bundle, thereby reproducing the observed formation of the contractile ring [Cao 1990c]. This increase in thickness (see fig. 2.24 B) results from the competition between cortical flow and actin turnover. The contractile ring starts to pinch the cell, increasing the cytoplasmic pressure (fig. 2.23 *B*) to conserve its volume (fig. 2.23 *A*). The pole-to-pole distance increases rapidly (fig. 2.21 *up*) and the cell adopts a prolate like shape (fig. 2.21 at time $t_1 = 0.50\,T_a$), consistent with the so-called anaphase cell elongation [Hickson 2006].

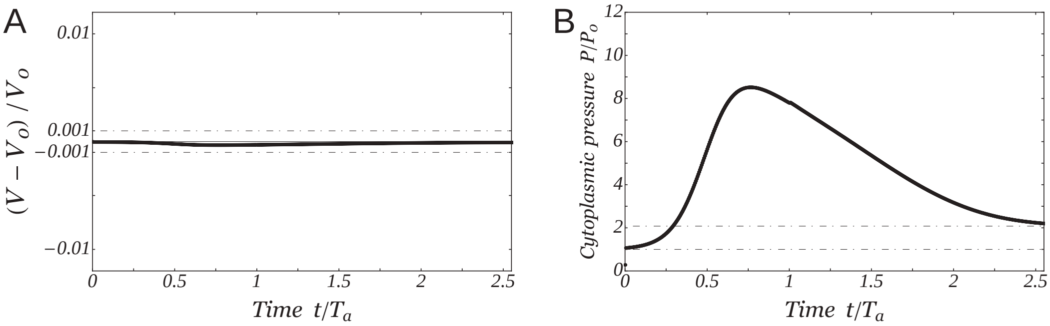

Figure 2.23: **Cytoplasmic volume conservation and pressure evolution corresponding to fig. 2.21**: *(A)* Plot of the cytoplasmic volume variation $(V - V_0)/V_0$ over time. We added two horizontal lines to show that the error is below 0.1%. *(B)* Cytoplasmic pressure P rescaled by the initial Laplace pressure $P_0 = 2N_0^a/R_0$. The cytoplasmic pressure increases rapidly during the transient phase and then decreases slowly toward a value roughly two times greater than the initial pressure.

Phase 2: Plateau of activity at the equator The amplitude of overactivity starts to saturate after a time interval of about $0.75\,T_a$ (fig. 2.22 *Inset*). The furrow adopts a constriction regime that is almost linear in time (fig. 2.22 *bottom*). The poles's stretch is revealed by the increase in the gaps between the simulation nodes on snapshot $t_2 = 1.25\,T_a$ in fig. 2.21. The two future daughter cells become increasingly non-spherical, especially in the furrow region. There, both the deformation and the tension are strongly anistropic (see fig. 2.25*C* and *D*), leading to widely different radii of curvature in the axial and azimuthal directions.

Phase 3: Constriction slowing-down When the furrow radius approaches zero, the pole-to-pole distance reaches a relative plateau (fig. 2.22 *up*). The constriction starts slowing down exponentially (fig. 2.22 *bottom*), because viscous dissipation due to the constriction of the furrow increases as its radius decreases (see fig. 2.35 *D* and fig. 2.F.1 B in section 2.F). A significant cortical flow persists from the poles toward the equator as long as the equatorial signal is maintained (time $t_3 = 2.00\,T_a$ in fig. 2.21). As this flow is balanced by turnover, the shape and surface of the polar regions no longer evolve significantly with time.

We represent in fig. 2.24 for the two representative times $t_1 = 0.5\,T_a$ and $t_2 = 1.25\,T_a$ the cortical flow V/V_a along the cortex, that is triggered by the gradient of activity signal ζ/ζ_0, and that results in a thickness increase e/e_0 at the equator. In fig. 2.25 we compare, for the two times $t_1 = 0.5\,T_a$ and $t_2 = 1.25\,T_a$, the active, viscous and total membrane tensions in the tangential and azimuthal directions.

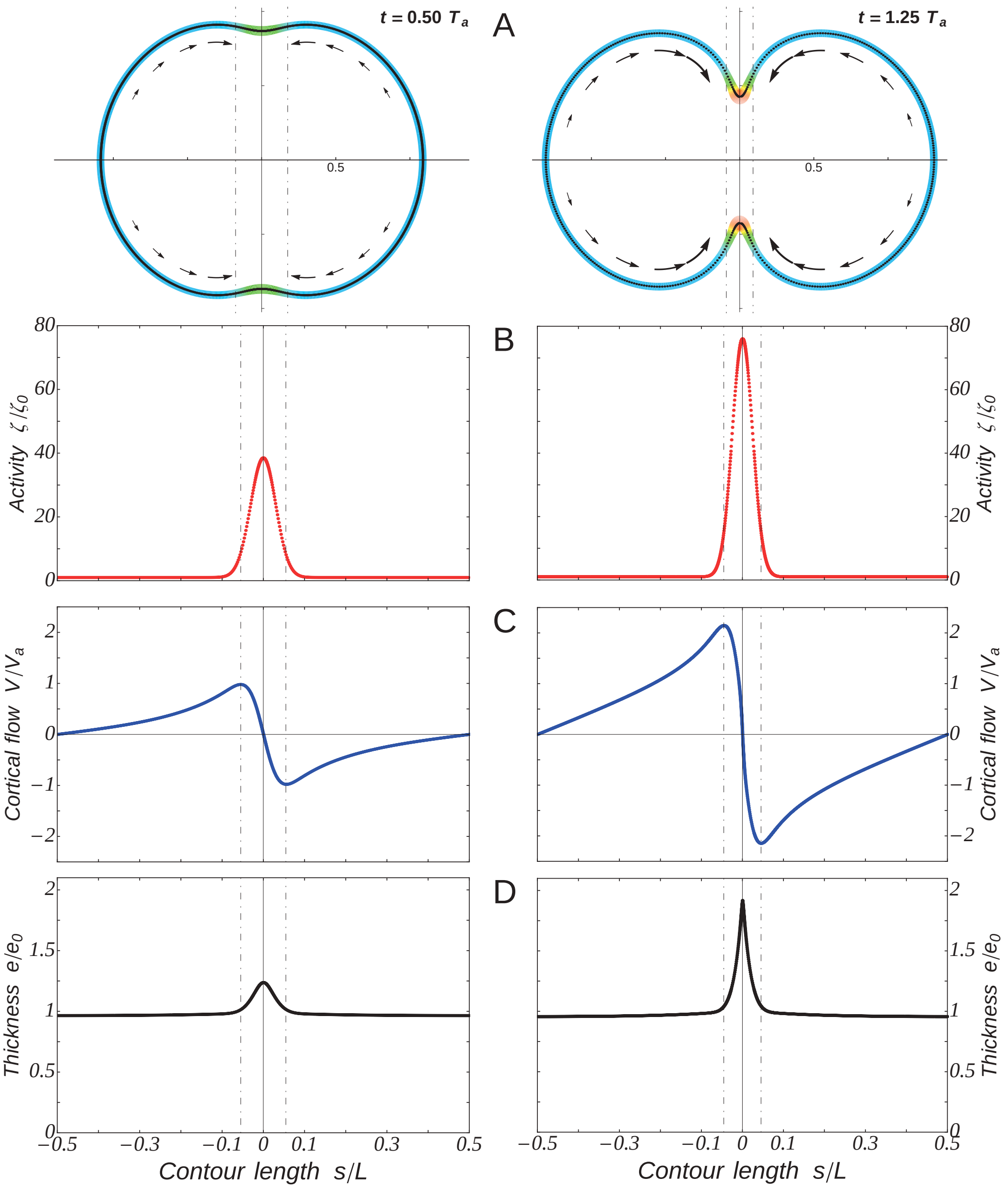

Figure 2.24: **Cortical flow, furrow region and thickness:** *(A)* Cell cortex shape and thickness at times $t = 0.5\,T_a$ (left) and $t = 1.25\,T_a$ (right). *(B, C and D)* Corresponding plots of, respectively, activity signal ζ/ζ_0, cortical flow velocity V/V_a ($V_a = R_0/T_a$) and thickness e/e_0 along the midline contour length s/L. The cortical flow is oriented toward the furrow region and its amplitude increases with the equatorial signal between $t = 0.5\,T_a$ *(left)* and $t = 1.25\,T_a$ *(right)*. Its extrema delimit the furrow region, demarcated by the two dot-dashed vertical lines in each figure. The increase of the cortical flow triggers a greater accumulation of actomyosin in the furrow region, leading to an expansion of its thickness.

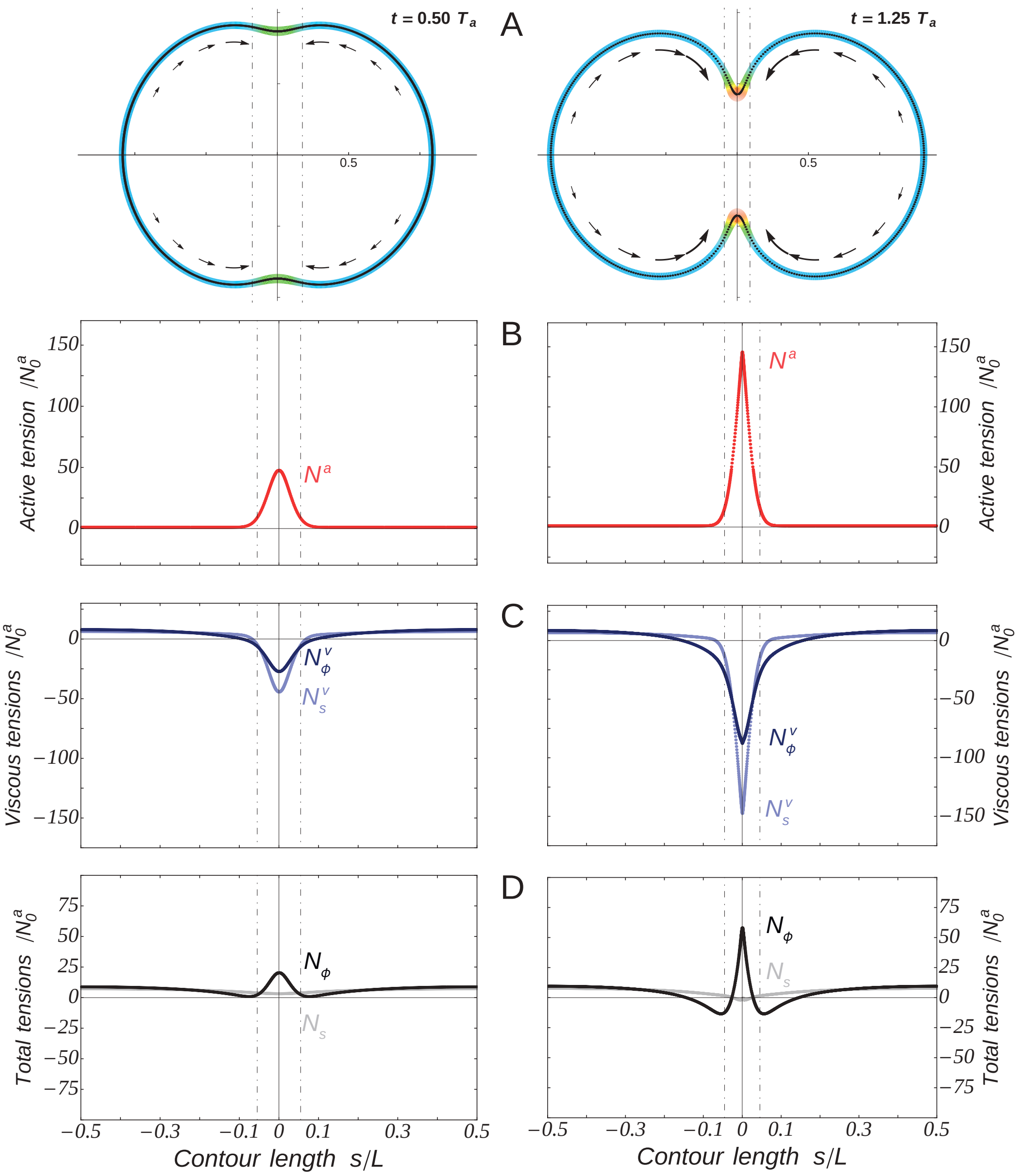

Figure 2.25: **Cortical tensions:** *(A)* Cell cortex shape and thickness at times $t = 0.5\,T_a$ *(left)* and $t = 1.25\,T_a$ *(right)*. *(B, C and D)* Corresponding plots of, respectively, the active tension N^a, the viscous tensions N_s^v, N_φ^v and the total tensions N_s, N_φ in the membrane, rescaled by the basal active tension N_0^a. The active tension is isotropic in the axial and azimuthal directions whereas the viscous tensions are appreciably anisotropic near the furrow region, delimited by dot-dashed vertical lines. It leads to total membrane tensions that are globally anisotropic: the azimuthal tension is markedly greater than the axial tension in the furrow region leading to a furrow line tension that constricts the cell, whereas the regions bordering the furrow are more stretched in their axial direction leading to non-sperical shapes.

2.3.1.2 A threshold for complete furrow constriction

We plot in fig. 2.26 *B* the furrow ingression as a function of time for six values of the equatorial overactivity $\delta\zeta^\infty/\zeta_0$ between 10 and 100.

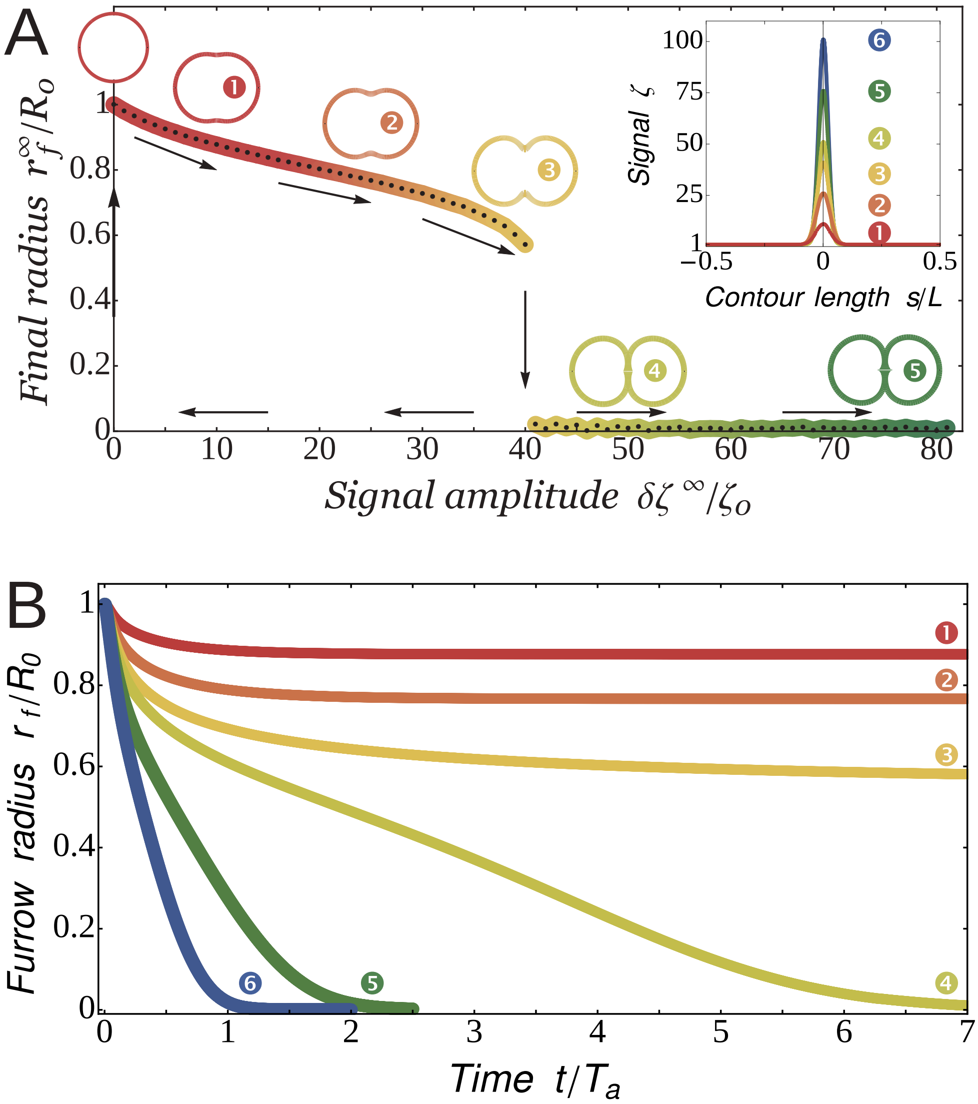

Figure 2.26: Constriction completion and failure: *(A)* Bifurcation diagram representing the final furrow radius r_f^∞/R_0 as a function of the amplitude of equatorial over-activity $\delta\zeta^\infty/\zeta_0$. The diagram displays a jump from constriction failure to completion for a critical amplitude $\delta\zeta^\infty/\zeta_0 \approx 40$. Final cell shape are plotted for the six activity signals ζ, of amplitudes $\delta\zeta^\infty/\zeta_0 = 10$ (❶), 25 (❷), 40 (❸), 50 (❹), 75 (❺) and 100 (❻) as represented in *(Inset)* as function of the contour length from equator s/L along the membrane (of length L). Arrows illustrate an hysteresis loop: starting from a divided state above the threshold (❹ for example), we decrease the equatorial signal: the cell remains divided, unless the signal is dropped down to zero, point where it goes back to the spherical state. *(B)* Furrow radius evolution r_f/R_0 as a function of time t/T_a for the six signals ζ represented in *(Inset)* of *(A)*.

For $\delta\zeta^\infty/\zeta_0 > 40$ the furrow fully constricts (❹, ❺, ❻), but slows down when the equatorial signal is decreased. For $\delta\zeta^\infty/\zeta_0 \leq 40$ the furrow radius reaches a plateau (❶, ❷, ❸). Full constriction therefore requires that the over-activity at the equator exceeds a threshold, and the rate of constriction is dose-dependent, consistently with observations reported in [Loria 2012]. The final stationary furrow radius r_f^∞ is plotted as a function of the overactivity amplitude $\delta\zeta^\infty/\zeta_0$ in fig. 2.26 *A*. The diagram displays a saddle-node bifurcation near $\delta\zeta^\infty \approx 40$. The longer delay required to complete ingression around threshold (fig. 2.26 *B* ❹) is therefore interpreted as a critical slowing down. Shape evolutions leading to constriction failure and completion are compared in fig. 2.27.

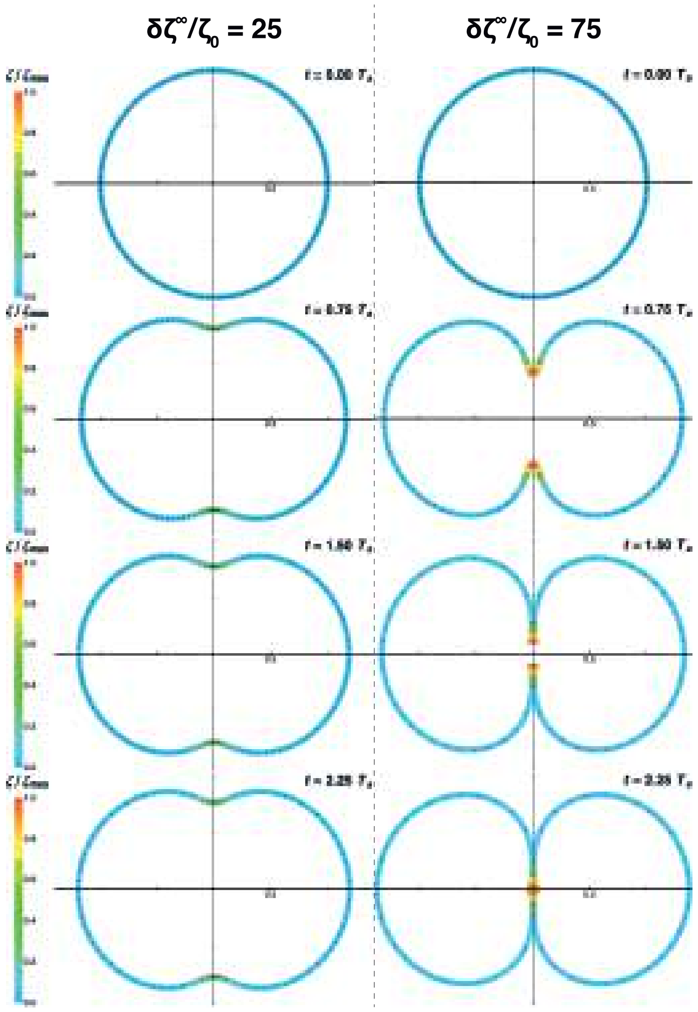

Figure 2.27: Comparison of the cell shape and cortex thickness dynamics in a section plane $(\mathbf{e}_z, \mathbf{e}_r)$ for the two equatorial signal amplitude $\delta\zeta^\infty/\zeta_0 = 25$ and $\delta\zeta^\infty/\zeta_0 = 75$, corresponding respectively to the furrow radius evolution ❷ and ❺ in fig. 2.26.

2.3.1.3 Constriction success also depends on the signal timing

The bifurcation diagram in fig. 2.26 *A* reveals a noticeable hysteretic behavior, represented by the arrows. If one reaches a fully constricted state at the end of cytokinesis ($r_f \approx 0$ and $\delta\zeta^\infty/\zeta_0 > 40$) and decreases the equatorial over-activity back under the threshold $\delta\zeta^\infty/\zeta_0 < 40$, the cell stays divided (unless the signal is decreased down to zero). This behavior is illustrated on fig. 2.29 *A*.

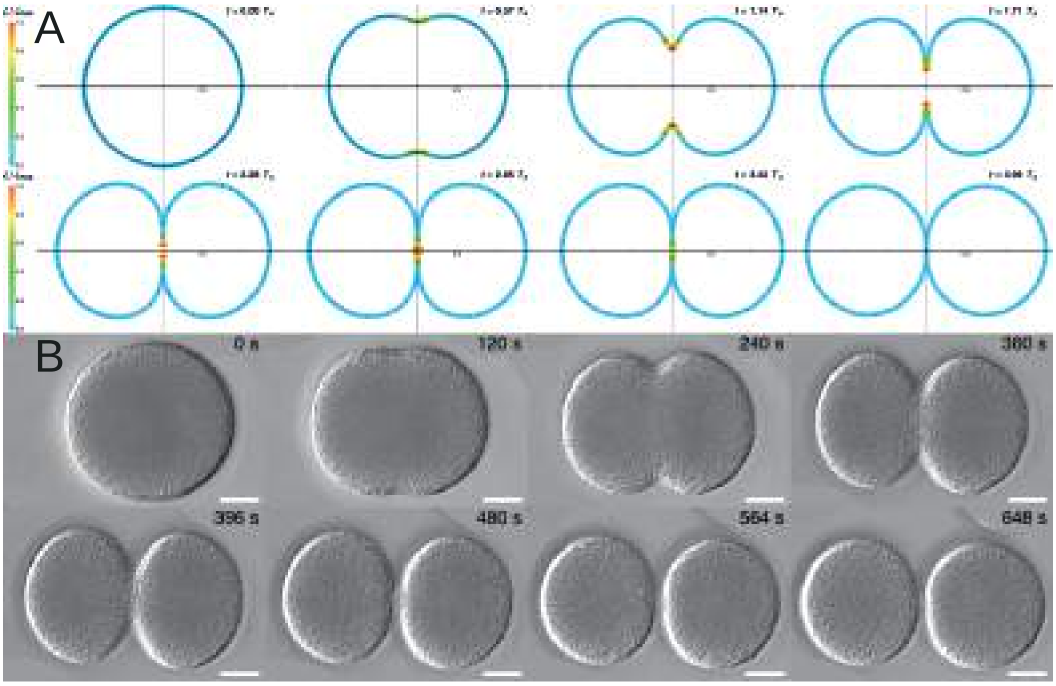

Figure 2.28: Hysteresis behavior: *(A)* Dynamics of the cell shape and cortex in a section plane $(\mathbf{e}_z, \mathbf{e}_r)$ during constriction and when the equatorial signal is decreased down to the value at poles after constriction completion. The cell stays divided and daughter cells adopt a spherical shape. *(B)* DIC microscopy images of Non-compressed S. purpuratus egg deprived of its hyaline layer and cultured in calcium-free artificial sea-water to prevent cell-cell adhesion. The rounding up of the daughter cells at the end of furrow constriction may be attributed to a decrease of the equatorial signal according to the numerical results above. (Scale bar is $20\mu m$, credits: G. Von Dassow)

We observe furthermore that the daughter cells adopt a spherical shape when the equatorial signal is significantly decreased after cytokinesis completion, consistent with a drop of the cortical tension anisotropy because of vanishing cortical flows toward equator. This rounding up of daughter cells is classically observed experimentally at the end of sea-urching eggs cytokinesis when cell-cell adhesion is artificially lowered (fig. 2.29 *B*) and may be therefore attributed to a decrease of the equatorial signal according to the numerical results. As long as some slight equatorial tension is maintained, the divided state is therefore mechanically stable, which may prevent the furrow to regress erroneously during the midbody formation [Lekomtsev 2012]. On the contrary if the signal is decreased prematurely in the course of ingression (for $r_f/R_0 > 0.6$), the furrow regresses and cytokinesis fails, as illustrated numerically on fig. 2.29 and presumably happens experimentally in [Argiros 2012]. A tight synchronization between the signaling machinery and the furrow constriction is therefore essential.

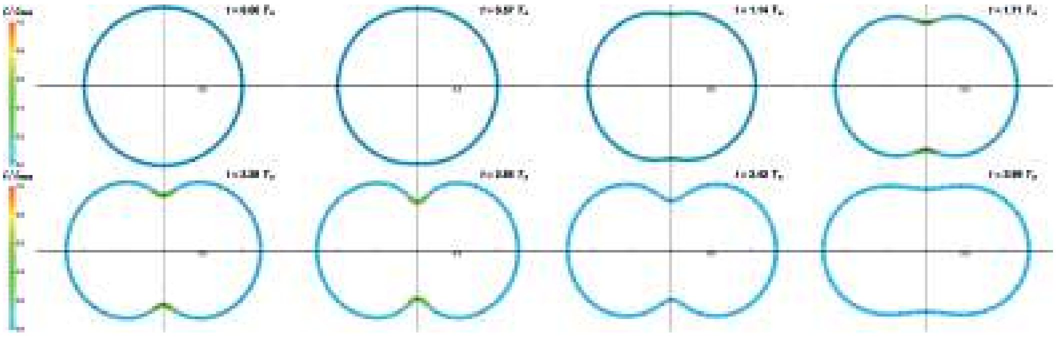

Figure 2.29: Hysteresis behavior: Dynamics of the cell shape and cortex in a section plane $(\mathbf{e}_z, \mathbf{e}_r)$ during constriction and when the equatorial signal is prematurely decreased down to the value at poles in the course of furrow constriction. The furrow, which has not reached the critical radius $r_f \approx 0.6$ regresses, and cytokinesis fails.

2.3.1.4 Constriction dynamics depends on turnover

In fig. 2.30 and fig. 2.31 we compare the constriction dynamics for three different turnover rates $k_\mathrm{d} T_a = 30$ (①), $k_\mathrm{d} T_a = 40$ (②) and $k_\mathrm{d} T_a = 80$ (③) while keeping $e_0 = v_\mathrm{p}/k_\mathrm{d}$ and $\delta\zeta^\infty/\zeta_0 = 75$ constant.

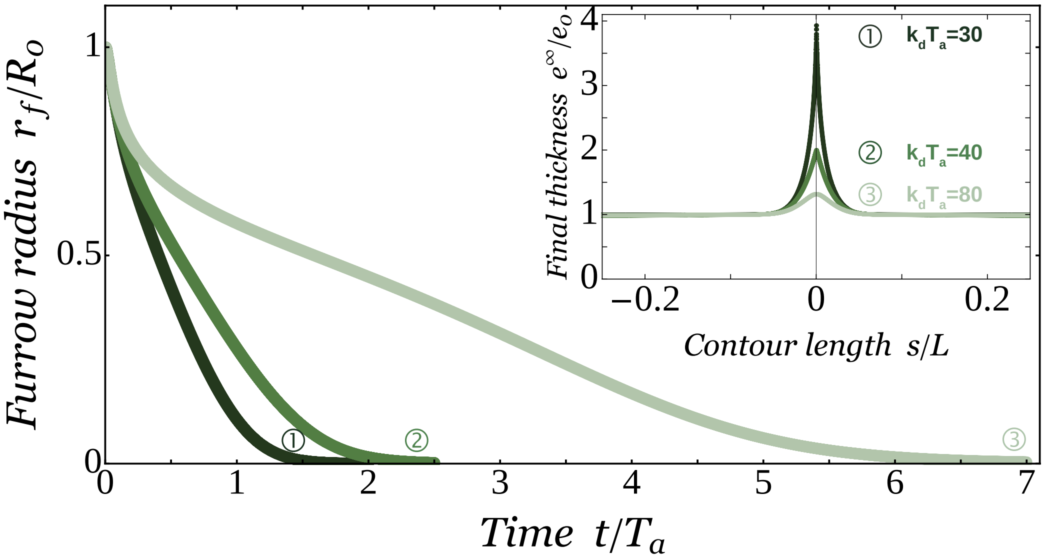

Figure 2.30: Influence of turnover on constriction: Furrow radius r_f/R_0 as a function of normalized time t/T_a for three turnover rates: $k_\mathrm{d}T_a = 30$ (①), $k_\mathrm{d}T_a = 40$ (②) and $k_\mathrm{d}T_a = 80$ (③). *(Inset)* Corresponding steady-state membrane thickness e^∞/e_0 along the rescaled contour length s/L from equator (L is the total membrane mid-line length).

The stationary thickness e_f^∞ in the furrow results from a competition between incoming cortical flows and turnover, and therefore decreases at higher turnover rates (fig. 2.30 *Inset*). The active tension in the furrow is proportional to the local thickness (2.62) and therefore decreases at high turnover rates, which lowers the rate of furrow ingression as shown on fig. 2.30. We expect a large increase of turnover to impair the completion of the furrow ingression if the equatorial signal is close to the constriction threshold. Actin turnover is therefore a critical variable for cytokinesis completion; it has to be tightly regulated by the cell directly via depolymerization and polymerization and indirectly via active cortical flows.

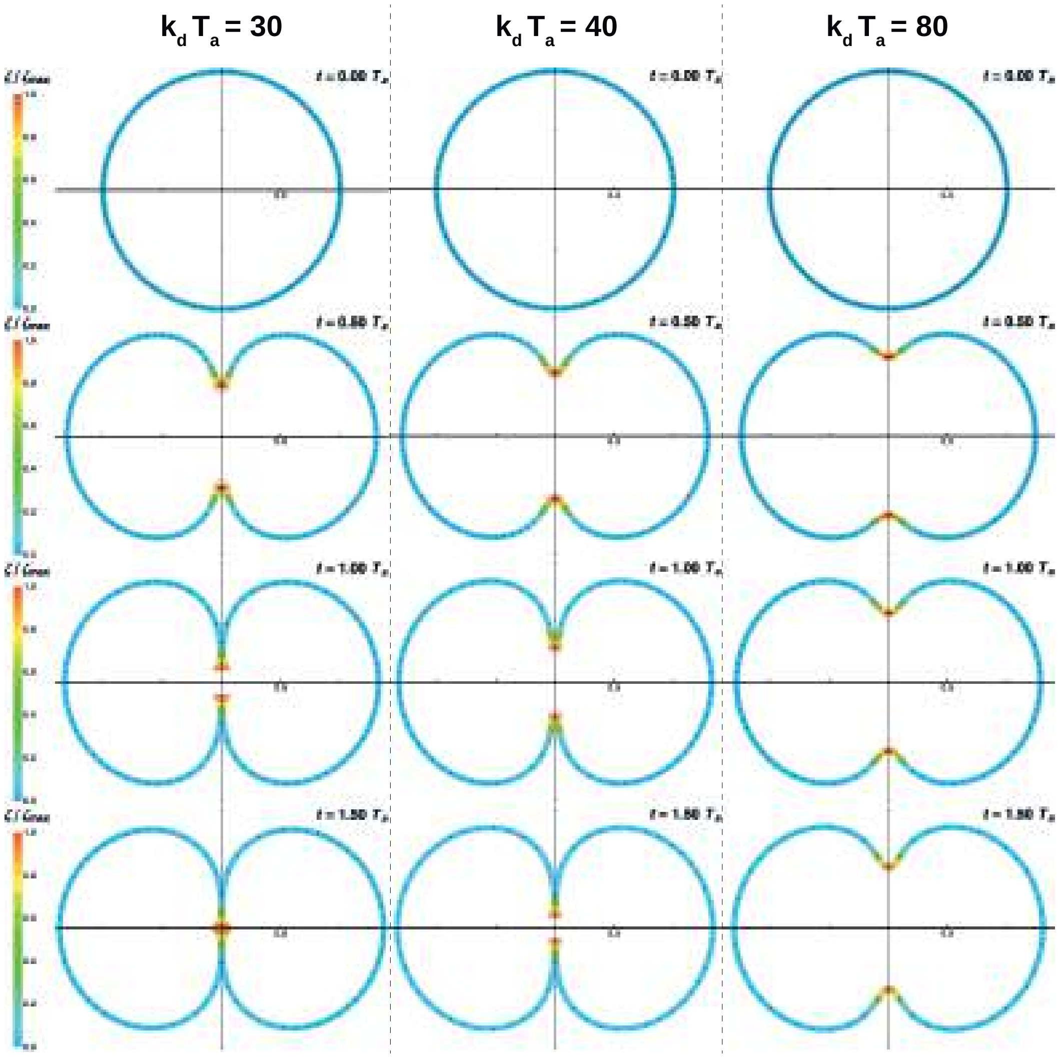

Figure 2.31: Influence of turnover: comparison of the cell shape and cortex thickness dynamics in a section plane $(\mathbf{e}_z, \mathbf{e}_r)$ for the three turnover rates $k_{\mathrm{d}} T_a = 30$, $k_{\mathrm{d}} T_a = 40$ and $k_{\mathrm{d}} T_a = 80$ at fixed equatorial activity amplitude $\delta\zeta^{\infty}/\zeta_0 = 75$, corresponding respectively to the furrow time evolutions ①, ② and ③ in fig. 2.30.

2.3.1.5 Cytokinesis duration is independent of initial cell size

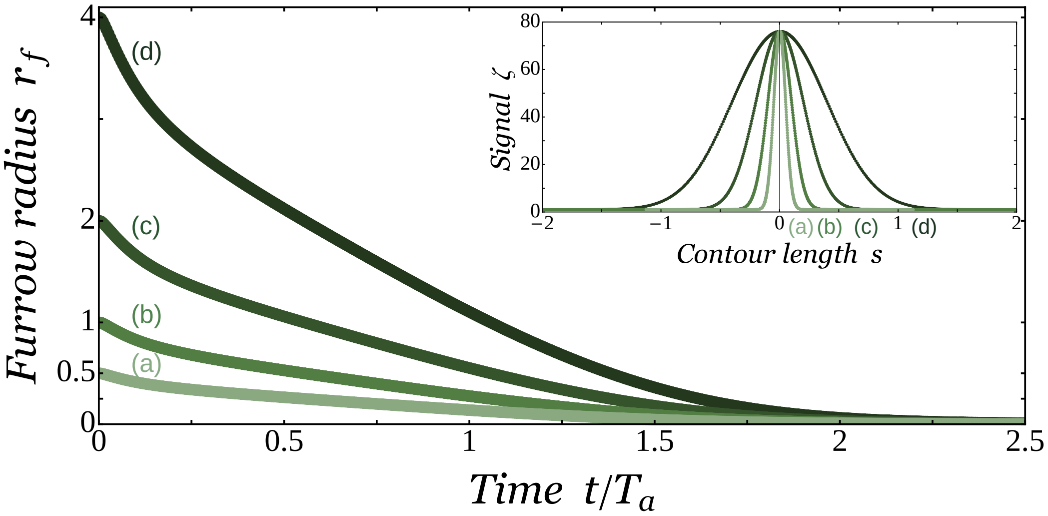

Figure 2.32: Cytokinesis duration is independent of initial cell size: Furrow radius r_f as a function of time t/T_a for four initial cell radii $R_0 = 0.5$, 1, 2 and 4. *(Inset)* Corresponding Gaussian activity signals of width w proportional to R_0, plotted as a function of the membrane mid-line contour length s.

The duration of cytokinesis has been recently reported to be independent of cell initial size in *C. Elegans* embryos [Carvalho 2009]. This remarkable property ensures the tight synchronization of daughter cells development during embryogenesis. We performed numerical constrictions with various initial cell size radii R_0 between 0.5 and 4. Measurements performed on embryos of several organisms [Bement 2005] show the existence of a linear relationship between the initial cell size R_0 and the width w of the Gaussian RhoA-GTP zone (see fig. 1.20): we thus choose w proportionally to R_0, keeping all the other parameters constant. The evolution of the furrow radius with time is plotted in fig. 2.32 for four different values of R_0 and w. We observe that the duration of furrow constriction is independent of R_0 provided that $w \propto R_0$. Our model reproduces this robust feature of cytokinesis.

2.3.2 Scaling arguments

The numerical results can be interpreted in terms of scaling arguments based on a minimal geometry sketched in fig. 2.33, that was proposed by M. Yoneda and K. Dan in 1972 [Yoneda 1972].

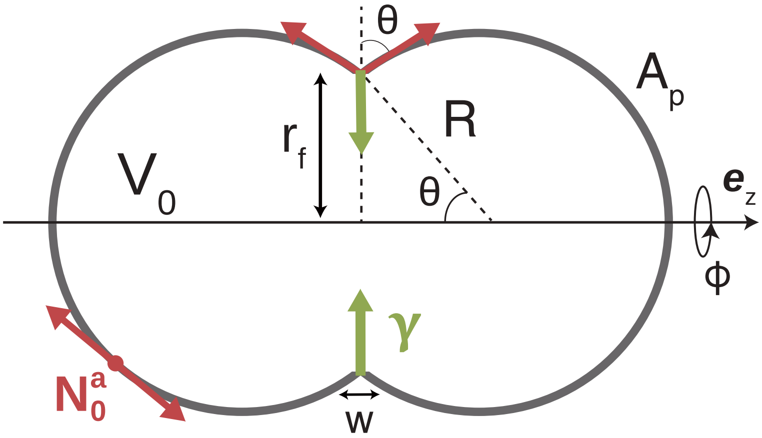

Figure 2.33: Scaling model: Sketch of the minimal geometry proposed by Yoneda and Dan [**?**]: Two portions of sphere of surface A_p and surface tension N_0^a are pinched by an equatorial ring of radius r_f, of width w and of line tension γ. The opening angle θ characterizes the constriction state of the cell and the cytoplasmic volume enclosed V_0 is conserved.

The cell poles are represented by two portions of sphere of radius R under constant active tension $N_0^a = e_0\zeta_0\Delta\mu/2$ and are connected by a ring of radius r_f and width w. The contractile ring is submitted to an active line tension

$$\gamma \approx w\left(N_f^a - N_0^a\right) , \tag{2.114}$$

where N_f^a is the mean contractile surface tension in the furrow. The competition with cortical tension at cell poles is measured by the dimensionless parameter

$$\kappa = \frac{\gamma}{2R_0 N_0^a} \approx \frac{w}{2R_0}\left(N_f^a - N_0^a\right)/N_0^a . \tag{2.115}$$

The opening angle θ defined in fig. 2.33 is a measure of the constriction state of the cell: $\theta = \frac{\pi}{2}$ corresponds to a spherical cell, $\theta = 0$ corresponds to a divided cell.

2.3.2.1 Cytokinesis completion is controlled by the difference of contractility between the contractile ring and the poles

The polar contractility tends to reduce the surface $A_p = 2\pi R^2\left(1+\cos\theta\right)$ of the cell poles, whereas the line tension tends to reduce the contractile ring circumference $r_f = R\sin\theta$. These effects are captured by a simple mechanical energy

$$\mathcal{E} = 2\pi\, r_f\gamma + 2A_p\, N_0^a . \tag{2.116}$$

Cytoplasmic volume conservation can be written as $R = R_0\, F(\theta)^{1/3}$, where $F(\theta)$ is a smooth function of θ:

$$R_0^3 = R^3 \left[1 + \frac{3}{2}\cos\theta - \frac{1}{2}\cos^3\theta\right] \equiv R^3 F(\theta)\,. \tag{2.117}$$

The mechanical energy, rescaled by the value $\mathcal{E}_0 = 4\pi R_0^2 N_0^a$ for a spherical cell, depends only on κ and θ and reads

$$\frac{\mathcal{E}}{\mathcal{E}_0} = \frac{\kappa\,\sin\theta}{F(\theta)^{1/3}} + \frac{1+\cos\theta}{F(\theta)^{2/3}}. \tag{2.118}$$

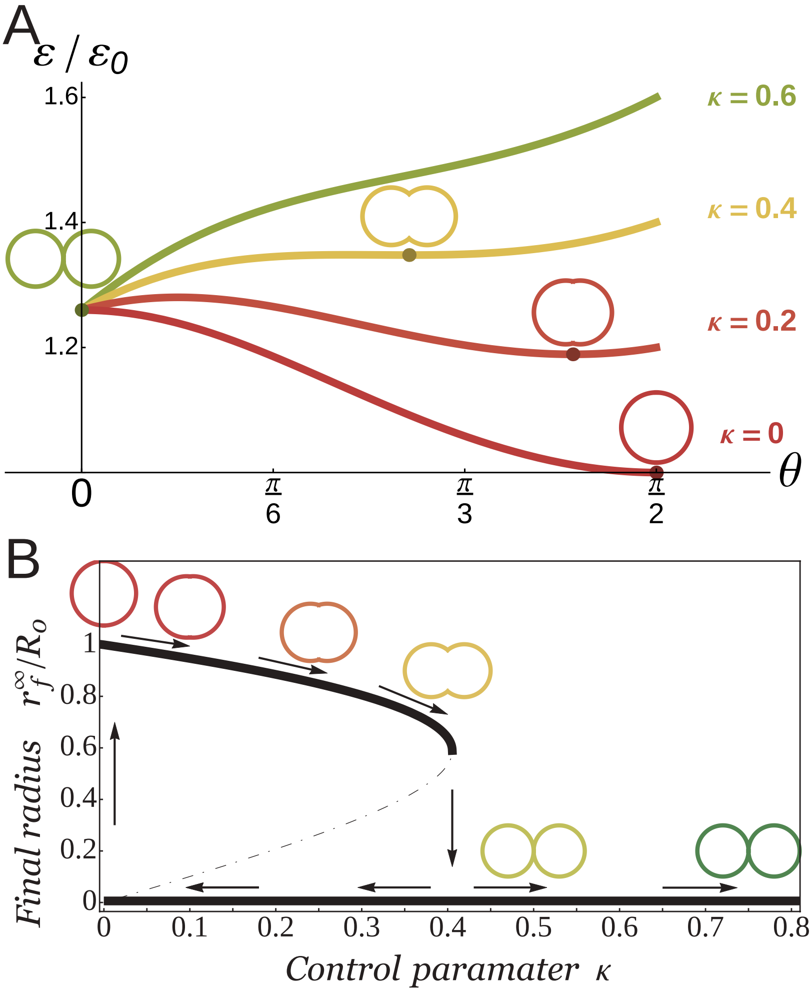

Figure 2.34: Static approach: *(A)* Mechanical energy profile $\mathcal{E}/\mathcal{E}_0$ as a function of the constriction state θ for four values of $\kappa = \gamma/2R_0N_0^a$. Local minima of the energy correspond to equilibrium states and are illustrated by darker points, above which are plotted the corresponding cell shapes. *(B)* Bifurcation diagram representing the final furrow radius r_f^∞/R_0 as a function of the control parameter κ. The upper branch and the branch $r_f = 0$ are the stable branches whereas the dot-dashed branch is unstable. The critical point is a saddle-node, and the bifurcation classically exhibits an hysteresis illustrated by the arrows. Final cell shapes, starting from a spherical cell, are plotted for the six following values of the control parameter $\kappa = 0$, 0.1, 0.25, 0.4, 0.5, and 0.75.

We plot in fig. 2.34 A the mechanical energy $\mathcal{E}/\mathcal{E}_0$ as a function of θ for various values of κ. The minima of $\mathcal{E}/\mathcal{E}_0$ are the local equilibrium states of the cell. Starting from a spherical cell at $\theta = \frac{\pi}{2}$, the final shape is reached at the first local minimum of energy. For $\kappa = 0$ *(red curve)*, in absence of any contractile ring, the spherical cell is the minimum of energy. As the control parameter κ increases, i.e. the contractile ring line tension increases, the first local minimum of $\mathcal{E}$ shifts towards a more constricted state ($\theta < \frac{\pi}{2}$), but the constriction is still incomplete. For $\kappa \gtrsim 0.4$ the local minimum disappears at the benefit of a single global minimum, corresponding to the fully constricted state $\theta = 0$ *(green curve)*: constriction succeeds. This simple energetic approach of the constriction completion uncovers the fundamental mechanism of cytokinesis: cell volume conservation enforces a competition between the line tension of the ring, that tends to minimize its circumference, and the contractility of the poles that resists the associated cell surface increase. This competition drives a first-order transition from cytokinesis failure to constriction completion.

We plot alternately in fig. 2.34 B the bifurcation diagram of the final constriction state r_f^∞ (corresponding to the first minimum of energy in fig. 2.34 A) as a function of the control parameter κ. Similarly to the numerical results (fig. 2.26 A), scaling arguments reveal a jump from partial to complete constriction above a critical threshold of the difference of contractility between the furrow and the poles κ_c. The critical point (κ_c, θ_c) is given by

$$0 = \left.\frac{\partial \mathcal{E}}{\partial \theta}\right|_{\theta_c}, \qquad 0 = \left.\frac{\partial^2 \mathcal{E}}{\partial \theta^2}\right|_{\theta_c}. \tag{2.119}$$

Using Mathematica® 9.0.1 we solve this system of equations and get the following numerical values for complete constriction threshold $\kappa_c \approx 0.4053$, corresponding to a constriction state $\theta_c \approx 46.46°$ or equivalently $r_{f_c} = 0.5884\, R_0$.

The energy plot in fig. 2.34A shows clearly that $\theta = 0$ is a possible local energy minimum for $\kappa > 0$, and therefore that the divided state is mechanically stable, which clarifies the origin of the hysteresis behavior, illustrated by arrows on fig. 2.34B.

2.3.2.2 The contractility difference between the contractile ring and poles also controls the dynamics of constriction

In the continuum model the mechanical power of active effects (2.118) is exactly dissipated by viscous cell deformations as shown in fig. 2.F.1 A. We apply here the same principle that reads simply

$$\frac{d\mathcal{E}}{dt} + \mathcal{P}_\mathrm{d} = 0 \tag{2.120}$$

where $\mathcal{P}_\mathrm{d}$ is the viscous dissipation, made of two contributions: the stretching of the poles and the constriction of the ring, which we estimate in scaling. The volume of actomyosin in the poles is $V_p = 2A_p\, e_p$ and in the ring $V_f = 2\pi r_f\, w e_f$, where w and e_f are the width and thickness of the contractile ring. According to the numerical results (see fig. 2.30 *Inset* and fig. 2.25*D*), the thickness of the actin layer at the poles does not vary appreciably $e_p \approx e_0$ and the ring thickness e_f reaches a steady-state value that depends on turnover. This yields the viscous dissipated power

$$\mathcal{P}_{\mathrm{d}} = \frac{1}{2}\eta \left[V_p \left(\frac{1}{R} \frac{dr_f}{dt} \right)^2 + V_f \left(\frac{1}{r_f} \frac{dr_f}{dt} \right)^2 \right] \tag{2.121}$$

Inserting the values of r_f, R, V_f and V_p as a function of θ the dissipated power becomes

$$\mathcal{P}_{\mathrm{d}} = 4\pi e_0\, \eta \left(\frac{dr_f}{dt} \right)^2 \left[(1+\cos\theta) + \lambda \frac{F(\theta)^{1/3}}{\sin\theta} \right] , \tag{2.122}$$

where we defined the parameter

$$\lambda \equiv \frac{w}{2R_0} \frac{e_f}{e_0} . \tag{2.123}$$

We calculate the time variation of the mechanical energy $\frac{d\mathcal{E}}{dt} = -\mathcal{P}_d$ rescaled by $\mathcal{E}_0$:

$$\begin{aligned} \frac{1}{\mathcal{E}_0} \frac{d\mathcal{E}}{dt} &= \frac{\partial \mathcal{E}/\mathcal{E}_0}{\partial \theta} \frac{\partial \theta}{\partial r_f} \frac{dr_f}{dt} \\ &= -\frac{\mathcal{P}_{\mathrm{d}}}{\mathcal{E}_0} \\ &= -\frac{T_a}{R_0^2} \left(\frac{dr_f}{dt} \right)^2 \left[(1+\cos\theta) + \lambda \frac{F(\theta)^{1/3}}{\sin\theta} \right] , \end{aligned}$$

with $T_a = \frac{\eta e_0}{N_0^a}$ defined as in the continuum formulation. This leads to

$$\begin{aligned} \frac{T_a}{R_0} \frac{dr_f}{dt} &= -\frac{\partial \mathcal{E}/\mathcal{E}_0}{\partial \theta} \left(\frac{\partial r_f/R_0}{\partial \theta} \right)^{-1} \left[(1+\cos\theta) + \lambda \frac{F(\theta)^{1/3}}{\sin\theta} \right]^{-1} \\ &\equiv -\mathcal{H}(\theta, \kappa, \lambda) . \end{aligned} \tag{2.124}$$

Since $\mathcal{E}/\mathcal{E}_0$ depends only on θ and κ according to (2.118), the rate of constriction $\frac{dr_f}{dt}$ reduces to a simple function $\mathcal{H}$ of θ, κ and λ only:

$$T_a \frac{dr_f}{dt} = -R_0\, \mathcal{H}(\theta, \kappa, \lambda) , \qquad \text{with } \lambda \equiv \frac{e_f}{e_0} \frac{w}{2R_0} \tag{2.125}$$

One can solve for the radius of the contractile ring as a function of time for given values of κ and λ by inserting $r_f/R_0 = \sin\theta\, F(\theta)^{-1/3}$ in Eq. (2.124), then integrating numerically the non-linear differential equation for $\theta(t)$ and finally recalculating $r_f\,(\theta(t))$.

We solve numerically Eq. (2.124) with Mathematica® 9.0.1., varying the activity in the furrow ζ_f/ζ_0 or its width w/R_0 to mimick the RhoA-GTP signal and/or the furrow thickness e_f/e_0 to mimick the effect of turnover. We plot the results in fig. 2.35

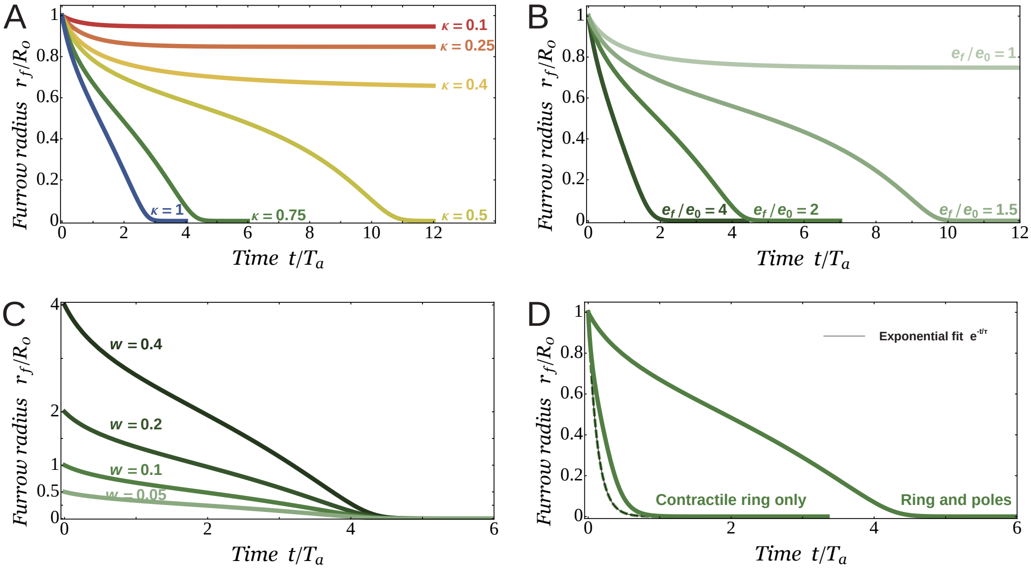

Figure 2.35: Constriction dynamics in scaling. Normalized furrow radius evolution r_f/R_0 with time t/T_a: *(A)* For $\kappa = 0.1, 0.25, 0.4, 0.5, 0.75$ and 1, with constant $\lambda = 0.1$. For $\kappa \lesssim 0.4$, the furrow radius reaches a plateau indicating constriction failure, whereas for $\kappa \gtrsim 0.4$ constriction is complete and its speed increases with κ. *(B)* For e_f/e_0 between 1 and 4, keeping $\zeta_f/\zeta_0 = 8$ and $w/R_0 = 0.1$ constant. Constriction slows down when e_f/e_0 decreases from 4 to 1.5, and can even fail when it drops to 1. *(C)* For four initial cell radii $R_0 = 0.5$, 1, 2 and 4, where the ring width w is increased proportionally $w = 0.05, 0.1, 0.2,$ and 0.4. $e_f/e_0 = 2$ and $\zeta_f/\zeta_0 = 8$ are maintained constant. The rate of constriction increases proportionally to the ring width leading to the same constriction duration for the four cell sizes. *(D)* For a cell with dissipation due to the ring constriction only and with dissipation due to poles stretching and ring constriction ($\zeta_f/\zeta_0 = 8$, $e_f/e_0 = 2$, $w/R_0 = 0.1$). The dashed line corresponds to the constriction of an isolated ring (no poles) fitted with the exponential function $e^{-t/\tau}$ with $\tau = 2\eta/\zeta_f\Delta\mu$.

From the dynamics results we can conclude that:

- The constriction time-scale is set by $T_a = \frac{\eta\, e_0}{N_0^a}$, as defined in (2.112), which measures the typical active time of viscous stretching of the poles.
- κ and λ control the rate of constriction. $\kappa \approx \frac{w}{2R_0}\left(\frac{\zeta_f\, e_f}{\zeta_0\, e_0} - 1\right)$ characterizes the dependence of the constriction rate on the contractility difference between the ring and the poles, and depends on the normalized furrow activity ζ_f/ζ_0 and on turnover via the normalized thickness e_f/e_0. λ depends essentially on turnover via e_f. We plot in fig. 2.35 *A* the furrow radius r_f evolution as a function of time for various values of κ between 0.1 and 1, at fixed $\lambda = 0.1$ and recover qualitatively the same dynamics as in the numerical results. In fig. 2.35 *B* we keep ζ_f/ζ_0 constant and plot r_f as a function of time t/T_a for four values of e_f/e_0 between 1 and 4, thereby mimicking the competition between cortical flows and actin turnover. Again we retrieve qualitatively the same behavior as for the continuous model: decreasing the furrow thickness e_f, thereby enhancing turnover, slows down the constriction and can even impede its completion (see curve $e_f/e_0 = 1$).

- If we assume that w scales linearly with R_0 then κ and λ, which are both proportional to w/R_0, become independent of the initial cell radius and so does $\mathcal{H}$: the constriction rate in (2.125) is proportional to the initial radius and the cytokinesis duration becomes independent of initial cell size, as illustrated in fig. 2.35 *C*, that reproduce the numerical results of fig. 2.32.

One should note however that κ and λ are not independent in the continuous model. In particular $\lambda \propto \frac{e_f}{e_0}$ should increase with $\kappa \propto N_f^a - N_0^a$ at fixed turnover because of increased cortical flows that we neglected here. Conversely, κ depends on the ratio e_f/e_0 as we show using the continuous expressions for active tensions:

$$\kappa \approx \frac{w}{2R_0}\frac{N_f^a - N_0^a}{N_0^a} \approx \frac{w}{2R_0}\left(\frac{\zeta_f}{\zeta_0}\frac{e_f}{e_0} - 1\right) , \tag{2.126}$$

where ζ_f and ζ_0 are the activities respectively in the furrow and at poles.

Finally we show that the dissipation associated to the poles stretching participates largely to the slowing down of furrow constriction, consistently with numerical results (see fig. 2.F.1 B): the decrease of r_f is indeed much more rapid in fig. 2.35*D* for vanishing poles dissipation ($V_p \to 0$ in eq. (2.121)). These results suggest that not only the contractility but also the viscosity of the polar cortex is a critical parameter to consider to account for the dynamics of furrow constriction.

In the limiting case of an isolated visco-active ring (no poles at all), scaling arguments yield a purely exponential constriction dynamics (*dashed line* in fig. 2.35 *D*), consistent with experimental contraction of isolated rings in-vitro [Reymann 2012]. We can retrieve this scaling by a simple balance of viscous forces $\eta \frac{w\, e_f}{r_f}\frac{dr_f}{dt}$ with the constricting force $\gamma = w\, N_f^a = w\, e_f\, \zeta_f \Delta\mu$ in the ring, which leads immediately to $r_f/R_0 = e^{-t/\tau}$, with $\tau = 2\eta/\zeta_f\Delta\mu$ the characteristic active time-scale of the problem. The constriction dynamics of an isolated visco-active ring depends therefore strongly on the ratio of myosin activity ζ_f and actomyosin viscosity η (controlled by cross-linking) but becomes independent of actin turnover, consistent with recent experimental results [Mishra 2013].

2.3.3 Discussion

2.3.3.1 Summary of the results

Using both numerical and scaling analyses we rationalize the physical mechanisms governing ring constriction in the cytokinesis of animal cells. Following the seminal work of Bray, White and Borisy [White 1983, Bray 1988], we show that a gradient of surface contractility from the poles to the equator is sufficient to drive cytokinesis and to reproduce its main features: formation of the contractile ring, cortical flow toward the equator and furrow constriction as illustrated in fig. 1.14 B. Starting from a quite fundamental physical model of the cortex — a thin viscous layer producing active contraction and subjected to a uniform cytoplasmic pressure — we are able to reproduce realistic shapes of dividing embryos. We provide quantitative criteria for cytokinesis completion and propose a general framework for interpreting and characterizing constriction failure. We furthermore demonstrate the physical mechanism leading to the independence of cytokinesis duration on the initial cell size in embryos [Carvalho 2009], and we highlight the critical influence of actin turnover. A scaling model is then proposed to interpret the numerical results. It explains and successfully reproduces the properties of furrow constriction, despite its simplified geometry. It notably demonstrates that the contractility difference between the poles and the furrow is the key parameter for both cytokinesis completion and constriction dynamics. This highlights a critical role of the polar cortex in cytokinesis success and dynamics.

We discuss below the different model approximations and the possible future refinements and extensions of our model for cytokinesis:

2.3.3.2 Uniformity of the turnover

We reproduce accurately the experimental constriction dynamics and shape evolution of a sand dollar embryo. Precise spatio-temporal measurements of RhoA-GTP along the cortex over the entire time of constriction would however be required to make a detailed quantitative fit of our theory to experiments. Estimates for the cortex turnover time are also required to account for the accumulation of actin in the ring via cortical flows, which can play a major role in constriction dynamics. FRAP measurements of the cortex provide reasonable values for the turnover time-scale [Fritzsche 2013], but we have neglected here the possible non-uniformity of turnover along the cortex for the sake of simplicity. RhoA-GTP is indeed known for also promoting actin polymerization via the formin mDia1 [Dean 2005], and the ring formation is then likely to be the result of both accumulation by cortical flows and higher polymerization [Guha 2005, Murthy 2005]. On the contrary, myosin activity, promoted by RhoA-GTP via its effector ROCK, has been shown to enhance actin filament disassembly both in-vitro and in-vivo [Guha 2005, Murrell 2012, Vogel 2013]. Altogether, the local activation of RhoA is likely to enhance non-uniformly turnover. A more rigorous implementation of non-uniform turnover would require substantial progress in the theoretical understanding and quantitative characterization of in-vivo disassembly of actin by myosin motors, which is far beyond this study. We argue nevertheless that the fundamental trends highlighted in our study will remain valid.

2.3.3.3 Negligible friction and viscous bending losses

Based on quantitative studies in *C. Elegans* [Mayer 2010], our model assumed that the frictional loss associated with cortex sliding along the plasma membrane was negligible compared to viscous dissipation associated with cortex deformation. However the cortical flows in sea-urchin eggs are reported to be lower that in *C. Elegans* (G. Von Dassow, personal communication). A tangential friction may limit their extension in this cell type. The friction loss may be attributed for example to the dense coverage of the sea-urchin cell surface by villis, impeding its movement. It would therefore be interesting to evaluate the effect of friction on the constriction dynamics in a further development of the model.

We used a membrane approximation of the cell cortex, and thereby we neglected the bending moments relatively to the tensions of the thin shell. However we can observe that the membrane does not remain tensile everywhere during the constriction process: the azimuthal total tension N_φ in fig. 2.25D becomes negative at time $t = 1.25 T_a$ in a close cylindrical area surrounding the furrow region. There we expect therefore possible foldings of the membrane that can only been described by reintroducing the small bending moments. These folds have indeed been observed in the cleavage of eggs as illustrated in fig. 2.36 We also expect bending moments to become non-negligible in the highly curved furrow region at the end of cytokinesis, where the typical tangential radius of curvature becomes of the same order as the shell thickness. An exhaustive thin shell theory and not only a membrane approximation of the cortex would therefore been required to describe more thoroughly the late stages of constriction. The membrane approximation has however the advantage to clearly identify the main ingredients controlling the constriction process, and adding the bending moments and shearing forces would complicate drastically the numerical implementation.

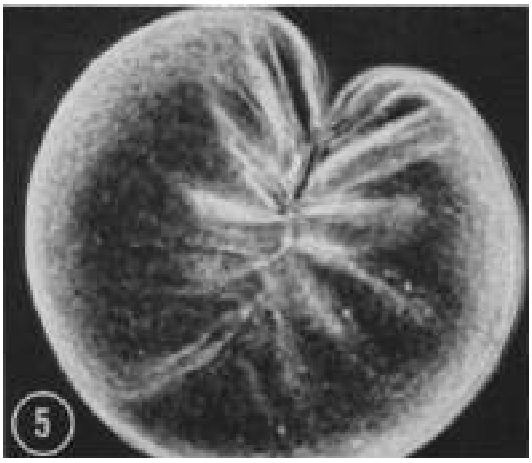

Figure 2.36: Large surface folds along the azimuthal direction in the furrow region of *Aequorea eggs* observed in phase contrast during asymmetric cleavage. Adapted from [Szollosi 1970].

2.3.3.4 Isotropy of the filament orientation

We neglected here the anisotropy in actin filament orientation. Their spatial organization in the plane of the membrane is however dynamically coupled to cortical flows, as described by the active-gel theory [Kruse 2005, Salbreux 2009]. In cytokinesis the cortical flows toward the equator are expected to lead to two effects, illustrated schematically in fig. 2.37

1. A parallel alignment of filaments to the cortical flow in a region adjacent to

the furrow.

2. An azimuthal alignment of filaments in the furrow region as a result of their confinement.

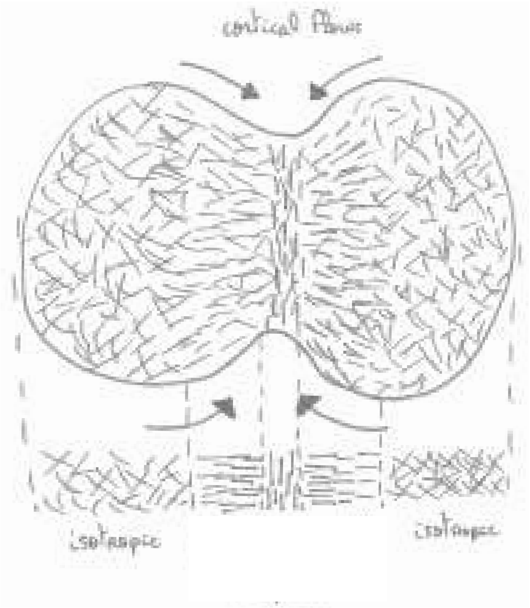

Figure 2.37: Sketch of the expected filament orientation organisation on the cell surface as a result of the cortical flows.

The nematic effects were calculated in perturbation on a sphere [Salbreux 2008] and on a cylinder [Salbreux 2009] at leading order and agree qualitatively with experimental results in [Fishkind 1993]. To solve the problem beyond the perturbation theory, we would need to associate a new dynamical scalar variable $\tilde{Q}$, quantifying the nematic orientation of the filaments, to the segments in the numerical implementation. We can however already conjecture that the alignments effects will increase the azimuthal component of the active tension N^a_φ in the furrow region, thereby contributing to constriction and lowering the activity threshold for cytokinesis success.

2.3.3.5 Volume conservation

We also expect the threshold value to drop rapidly, or even to vanish, if the constraint of cytoplasm incompressibility is partially relaxed.

We neglected so far the possible emergence of blebs at poles during furrow constriction of certain cell types in culture and in-vivo, as illustrated in fig. 2.38 If the total cell volume is globally conserved some intracortical volume may be transferred in blebs. We expect this effect to facilitate the furrow ingression. In collaboration with Chantal Roubinet in the group of Clemens Cabernard at the Universität Basel we started a quantitative experimental study on the influence of blebs in furrow ingression.

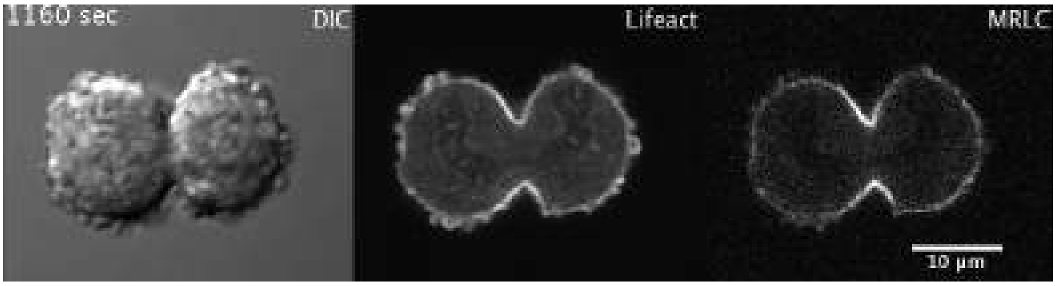

Figure 2.38: Bleb formation during cytokinesis in a dividing L929 mouse fibroblast. F-actin and myosin are visualized using Lifeact-GFP and MRLC-tdRFP respectively. (Adapted from [Sedzinski 2011])

Preliminary measurements performed in-vitro show that specific cell types in culture may release the excess of hydrostatic pressure by expelling some cytoplasmic volume during the furrow constriction (Matthieu Piel, personal communication). Hence, the permeation of water through membrane pores (aquaporins) may also be a way to avoid cytokinesis failure. We started to implement the effect of permeation and ion fluxes dynamics in our numerical code to study this problem.

Different strategies for ensuring constriction success may therefore have been developed among animal species, or even among differentiated cells in a same organism.

Appendix

Contents

2.A Force and moment balance in an axisymmetric thin shell

To derive the balance of forces and moments acting on the shell, we consider a patch of thickness e between s and $s+ds$, ϕ and $\phi+d\phi$. Its mid-surface is therefore $rd\phi\,ds$. We project the equilibrium on the local Frenet frame $(\mathbf{t},\mathbf{n},\mathbf{e}_\varphi)$.

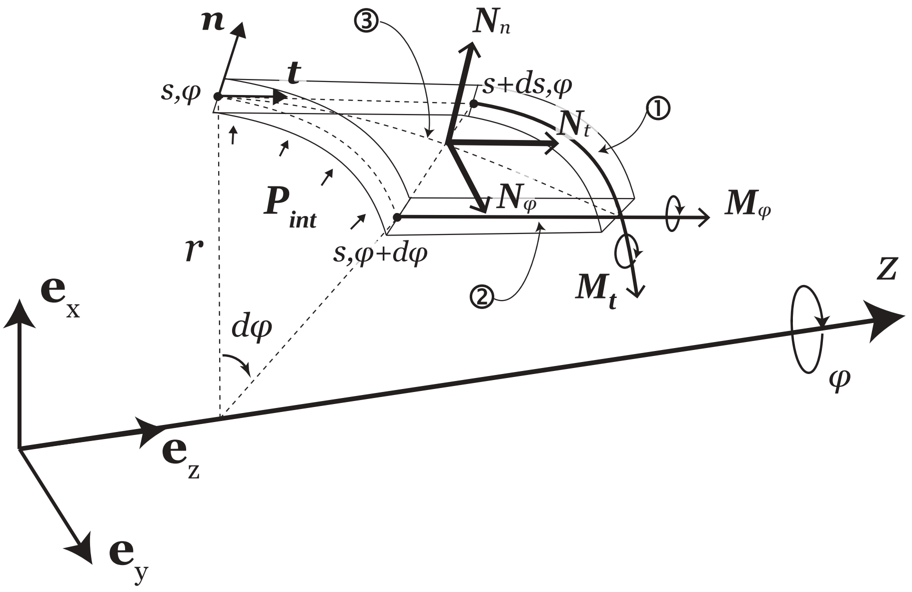

Figure 2.A.1: Force and moment balance on a thin shell: definition of the tensions and couples

2.A.1 Balance of forces

We first evaluate the force exerted on the three faces ①, ② and ③ defined on fig. 2.A.1:

$$
\begin{aligned}
\boldsymbol{\mathcal{F}}_1(s,\phi) &= \int_{-e/2}^{e/2} d\xi\;(r+\xi\sin\psi)\,d\phi\;(\sigma_{tt}\,\mathbf{t}+\sigma_{nt}\,\mathbf{n}+\sigma_{\varphi t}\,\mathbf{e}_\varphi)\\
&= rd\phi\int_{-e/2}^{e/2} d\xi\left(1+\xi\frac{\sin\psi}{r}\right)(\sigma_{tt}\,\mathbf{t}+\sigma_{nt}\,\mathbf{n})\\
&= rd\phi\;(N_t\,\mathbf{t}+N_n\,\mathbf{n})\;,
\end{aligned}
$$

where we define N_t the tension in the tangential direction, and N_n the transverse shear force by

$$
N_t \equiv \int_{-e/2}^{e/2} \sigma_{tt}\left(1+\xi\frac{\sin\psi}{r}\right)d\xi \tag{2.127}
$$

$$
N_n \equiv \int_{-e/2}^{e/2} \sigma_{nt}\left(1+\xi\frac{\sin\psi}{r}\right)d\xi\,. \tag{2.128}
$$

$$\begin{aligned}\boldsymbol{\mathcal{F}}_2(s,\phi) &= \int_{-e/2}^{e/2} d\xi \left(1+\xi\frac{\partial\psi}{\partial s}\right) ds\ (\sigma_{t\varphi}\,\mathbf{t}+\sigma_{n\varphi}\,\mathbf{n}+\sigma_{\varphi\varphi}\,\mathbf{e}_\varphi)\\ &= ds\int_{-e/2}^{e/2} d\xi\ \left(1+\xi\frac{\partial\psi}{\partial s}\right)\sigma_{\varphi\varphi}\,\mathbf{e}_\varphi\\ &= ds\,N_\varphi\,\mathbf{e}_\varphi\,,\end{aligned}$$

where we define N_φ the tension in the azimuthal direction

$$N_\varphi \equiv \int_{-e/2}^{e/2}\sigma_{\varphi\varphi}\left(1+\xi\frac{\partial\psi}{\partial s}\right) d\xi \tag{2.129}$$

$$\boldsymbol{\mathcal{F}}_3(s,\phi,\xi) = ds\,rd\phi\left(1+\xi\frac{\sin\psi}{r}\right)\left[\sigma_{nn}(s,\xi)\,\mathbf{n}+\sigma_{tn}(s,\xi)\,\mathbf{t}\right]\,,$$

The balance of forces on the shell patch reads

$$\mathbf{0}=\boldsymbol{\mathcal{F}}_3\left(\frac{e}{2}\right)-\boldsymbol{\mathcal{F}}_3\left(\frac{e}{2}\right)+\boldsymbol{\mathcal{F}}_1\left(s+\frac{ds}{2}\right)-\boldsymbol{\mathcal{F}}_1\left(s-\frac{ds}{2}\right)+\boldsymbol{\mathcal{F}}_2\left(\phi+\frac{d\phi}{2}\right)-\boldsymbol{\mathcal{F}}_2\left(\phi-\frac{d\phi}{2}\right)$$

We evaluate the sum term by term

$$\begin{aligned}\boldsymbol{\mathcal{F}}_1\left(s+\frac{ds}{2}\right)-\boldsymbol{\mathcal{F}}_1\left(s-\frac{ds}{2}\right) &= d\phi\,ds\,\frac{\partial}{\partial s}\Big\{rN_t\,\mathbf{t}+rN_n\,\mathbf{n}\Big\}\\ &= d\phi\,ds\,\left\{\left[\frac{\partial rN_t}{\partial s}-\frac{\partial\psi}{\partial s}rN_n\right]\,\mathbf{t}+\left[\frac{\partial\psi}{\partial s}rN_t+rN_n\right]\,\mathbf{n}\right\}\end{aligned}$$

$$\begin{aligned}\boldsymbol{\mathcal{F}}_2\left(\phi+\frac{d\phi}{2}\right)-\boldsymbol{\mathcal{F}}_2\left(\phi-\frac{d\phi}{2}\right) &= ds\,d\phi\,\frac{\partial}{\partial\varphi}\Big\{N_\varphi\,\mathbf{e}_\varphi\Big\}\\ &= -d\phi\,ds\,N_\varphi\left[\cos\psi\,\mathbf{t}+\sin\psi\,\mathbf{n}\right]\end{aligned} \tag{2.130}$$

$$\begin{aligned}\boldsymbol{\mathcal{F}}_3\left(\frac{e}{2}\right)-\boldsymbol{\mathcal{F}}_3\left(\frac{e}{2}\right) &= ds\,rd\phi\,\left[\left(1+\xi\frac{\sin\psi}{r}\right)\Big(\sigma_{nn}(s,\xi)\,\mathbf{n}+\sigma_{nt}(s,\xi)\,\mathbf{t}\Big)\right]_{-e/2}^{e/2}\\ &= ds\,rd\phi\,\left[\Big(\sigma_{nn}(s,\xi)\,\mathbf{n}+\sigma_{nt}(s,\xi)\,\mathbf{t}\Big)\right]_{-e/2}^{e/2}+\mathcal{O}(e^3)\\ &\equiv ds\,rd\phi\,\Big\{\Delta p_n\,\mathbf{n}+\Delta p_t\,\mathbf{t}\Big\}\end{aligned} \tag{2.131}$$

where $\Delta p_n = \sigma_{nn}(s, e/2) - \sigma_{nn}(s, -e/2)$ and $\Delta p_t = \sigma_{nt}(s, e/2) - \sigma_{nt}(s, -e/2)$ are the difference of, respectively, normal and shear stress accross the shell, which are imposed as boundary conditions of the problem.

We rewrite the force balance on the shell patch, divided by its surface $r d\phi\, ds$ and projected on local the Frenet frame $(\mathbf{t}, \mathbf{n})$

$$
\begin{align}
-\Delta p_t &= \frac{\partial N_t}{\partial s} + \frac{N_t - N_\varphi}{r}\frac{\partial r}{\partial s} + N_n \frac{\partial \psi}{\partial s} \tag{2.132a}\\
-\Delta p_n &= N_t \frac{\partial \psi}{\partial s} + N_\varphi \frac{\sin\psi}{r} - \frac{1}{r}\frac{\partial\, r N_n}{\partial s} \tag{2.132b}
\end{align}
$$

2.A.2 Balance of moments

We also evaluate the two moments $\boldsymbol{\mathcal{M}}_t$ and $\boldsymbol{\mathcal{M}}_\varphi$ acting on the shell, as defined on fig. 2.A.1.

We consider the center O_1 of the face ① and a point M on the face ①. The moment on the face ① at $s + ds/2$ reads

$$
\begin{aligned}
\boldsymbol{\mathcal{M}}_t(s + ds/2) &= \int (\mathbf{X0}_1 + \mathbf{0}_1\mathbf{M}) \times d\boldsymbol{\mathcal{F}}_1\\
&= \int_{-e/2}^{e/2} \int_{\phi - d\phi/2}^{\phi + d\phi/2} \left[\frac{ds}{2}\,\mathbf{t} + \xi\,\mathbf{n} + (r + \xi\sin\psi)\left(\phi' - \phi\right)\,\mathbf{e}_\varphi\right]\\
&\quad \times \Big[\sigma_{tt}\,\mathbf{t} + \sigma_{nt}\,\mathbf{n}\Big] \left(1 + \xi\frac{\sin\psi}{r}\right) d\xi\, r d\phi'\\
&= r d\phi\, \mathbf{e}_\varphi \int_{-e/2}^{e/2} \left\{\frac{ds}{2}\sigma_{nt} - \xi\sigma_{tt}\right\} \left(1 + \xi\frac{\sin\psi}{r}\right) d\xi + \mathcal{O}\left(d\phi^2\right)\\
&\equiv \mathbf{e}_\varphi\, r d\phi \left\{\frac{ds}{2}\tau_n - g_t\right\},
\end{aligned}
$$

where we define g_t the effective 2d moment acting along $-\mathbf{e}_\varphi$

$$
g_t = \int_{-e/2}^{e/2} \sigma_{tt}\,\xi \left(1 + \xi\frac{\sin\psi}{r}\right) d\xi\ . \tag{2.133}
$$

We consider the center O_2 of the face ② and a point M on the face ②. The moment on the face ② at $\varphi + \varphi/2$ reads

$$
\begin{aligned}
\boldsymbol{\mathcal{M}}_\varphi &= \int (\mathbf{X0}_2 + \mathbf{0}_2\mathbf{M}) \times d\boldsymbol{\mathcal{F}}_2\\
&= \int_{-e/2}^{e/2} \int_{s - ds/2}^{s + ds/2} \left[s'\,\mathbf{t} + \xi\,\mathbf{n} + (r + \xi\sin\psi)\,\frac{d\varphi}{2}\mathbf{e}_\varphi\right] \times \left[\sigma_{\varphi\varphi}\left(1 + \xi\frac{\partial\psi}{\partial s}\right) d\xi\, ds'\,\mathbf{e}_\varphi\right]\\
&= \mathbf{t}\, ds \int_{-e/2}^{e/2} \sigma_{\varphi\varphi}\xi \left(1 + \xi\frac{\partial\psi}{\partial s}\right) d\xi + \mathcal{O}\left(ds^2\right)\\
&\equiv \mathbf{t}\, ds\, g_\varphi
\end{aligned}
$$

where we define g_φ the effective 2d moment acting along $\mathbf{t}$

$$g_\varphi = \int_{-e/2}^{e/2} \sigma_{\varphi\varphi}\, \xi \left(1 + \xi \frac{\partial \psi}{\partial s}\right) d\xi \tag{2.134}$$

The sum of moments acting on the shell patch reads

$$0 = \boldsymbol{\mathcal{M}}_t\left(s + \frac{ds}{2}\right) - \boldsymbol{\mathcal{M}}_t\left(s - \frac{ds}{2}\right) + \boldsymbol{\mathcal{M}}_\varphi\left(\varphi + \frac{d\varphi}{2}\right) - \boldsymbol{\mathcal{M}}_\varphi\left(\varphi - \frac{d\varphi}{2}\right).$$

Again we evaluate the sum term by term:

$$\begin{aligned}
\boldsymbol{\mathcal{M}}_t\left(s + \frac{ds}{2}\right) - \boldsymbol{\mathcal{M}}_t\left(s - \frac{ds}{2}\right) &= \mathbf{e}_\varphi\, d\phi \left\{ r(s + ds/2)\left[\frac{ds}{2} N_n - g_t(s + ds/2)\right]\right. \\
&\qquad \left. - r(s - ds/2)\left[\frac{-ds}{2} N_n - g_t(s - ds/2)\right]\right\} \\
&= \mathbf{e}_\varphi\, r d\phi\, ds \left\{ N_n - \frac{\partial\, r g_t}{\partial s}\right\} + \mathcal{O}(ds^2)
\end{aligned}$$

$$\begin{aligned}
\boldsymbol{\mathcal{M}}_\varphi\left(\varphi + \frac{d\varphi}{2}\right) - \boldsymbol{\mathcal{M}}_\varphi\left(\varphi - \frac{d\varphi}{2}\right) &= ds\, d\varphi\, g_\varphi \frac{\partial \mathbf{t}}{\partial \varphi} \\
&= ds\, d\varphi\, g_\varphi \left(-\cos\psi\, \mathbf{e}_\varphi\right) \\
&= -ds\, d\varphi\, g_\varphi \frac{\partial r}{\partial s}\, \mathbf{e}_\varphi
\end{aligned}$$

We rewrite the moment balance on the shell patch, divided by its surface $r d\phi\, ds$ and projected on the azimuthal direction $\mathbf{e}_\varphi$

$$N_n = g_\varphi \frac{\partial r}{\partial s} + \frac{1}{r}\frac{\partial\, r g_t}{\partial s} \tag{2.135}$$

2.B Local volume conservation: direct calculation

We write the conservation of the volume $dV = 2\pi\, r\, d\xi\, ds$ of a small piece of the thin shell between t and $t + dt$, as sketched on fig. 2.B.1.

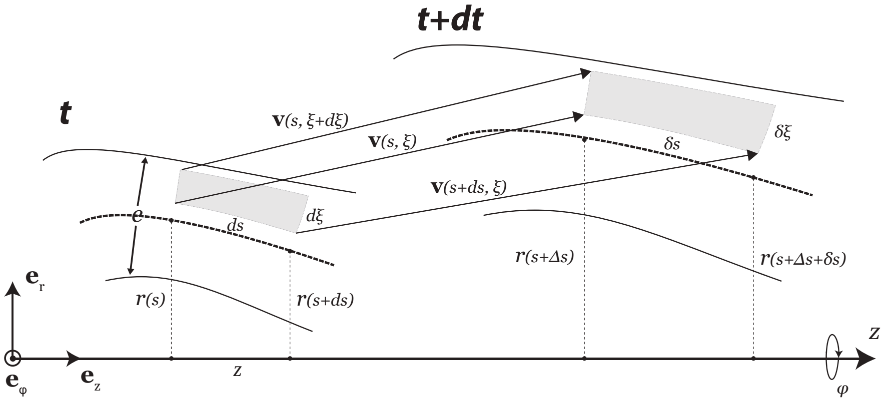

Figure 2.B.1: Deformation of a piece of the thin shell: volume conservation

By vector summation we obtain

$$[\mathbf{v}(s + ds, \xi, t) - \mathbf{v}(s, \xi, t)] = \delta s(s, \xi)\, \mathbf{t}(s + \Delta s, t + dt) - ds\, \mathbf{t}(s, t)\,.$$

We project this equation on $\mathbf{t}(s, t)$ to get

$$\delta s(s, \xi) \approx ds \left(1 + \mathbf{t}.\frac{\partial \mathbf{v}}{\partial s}(s, \xi, t)\, dt\right)\,.$$

We apply the same procedure to the transverse coordinate:

$$[\mathbf{v}(s, \xi + d\xi, t) - \mathbf{v}(s, \xi, t)] = \delta\xi(s, \xi)\, \mathbf{n}(s + \Delta s, t + dt) - d\xi\, \mathbf{n}(s, t)\,,$$

equation that we project on $\mathbf{n}(s, t)$ to get

$$\delta\xi(s, \xi) \approx d\xi \left(1 + \mathbf{n}.\frac{\partial \mathbf{v}}{\partial \xi}(s, \xi, t)\, dt\right)\,.$$

We calculate δr

$$\delta r(s, \xi) = r(s + \Delta s, \xi + \Delta\xi, t + dt) - r(s, \xi, t) = \mathbf{e}_r.\mathbf{v}(s, \xi, t)\, dt\,.$$

Volume conservation reads then $2\pi r\, d\xi\, ds = 2\pi(r + \delta r)\, \delta\xi\, \delta s$, which yields at first order in dt

$$0 = \mathbf{e}_r.\mathbf{v} + r\left(\mathbf{t}.\frac{\partial \mathbf{v}}{\partial s} + \mathbf{n}.\frac{\partial \mathbf{v}}{\partial \xi}\right) \tag{2.136}$$

Using the decomposition of $\mathbf{v}(s, \xi)$ on the local Frenet basis (2.12) we can rewrite the local volume conservation as

$$0 = -v_t \cos\psi + v_n \sin\psi + r\left(\frac{\partial v_t}{\partial s} + v_n \frac{\partial \psi}{\partial s} + \frac{\partial v_n}{\partial \xi}\right) \tag{2.137}$$

2.C Divergence of the axisymmetric stress tensor in a curvilinear Frenet frame

We derive below the formula for the divergence of the stress tensor in the Frenet frame $(\mathbf{t}, \mathbf{n}, \mathbf{e}_\varphi)$.

In axisymmetric geometry, the stress tensor, decomposed onto the Frenet frame, reduces to

$$\boldsymbol{\sigma} = \sigma_{tt}\, \mathbf{t} \otimes \mathbf{t} + \sigma_{nn}\, \mathbf{n} \otimes \mathbf{n} + \sigma_{tn}\, (\mathbf{t} \otimes \mathbf{n} + \mathbf{n} \otimes \mathbf{t}) + \sigma_{\varphi\varphi}\, \mathbf{e}_\varphi \otimes \mathbf{e}_\varphi\,. \tag{2.138}$$

The divergence of the stress tensor σ reads formally

$$\boldsymbol{\nabla} \cdot \boldsymbol{\sigma} = \underset{①}{\left(\frac{\partial \boldsymbol{\sigma}}{\partial s}\right)} \cdot \mathbf{t} + \underset{②}{\left(\frac{\partial \boldsymbol{\sigma}}{\partial \xi}\right)} \cdot \mathbf{n} + \underset{③}{\left(\frac{1}{r}\frac{\partial \boldsymbol{\sigma}}{\partial \varphi}\right)} \cdot \mathbf{e}_\varphi\,.$$

We evaluate the divergence term by term

$$① = \frac{\partial \sigma_{tt}}{\partial s}\,\mathbf{t} + \sigma_{tt}\frac{\partial \psi}{\partial n}\,\mathbf{n} - \sigma_{nn}\frac{\partial \psi}{\partial n}\,\mathbf{n} + \frac{\partial \sigma_{tn}}{\partial s}\,\mathbf{n}\,,$$

$$③ = \frac{\partial \sigma_{nn}}{\partial \xi}\,\mathbf{n} + \frac{\partial \sigma_{tn}}{\partial \xi}\,\mathbf{t}\,,$$

$$② = -\frac{\cos\psi}{r}\sigma_{tt}\,\mathbf{t} + \sigma_{\varphi\varphi}\left(\frac{\cos\psi}{r}\,\mathbf{t} - \frac{\sin\psi}{r}\,\mathbf{n}\right) + \sigma_{nn}\frac{\sin\psi}{r}\,\mathbf{n} + \sigma_{tn}\left(\frac{\sin\psi}{r}\,\mathbf{t} - \frac{\cos\psi}{r}\,\mathbf{n}\right)\,.$$

The projection of the local mechanical equilibrium $\boldsymbol{\nabla} \cdot \boldsymbol{\sigma}$ on the Frenet frame reads finally

$$0 = \frac{\partial \sigma_{tt}}{\partial s} + \cos\psi\frac{\sigma_{\varphi\varphi} - \sigma_{tt}}{r} + \frac{\sin\psi}{r}\sigma_{tn} + \frac{\partial \sigma_{tn}}{\partial \xi}\,, \tag{2.140a}$$

$$0 = (\sigma_{tt} - \sigma_{nn})\,\frac{\partial \psi}{\partial s} + \sin\psi\frac{\sigma_{nn} - \sigma_{\varphi\varphi}}{r} + \frac{\partial \sigma_{tn}}{\partial s} - \frac{\cos\psi}{r}\sigma_{tn} + \frac{\partial \sigma_{nn}}{\partial \xi}\,. \tag{2.140b}$$

2.D Spherical harmonics and Legendre polynomials

2.D.1 Spherical Harmonics

Spherical harmonics are the angular portion of the fundamental solutions to the Laplace's equation in spherical coordinate

$$\boldsymbol{\nabla}^2\psi(r,\theta,\varphi) = 0\,, \tag{2.141}$$

where the Laplacian operator is spherical coordinates reads

$$\boldsymbol{\nabla}^2 = \frac{1}{r^2}\frac{\partial}{\partial r}\left(r^2\frac{\partial}{\partial r}\right) + \frac{1}{r^2\sin^2\theta}\frac{\partial}{\partial\theta}\left(\sin\theta\frac{\partial}{\partial\theta}\right) + \frac{1}{r^2\sin^2\theta}\frac{\partial}{\partial\varphi^2}\,. \tag{2.142}$$

More specifically the general solution of Laplace's equation is a sum of functions

$$\psi_{lm}(r,\theta,\varphi) = \left(A_{lm}r^l + B_{lm}r^{-(l+1)}\right)\mathcal{Y}_{lm}(\theta,\phi)\,,$$

where $l \geq 0$ and m are two integers verifying $-l \leq m \leq l$.

Problems close to the spherical geometry are therefore generally treated with spherical harmonics $\mathcal{Y}_{lm}(\theta,\phi)$. The normalized spherical harmonics $\mathcal{Y}_{lm}$ of degree l and order m is the product of a complex exponential and an associated Legendre polynomials

$$\mathcal{Y}_{lm}(\theta,\phi) = \sqrt{\frac{2l+1}{4\pi}\frac{(l-m)!}{(l+m)!}}\,\mathcal{P}_{lm}(\cos\theta)\,e^{im\varphi}\,.$$

We will not discuss in details the properties of spherical harmonics, but on the contrary present without justification important results and relations.

Spherical harmonics form an orthogonal basis

$$\int_{\theta=0}^{\pi}\int_{\varphi=0}^{2\pi}\mathcal{Y}_{lm}\mathcal{Y}^*_{l'm'}\,d\Omega = \delta_{ll'}\delta_{mm'}\,. \tag{2.143}$$

where δ_{ij} is the Kronecker delta and $d\Omega = \sin\theta d\varphi d\theta$ a solid angle infinitesimal element.

One can therefore expand any real square-integrable function $f(\theta,\varphi)$ in spherical harmonics

$$f(\theta,\varphi) = \sum_{l=0}^{\infty}\sum_{m=-l}^{l} f_{lm}\,\mathcal{Y}_{lm}(\theta,\varphi)\,. \tag{2.144}$$

Spherical harmonics as defined above are normalized

$$\int\left|\mathcal{Y}_{lm}\right|^2 d\Omega = 1\,, \tag{2.145}$$

and the coefficients f_{lm} of the expansion can therefore be calculated as

$$f_{lm} = \int f(\theta,\varphi)\,\mathcal{Y}_{lm}(\theta,\varphi)\,d\Omega. \tag{2.146}$$

Two important relations are the closure relation

$$\int d\Omega\,|u(\Omega)|^2 = \sum_{l\geq 0}\sum_{m=-l}^{l} |u_{lm}|^2\,, \tag{2.147}$$

and the eigenvalue equation

$$\boldsymbol{\nabla}_\perp^2 \mathcal{Y}_{lm} = -l(l+1)\,\mathcal{Y}_{lm}\,, \tag{2.148}$$

where the operator $\boldsymbol{\nabla}_\perp$ is the gradient in spherical coordinates, restricted to the variables (θ,φ)

$$\boldsymbol{\nabla}_\perp \equiv \mathbf{e}_\theta \frac{\partial}{\partial\theta} + \frac{\mathbf{e}_\varphi}{\sin\theta}\frac{\partial}{\partial\varphi} \tag{2.149}$$

2.D.2 Legendre polynomials

We sum up here useful relations concerning Legendre polynomials, functions that naturally emerge in problems with spherical geometry.

In spherical problems with symmetry of revolution, only the spherical harmonics with $m=0$ contribute. They are called cylindrical harmonics and do not depend on the azimuthal angle φ. They reduce to simple Legendre polynomials of degree l of $\cos\theta$: $\mathcal{Y}_l(\theta) = \sqrt{\frac{2l+1}{4\pi}}\mathcal{P}_l(\cos\theta)$.

The polar representation $r = r_0 + r_1\,\mathcal{Y}_l(\theta)$ of the four first cylindrical harmonics $\mathcal{Y}_1$, $\mathcal{Y}_2$ and $\mathcal{Y}_3$ reveal their symmetry on fig. 2.D.1

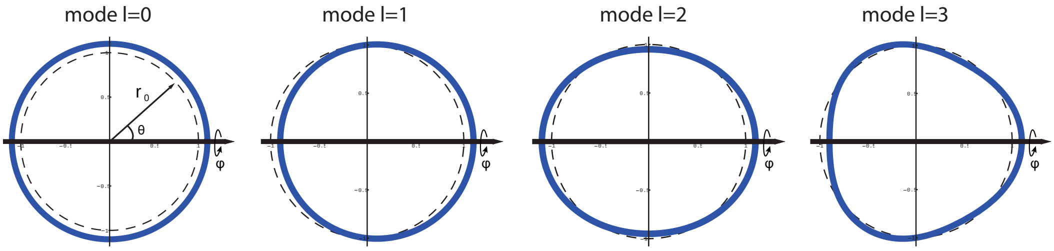

Figure 2.D.1: Polar representation $r = r_0 + r_1\,\mathcal{Y}_l(\theta)$ ($r_1 = 0.1\,r_0$) of the four first cylindrical harmonics. The revolution axis is horizontal. *Mode l=0*: isotropic expansion; *Mode l=1*: axial translation; *Mode l=2 and 3*: deformations with symmetry of order 2 and 3.

The serie of Legendre polynomials $\mathcal{P}_l(x)$ is defined as the solution of the Legendre's differential equation

$$\frac{d}{dx}\left[(1-x^2)\frac{d}{dx}\mathcal{P}_l(x)\right] + l\,(l+1)\,\mathcal{P}_l(x) = 0 \qquad \text{for } 0\leq l\leq\infty\,,$$

and forms an orthogonal basis

$$\int_{-1}^{1} \mathcal{P}_l(x)\mathcal{P}_k(x)dx = \frac{2\delta_{kl}}{2l+1}$$

or equivalently

$$\int_0^{\pi} \mathcal{P}_l\left(\cos\theta\right)\mathcal{P}_k\left(\cos\theta\right)\,\sin\theta d\theta = \frac{2\delta_{kl}}{2l+1}$$

Any function $f(\theta)$ $\mathcal{C}^{\infty}$ can therefore be decomposed as

$$f(\theta) = \sum_{l=0}^{\infty} C_l\,\mathcal{P}_l\left(\cos\theta\right)\,, \tag{2.150}$$

where the decomposition coefficients C_l are given by

$$C_l = \frac{2l+1}{2}\int_0^{\pi} f(\theta)\mathcal{P}_l\left(\cos\theta\right)\,\sin\theta d\theta\,. \tag{2.151}$$

We use also the serie of Gegenbauer polynomials, which constitutes an orthogonal basis as well and can be defined from Legendre polynomials as

$$\mathcal{I}_{l+1} = \frac{\mathcal{P}_{l-1} - \mathcal{P}_{l+1}}{2l+1}\,. \tag{2.152}$$

We sum up below the useful relations between these two families of polynomials. We use them in section 2.1.2.2 to obtain the system of equations (2.52) relating coefficients of Legendre and Gegenbauer series decomposition from the continuous differential equations (2.49).

$$\partial_\theta\left[\mathcal{P}_l(\cos\theta)\right] = -l\left(l+1\right)\frac{\mathcal{I}_{l+1}(\cos\theta))}{\sin\theta}\,, \tag{2.153a}$$

$$\left\{\partial_\theta^2 + \cot\theta\partial_\theta\right\}\left[\mathcal{P}_l(\cos\theta)\right] = -l(l+1)\,\mathcal{P}_l(\cos\theta)\,, \tag{2.153b}$$

$$\partial_\theta\left[\mathcal{I}_{l+1}(\cos\theta)\right] = \sin\theta\,\mathcal{P}_l(\cos\theta)\,, \tag{2.153c}$$

$$\left\{\partial_\theta + \cot\theta\right\}\left[\frac{\mathcal{I}_{l+1}(\cos\theta)}{\sin\theta}\right] = \mathcal{P}_l(\cos\theta)\,, \tag{2.153d}$$

$$\left\{\partial_\theta^2 + \cot\theta\partial_\theta - \cot^2\theta\right\}\left[\frac{\mathcal{I}_{l+1}(\cos\theta)}{\sin\theta}\right] = \left[1 - l\left(l+1\right)\right]\frac{\mathcal{I}_{l+1}(\cos\theta)}{\sin\theta}\,. \tag{2.153e}$$

2.E Visco-active membrane subjected to an axial force

An axial force f can be added in our membrane model by considering that its surface is not a closed in the integrated formulation (2.42) of the equations of motion.

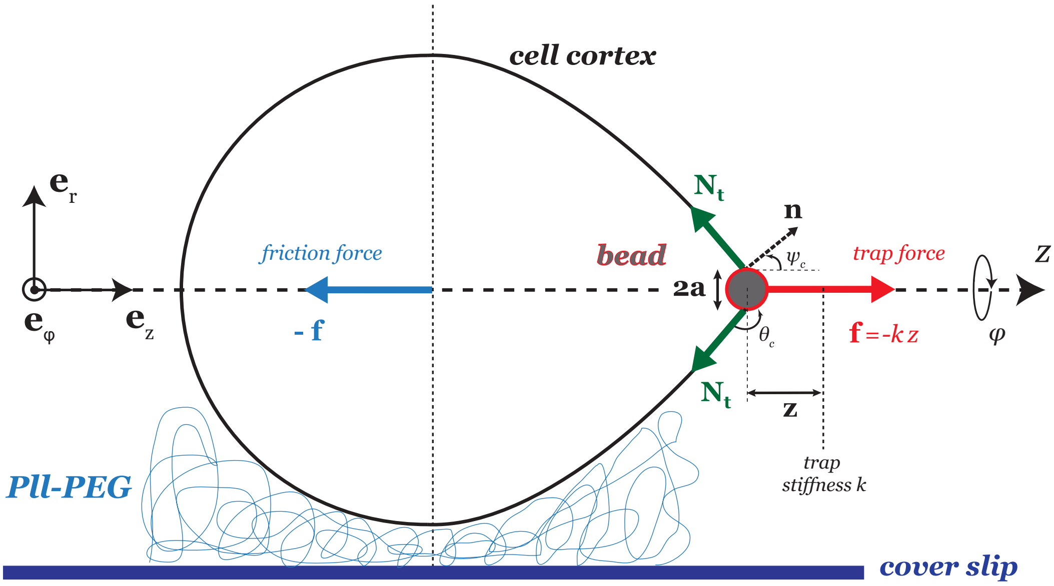

Figure 2.E.1: Sketch of the polarized cell submitted to an axial force $\mathbf{f} = -kx\,\mathbf{e}_z$ from a bead trapped in an optical tweezer of stiffness k. The cell cortex connects the bead of radius a with a contact angle θ_c. The mechanical balance requires an opposite axial force $-\mathbf{f}$ on the cell, that is exerted as a friction form the Pll-PEG cushion on which lies the cell.

If we assume that the membrane connects the bead of radius a with a contact angle $\theta_c = \frac{\pi}{2} + \psi_c$, as shown on fig. 2.E.1. The equilibrium of the bead along $\mathbf{e}_\varphi$ reads therefore $2\pi a N_t \sin\psi_c = f + \Delta P \pi a^2$. Using the general solution (2.41) for the tangential tension N_t, we get $f + \Delta P \pi a^2 = 2\pi\left(B + \Delta P \frac{a^2}{e}\right)$, which leads immediately to $B = \frac{f}{2\pi}$, and therefore

$$N_t = \frac{\Delta P + f/\pi r^2}{2\kappa_\varphi}\,, \tag{2.154a}$$

$$N_\varphi = \frac{\Delta P + f/\pi r^2}{2\kappa_\varphi}\left(2 - \frac{\kappa_t}{\kappa_\varphi}\right)\,, \tag{2.154b}$$

which is similar to the formula proposed in [Berk 1991] without calculation details.

2.F Cytoplasmic pressure force does not work when volume is conserved

We start from the force balance on the membrane eq. (2.68)

$$\boldsymbol{\nabla}\cdot\underline{\underline{\mathbf{N}}}+P\,\mathbf{n}=\mathbf{0}\,, \tag{2.68}$$

We formally derive the equation of dynamics in weak form: for any virtual motion $\hat{\mathbf{x}}(S,t)$ of the membrane

$$\int dA\;\left\{\boldsymbol{\nabla}\cdot\underline{\underline{\mathbf{N}}}+P\,\mathbf{n}\right\}\cdot\hat{\mathbf{x}}=0 \tag{2.155a}$$

Simple algebra gives

$$\boldsymbol{\nabla}\cdot\left(\underline{\underline{\mathbf{N}}}\cdot\hat{\mathbf{x}}\right)=\underline{\underline{\mathbf{N}}}:\underline{\underline{\boldsymbol{\nabla}\hat{\mathbf{x}}}}+\left(\boldsymbol{\nabla}\cdot\underline{\underline{\mathbf{N}}}\right)\cdot\hat{\mathbf{x}} \tag{2.155b}$$

We can choose freely the virtual motion so that it vanishes on C :

$$\int dA\,\boldsymbol{\nabla}\cdot\left(\underline{\underline{\mathbf{N}}}\cdot\hat{\mathbf{x}}\right)=\oint_C \mathbf{d}\ell\cdot\left(\underline{\underline{\mathbf{N}}}\cdot\hat{\mathbf{x}}\right)=0 \tag{2.155c}$$

We therefore deduce the equations of motion in weak form

$$-\int dA\,\underline{\underline{\mathbf{N}}}:\underline{\underline{\boldsymbol{\nabla}\hat{\mathbf{x}}}}+\int dA\,P\mathbf{n}\cdot\hat{\mathbf{x}}=0 \tag{2.156}$$

We remark that by Green-Ostrogradski on a closed membrane

$$\oint\left(P\hat{\underline{x}}\right)\cdot d\mathbf{A}=\iiint\boldsymbol{\nabla}\cdot\left(P\hat{\mathbf{x}}\right)\,dV=\iiint\left(\boldsymbol{\nabla}P\cdot\hat{\mathbf{x}}+P\boldsymbol{\nabla}\cdot\hat{\mathbf{x}}\right)\,dV \tag{2.157}$$

Since P is uniform $\boldsymbol{\nabla}P=\mathbf{0}$. For the real motion $\hat{\mathbf{x}}=\mathbf{u}$, the work of internal pressure tends to 0 when the fluid becomes incompressible $\boldsymbol{\nabla}\cdot\mathbf{u}=0$:

$$\oint\left(P\hat{\mathbf{x}}\right)\cdot d\mathbf{A}=P\iiint\boldsymbol{\nabla}\cdot\mathbf{u}\,dV=0 \tag{2.158}$$

Numerically, we show on fig. 2.F.1 that for a bulk modulus $K\gg 1$, volume is nearly conserved and the work of cytoplasmic pressure vanishes.

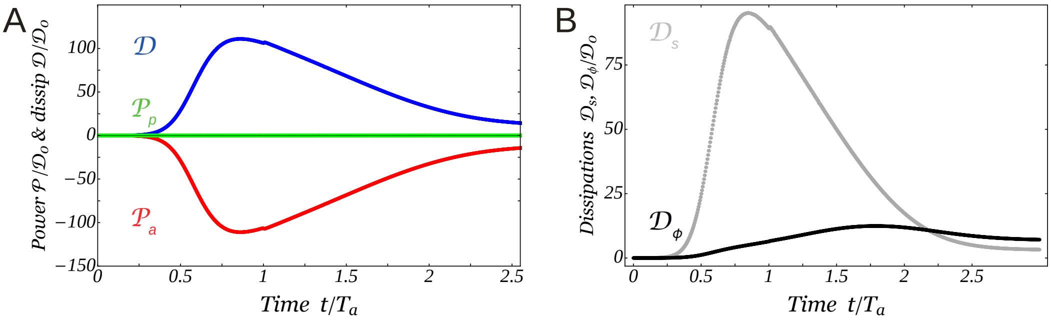

Figure 2.F.1: Active and dissipated power corresponding to fig. 2.22. *(A)* Plot of the time evolution of the total dissipation $\mathcal{D}$, of the work of active forces $\mathcal{P}_a$ in the membrane and of the work of cytoplasmic pressure $\mathcal{P}_p$, rescaled by $\mathcal{D}_0 = 4\pi R_0^2 N_0^a / e_0 \eta$. We make the cytoplasm nearly incompressible by assigning a high value of its bulk modulus $K = 250$. As a result it does not store any elastic energy and its work vanishes. The work of active forces $\mathcal{P}_a$ in the membrane is therefore fully dissipated by viscous effects $\mathcal{D}$. The work of active forces increases in the transient regime and then decreases almost linearly in time and finally relaxes exponentially towards a plateau above 0. We find again the successive phases of constriction described in fig. 2.22 and we confirm that maintaining a signal at equator sustains a cortical flow after constriction completion that maintains dissipation non-zero. *(B)* Plot of the time evolution of axial and azimuthal components $\mathcal{D}_s$ and $\mathcal{D}_\varphi$ of the viscous dissipation. The axial components reveals the dissipation due to cortical flows whereas the azimuthal component is essentially due to the furrow constriction. We observe that most of the dissipation comes from cortical flows occuring from the poles to the equator, except in the last phase of constriction for $t/T_a \gtrsim 2.5$ where the cortical flows decrease significantly.

2.G Table of the numerical parameters used for cytokinesis figures.

Fig(s).	**Radius** R_0	**Signal amplitude** $\delta\zeta^\infty$	**Signal width** w/R_0	**Depol. rate** $k_d\,T_a$	**Bulk mod.** K
figs. 2.21 and 2.22 figs. 2.23 to 2.25 fig. 2.27 *(Right)* fig. 2.29	1	75	0.1	40	250
fig. 2.26 *B* and *A* *(inset)*	1	❶: 10 ❷: 25 ❸: 40 ❹: 50 ❺: 75 ❻: 100	0.1	40	250
fig. 2.26 *B* *(diagram)*	1	0 to 81 by 1	0.1	40	250
figs. 2.30 and 2.31	1	75	0.1	①: 30 ②: 40 ③: 80	250
fig. 2.32	(a): 0.5 (b): 1 (c): 2 (d): 4	75	(a): 0.1 (b): 0.2 (c): 0.3 (d): 0.4	40	250

Table 2.G.1: Table of the numerical parameters used for generating the figures (except for code validation, see sections 2.2.2.5 and 2.2.2.5). The value of following parameters remains unchanged: $e_0/R_0 = 0.02$, $v_p = e_0\,k_d$, $n_0 = 501$.

Part II

Active fluctuations of the red-blood cell membrane

Chapter 3

Introduction: the RBC cell membrane and cytoskeleton

Contents

3.1 The red blood cell, structure and functions

3.1.1 Structure

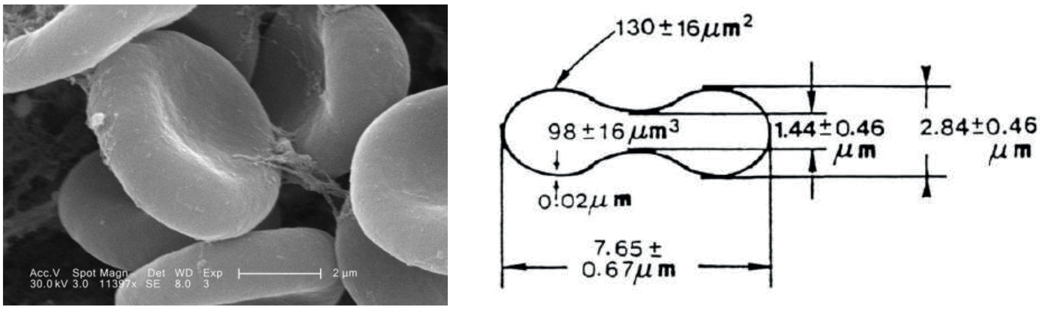

Figure 3.1: **(Left)** Scanning electron micrograph of human erythrocytes. **(Right)** Typical dimensions of the human red blood cell. (Adapted from [Evans 1972])

Human red-blood cells (RBCs), or erythrocytes, have a distinguishable biconcave disk shape (or discocyte) represented in fig. 3.1 (Left). Much thinner than most other human cells, they have a diameter of 6-8 μm and a thickness of about $2\mu m$ (see fig. 3.1 (Right)). Anucleated, they do not synthesize proteins nor divide and therefore need only a very reduced metabolism. This metabolism, anaerobic, produces ATP in the absence of mitochondria. RBCs do not actively change shape during their life cycle of about 100 days. However they have a fascinating ability to deform in order to pass through small capillaries of μm size, recovering their initial shape afterwards. These noteworthy mechanical properties rely on their plasma membrane and a simplified membrane skeleton, composed of spectrin filaments. Their simplicity have made RBCs an interesting model system for biophysicists in between passive vesicles and sophisticated nucleated cells. A large theoretical and experimental literature has been produced over the last decades to explain the shape and fluctuations of their surface. We try to give here a short – and necessarily partial – overview of the major results in the field.

The RBC membrane is composed of a lipid bilayer, under which is anchored a bidimensional network of spectrin filaments. Spectrin filaments constitute the only cytoskeleton component in RBCs, as shown in fig. 3.3

3.1.1.1 Lipid bilayer and multiproteins complexes

The inner volume of the RBC is delimited by a lipid-bilayer composed of hundreds of different lipid species, but mainly of phospholipids (62,7%). Phospholipids are amphiphilic molecules: they are made of a polar hydrophilic head and a hydrophobic apolar tail (see fig. 3.2 A). Depending on the relative sizes of the head relative to the tail, amphiphilic molecules spontaneoulsy self-organize into lipid-bilayers or micelles in aqueous solutions to minimize the exposure of their apolar tail to water molecules (see fig. 3.2 B). The RBC lipid bilayer is about 5-6nm thick and is a

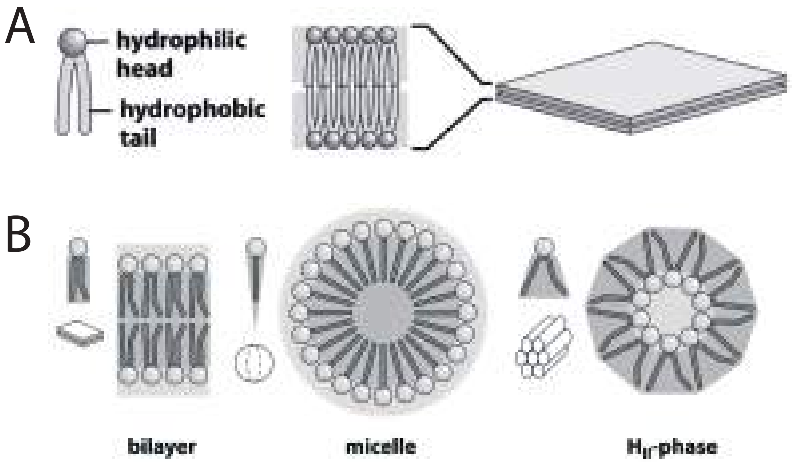

Figure 3.2: **A** Schematic illustration of amphiphilic molecules and their possible arrangement into bilayers. **B** Coarse-grained respresentation of different lipid geometries and their effect on the large scale arrangement of lipids. (Adapted from [Phillips 2008])

bidimensional fluid, in which embedded proteins can diffuse[1]. Half of the RBC membrane mass is occupied by a hundred of different proteins that can be classified into two main types: the transmembrane proteins that cross through the lipid bilayer and peripheral proteins that lie on the membrane surface and are linked to the inner membrane via transmembrane proteins.

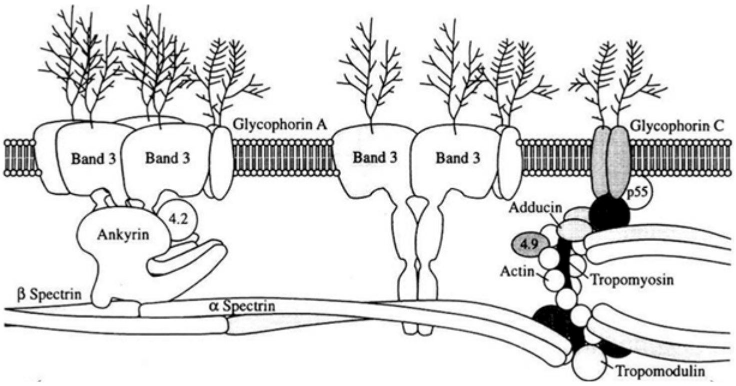

Figure 3.3: Schematic model of the red blood cell membrane, showing the major proteins involved in the two anchor points structures of the spectrin membrane skeleton to the lipid bilayer. (Adapted from [Gallagher 2005])

Band 3 is the most abundant transmembrane protein in the RBC membrane. It transports negative ions Cl^- and ${HCO_3}^-$ across the membrane and is a component of the multiprotein complex junction 4.1 R. The other principal transmembrane proteins are: glycophorins A and C (GPA, GPC) and p55. Recent work [Mohandas 2008] has shown that these proteins are assembled into two multiprotein

---

[1] Out of plane deformations are however elastic-like and are described in section 3.2

complexes. The first, called the 4.1 R complex, comprises the three principal components of the skeletal network junctions (spectrin, actin and 4.1 R), together with tropomyosin, tropomodulin and the transmembrane proteins GPC, band 3 and p_{55} as shown on figs. 3.3 and 3.3.

The second multiprotein complex is commonly called ankyrin R-based complex and contains ankyrin R, band 3 and GPA, protein 4.2. Both ankyrin R- and 4.1 R-based complexes participate in linking the membrane skeleton to the lipid-bilayer as shown on fig. 3.3 and thereby contribute to the mechanical property of the RBC membrane.

3.1.1.2 Spectrin cytoskeleton

The major skeletal proteins are spectrin filaments (25% of the protein mass). They are linked to each other via the 4.1 R complex junctions and give the red cell membrane its strength and integrity.

The spectrin protein is composed of two α- and β-helices forming a flexible filament. The two α- and β- chains form a dimer, of contour-length $100nm$. Dimers self-associate into tetramers, of double contour length $200nm$. The spectrin tetramers display elastic properties upon extension [Paramore 2006] and their resting length is of the order of $70 - 80nm$.

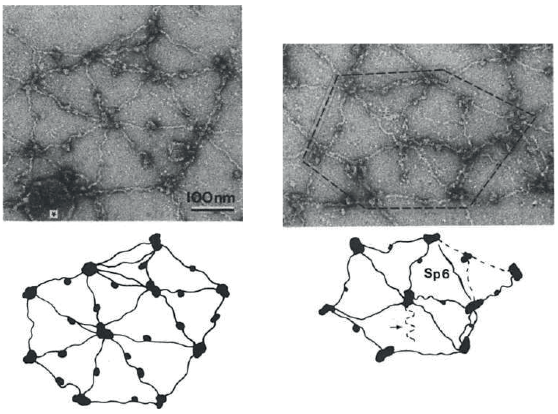

Figure 3.4: Electron microscopy images of the RBC membrane skeleton, showing spectrin filaments and anchor points to the bilayer (Band 3). Junction coordination can be imperfect (Left: Sp5 and Sp7) and filaments can have a free end (Right). (Adapted from [Liu 1987])

Multiple tetramers interact at their tail ends with actin protofilaments stabilized by tropomyosin, tropomodulin and adducin. Protein 4.1 R, which associates to the transmembrane protein glycophorin C, interacts at the actin binding domain and increases the affinity of the spectrin-actin binding. These junctions are connected to an average of six tetramers, thereby forming a triangular meshwork of spectrin filaments, as confirmed by high resolution electron microscopy of the skeleton (see fig. 3.4). The meshwork can however be imperfect, with penta- and heptahedrally coordinated junctions and free spectrin ends.

The tetramers are also linked by ankyrin to the cytoplasmic domain of the transmembrane protein band 3. Protein 4.2 binds to band 3 at the same position and may enhance the ankyrin-band 3 interaction.

The phosporylation of these two anchor complexes has been shown to weaken the junction of the cytoskeleton to the lipid-bilayer (see fig. 3.5), thereby decreasing the mechanical strength of the RBC membrane [Eder 1986, Boivin 1988, Danilov 1990, Subrahmanyam 1991, Manno 2005, Gauthier 2011].

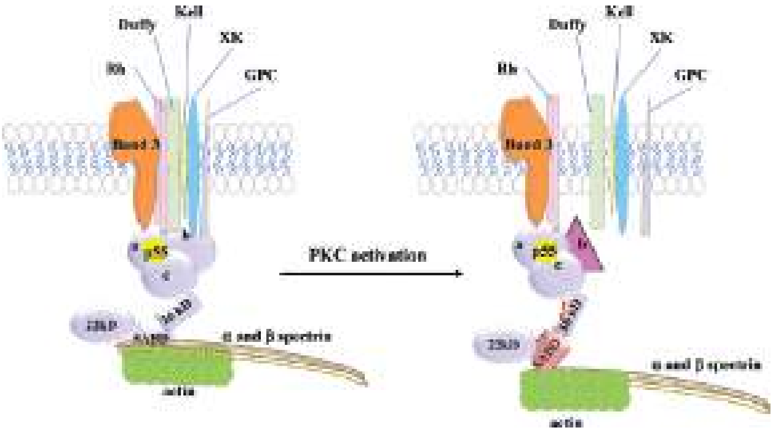

Figure 3.5: 4.1 R multiprotein complex composition and actual model for the effect of its phosphorylation by the protein kinase C (PKC). The phosphorylation of the 10 kDa spectrin-actin domain suppresses the ability of 4.1 R to bind the transmembrane proteins GPC, Duffy, XK and Kell and affects the stability of the ternary spectrin-actin-4.1 R complex, thereby weakening the affinity of 4.1 R for β-spectrin. (Adapted from [Gauthier 2011])

In the following we will adopt an idealized picture of the membrane skeleton and its anchoring in the membrane, by considering it as a perfect triangular network where filaments ends are able to disconnect from the junction 4.1 R by direct phosphorylation by an ATP molecule as represented in fig. 3.6.

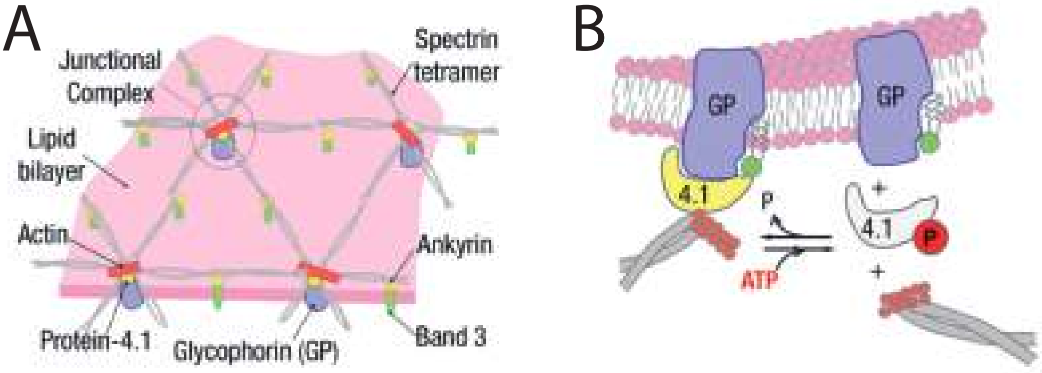

Figure 3.6: Idealized spectrin network organization and junction to the lipid bilayer. **(A)** Illustration of the major proteins anchoring the spectrin cytoskeleton to the lipid bilayer. **(B)** Putative model of 4.1 R junction weakening by phosphorylation. (Adapted from [Park 2010])

3.1.2 Cytoplasmic composition, function and diseases

The erythrocyte is a differentiated cell in charge of the transport of oxygen from the lungs to the body tissues via the blood flow through the circulatory system. This transport is mediated by hemoglobin, that gives the blood its red color. Deprived of organelles like mitochondria or Golgi apparatus, and lacking any cytoplasmic cytoskeleton, the erythrocyte cytoplasm is essentially a solution of hemoglobin, which can be considered as a Newtonian fluid of viscosity $\eta \approx 6.10^{-3}\, Pa.s$.

Several diseases are associated with defective spectrin or defective attachment of the spectrin skeleton to the lipid bilayer, such as hereditary elliptocytosis [Mohandas 1994], which leads generally lead to anemia.

3.2 Mechanics of the membrane and spectrin skeleton

3.2.1 Shape of RBC: theoretical approaches

Shape transitions in the red cell are essentiall due to changes in the composition or the structure of the lipid membrane or the underlying spectrin cytoskeleton.

Bidimensional elasticity

The composite membrane of the red blood cell is about 10 nanometers thick whereas other dimensions are of the order of the micrometer. It can therefore be considered as a bidimensional object. Any deformation of a bidimensional object is the superposition of three elementary deformations: isotropic extension or compression, pure bending and pure shearing as depicted on fig. 3.1.

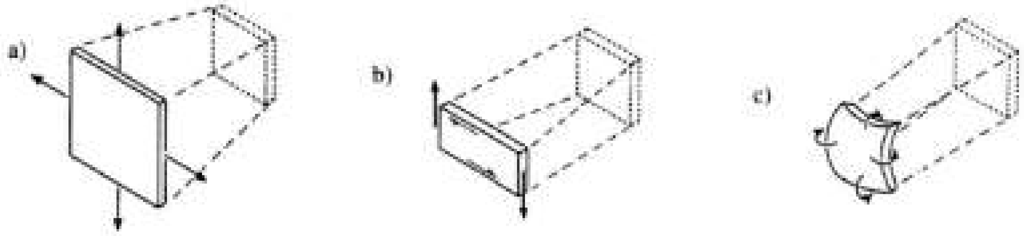

Figure 3.1: Skematical representation of the three independent modes of deformation: **a)** isotropic extension, **b)** pure bending and **c)** pure shear. (Adapted from [Evans 1987])

A pure extension corresponds to an area dilation without shape deformation. The corresponding variation of energy is characterized by an extension modulus K_c of dimension $\frac{energy}{surface}$. One can write the surface density of extensional energy as

$$h_{\text{extension}} = \frac{1}{2} K_c \left(\frac{\Delta A}{A} \right)^2 , \tag{3.1}$$

where A is the surface considered and ΔA its the variation. The extension generates a tension in the membrane that is generally denoted σ.

A pure shear deformation corresponds on the contrary to a shape deformation without surface change. It is measured by a shear elastic modulus μ which has the same dimension as K_c. The lipid-bilayer being fluid, shear elasticity can only come from the underlying spectrin cytoskeleton elasticity. The surface density of energy can be written

$$h_{\text{shearing}} = \frac{1}{2} \mu \left(\lambda^2 + \lambda^{-2} - 2 \right) , \tag{3.2}$$

where the strain is measured by an the elongation ratio $\lambda = (L_0 + \delta L)/L_0$. Note that for a perfect and uniform triangular network of springs, the extension and shear modulus are both simply proportional to the spring stiffness k, as proved by [Kantor 1987]

$$K = 2\mu = \frac{\sqrt{3}}{2} k \, . \tag{3.3}$$

Finally, pure bending deformation corresponds to a change in the curvature tensor without any surface strain in any direction. The associated energy variation is characterized by a bending modulus usually denoted κ and a Gaussian bending modulus κ_G, both having the dimension of an energy. It can be written

$$h_{\text{bending}} = \frac{\kappa}{2}(C - C_0)^2 + \kappa_G\, K\,, \tag{3.4}$$

where $C = 1/R_1 + 1/R_2$ is the mean local curvature of the surface, $K = 1/R_1R_2$ is the Gaussian curvature, given in terms of the two local principle radii of curvature R_1 and R_2 as shown on fig. 3.2. C_0 is the spontaneous curvature which describes the natural curvature of the surface in the relaxed state.

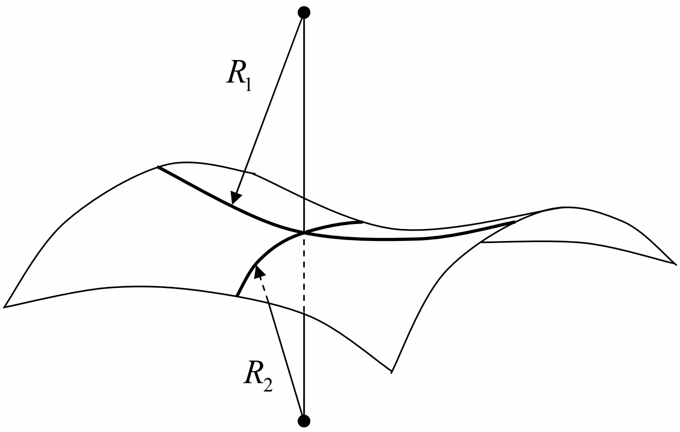

Figure 3.2: Principal radii of curvature R_1 and R_2 associated with one local position on the surface.

3.2.2 The Canham-Helfrich model

The first theories on the elastic energy of a lipid bilayer membrane have benn proposed independently by Canham [Canham 1970] and Helfrich [Helfrich 1973]

3.2.2.1 Bending energy for a closed lipid bilayer surface

Bending a lipid bilayer requires to push away polar heads of the external layer and to squeeze the heads of the internal layer, or conversely to generate a negative curvature. The bending energy κ associated to this deformation is generally of a few tens of $k_{\mathrm{B}}T$. Helfrich made an analogy between the lipid-bilayer an a smectic A liquid crystal of thickness twice that of the size of a lipid molecule [Helfrich 1973]. Based on the Frank-Oseen free energy density for uniaxial liquid crystals with the normal of the membrane as the director of the liquid crystal, Helfrich deduced the bending elasticity energy of the membrane as the sum of the bending density of energy exposed above

$$\mathcal{H}_\kappa = \int_{\mathcal{A}} h_{\text{bending}} dA = \int_{\mathcal{A}} \left[\frac{\kappa}{2}(C - C_0)^2 + \kappa_G\, K\right] dA\,, \tag{3.5}$$

where $\mathcal{A}$ is the lipid-bilayer surface. In this analogy κ and κ_G are equivalent, respectively, to the splay and saddle splay coefficients in the Frank-Oseen energy for liquid crystals [Frank 1958].

In the following we consider only lipid-bilayers with zero spontaneous curvature $C_0 = 0$. The Gaussian curvature term reduces to a constant for a closed surface, according to the Gauss-Bonnet theorem

$$\oint_{\mathcal{A}} \kappa_G \, K \, dA = 4\pi \, (1-g) \ , \tag{3.6}$$

where the genius g of the surface $\mathcal{A}$ is a constant and that depends only on the topology. It vanishes for a spherical topology for example. For a periodical planar topology, the Gaussian curvature term vanishes as well.

3.2.2.2 Surface tension

Stretching the lipids from one-another in a lipid-bilayer cost much energy and the membrane surface A remains approximately constant. It can however vary slightly under mechanical extensional force or with transverse fluctuations around its equilibrium value A_0. The energy required for extending the membrane surface reads

$$\mathcal{H}_\sigma = \int_{\mathcal{A}} dA h_{\text{extension}} = \frac{1}{2} K_c \left(\frac{\Delta A}{A}\right)^2 A_0 \, ,$$

which allows to define the membrane tension as

$$\sigma = \frac{d\mathcal{H}_\sigma}{dA} = K_c \frac{A - A_0}{A_0} \, . \tag{3.7}$$

3.2.2.3 Canham-Helfrich Hamiltonian

The Canham-Helfrich Hamiltonian is generally written as the sum of the bending and surface tension energies

$$\mathcal{H} = \mathcal{H}_\kappa + \mathcal{H}_\sigma = \int_{\mathcal{A}} \left\{ \frac{\kappa}{2} (C - C_0)^2 + \sigma \right\} dA \tag{3.8}$$

3.2.3 Area Difference Elasticity (ADE) model

The area difference model, suggested by [Sheetz 1974], proposes that different lipid composition between inner and outer leaflets of the plasma membrane induces a difference of area between them. The elastic stretching energy associated with this difference $\Delta A - \Delta A_0$ was combined by [Miao 1994] to the Helfrich energy 3.8, to lead to the so-called area-difference elasticity (ADE) model:

$$\mathcal{H}_{\text{ADE}} = \int_{\mathcal{A}} \left\{ \frac{\kappa}{2} (C - C_0)^2 + \sigma \right\} dA + \frac{\bar{\kappa}}{2} \frac{\pi}{A d^2} \left(\Delta A - \Delta A_0\right)^2 \ , \tag{3.9}$$

where d is the bilayer thickness, A is the membrane surface area, $\Delta A_0 = A_0^{\text{out}} - A_0^{\text{in}}$ is the differential area of the two leaflets in the relaxed state and $\bar{\kappa}$ the non-local bending moduli of the membrane. The ADE model has four different length scales R_A and R_V, defined as $A \equiv 4\pi R_A^2$ and $V \equiv \frac{4}{3}\pi R_V^3$, C_0^{-1} and $\Delta A_0/d$. One can re-scale these variables by R_A, thereby defining a reduced volume $v = \frac{V}{\frac{4}{3}\pi R_A^3}$, a reduced spontaneous curvature $c_0 = C_0 R_A$ and a reduced equilibrium area difference $\Delta a_0 = \frac{\Delta A_0}{2dR_A}$. The effects of spontaneous curvature and area difference elasticity can furthermore be combined into an effective differential area parameter

$$\Delta \bar{a}_0 = \Delta a_0 - \frac{c_0}{2\pi\xi}\,, \tag{3.10}$$

where $\xi = \frac{\bar{\kappa}}{\kappa}$.

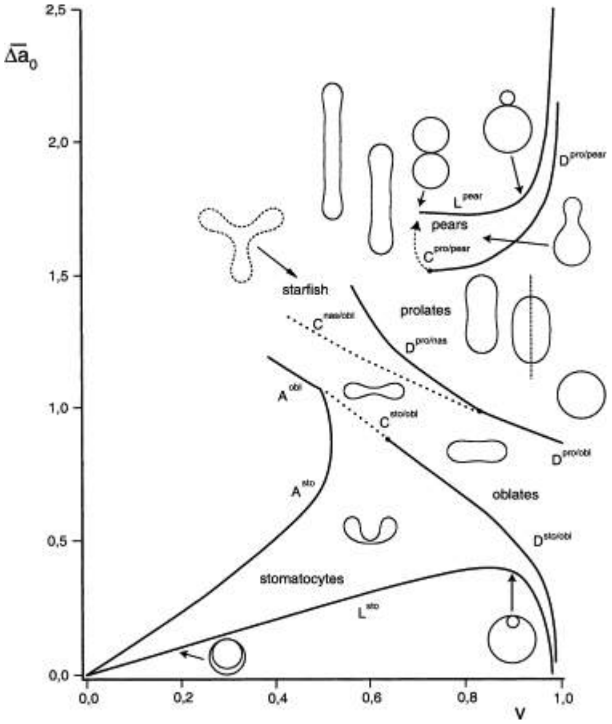

Figure 3.3: Phase diagram of vesicles shapes predicted by the ADE model, with a fixed ratio of bending moduli ξ. (Adapted from [Döbereiner 2000])

Using this model, it is possible to predict successfuly the morphology and vast zoology of shape changes of vesicles as shown on fig. 3.3. In particular the ADE model exhibits the stable discocyte shape of red blood cells, and can reproduce the transition to stomatocytes when $\Delta\bar{a}_0$ is decreased at fixed reduced volume. However it fails in reproducing the transition to echinocytes.

3.2.4 The need for spectrin shear elasticity

Red blood cells have a discocyte shape in physiological conditions. However they can exhibit different stable shapes if these conditions are changed: stomatocytes and echinocytes are two examples shown on fig. 3.4. ATP concentration has notably shown to control RBC shape [Sheetz 1977]. To explain the observed echinocyte shape of red blood cells, Lim et al. added the elastic effect of the spectrin skeleton. The contribution of the membrane skeleton is added to the ADE model as

$$\mathcal{H}_{\mathrm{RBC}} = \mathcal{H}_{\mathrm{ADE}} + \mathcal{H}_{\mathrm{skeleton}} \,, \tag{3.11a}$$

$$\mathcal{H}_{\mathrm{skeleton}} = \frac{K_\alpha}{2} \oint_{\mathcal{A}} dA \left(\alpha^2 + a_3\alpha^3 + a_4\alpha^4\right) + \mu \oint_{\mathcal{A}} dA \left(\beta + b_1\alpha\beta + b_2\beta^2\right) \,, \tag{3.11b}$$

where $\alpha = \frac{dA}{dA_0} - 1 = \lambda_1\lambda_2 - 1$ and $\beta = (\lambda_1 - \lambda_2)^2/2\lambda_1\lambda_2$ are the local area and strain invariants, with λ_1 and λ_2 the local principle stretches. K_α and μ are the linear elastic moduli for stretch and shear.

With this refined of version the RBC membrane mechanics, the sequence from stomatocyte to echinocyte can be reproduced as shown on fig. 3.4.

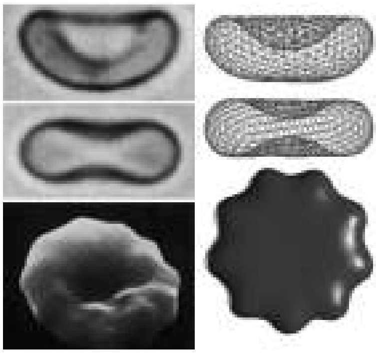

Figure 3.4: Representative shapes from the stomatocyte-discocyte-echinocyte sequence, experimental (Left) or calculated as mimimum of energy shape (Right). (Adapted from [Lim H. W. 2002])

3.3 Membrane fluctuations: theoretical and numerical models

3.3.1 Theoretical models of membrane fluctuations

It has been known from 1890 that red blood cells are flickering, when observed through an ordinary microscope. This flickering phenomenon is attributed to fluctuations of the red cell membrane in a direction transverse to the focal plane of the microscope. These fluctuations, of thermal and/or biochemical origin, have a typical amplitude of a few nm, which is very low compared the erythrocyte μm size. We can therefore assume that membrane elongations are in the linear regime of elasticity. The role of the fluctuations remains elusive, but they may prevent the red cell to adhere to blood vessels or other tissues by exerting a repulsive force of entropic origin, and could also facilitate the diffusion and hence the uniformization of transmembrane proteins within the membrane.

3.3.1.1 First quantitative study of RBC fluctuations

The first quantitative study of the RBC flickering effect has been achieved by Brochard and Lennon in 1975 [Brochard 1975]. They used a phase contrast microscope to measure the power density spectrum (PSD) of the thickness variation of the red cell $\left\langle \delta d^2(\omega) \right\rangle$ and its spatial correlations $P(\omega, \mathbf{R}_{12}) = \langle \delta d(\mathbf{r}_1, \omega) \delta d(\mathbf{r}_2, \omega) \rangle$, with $\mathbf{R}_{12} = \mathbf{r}_1 - \mathbf{r}_2$.

The frequency spectrum, reproduced in a log-log plot on fig. 3.1, displays a typical $-\frac{4}{3}$ slope behavior at high frequency:

$$\left\langle \delta d^2(\omega) \right\rangle \propto \omega^{-4/3} \qquad \text{for} \quad \omega/2\pi > 1\, Hz \tag{3.12}$$

A theoretical study is proposed to explain this behavior and considers the bending Helfrich energy as a starting point and supposes that the membrane tension vanishes. Using the fluctuation-dissipation theorem (see section 4.A) and considering the drag of the surrounding viscous fluid (see section 4.B), they recover the $-4/3$ power behavior of the dynamical fluctuation autocorrelation function. We detail in the next paragraph a calculation of the static fluctuation spectrum of a lipid-bilayer membrane in the same spirit. Experimentally, the fluctuations amplitude $\sqrt{\langle \delta d^2 \rangle}$ is found to be of the order of $80\, nm$, in good agreement with the linear response theory framework.

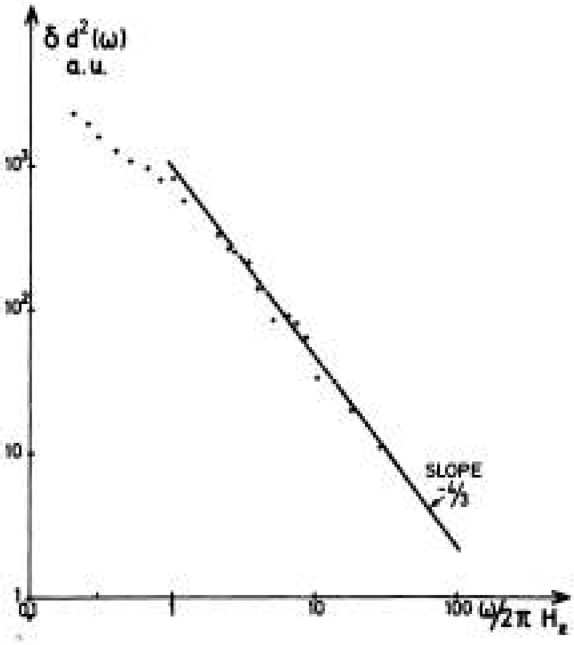

Figure 3.1: Power spectrum density of the thickness fluctuations of a human erythrocyte plotted in log-log scales. (Adapted from [Brochard 1975])

3.3.1.2 Fluctuation spectrum of lipid bilayer membranes

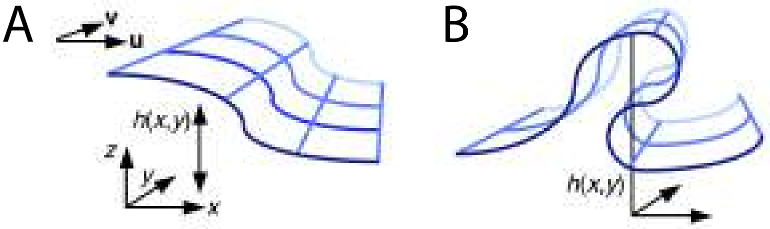

Figure 3.2: Monge representation: **A** A surface can be defined by a function $h(x, y)$ of Cartesian coordinates x, y. **B** Overhangs cannot be described in the the Monge representation. (Adapted from [Boal 2012])

We consider an Canham-Helfrich membrane in the Monge representation: the position vector of the bilayer mid-plane is given by $\Big(x, y, h(x, y)\Big) = \Big(\mathbf{r}, h(\mathbf{r})\Big)$ as represented in fig. 3.2. In the limit of small deformations $\big|\boldsymbol{\nabla} h(\mathbf{r})\big| \ll 1$, the membrane curvature is given approximately by $\boldsymbol{\nabla}^2 h = \Delta h$ and the membrane surface element by $dA = \sqrt{1 + (\boldsymbol{\nabla} h)^2 dxdy} \approx \Big(1 + \frac{1}{2}\big(\boldsymbol{\nabla} h(\mathbf{r})\big)^2\Big) d^2r$. We can therefore rewrite the Canham-Helfrich energy (3.8), ignoring the constant term, as

$$\mathcal{H} = \int_S d^2r \left[\frac{\kappa}{2}\big(\boldsymbol{\nabla} h^2(r)\big)^2 + \frac{\sigma}{2}\big(\boldsymbol{\nabla} h(r)\big)^2\right] , \tag{3.13}$$

where S is the membrane area projected on the plane (x, y). The bending modulus and surface tension define a characteristic length $\lambda_\sigma = \sqrt{\frac{\kappa}{\sigma}}$.

We consider a square piece of membrane with periodic boundary conditions and projected area $S = L^2$. It is more convenient to work in spatial Fourier space. The Fourier component $\tilde{h}_{\mathbf{q}}$ is defined as

$$\tilde{h}(q_x, q_y) = \tilde{h}_{\mathbf{q}} = \frac{1}{\sqrt{L}} \int_0^L dx\, e^{-iq_x x} \frac{1}{\sqrt{L}} \int_0^L dy\, e^{-iq_y y} h(x, y) = \frac{1}{\sqrt{S}} \int_0^S d^2 r\, h(\mathbf{r})\, e^{-i\mathbf{q}\cdot\mathbf{r}}\,, \tag{3.14a}$$

$$h(\mathbf{r}) = \frac{1}{\sqrt{S}} \sum_{\mathbf{q}} \tilde{h}_{\mathbf{q}}\, e^{i\mathbf{q}\cdot\mathbf{r}}\,. \tag{3.14b}$$

Inserting the previous equation (3.14b) in the Helfrich Hamiltonian (3.13) yields

$$\mathcal{H} = \frac{1}{2} \sum_{\mathbf{q}} \left(\sigma \mathbf{q}^2 + \kappa \mathbf{q}^4\right) \tilde{h}_{\mathbf{q}} \tilde{h}_{-\mathbf{q}}\,. \tag{3.15}$$

At thermal equilibrium, we can use the equipartition theorem that assigns an average energy $k_{\mathrm{B}}T/2$ energy for each Fourier mode and leads to the static fluctuation spectrum

$$\left\langle |\tilde{h}_{\mathbf{q}}|^2 \right\rangle = \frac{k_{\mathrm{B}}T}{\sigma \mathbf{q}^2 + \kappa \mathbf{q}^4}\,, \tag{3.16}$$

where $\langle . \rangle$ denotes a statistical average. Note that, depending on the definition used for Fourier transforms, the projected surface S can appear in the eq. (3.16).

Two regimes can be identified, depending on the wavelength $\lambda = |\mathbf{q}|^{-1}$:

- If $\lambda \ll \lambda_\sigma$, the fluctuations are dominated by the $\mathbf{q}^4$ modes, and therefore by the bending elasticity. We can evaluate the order of magnitude of the maximum thermal fluctuation amplitude, by integrating the eq. (3.16) between $q_{\mathrm{min}} = \frac{2\pi}{L}$ and $q_{\mathrm{max}} = \frac{2\pi}{a}$, where L is the typical membrane size and a a microscopic cut-off. One obtains

  $$\sqrt{\langle h^2(L) \rangle} \sim \sqrt{\frac{k_{\mathrm{B}}T}{\kappa}} L\,. \tag{3.17}$$

  For a lipid bilayer of size $L \sim 10\,\mu m$ and bending modulus $\kappa \sim 10\,k_{\mathrm{B}}T$ with zero tension, we have therefore $\sqrt{\langle h^2(L) \rangle} \approx 3\,\mu m$.

- If, on the contrary, $\lambda \gg \lambda_\sigma$, the tension term dominates, and one can similarly calculate the maximum fluctuation amplitude

  $$\sqrt{\langle h^2(L) \rangle} \sim \sqrt{\frac{k_{\mathrm{B}}T}{\sigma} \log \frac{L}{a}}\,, \tag{3.18}$$

  which leads to $\sqrt{\langle h^2(L) \rangle} \approx 60\,nm$ for typical tension $\sigma \sim 10^{-5}\,J.m^{-2}$ and cutoff $a \sim 0.5\,nm$. The amplitude of the fluctuations is strongly reduced when the membrane is tensed.

3.3.1.3 Surface excess

In the Monge representation, the projected area S is inferior to the real membrane area A, and one can defined a surface excess

$$\alpha = \frac{\Delta A}{A} = \frac{A - S}{A} = \frac{1}{2}\int_S d^2r \boldsymbol{\nabla}^2 h(\mathbf{r})\,. \tag{3.19}$$

Using the Parseval-Plancherel theorem, we can evaluate this excess area α by integrating the static fluctuation spectrum (3.16) over all the Fourier modes $\mathbf{q}$, which leads to the excess area due to membrane fluctuations [Helfrich 1984]:

$$\alpha = \frac{k_\mathrm{B}T}{8\pi\kappa}\log\frac{\pi^2/a^2 + \sigma/\kappa}{\pi^2/L^2 + \sigma/\kappa}\,, \tag{3.20}$$

which leads to $\alpha = \frac{k_\mathrm{B}T}{4\pi\kappa}\log\frac{L}{a}$ for zero tension. Using the same numerical values as previously, we get a surface excess $\alpha \approx 8\%$ due to fluctuations in a membrane with vanishing tension. For intermediate values of the tension $\kappa\pi^2/L^2 \ll \sigma \ll \kappa\pi^2/a^2$, we have

$$\alpha = \frac{k_\mathrm{B}T}{8\pi\kappa}\log\frac{\kappa\pi^2}{\sigma a^2} \approx 5\%\,. \tag{3.21}$$

One remarks therefore that the surface of a weakly tensed membrane can be extended non-negligibely by unfolding the thermal fluctuations.

As proposed by [Fournier 2001], the area excess between the microscopic total membrane surface $\bar{A}$ and the macroscopic optically visible area A can be defined as the sum of two contributions, sketched on fig. 3.3:

- A term which accounts for the surface stored in membrane folding due to fluctuations, as described above (3.21).

- A term which accounts for the extent of lipid stretch under the action of the tension (see (3.7)).

$$\frac{\bar{A} - A}{\bar{A}} = \frac{k_\mathrm{B}T}{8\pi\kappa}\log\frac{\kappa\pi^2}{\sigma a^2} + \frac{\sigma}{K_c}\,. \tag{3.22}$$

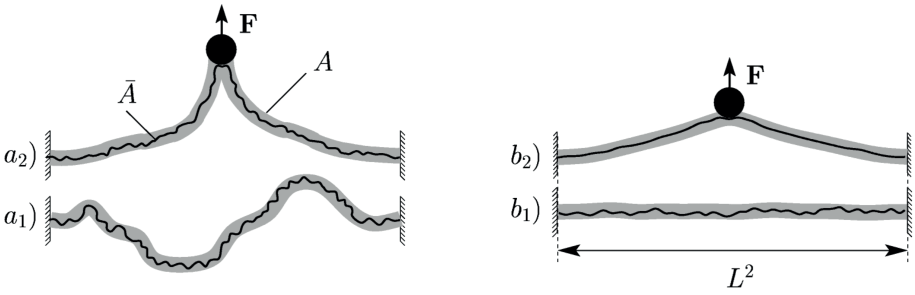

Figure 3.3: Membranes with a microscopic area $\bar{A}$ and optically visible area A, attached to solid frame of surface $S = L^2$. A floppy membrane has large fluctuations that are optically visible (a1). By pulling sufficiently on the membrane (a2), one can hinder optically visible fluctuations, without suppressing fluctuations of lower length scales. Similarly an initially "flat" membrane (b1) has a small microscopic excess area and can be further extended (b2) by a small perturbation. (Adapted from [Fournier 2001])

This property was confirmed by tension and macroscopic area measurements on vesicles [Evans 1990, Rawicz 2000] as illustrated on fig. 3.4

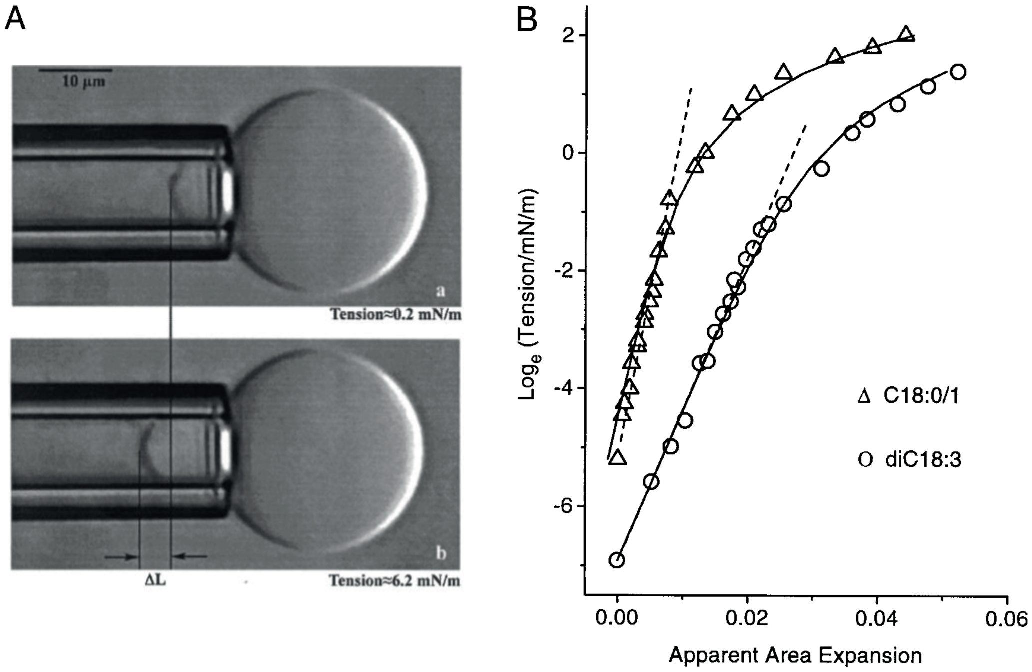

Figure 3.4: Variation of macroscopic surface and tension of a vesicle aspirated by a micropipette. **A** Video micrograph of a vesicle area expansion, at low tension (a) and at high tension (b). The change in projection length ΔL is proportional to the change in apparent surface area ΔA. **B** Semi-log plot of tension as a function of apparent area expansion, fitted by the elastic compressibility relation (3.22). (Adapted from [Rawicz 2000])

3.3.1.4 Confinement by the spectrin skeleton

The spectrin skeleton has been proposed to confine the lipid bilayer membrane fluctuations by a harmonic potential at lowest order [Gov 2003]

$$V = \frac{1}{2}\int d^2r\,\gamma h(\mathbf{r})^2\,. \tag{3.23}$$

This term acts as a Lagrange multiplier that constrains the mean square amplitude of fluctuations to be equal to $d^2 = \frac{1}{8}k_{\mathrm{B}}T/\sqrt{\gamma\kappa}$. This is equivalent to consider that the spectrin cytoskeleton acts as a rigid plan at $h = 0$ that maintains the membrane at an average distance d by an harmonic potential. The static fluctuation spectrum in Fourier can be easily generalized to

$$\langle|h_{\mathbf{q}}|^2\rangle = \frac{k_{\mathrm{B}}T}{\gamma + \sigma\mathbf{q}^2 + \kappa\mathbf{q}^4}\,. \tag{3.24}$$

The confinement parameter γ defines a new characteristic length $\lambda_\gamma = \left(\frac{\kappa}{\gamma}\right)^{1/4}$. For large wavelengths $\lambda \gg \lambda_\gamma$, the fluctuations are confined. Adding a confinement parameter $\gamma \sim 10^7\, J.m^{-4}$ to the fluctuation spectrum allows for a better fit of the experimental data in [Zilker 1987] (see fig. 3.6).

3.3.1.5 Coarse-grained model of the spectrin skeleton

Another model has been proposed to explain this tension jump in [Fournier 2004]. The RBC membrane energy is supposed to be the sum of the lipid bilayer energy and an elastic energy of the spectrin skeleton:

$$\mathcal{H} = \mathcal{H}_{\text{bil}} + \mathcal{H}_{\text{el}}\,, \tag{3.25}$$

where the lipid bilayer energy is the Canham-Helfrich Hamiltonian including a confinement parameter

$$\mathcal{H}_{\text{bil}} = \frac{1}{2}\sum_{\mathbf{q}} \left(\gamma + \sigma q^2 + \kappa q^4\right) |h_{\mathbf{q}}|^2\,. \tag{3.26}$$

The spectrin skeleton is supposed to be a perfect network of N entropic springs of length ξ in actual state, of resting length l_0 and of stiffness k. The associated elastic energy reads therefore

$$\mathcal{H}_{\text{el}} = \frac{1}{2} N\, k\, (\xi - l_0)^2\ . \tag{3.27}$$

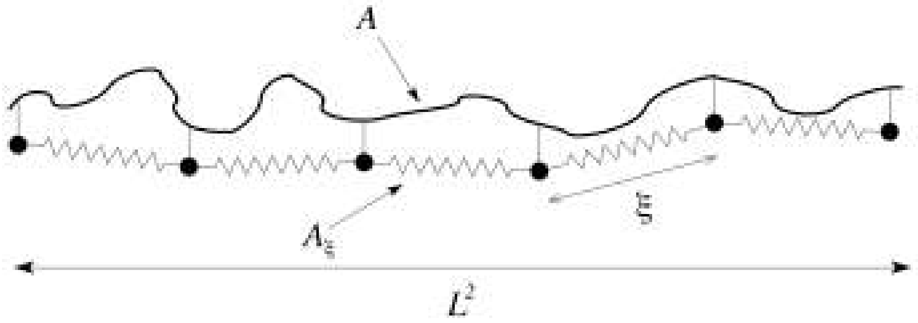

Figure 3.5: Sketch of a nearly planar membrane of microscopic area A, of coarse-grained area A_ξ and of projected area L^2. The spectrin filaments are represented by springs of length ξ and are anchored at fixed points in the membrane (plain line). (Adapted from [Dubus 2007])

The filaments are anchored to the lipid bilayer and therefore their instantaneous extension depends on membrane fluctuations (see fig. 3.5). The coarse-grained area A_ξ that they define is lower than the microscopic lipid bilayer area A. If we suppose that the network is periodic, the coarse-grained area is the sum of the areas delimited by a spectrin lattice unit: $A_\xi = N\xi^2/g$, where g depends on the topology of the network. For a triangular lattice $g = 2\sqrt{3}$, for a square lattice $g = 2$.

We consider a nearly planar membrane of height $h(\mathbf{r})$ in the Monge representation, sketched in fig. 3.5. Its microscopic area is A, the network coarse-grained area

A_ξ and the projected area is L^2. The coarse-grained area can be decomposed into Fourier modes with wave-vectors smaller than ξ^{-1}:

$$A_\xi\left[h_{\mathbf{q}}\right] = L^2 + \sum_{q \leq \xi^{-1}} \frac{1}{2} q^2 |h_{\mathbf{q}}|^2 + \mathcal{O}(h_{\mathbf{q}}^4) = \frac{N}{g}\xi^2 \,. \tag{3.28}$$

At zeroth order in h_q, we can define an average filament extension length

$$\xi_0^{-1} = \frac{N}{gA} \tag{3.29}$$

We inject in the energy (3.30) the expression of ξ deduced from eq. (3.28) :

$$\mathcal{H}_{\text{el}} = \mathcal{H}_{\text{el}}^{(0)} + \Delta\sigma \sum_{q<\xi_0^{-1}} \frac{1}{2} q^2 |h_{\mathbf{q}}|^2 + \mathcal{O}(h_{\mathbf{q}}^4) \,, \tag{3.30a}$$

$$\text{with} \quad \Delta\sigma = \frac{1}{2} g\, k \left(1 - \frac{l_0}{\xi_0}\right) \,. \tag{3.30b}$$

We can therefore rewrite the total membrane energy (3.25) as

$$\mathcal{H} = \mathcal{H}_{\text{bil}} + \mathcal{H}_{\text{el}} = \frac{1}{2} \sum_{q<\xi_0^{-1}} \Delta\sigma\, q^2 |h_{\mathbf{q}}|^2 + \frac{1}{2} \sum_{\mathbf{q}} \left(\gamma + \sigma q^2 + \kappa q^4\right) |h_{\mathbf{q}}|^2 \tag{3.31}$$

Note that the contribution of the spectrin network to the energy is limited to wave-vectors smaller than ξ_0^{-1}.

With the equipartition theorem we deduce the following static power spectrum of the membrane height fluctuations at equilibrium

$$\left\langle |h_{\mathbf{q}}|^2 \right\rangle = \frac{k_{\text{B}} T}{\gamma + (\sigma + \Delta\sigma)\mathbf{q}^2 + \kappa \mathbf{q}^4} \qquad \text{for } q \lesssim \xi_0^{-1} \,, \tag{3.32a}$$

$$\left\langle |h_{\mathbf{q}}|^2 \right\rangle = \frac{k_{\text{B}} T}{\gamma + \sigma \mathbf{q}^2 + \kappa \mathbf{q}^4} \qquad \text{for } q \gtrsim \xi_0^{-1} \,. \tag{3.32b}$$

The spectrin elastic energy leads therefore to a tension jump when the wavelength goes beyond the mesh size of the network, as expected: for wavelengths much smaller than the mesh size, the lipid-bilayer doesn't feel the spectrin network; on the contrary, for wavevelengths greater than the mesh size, the fluctuations are damped by the elastic network. This adds an extra tension term to the fluctuation spectrum. Note that the tension jump exists only for a prestressed network ($\xi_0 \neq l_0$) at this order of approximation ($\mathcal{O}(h_{\mathbf{q}^4})$). For vanishing prestress, the calculation should be carried up to 4th. order in $h_{\mathbf{q}}$ to calculate the effective membrane tension, which requires the use of the renormalization group techniques. Note also that the spectrin network should in fact renormalize also the effective membrane tension at wavelengths smaller than ξ_0 if we take into account the constraint of microscopic area conservation: $\frac{1}{2}\sum_{\mathbf{q}} q^2 \left\langle |h_{\mathbf{q}}|^2 \right\rangle = A - L^2$.

Fournier et al. reinterpreted the data of [Zilker 1987] with this result (3.32a) by plotting in fig. 3.6 the ratio $\kappa/\kappa_{\mathbf{q}}$, where the effective bending modulus, depending on $\mathbf{q}$, is defined as

$$\left\langle |h_{\mathbf{q}}|^2 \right\rangle = \frac{k_{\mathrm{B}}T}{\kappa_{\mathbf{q}}^4} \,. \tag{3.33}$$

The fit leads to a confinement parameter $\gamma \sim 5 \times 10^6\, J.m^{-4}$, a tension at small wave-vectors $\sigma^{<} = \sigma + \Delta\sigma \sim 1.5 \times 10^{-6}\, J.m^{-2}$ and a tension at high wave-vectors $\sigma^{>} = \sigma \sim -0.8 \times 10^{-7}\, J.m^{-2}$. The positive sign of $\Delta\sigma = \sigma^{<} - \sigma^{>} \sim 1.6\, 10^{-6}\, J.m^{-2}$ suggests that the spectrin network is under tension, and gives an order of magnitude of the spectrin filament stiffness $k \sim 10^{-6}\, J.m^{-2}$, in good agreement with measurements made in [Lenormand 2001].

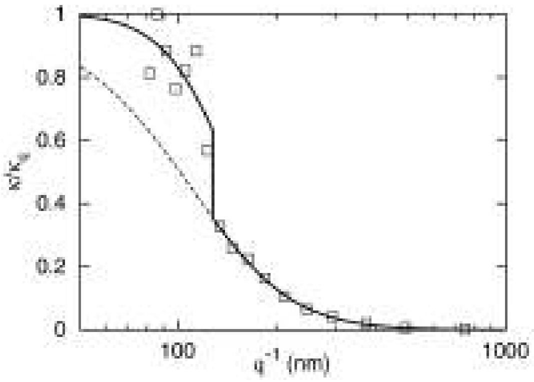

Figure 3.6: Fit (plain line) of the measured fluctuation spectrum of a human red blood cell from the data (squares) of [Zilker 1987]. The dashed line extrapolates the large length-scale fit. The discontinuity and the corresponding tension jump occurs at a length scale $\approx 125\,nm$ comparable to the spectrin skeleton mesh. (Adapted from [Fournier 2004])

It is quite remarkable to find that $\sigma^{>}$ is close to zero, or even negative. The spectrin cytoskeleton may lead to extra-folding of the membrane, thereby regulating the membrane tension at length scales shorter than the cytoskeleton mesh size, via the area constraint.

3.3.1.6 Refined static model of the spectrin skeleton

Starting with similar hypothesis as above, Dubus et Fournier proposed a refined model of the effective membrane fluctuation spectrum in presence of an elastic triangular spectrin network [Dubus 2006]. Their Hamiltonian in 2 dimensional curvilinear coordinates (x^1, x^2) is the sum of the classical Canham Helfrich energy and a discrete elastic spectrin energy

$$\mathcal{H} = \int_0^{L_1}\int_0^{L_2} \sqrt{g} dx^1 dx^2 \left[\frac{\kappa}{2}(\partial_\alpha\partial^\alpha h)^2 + \frac{\sigma}{2}(\partial^\alpha h)(\partial_\alpha h)\right] + \sum_{n=1}^{N} \frac{\mu_n}{2}\left[h(\mathbf{R_n}) - h(\bar{\mathbf{R}}_\mathbf{n})\right]^2, \tag{3.34}$$

where μ_n is related to the spring stiffness by $\mu_n = k\left(1 - l_0/|\mathbf{R_n} - \bar{\mathbf{R}}_\mathbf{n}|\right)$. The vectors $\mathbf{R}_n$ and $\bar{\mathbf{R}}_n$ are the projections of the n-th spring end points, as shown on fig. 3.7.

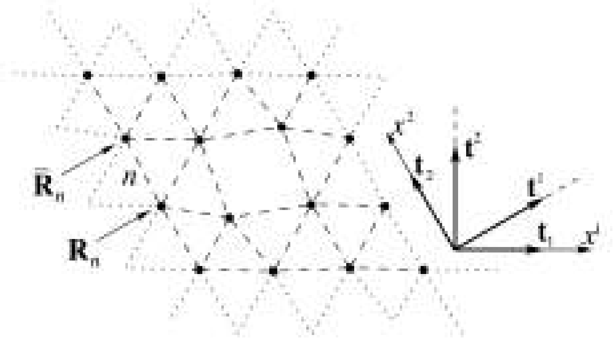

Figure 3.7: Network of N springs in a $M \times M$ unit cell of a cytoskeleton with periodic boundary conditions. The extremities of the n-th spring have projections $\mathbf{R}_n$ and $\bar{\mathbf{R}}_n$ onto the reference plane. (Adapted from [Dubus 2006])

Using an Hubbard-Stratanovitch transformation to treat the discrete spectrin energy in the previous Hamiltonian (3.34), they calculated the effective fluctuation spectrum with equipartition theorem for a triangular network with no defect, in the regime $q \ll \xi_0^{-1}$:

$$\frac{k_\mathrm{B}T}{\langle |h_\mathbf{q}|^2\rangle} \sim \sigma_\mathrm{eff}\, q^2 + \kappa_\mathrm{eff}\, q^4\,, \tag{3.35}$$

with

$$\sigma_\mathrm{eff} = \sigma + \frac{3}{2\sqrt{g}}\mu = \sigma + k\sqrt{3}\big(1 - l_0/\xi_0\big)\,, \tag{3.36a}$$

$$\kappa_\mathrm{eff} = \kappa - \frac{3}{32\sqrt{g}}\mu\xi_0^2 = \kappa - \frac{\sqrt{3}}{16}k\xi_0^2\big(1 - l_0/\xi_0\big) \tag{3.36b}$$

They obtained therefore the same tension jump as [Fournier 2004], but calculated also the small cytoskeleton renormalization of the membrane bending modulus.

3.3.2 Numerical models of membrane fluctuations

3.3.2.1 Percolation model

Saxton studied the RBC cytoskeleton elasticity by a percolation model [Saxton 1990]. The system consists in a triangular network of springs from which a fraction $1 - b$ of spectrin filaments are removed randomly (see fig. 3.8). The percolation threshold is reached for $b = 2\sin(\pi/18) \sim 0.347$, which corresponds to a mean number of 2.08 links per node. The shear modulus is calculated as a function of b and the spring stiffness $k_\parallel$ and reaches zero for $b \sim 0.642$, a fraction much larger than the percolation threshold. A further stiffness $k_\perp$, that opposes to angle changes, has a significant effect, since for $k_\perp/k_\parallel \gtrsim 0.2$ the shear modulus reaches zero only at the percolation threshold. This model however doesn't take into account transverse and parallel displacement of the nodes nor the composite structure of the RBC membrane.

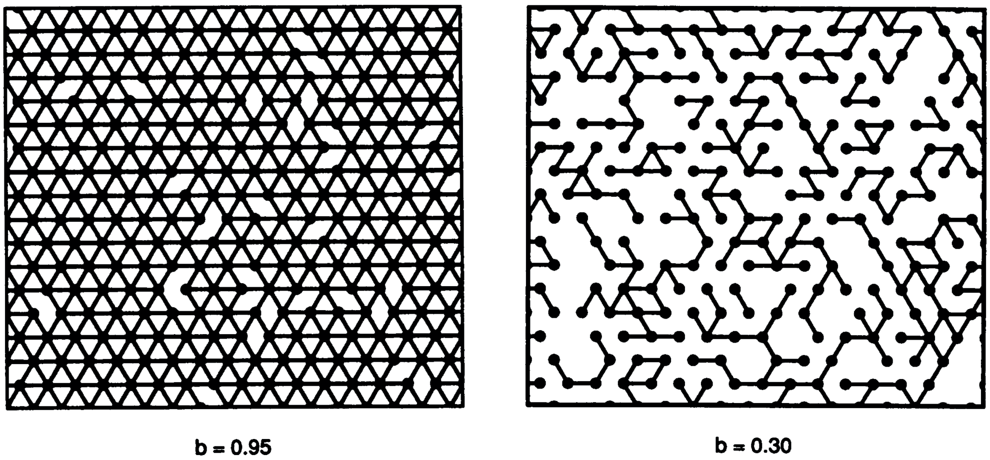

Figure 3.8: Percolation model of the spectrin cytoskeleton triangular network. Spectrin filaments (links) are removed randomly with a fraction $1 - b$. The percolation threshold is reached for $b \sim 0.35$. (Adapted from [Saxton 1990])

3.3.2.2 Langevin dynamics with filament breaking

In a recent numerical model [Zhang 2008], the authors started from an Helfrich energy coupled via mobile anchor points to a quasi-planar network of springs, very similarly to [Dubus 2006]. The membrane and cytoskeleton is represented in fig. 3.9 A. Adapting their notations, their Hamiltonian reads

$$\mathcal{H} = \int_S d^2r \, \frac{\kappa}{2} \left[\boldsymbol{\nabla}^2 h(\mathbf{r})\right]^2 + \sum_{\langle i,j \rangle} b_{ij}(t) \left\{ \frac{\mu}{2} \left(\mathbf{r}_i - \mathbf{r}_j\right)^2 + \frac{\mu}{2} \left[h(\mathbf{r}_i) - h(\mathbf{r}_j)\right]^2 - E_\mathrm{B} \right\}, \quad (3.37)$$

with $\mathbf{r} = (x, y)$. $E_\mathrm{B} > 0$ is the bond free energy associated with disconnecting an attached filament and μ is the shear modulus of the elastic spectrin triangular network. The sum is made on each distinct pair of neighboring nodes $\langle i, j \rangle$. $b_{ij}(t)$ accounts for the random detachment of the network: it is 1 when the ij link is connected and 0 otherwise.

The Hamiltonian (3.37) is very similar to the one of [Dubus 2006], but the lateral positions of the nodes are mobile here, and the links can break and reform dynamically. Note that the lipid-bilayer tension is supposed to vanish in this study. An effective tension may therefore emerge only from the spectrin network elasticity.

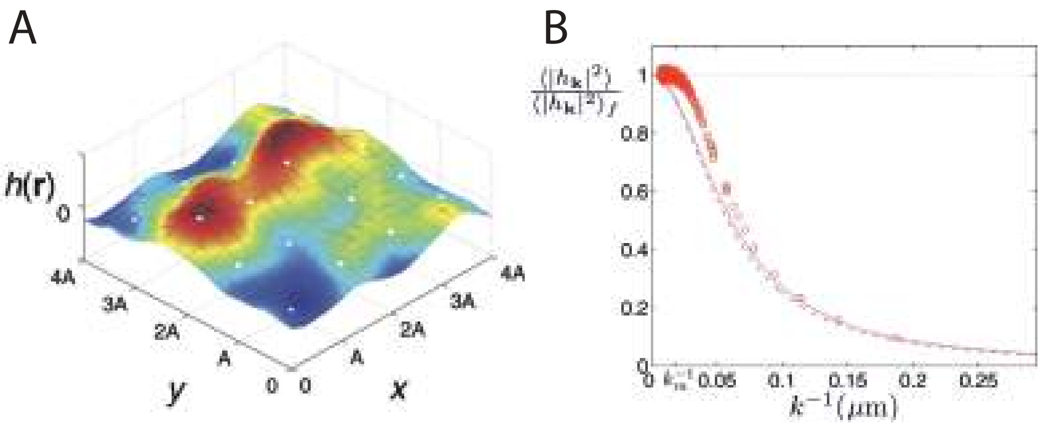

Figure 3.9: **A** Snapshot of the quasi-planar RBC membrane in simulations. The lipid bilayer is connected to spectrin by a network of laterally mobile anchoring nodes (white dots). These nodes are interconnected by springs to model the cytoskeleton elasticity. Individual links are allowed to break and reform randomly. The average mesh size is 100 nm. **B** Comparison of simulation results and theoretical prediction of [Dubus 2006] (see (3.35)) for the Fourier amplitude of fluctuations $\langle |h_k|^2\rangle$ versus the wavelength k^{-1}. The solid line is the theoretical prediction and fits correctly the simulation results only for wavelengths larger than the mesh size. (Adapted from [Zhang 2008])

They deduce the following overdamped Langevin equations for the membrane height $h(\mathbf{r},t)$ and lateral position of nodes $\mathbf{r}_i(t)$:

$$\frac{\partial h(\mathbf{r},t)}{\partial t} = \int_{-\infty}^{\infty} d\mathbf{r}'\,\Lambda(\mathbf{r}-\mathbf{r}')\big[f(\mathbf{r}',t)+\zeta(\mathbf{r}',t)\big]\,, \tag{3.38a}$$

where $f(\mathbf{r},t)$ is the force per unit area on the membrane,

$$\begin{aligned} f(\mathbf{r},t) &= -\frac{\delta\mathcal{H}}{\delta h(\mathbf{r},t)} \\ &= -\kappa\boldsymbol{\nabla}^4(\mathbf{r},t) - \sum_j \mu\, b_{ij}(t)\,\delta^2(\mathbf{r}-\mathbf{r}_i)\,\big[h(\mathbf{r},t)-h(\mathbf{r}_j,t)\big]\,, \end{aligned} \tag{3.38b}$$

where δ^2 is a delta function on the surface,

$$\frac{\partial \mathbf{r}_i(t)}{\partial t} = \frac{D}{k_{\mathrm{B}}T}\Big[\mathbf{f}_i(t)+\zeta_i t\Big]\,, \tag{3.38c}$$

where $\mathbf{f}_i(t)$ is the force on the node $\mathbf{r}_i(t)$

$$\mathbf{f}_i(t) = -\frac{\delta\mathcal{H}}{\delta\mathbf{r}_i} = -\sum_j \mu\, b_{ij}(t)\left\{(\mathbf{r}_i-\mathbf{r}_j)+\big[h(\mathbf{r}_i)-h(\mathbf{r}_j)\big]\frac{\partial h(\mathbf{r}_i)}{\partial \mathbf{r}_i}\right\}. \tag{3.38d}$$

D is the lateral diffusion constant of the nodes in the membrane and $\Lambda(\mathbf{r})$ is the diagonal part of the Oseen tensor, that accounts for hydrodynamic flow in the surrounding fluid of viscosity η, and is given by (see section 4.B)

$$\Lambda(\mathbf{r}) = \frac{1}{8\pi\eta|\mathbf{r}|}\,. \tag{3.39}$$

$\zeta(\mathbf{r},t)$ and $\zeta_i(t)$ are spatially local Gaussian white noise satisfying the fluctuation-dissipation theorem (see section 4.A)

$$\langle\zeta(\mathbf{r},t)\rangle = 0\,, \tag{3.40a}$$

$$\big\langle\zeta(\mathbf{r},t)\zeta(\mathbf{r}',t')\big\rangle = 2k_{\mathrm{B}}T\Lambda^{-1}(\mathbf{r}-\mathbf{r}')\delta(t-t')\,, \tag{3.40b}$$

$$\langle\zeta_i(t)\rangle = 0\,, \tag{3.40c}$$

$$\langle\zeta_i(t)\zeta_j(t)\rangle = 4\frac{(k_{\mathrm{B}}T)^2}{D}\delta_{ij}\delta(t-t')\,. \tag{3.40d}$$

For the dynamics of the breaking and reforming of spectrin springs, they consider a simple two-state model with a rate k_c to reconnect a link and a rate k_d to dissociate a link. At steady-state the probability of a link to be connected reads simply

$$p = \frac{k_c}{k_c + k_d}\,. \tag{3.41}$$

However their model does not account for the change in on the kinetic due to the energy of filament elongation, and therefore does not obey the detailed balance.

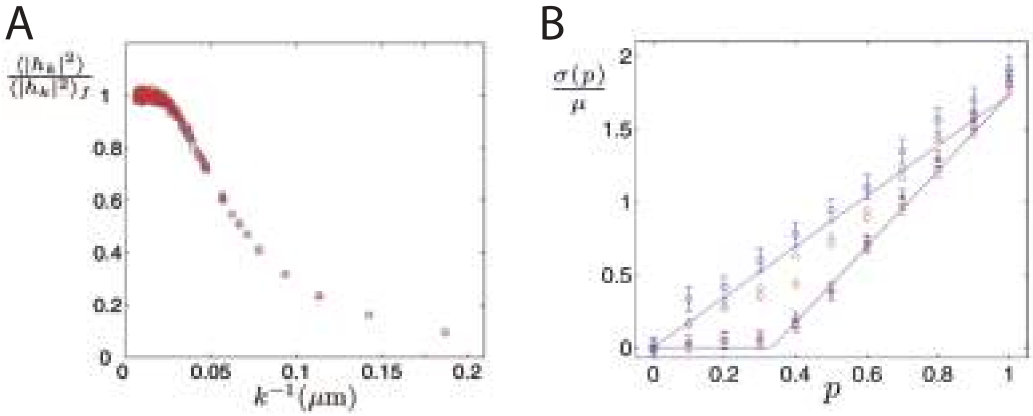

Figure 3.10: **A** Simulation results of the {membrane+spectrin} correlation amplitude $\langle|\,h_k\,|^2\rangle$ as a function of the wave-number k for an hexagonal 2-dimensional lattice. Circles are the data for the case of immobile nodes placed on a perfect lattice, while triangles are the data for the case of mobiles nodes. Mobility of the cytoskeleton attachment points does not significantly alter the simulation results. **B** Normalized tension $\sigma(p)$ versus spectrin link attachment probability p for a hexagonal lattice. The circles, triangles and diamonds are simulation results for $(k_d+k_c)^{-1} \ll \tau_m$ (fast spectrin kinetics), $(k_d+k_c)^{-1} \sim \tau_m$ (intermediate regime) and $(k_d+k_c)^{-1} \gg \tau_m$ (slow spectrin kinetics). The dashed line is the prediction of eq. (3.42a); the solid line is the prediction of eq. (3.42b) (Reproduced from [Zhang 2008])

The authors simulate the Langevin equations in spatial Fourier space with Fourier Monte Carlo (FMC) [Gouliaev 1998] and Fourier space Brownian dynamics (FSBD) [Lin 2004, Lin 2005]. For a hexagonal lattice (triangular mesh), and no spring disconnection, the model of [Dubus 2006] fits correctly the fluctuation spectrum for wavelengths larger than the typical spectrin mesh size 125 nm, as shown on fig. 3.9 B.

In the limit of association and dissociation rates much faster than the membrane relaxation time scale $\tau_m \gg (k_d+k_c)^{-1}$, each cytoskeletal link behaves as an intact link with a reduced spring constant, leading to the effective membrane tension (3.42a). On the contrary for (re)association rates much slower than the membrane relaxation time scale τ_m, the membrane evolves under the influence of quenched network disorder, with a behavior analogous to the 2 dimensional percolation problem [Saxton 1990] briefly exposed above. Here the percolation threshold is $p = p_c = 2/z = 1/3$ for a bond valence $z = 6$ for the hexagonal lattice, and the effective tension vanishes at this point (3.42b).

$$\sigma^{\text{eff}} = \sqrt{3}\mu\, p \qquad \text{(fast spectrin kinetics)}\,, \tag{3.42a}$$

$$\sigma^{\text{eff}} = \frac{3\sqrt{3}}{2}\mu\left(p - \frac{1}{3}\right) \qquad \text{(slow spectrin kinetics)}\,, \tag{3.42b}$$

3.3.3 Active membranes fluctuations

Membranes can exchange lipids with their environment, and transmembrane or peripheral proteins can be involved in active processes such as pumping ions or bond breaking. These processes are called *active* because they require an external input of energy, generally mediated by the ATP molecules. These systems are therefore maintained out-of-equilibrium by a permanent influx of energy, and this non-equilibrium behavior can be transduced into non-thermal membrane fluctuations. Active membranes refer therefore here to the presence of fluctuations of non-thermal origin, i.e. that can not be derived from the fluctuation-dissipation theorem. We review below a few important hydrodynamic models of active membranes.

3.3.3.1 Ion pump shot noise

The first hydrodynamic model of active membranes was proposed by J. Prost and R. Bruinsma in 1996 [Prost 1996]. The activity originates from ion channels embedded in the membrane and mobile. Switching stochastically between open and closed states, these channels can produce a collective noise called shot noise. This process is described by a two-state variable $S_i(t) = 1$ if the ion is active and 0 if not. The noise is exponentially correlated in time $g(t) = \langle S_k(t)S_k(0)\rangle - \langle S_k\rangle^2 = g(0)\, e^{-t/\tau}$, with a typical correlation time τ. The ion pumping effect generates a pressure variation of the form

$$\delta p(\mathbf{r}, t) \propto f \sum_i S_i(t)\, \delta\big(\mathbf{r} - \mathbf{R}_i(t)\big)\,,$$

where $f \sim k_{\text{B}}T/d$ is the typical force dipole exerted on the membrane of thickness d. The membrane is supposed here to have a non-zero permeability denoted λ_{p}.

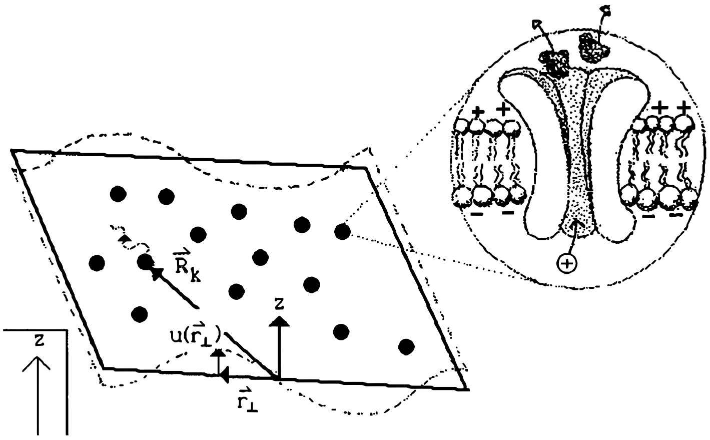

Figure 3.11: Fluctuating nearly flat membrane with mobile ion channels. The membrane displacement with respect to the plane $z = 0$ is denoted $u(\mathbf{r}_\perp)$ with $\mathbf{r}_\perp$ the in-plane position. The ion channels are located at $\mathbf{R}_k(t)$ and allow the passage of ions and water molecules. (Adapted from [Prost 1996])

Around steady-state the authors show that the membrane fluctuations can be described by the following Langevin equation for the height displacement $u_\mathbf{q}(t)$

$$\frac{\partial u_\mathbf{q}(t)}{\partial t} + \tau(\mathbf{q})^{-1} u_\mathbf{q}(t) = \zeta_\mathbf{q}(t) + \Gamma \sum_i S_i(t)\, e^{i\mathbf{q}\cdot\mathbf{R}_i(t)}\,, \tag{3.43}$$

where $\Gamma = \lambda_\mathrm{p}$ and $\tau(\mathbf{q})^{-1}$ is the sum of the traditional relaxation time for an impermeable membrane in Fourier space and an additional permeation term.

$$\tau(\mathbf{q})^{-1} = \frac{\kappa}{4\eta} q^3 + \kappa \lambda_\mathrm{p} q^4\,. \tag{3.44}$$

The first term $\zeta_\mathbf{q}(t)$ in the right-hand side of eq. (3.43) is the equilibrium thermal noise, which obeys the fluctuation-dissipation theorem, whereas the second term is a non-equilibrium noise due to the ion pumps activity. In the long wavelength limit, this model is able to predict that active noise can dominate over thermal noise

$$\left\langle |u_\mathbf{q}|^2 \right\rangle \sim_{q\to 0} \frac{k_\mathrm{B}T}{\kappa} \left(q^{-4} + \xi_\mathrm{ne}^{-1} q^{-5} \right)\,, \tag{3.45}$$

where $\xi_\mathrm{ne} = DE/16\eta\big(\Gamma\rho\langle S\rangle\big)^2$ is a length-scale that diverges close to equilibrium $\Gamma \to 0$ (D is the diffusion constant of the ion pumps and E an area compression modulus)

3.3.3.2 Curvature coupling

The first experimental realization of active membranes was done by reconstituting the transmembrane protein bacteriorhodopsin in giant unilamellar vesicles [Manneville 1999, Manneville 2001]. A new theoretical model coupling protein activity to the membrane via curvature was conjointly proposed to explain the experimental results [Ramaswamy 2000]. The possible asymmetry of the ion pumps shape is the main new ingredient added to the seminal work of Prost and Bruinsma [Prost 1996]. It introduces a preference of these proteins for positive or negative membrane curvature regions, depending on the ratio of their head-to-tail size (see fig. 3.12 A). This coupling between mobile force centers and curvature can lead to traveling waves or instabilities. Proteins that prefer positive curvature can trigger an instability, since the pumping region is more curved and therefore attracts more pumps, as sketched on fig. 3.12 B.

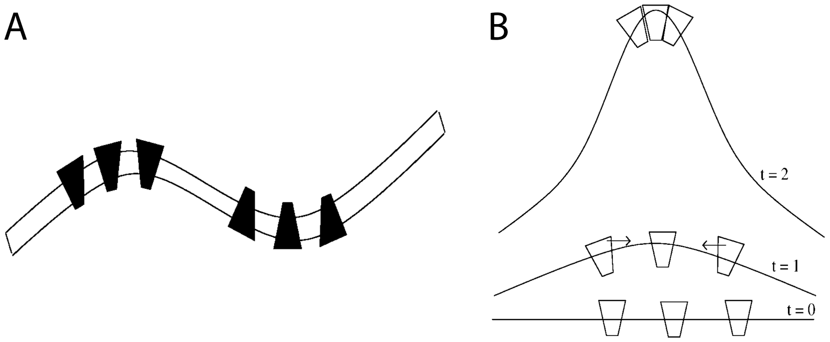

Figure 3.12: **A** Asymmetric proteins are drawn to regions with curvature adapted to their shape. **B** An instability develops if the curvature produced by pumping attracts more pumps. (Adapted from [Ramaswamy 2000])

This approach was followed by a subsequent interest in the field [Chen 2004, Gov 2004, Lomholt 2006]. We note that in [Lacoste 2005, Chen 2010] the active membrane models are constructed based on the idea of switching between several internal states of the active proteins. The membrane fluctuations become therefore non-equilibrium fluctuations because the transitions between the various internal states of the proteins do not obey detailed balance.

3.3.3.3 Direct force

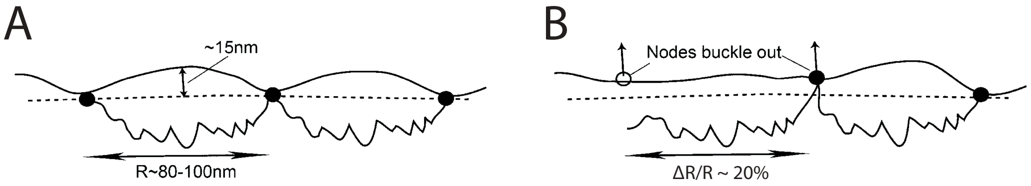

Figure 3.13: **A** Schematic side view of the RBC composite membrane with fully connected spectrin filaments. **B** Sketch of the dissociation of a filament that drives supposedly a direct force event by membrane unbuckling. (Adapted from [Gov 2005])

In [Gov 2004] the authors distinguish two possible types of active forces, direct forces and curvature forces, depending on whether active proteins are coupled or not to the membrane curvature. Direct forces are suggested to be triggered by the detachment under ATP hydrolysis of one spectrin filament end in RBC membranes

[Gov 2005, Gov 2007]. Balancing the tension developed by a stretched filament with the energy needed to buckle the membrane, they predict a steady-state stretching of spectrin of approximately 20% (see fig. 3.13). Assuming that detachment events are correlated over the sum of the dissociation and re-association times, they calculate the non-thermal fluctuation spectrum originating from such direct forces. They also propose the transition from discocyte to echinocyte shapes to be mediated directly by the loss of ATP that stiffens the network.

3.3.3.4 Non-equilibrium fluctuations and excess area

The previous models for active fluctuations neglect the interplay between tension and excess area of the membrane (3.22), discussed above for passive membranes in section 3.3.1.3. In [Loubet 2012] the authors show that this interplay can be important in active membranes. The activity is described by various sources of non-equilibrium noise taken from literature: direct force, curvature force or permeation force. A direct force corresponds to an external medium pushing on the membrane, a curvature force is a fluctuating spontaneous curvature and a permeation force comes from the active transport of fluid through the membrane. Deriving the shape fluctuations for a quasi-spherical membrane, the active tension is defined as the passive case [Seifert 1995] as the Lagrange multiplier that maintains the total membrane area constant, which leads to a self-consistent relation between the membrane area excess and the membrane tension. Adding a correlated active noise of any of the three types described above, they relate the active tension and the excess area and show that the active correction to the tension is always positive. The effect of activity is therefore twofold: it contributes directly to the fluctuation spectrum by adding extra-fluctuations but it also indirectly renormalizes the tension through the area constraint (these extra-fluctuations decreasing the projected area). For the direct force model proposed in [Gov 2004] (see section 3.3.3.3), we expect therefore a ATP concentration increase to raise the average level of fluctuations, in agreement with experimental results of [Tuvia 1998], but conjointly to increase the membrane tension, which is in contradiction to recent experimental data [Betz 2009].

3.3.3.5 The RBC cytoskeleton as an active network ?

We have reported in section 3.1.1.2 that ATP hydrolysis controls membrane-spectrin attachment strength via the phosphorylation of the 4.1 R protein. In particular a clear mechanical difference between healthy and ATP-depleted RBCs has been reported for the membrane response to tether pulling assay [Borghi 2007], whereas no significant difference is detectable for a pure fluid bilayer in the same two conditions.

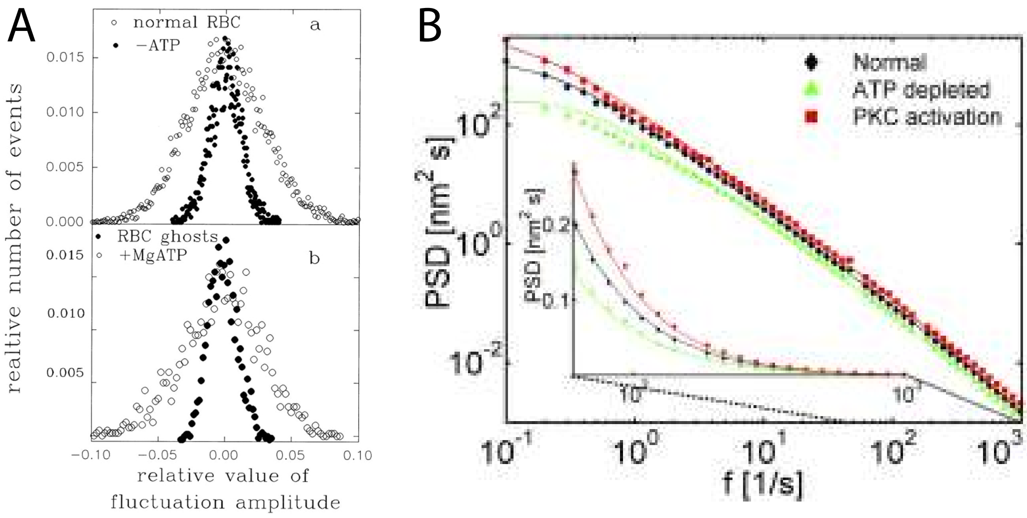

Figure 3.14: **A** Effect of ATP on the amplitude distribution of membrane fluctuations in human RBC and RBC ghosts. (a) Amplitude histogram for intact RBCs *(open circle)* and in ATP-depleted RBCs *(closed circle)*. (b) Amplitude histogram for RBC ghosts in the absence *(closed circles)* and the presence of 1 mM MgATP *(open circles)*. (Reproduced from [Tuvia 1998]). **B** Mean power spectral density (PSD) of normal RBCs *(black)*, ATP-depleted *(green)* and PKC-activated *(red)*. (Inset: Semilog plot of the same data for the high frequency range). (Reproduced from [Betz 2009])

The static fluctuation amplitude has been shown to decrease strongly under ATP-depletion conditions in RBCs and ghosts[2] [Tuvia 1998] (see fig. 3.14 A). More recently, using an optical tweezer coupled to a quadrant photodiode, the dynamics of an edge of the RBC membrane has been recorded with sub-nanometer resolution and over a frequency range of more than four orders of magnitute. The power spectrum density has been compared for healthy and ATP-depleted RBCs and are shown on fig. 3.14 B. The results are consistent with [Tuvia 1998], showing a clear decrease of the fluctuations amplitude at low frequencies for ATP-depleted cells. Fitting the data with a quasi-spherical Helfrich membrane theory, they could measure precisely the apparent surface tension and bending rigidity in these two conditions. The effective tension is shown to increase threefolds in ATP-depleted red cells compared to healthy RBCs, whereas fluctuations are decreased concomitantly. Finally, the activation of the protein kinase C (PKC), that leads to phosphorylation of the 4.1 R protein, results also in enhanced fluctuations as compared to normal cells, confirming the presumable role of the spectrin cytoskeleton in the ATP-dependent extra-fluctuations. These results are consistent with the study of [Park 2010] where the authors record the transverse fluctuations over an entire face of the cell surface with laser interferometry for healthy and ATP-depleted cells (see fig. 3.15 A and B). They furthermore measure the deviation from Gaussian statistics of these fluctuations via the 4th. cumulant, that compares the fourth and second moment of the

---

[2] A ghost is an RBC which has been treated with mild detergents; the detergents lysed the cells, thereby washing out the hemoglobin and other cytoplasmic components. The spectrin network remains however intact and functional.

membrane height displacement.

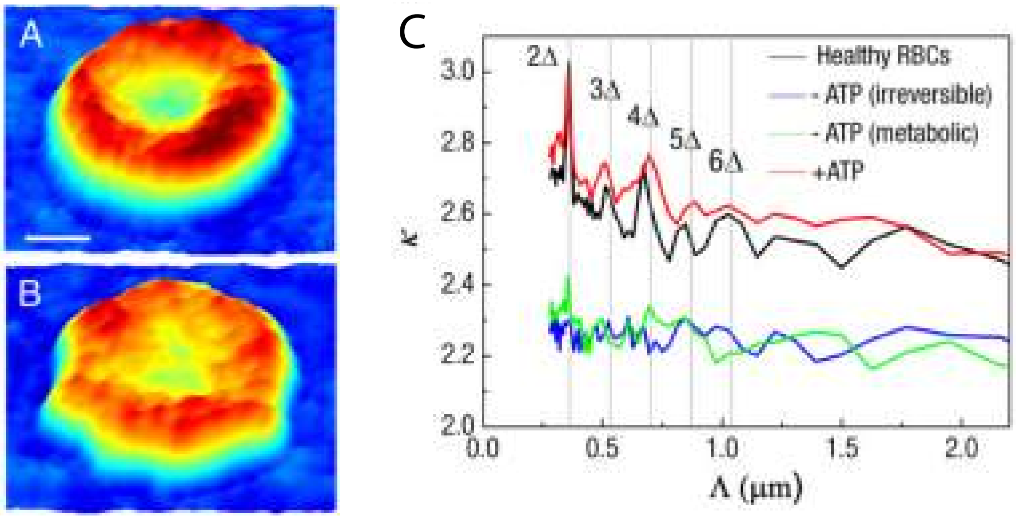

Figure 3.15: **A** Topography of the surface fluctuations of a healthy RBC, and **B** an ATP-depleted RBC. **C** Non-Gaussian parameter κ as a function of spatial wavelength Γ. The presence of ATP leads to non-thermal fluctuations with peaks at the successive multiple of the neighboring junction distance Δ, indicating that ATP-enhanced fluctuations are correlated with the network structure of the underlying cytoskeleton. (Adapted from [Park 2010])

This parameter, which is expected to be equal to two for thermal fluctuations, is shown to be higher in healthy RBCs (see fig. 3.15 C). All these results suggest that RBC behave as active membrane, in the sense that they display non-equilibrium fluctuations. However the comparison of healthy RBCs and ATP-depleted RBCs – which relies on the assumption that ATP is the only possible source of energy in a cell – cannot constitute a definitely conclusive physical proof of the non-equilibrium feature of the RBC membrane. The correct way to determine if a system is out-of-equilibrium is to show that it violates the fluctuation-dissipation theorem (FDT), that relates the fluctuation spectrum and the response function of a system only at equilibrium (see section 4.A). It was recently claimed, based on measurements of fluctuations amplitudes by digital holographic microscopy, that RBC membrane fluctuations are in agreement with thermal equilibrium theory, and that ATP controls only its mechanical properties, but doesn't inject extra-fluctuations in the system [Boss 2012]. We present in the chapter 4 contradictory measurements of Timo Betz that motivated our theoretical work and that show a clear violation of the fluctuation-dissipation theorem.

Chapter 4

A theory of active RBC membrane fluctuations

Contents

4.1 Introduction

4.1.1 Theoretical approach

In this chapter we try to reconcile the different approaches presented in the previous chapter and to propose a new theory that clarifies the origin and conditions for active (non-equilibrium) fluctuations of the RBC membrane at steady-state. We mention here that this work is still ongoing, the results remains therefore preliminary.

To simplify the calculations we start with a one-dimensional membrane model. Similarly to [Fournier 2004] and [Dubus 2006] we include explicitly an elastic energy contribution of the spectrin network to calculate the zeroth-order renormalization of the membrane mechanics (tension and bending) for wavelengths larger than the network mesh size. But, since we are interested in the fluctuations, we also allow for random filament unbinding, which we consider a source of active noise in the system, as suggested in [Gov 2005]. Our starting energy in section 4.2.1 is therefore very similar to the Hamiltonian proposed in [Zhang 2008], eventhough we do not allow for the junctions to move laterally within the membrane. Adding this further degree of freedom had indeed only very weak effects in their numerical study (see fig. 3.10 B). However, here we take into account explicitly, in the kinetic scheme of attachment/detachment, the energetic contribution of the filament elongation. This more complete description of the thermodynamics allows to clearly identify the conditions for thermal equilibrium or non-equilibrium for the system.

In section 4.2.2 we show that an elementary binding/unbinding reaction is not sufficient to lead to non-equilibrium fluctuations, since such a reaction is necessarily at equilibrium at steady-state. To break thermal equilibrium, a cyclic kinetic scheme called phosphorylation-dephosphorylation cycle (PdPc) has to be coupled to the membrane mechanics. It is composed of at least two reversible binding/unbinding reactions, the first one involving the consumption of ATP and the second one being independent of ATP concentration. A constant supply of ATP forces the system to browse the cycle preferentially in one way, thereby maintaining a non-equilibrium steady-state.

In section 4.3 we generalize the results to 2-dimensional quasi-spherical membranes using a decomposition in spherical harmonics. We calculate the membrane fluctuation spectrum and the response function of the coupled system membrane - phosphorylation-dephosphorylation cycle and we show that the fluctuation-dissipation theorem can be violated when a constant flux of ATP is maintain. On the contrary, if there is no constant supply of ATP, the system relaxes towards equilibrium.

Finally, in section 4.4, we compare numerical results to experimental measurements of fluctuations and response function in human RBCs.

4.1.2 Notations

In order to model the mechanical coupling between a Helfrich membrane and the underlying spectrin network, we describe the spectrin network as an assembly of identical connected entropic springs embedded in the membrane ("phantom" network) as illustrated in fig. 4.2 and similarly to [Fournier 2004, Dubus 2006]. To simplify the calculations, we start deriving results for a 1-dimensional nearly flat membrane and then a 1-dimensional nearly circular membrane. We generalize the procedure to 2-dimensional nearly spherical membranes in section 4.3. General notations are therefore introduced here directly in the more general 2 dimensions case.

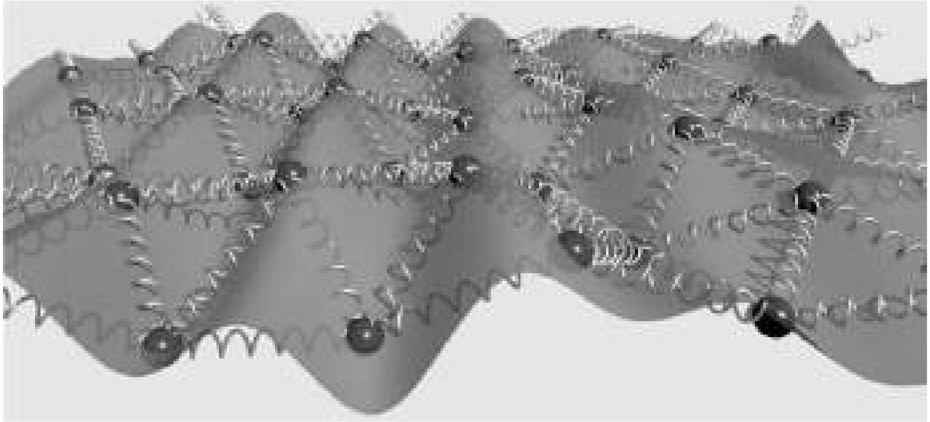

Figure 4.1: Sketch of a 2D membrane and phantom spectrin network. Spectrin filaments are modelled as entropic springs, the ends of which are embedded in the membrane. (Adapted from [Dubus 2006])

The state of zero energy of the composite membrane is the following: the membrane is flat, the network is fully relaxed and fully disconnected. We denote by the subscript 0, the average state of the RBC membrane – called reference state in the text – around which we study the fluctuations. In this average state: (1) the membrane geometry is either flat, circular or spherical. (2) The network is prestressed by imposing the average spectrin elongation ξ_0 larger than its resting length l_0. (3) The spectrin network is connected to the membrane with an average density ρ_0^{B} (defined in eq. (4.5)).

The internal energy of the system is defined as the sum $\mathcal{U} = \mathcal{U}_m + \mathcal{U}_S$ of the energy of the lipid bilayer membrane $\mathcal{U}_m$ and the energy of the spectrin filaments $\mathcal{U}_S$. We study both the fluctuations of the lipid-bilayer and the fluctuations of the network attachment.

The lipid-bilayer energy is given by the classical Helfrich equation, with by a bending energy κ_m and a surface tension σ_m. We write the Helfrich energy below in the Monge representation:

$$\Delta\mathcal{U}_m\left[h(\mathbf{r})\right] = \int_A d\mathbf{r}\left\{\frac{\kappa_m}{2}\left[\boldsymbol{\nabla}^2 h(\mathbf{r})\right]^2 + \sigma_m\left(1+\frac{1}{2}[\boldsymbol{\nabla} h(\mathbf{r})]^2\right)\right\} \tag{4.1}$$

The second contribution corresponds to the spectrin network. We start with a discrete definition of the energy stored in the network: we consider N elastic filaments that can bind and unbind the complex junctions in the membrane

$$\Delta\mathcal{U}_S\left[\,\{l_i, b_i\}\,\right] = \sum_{i=1}^{N} b_i \left\{\frac{k}{2}\left[l_i - l_0\right]^2 - E_B\right\}, \tag{4.2}$$

where k is the spring stiffness, l_i is the current spring length and l_0 its resting length, E_B is the typical binding energy and $b_{0\leq i\leq N}$ are N binary variables: $b_i = 1$ when the filament is bound (B), $b_i = 0$ when unbound (U).

On length scales much larger than the local mean elongation of springs, we define a spring density $\rho(\mathbf{r})$ to coarse-grain the problem

$$\rho(\mathbf{r}, t) = \sum_{i=1}^{N} \delta\Big(\mathbf{r} - (\bar{\mathbf{r}}_i + \mathbf{r}_i)/2\Big), \tag{4.3}$$

where $\frac{\bar{\mathbf{r}}_i + \mathbf{r}_i}{2}$ is the mean coordinate of the center of the ith spring.

The definition of the density of bound and unbound springs is deduced as

$$\rho^\mathrm{B}(\mathbf{r}, t) = \sum_{i=1}^{N} b_i(t)\,\delta\Big(\mathbf{r} - (\bar{\mathbf{r}}_i + \mathbf{r}_i)/2\Big), \tag{4.4a}$$

$$\rho^\mathrm{U}(\mathbf{r}, t) = \sum_{i=1}^{N} \Big(1 - b_i(t)\Big)\,\delta\Big(\mathbf{r} - (\bar{\mathbf{r}}_i + \mathbf{r}_i)/2\Big). \tag{4.4b}$$

We assume in the following that the springs are uniformly distributed in the membrane $\rho(\mathbf{r}, t) = \rho_0$. The average density of bound springs is therefore also uniform in space

$$\rho_0^\mathrm{B} = \langle\rho^\mathrm{B}(\mathbf{r}, t)\rangle = \rho_0 - \rho_0^\mathrm{U}, \tag{4.5}$$

The deviation from the average density of bound springs reads simply

$$\delta\rho^\mathrm{B}(\mathbf{r}, t) = \rho^\mathrm{B}(\mathbf{r}, t) - \rho_0^\mathrm{B}. \tag{4.6}$$

On this length scale we can also define a coarse-grained spectrin elongation $l(\mathbf{r})$ and the continous spectrin energy contribution is reformulated as

$$\Delta\mathcal{U}_S\left[l(\mathbf{r}), \rho^\mathrm{B}(\mathbf{r})\right] = \int_A d\mathbf{r}\,\rho^\mathrm{B}(\mathbf{r}) \left\{\frac{k}{2}\left[l(\mathbf{r}) - l_0\right]^2 - E_B\right\}. \tag{4.7}$$

In the following we consider only the fluctuations at length scales much larger than the mean spectrin filament length ξ_0: $q\xi_0 \ll 1$. In the regime $q\xi_0 > 1$ the fluctuation spectrum is dominated by the lipid bilayer mechanics alone.

4.2 Coupling the RBC membrane to the chemical reaction

4.2.1 Coupling of the spectrin cytoskeleton and lipid bilayer

The aim of this section is to express the local spectrin elongation $l(\mathbf{r})$ as a function of the membrane deflection $h(\mathbf{r})$ and to deduce the fluctuation spectrum of the composite membrane with unbinding events for

- a quasi-planar 1-dimensional membrane section 4.2.1.1
- a quasi-circular 1-dimensional membrane section 4.2.1.2

4.2.1.1 Nearly flat 1D membrane

We start with a nearly flat membrane in the Monge representation, and calculate the elongation of a single spring as a function of the membrane undulations. This elongation has a contribution to the energy of the RBC membrane that we evaluate at a coarse-grained level. We show that the effective mechanical parameters of the membrane (tension and bending) are renormalized by a prestressed spectrin network. We then allow for the density of spectrin stiffness to vary locally to take into account the possible local detachment or weakening induced by the presence of ATP molecules.

Discrete and continuous spectrin elongation

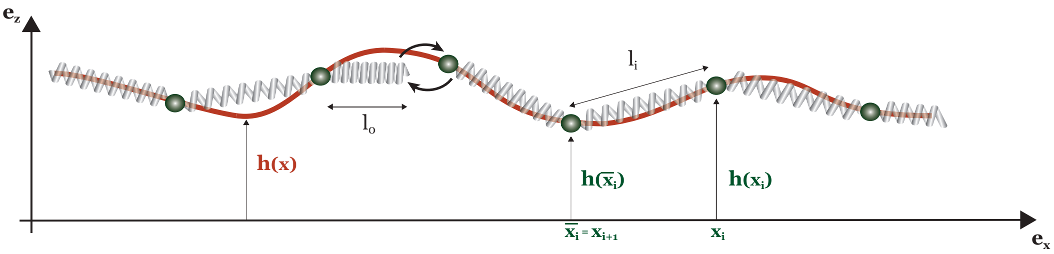

Figure 4.1: Sketch of the 1-dimensional lipid-bilayer and phantom spectrin network. The membrane shape is described in the Monge representation by the height $h(x)$. The springs ends can reversibly attach and detach to complex junctions represented by green dots. We assume that these junctions do not slide within the membrane: their longitudinal position $\bar{x}_i = x_{i+1}$ is kept fixed.

Each spring i is comprised between two anchoring nodes, lying in the membrane at the positions $\bar{\mathbf{r}}_i$ and $\mathbf{r}_i$. Their coordinates in the Monge representation are $\bar{x}_i$, x_i and $h(\bar{x}_i)$, $h(x_i)$ (see fig. 4.2). The density of bound spectrin filaments has units of L^{-1} here and reads

$$\rho^{\mathrm{B}}(x) = \sum_{i=1}^{N} b_i \, \delta\left(x - \frac{\bar{x}_i + x_i}{2}\right) , \tag{4.8}$$

We first evaluate the vectorial position difference between the two ends of the ith spring

$$\bar{\mathbf{r}}_i - \mathbf{r}_i = [\bar{x}_i - x_i]\,\mathbf{e}_x + [h(\bar{x}_i) - h(x_i)]\,\mathbf{e}_z\,. \tag{4.9}$$

We define the typical spectrin filament elongation for a perfectly flat membrane

$$\xi_0 \equiv x_i - \bar{x}_i \geq 0 \tag{4.10}$$

and evaluate the height difference up to order 2 in ξ_0

$$h(\bar{x}_i) - h(x_i) \approx \frac{\partial h}{\partial x}\xi_0 + \frac{1}{2}\frac{\partial^2 h}{\partial x^2}\xi_0^2 \tag{4.11}$$

The elongation l_i of a filament can be calculated as

$$\begin{aligned} l_i = \sqrt{(\bar{\mathbf{r}}_i - \mathbf{r}_i)^2} \quad &\approx \quad \sqrt{\xi_0^2 + \left[\frac{\partial h}{\partial x}\xi_0 + \frac{1}{2}\frac{\partial^2 h}{\partial x^2}\xi_0^2\right]^2} \\ &\approx \quad \xi_0\sqrt{1 + \left(\frac{\partial h}{\partial x} + \frac{\xi_0}{2}\frac{\partial^2 h}{\partial x^2}\right)^2} \\ &\approx \quad \xi_0\left[1 + \frac{1}{2}\left(\frac{\partial h}{\partial x} + \frac{\xi_0}{2}\frac{\partial^2 h}{\partial x^2}\right)^2\right] \end{aligned} \tag{4.12}$$

Energy of the composite membrane

We deduce the elastic energy stored in one spring up to order 2 in h and its derivatives

$$\begin{aligned} e_i^{\text{flat}} &= \frac{k}{2}\left\{l_i - l_0\right\}^2 \\ &\approx \frac{k}{2}\left\{(\xi_0 - l_0)^2 + 2(\xi_0 - l_0)\frac{\xi_0}{2}\left(\frac{\partial h}{\partial x} + \frac{\xi_0}{2}\frac{\partial^2 h}{\partial x^2}\right)^2 + \frac{\xi_0^2}{4}\left(\frac{\partial h}{\partial x} + \frac{\xi_0}{2}\frac{\partial^2 h}{\partial x^2}\right)^4\right\} \\ &\approx \frac{k}{2}\left\{(\xi_0 - l_0)^2 + \xi_0(\xi_0 - l_0)\left(\frac{\partial h}{\partial x} + \frac{\xi_0}{2}\frac{\partial^2 h}{\partial x^2}\right)^2\right\} \end{aligned} \tag{4.13}$$

The continuous spectrin energy for a 1-dimensional flat membrane reads finally as a function of $h(x)$

$$\Delta\mathcal{U}_S^{\text{flat}}[h(x), \rho^{\text{B}}(x)] = \int_L dx\,\rho^{\text{B}}(x)\left\{\frac{k\,\xi_0^2}{2}\left[\chi_0^2 + \chi_0\left(\frac{\partial h}{\partial x} + \frac{\xi_0}{2}\frac{\partial^2 h}{\partial x^2}\right)^2\right] - E_B\right\}, \tag{4.14}$$

where we have defined a spectrin network prestress parameter

$$\chi_0 \equiv 1 - \frac{l_0}{\xi_0}\,. \tag{4.15}$$

The sign of χ_0 determines the nature of the prestress

- $\chi_0 = 0$ corresponds to a fully relaxed network in average ($\xi_0 = l_0$).
- $\chi_0 > 0$ corresponds to a network under tension ($\xi_0 > l_0$).
- $\chi_0 < 0$ corresponds to a network under compression ($\xi_0 < l_0$).

Note that if the spectrin filament elongation ξ_0 in the reference state is exactly l_0 ($\chi_0 = 0$ fully relaxed network), the deflection of the membrane does not contribute to increase the spectrin elastic energy at our order of approximation. A theory taking into account the membrane deformation at higher order would probably require the use of renormalization group techniques [Peterson 1992].

We therefore maintain a positive prestress $\chi_0 > 0$ in the composite membrane by applying an longitudinal force $\mathbf{f}_0$ to both ends of the spectrin network $\mathbf{r}_0 = \bar{\mathbf{r}}_1$ and $\mathbf{r}_N$[1], as represented on fig. 4.2.

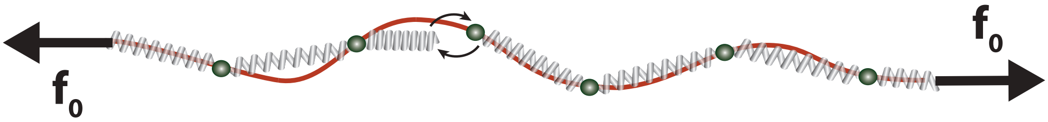

Figure 4.2: Sketch of the 1-dimensional membrane and spectrin network prestressed by a longitudinal force $\mathbf{f}_0$.

The work $\Delta\mathcal{W}^{\text{flat}}$ exerted by the force $\mathbf{f}_0$ between the prestressed state and a fully relaxed network reads

$$\Delta\mathcal{W}^{\text{flat}} = -\mathbf{f}_0 \cdot \Delta\mathbf{r} = -f\mathbf{e}_x \cdot \left[(\mathbf{r}_N - \mathbf{r}_0) - N\, l_0 \mathbf{e}_x\right] = -f_0 \int_L dx\; (\xi_0 - l_0) \tag{4.16}$$

The 1-dimensional lipid-bilayer energy in the Monge representation reads

$$\Delta\mathcal{U}_m^{\text{flat}}\left[h(x)\right] = \int_L dx \left\{ \frac{\kappa_m^{\text{1D}}}{2} \left[\frac{\partial^2 h}{\partial x^2}\right]^2 + \frac{\sigma_m^{\text{1D}}}{2} \left[\frac{\partial h}{\partial x}\right]^2 \right\}, \tag{4.17}$$

where σ_m^{1D} and κ_m^{1D} are the lipid-bilayer 1-dimensional tension and 1-dimensional bending modulus. Note their unusual dimensions, compared to classical 2-dimensional membranes: $\left[\sigma^{\text{1D}}\right] = \frac{\text{Energy}}{\text{Length}} = \left[\sigma^{\text{2D}}\right] \times \text{Length}$ and $\left[\kappa^{\text{1D}}\right] = \text{Energy} \times \text{Length} = \left[\kappa^{\text{2D}}\right] \times \text{Length}$.

The variation of energy for the composite membrane, composed by the lipid-bilayer and its underlying spectrin network, is the sum of the energy variations

---

[1] This force mimics the effect of a pressure for a curved and closed membrane.

$\Delta\mathcal{U}_m^{\text{flat}}$ (4.17), $\Delta\mathcal{U}_S^{\text{flat}}$ (4.15) and the work $\Delta\mathcal{W}^{\text{flat}}$ of the constant force $\mathbf{f}_0$ (4.16):

$$\begin{aligned}\Delta\mathcal{U}^{\text{flat}}\big(h(x),\rho^{\text{B}}(x)\big) = \int_L dx \Bigg\{ & \frac{\kappa_m^{\text{1D}}}{2}\left[\frac{\partial^2 h}{\partial x^2}\right]^2 + \frac{\sigma_m^{\text{1D}}}{2}\left[\frac{\partial h}{\partial x}\right]^2 \\ & + \rho^{\text{B}}(x)\left(\frac{k\,\xi_0^2}{2}\left[\chi_0^2 + \chi_0\left(\frac{\partial h}{\partial x} + \frac{\xi_0}{2}\frac{\partial^2 h}{\partial x^2}\right)^2\right] - E_B\right) \\ & - f_0\,(\xi_0 - l_0)\Bigg\}\end{aligned}$$

For the reference state $h(x) = 0$ and $\rho^{\text{B}}(x) = \rho_0^{\text{B}}$, the variation of the internal energy reads simply $\Delta\mathcal{H}_0^{\text{1D flat}} = L_0\rho_0^{\text{B}}\left[\frac{k(\xi_0-l_0)^2}{2} - -f_0(\xi_0 - l_0)\right]$. By deriving it with respect to ξ_0, we obtain the longitudinal force balance. We deduce that the force f_0 necessary to hold the system {membrane + spectrin} in a prestressed state is simply

$$f_0 = \rho_0^{\text{B}}\,k\,(\xi_0 - l_0) \tag{4.18}$$

Langevin equation for the membrane height

The dynamics of the membrane height is given by an overdamped Langevin equation

$$\frac{\partial h}{\partial t}(x,t) = \int_{-\infty}^{+\infty} dx'\,\Lambda^{\text{1D}}(x-x')\left\{-\frac{\delta\Delta\mathcal{U}^{\text{flat}}}{\delta h(x',t)} + \zeta^h(x',t)\right\} \tag{4.19}$$

where $\Lambda^{\text{1D}}(x)$ is the diagonal part of the Oseen tensor in one dimension that quantifies the viscous drag exerted by the surrounding fluid. Its expression is given in section 4.B.

$\zeta^h(x,t)$ is a Gaussian white noise satisfying the fluctuation-dissipation relation:

$$\left\langle \zeta^h(x,t)\right\rangle = 0\,, \tag{4.20a}$$

$$\left\langle \zeta^h(x,t)\zeta^h(x',t')\right\rangle = 2\,k_{\text{B}}T\,\Lambda^{\text{1D}\,-1}(x-x')\delta(t-t') \tag{4.20b}$$

The force per unit length on the membrane is calculated in real space as a functional derivative

$$\begin{aligned}f^{\text{1D flat}}(x,t) \equiv -\frac{\delta\Delta\mathcal{U}^{\text{flat}}}{\delta h(x,t)} = & -\kappa_m^{\text{1D}}\frac{\partial^4 h(x,t)}{\partial x^4} + \sigma_m^{\text{1D}}\frac{\partial^2 h(x,t)}{\partial x^2} \\ & + k\,\xi_0^2\chi_0\Bigg\{\frac{\partial}{\partial x}\left[n_B(x,t)\left(\frac{\partial h(x,t)}{\partial x} + \frac{\xi_0}{2}\frac{\partial^2 h(x,t)}{\partial x^2}\right)\right] \\ & - \frac{\xi_0}{2}\frac{\partial^2}{\partial x^2}\left[n_B(x,t)\left(\frac{\partial h(x,t)}{\partial x} + \frac{\xi_0}{2}\frac{\partial^2 h(x,t)}{\partial x^2}\right)\right]\Bigg\}\end{aligned} \tag{4.21}$$

Chemical Langevin equation for the bound spring density

We define the Helmotz free energy of the system {membrane+spectrin} as $\mathcal{F} = \mathcal{U} - TS$, where S is the Boltzmann entropy of the system classically defined by $S = k_\mathrm{B} \log \Omega$. Ω is the number of ways of arranging N_B bound springs and N_U unbound springs on the 1D lattice[2], where $N = N_\mathrm{B} + N_\mathrm{U}$ is the total number of springs or lattice sites.

The number of permutations of the N springs, taking into account the fact that the N_B bound springs and the N_U unbound springs are indistinguishable is

$$\Omega = \frac{N!}{N_\mathrm{B}!\, N_\mathrm{U}!} \,. \tag{4.22}$$

We use the Stirling's approximation $\log n! = \sum_k \log k \approx \int_1^n dk\, \log k = k \log k - k$ to evaluate the entropy difference from a fully disconnected network to the current configuration

$$\Delta S = -k_\mathrm{B} \left[N_\mathrm{B} \log \left(\frac{N_\mathrm{B}}{N} \right) + N_\mathrm{U} \log \left(\frac{N_\mathrm{U}}{N} \right) \right] \tag{4.23}$$

We recognize the classical mixing entropy for two ideal gases that we generalize to continuous variables

$$\Delta S_\mathrm{mix}^\mathrm{flat} = -k_\mathrm{B} \int_L dx \, \left[\rho^\mathrm{B}(x) \log \left(\frac{\rho^\mathrm{B}(x)}{\rho_0} \right) + \left(\rho_0 - \rho^\mathrm{B}(x) \right) \log \left(\frac{\rho_0 - \rho^\mathrm{B}(x)}{\rho_0} \right) \right]$$

The functional derivative of the free energy variation $\Delta \mathcal{F}^\mathrm{flat} = \Delta \mathcal{U}^\mathrm{flat} - T \Delta S_\mathrm{mix}^\mathrm{flat}$ with respect to $\rho^\mathrm{B}(x)$ leads to the chemical potential difference between the bound and unbound species

$$\begin{aligned} \Delta \mu^\mathrm{UB} &\equiv \frac{\delta \Delta \mathcal{F}^\mathrm{flat}}{\delta \rho^\mathrm{B}(x)} \\ &= \frac{k \xi_0^2}{2} \left[\chi_0^2 + \chi_0 \left(\frac{\partial h}{\partial x} + \frac{\xi_0}{2} \frac{\partial^2 h}{\partial x^2} \right)^2 \right] + k_\mathrm{B} T \log \left(\frac{\rho^\mathrm{B}(x)}{\rho_0 - \rho^\mathrm{B}(x)} \right) - E_\mathrm{B} \,. \end{aligned} \tag{4.24}$$

At equilibrium $\Delta \mu^\mathrm{UB} = 0$. This leads to the following local detailed balance

$$\frac{\rho^\mathrm{B}(x)}{\rho_0 - \rho^\mathrm{B}(x)} = \exp \left[\frac{E_\mathrm{B} - \frac{k \xi_0^2}{2} \left[\chi_0^2 + \chi_0 \left(\frac{\partial h}{\partial x} + \frac{\xi_0}{2} \frac{\partial^2 h}{\partial x^2} \right)^2 \right]}{k_\mathrm{B} T} \right] , \tag{4.25}$$

Let us consider explicitly the attachment/detachment reaction

$$\mathrm{Sp}^\mathrm{B} \underset{k_\mathrm{off}}{\overset{k_\mathrm{on}}{\rightleftharpoons}} \mathrm{Sp}^\mathrm{U} \,, \tag{4.26}$$

---

[2] The calculation would be exactly similar on a 2D lattice.

where Sp^{B} and Sp^{U} are respectively the bound and unbound states of the spectrin filament, and k_{on} and k_{off} the attachment and detachment reaction rates.

We can write a chemical Langevin equation for the bound density to describe this reaction dynamics (see section 4.D and section 4.2.2)

$$\frac{\partial \rho^{\mathrm{B}}(x,t)}{\partial t} = k_{\mathrm{on}}(x,t)\left(\rho_0 - \rho^{\mathrm{B}}(x,t)\right) - k_{\mathrm{off}}(x,t)\,\rho^{\mathrm{B}}(x,t) + \zeta^{\mathrm{B}}(x,t) \tag{4.27}$$

where $\zeta^{\mathrm{B}}(x,t)$ is a Gaussian chemical white noise satisfying the fluctuation-dissipation theorem

$$\left\langle \zeta^{\mathrm{B}}(x,t)\right\rangle = 0\,, \tag{4.28a}$$

$$\left\langle \zeta^{\mathrm{B}}(x,t)\zeta^{\mathrm{B}}(x',t')\right\rangle = 2\rho_0 \frac{k_{\mathrm{on}}k_{\mathrm{off}}}{k_{\mathrm{on}}+k_{\mathrm{off}}}\delta(x-x')\delta(t-t') \tag{4.28b}$$

The steady-state solution $\langle \rho^{\mathrm{B}}(x,t)\rangle$ verifies

$$\frac{\langle \rho^{\mathrm{B}}(x,t)\rangle}{\rho_0 - \langle \rho^{\mathrm{B}}(x,t)\rangle} = \frac{k_{\mathrm{on}}}{k_{\mathrm{off}}}\,. \tag{4.29}$$

From the detailed balance (4.25) and eq. (4.29) we can deduce the following expression for k_{on} and k_{off}

$$k_{\mathrm{on}}(x,t) = k^{o}\,\exp\left(-\frac{k\xi_0^2}{2\,k_{\mathrm{B}}T}\left[\chi_0^2 + \chi_0\left(\frac{\partial h}{\partial x} + \frac{\xi_0}{2}\frac{\partial^2 h}{\partial x^2}\right)^2\right]\right) = k^{o}\,\exp\left(-\frac{k\,(l(x)-l_0)}{2\,k_{\mathrm{B}}T}\right), \tag{4.30a}$$

$$k_{\mathrm{off}} = k^{o}\,\exp\left(\frac{-E_{\mathrm{B}}}{k_{\mathrm{B}}T}\right). \tag{4.30b}$$

Note other choices of k_{on} and k_{off} are possible, as long as they verify the detailed balance. The choice we make is guided by a Kramers approach to this problem (see section 4.A).

The Langevin dynamics for the bound density deviation $\delta\rho^{\mathrm{B}}(x)$ at first order in $\delta\rho^{\mathrm{B}}$ and $h(x,t)$ follows as

$$\frac{\partial \delta\rho^{B}(x,t)}{\partial t} = -\left(k_{\mathrm{on}0} + k_{\mathrm{off}}\right)\delta\rho^{\mathrm{B}}(x,t) + (\rho_0 - \rho_0^{\mathrm{B}})\delta k_{\mathrm{on}}(x,t) + \zeta^{\mathrm{B}}(x,t)\,. \tag{4.31}$$

Fourier space

We assume a periodic membrane sample of size L and turn previous equations into 1-dimensional spatial Fourier space.

Fourier transform of a function $g(x)$ is defined as $\tilde{g}_q = \int_L dx\, g(x)\, e^{-iqx}$. The quantity $\tilde{g}_q$ derives from a function periodic in x, as a consequence of the assumed periodicity of the system.

The inverse transform reads therefore $g(x) = \frac{1}{L}\sum_q \tilde{g}_q\, e^{iqx}$

We rewrite the Langevin equation for the membrane height (4.19) in Fourier space

$$\frac{d\tilde{h}_q}{dt} = \tilde{\Lambda}_q^{1\mathrm{D}} \left[\tilde{f}_q^{1\mathrm{D}} + \tilde{\zeta}_q^h(t)\right] . \tag{4.32}$$

The Fourier transform of the force on the membrane (4.21) reads

$$\begin{aligned} \tilde{f}_q^{1\mathrm{D}}(t) \;\; &= \;\; -\left[\kappa_m^{1\mathrm{D}} q^4 + \sigma_m^{1\mathrm{D}} q^2\right] \tilde{h}_q(t) \\ &\quad - k\xi_0^2\chi_0\, \frac{1}{L}\sum_{q'} \tilde{\rho}^{\mathrm{B}}_{q-q'}(t)\, \tilde{h}_{q'}(t) \left[qq' + i\, qq'(q'-q)\frac{\xi_0}{2} + \frac{\xi_0^2}{4}(qq')^2\right] , \end{aligned} \tag{4.33}$$

and the mechanical noise correlation becomes (4.20)

$$\left\langle \tilde{\zeta}_q^h(t)\tilde{\zeta}_{q'}^h(t')\right\rangle = 2\, k_B T\, L\tilde{\Lambda}_q^{-1}\delta(q+q')\delta(t-t') . \tag{4.34}$$

For the chemical Langevin equation of $\delta\rho_q^{\mathrm{B}}$, we obtain

$$\frac{d\delta\tilde{\rho}_q^B}{dt} = -\left(k_{\mathrm{on}0} + k_{\mathrm{off}}\right) \delta\tilde{\rho}_q^{\mathrm{B}}(t) + (\rho_0 - \rho_0^{\mathrm{B}})\delta\tilde{k}_{\mathrm{on\,q}}(t) + \zeta_q^{\mathrm{B}} , \tag{4.35}$$

with the chemical noise correlation in Fourier space at equilibrium (4.28b)

$$\left\langle \tilde{\zeta}_q^{\mathrm{B}}(t)\tilde{\zeta}_{q'}^{\mathrm{B}}(t')\right\rangle = 2\rho_0 \frac{k_{\mathrm{on}}k_{\mathrm{off}}}{k_{\mathrm{on}} + k_{\mathrm{off}}}\delta(q+q')\delta(t-t') . \tag{4.36}$$

Mechanical and chemical Langevin equations at first-order

We consider that $h_q(t)$ and $\delta\rho_q^{\mathrm{B}}$ are of same order (when normalized) and we limit ourselves to the first-order approximation.

$\delta k_{\mathrm{on\,q}} = \frac{\partial k_{\mathrm{on\,q}}}{\partial h_q} h_q$ is of second-order in h_q and therefore neglected. The chemical Langevin equation becomes independent of h_q at first-order

$$\frac{\partial\delta\rho_q^B}{\partial t} = -\left(k_{\mathrm{on}0} + k_{\mathrm{off}}\right) \delta\rho_q^{\mathrm{B}}(t) + \zeta_q^{\mathrm{B}} . \tag{4.37}$$

Similarly, the Langevin equation for the membrane height is independent of $\delta\rho_q^{\mathrm{B}}$ at first-order

$$\frac{d\tilde{h}_q}{dt} = \tilde{\Lambda}_q^{1\mathrm{D}} \left[f_q^{1\mathrm{D}} + \tilde{\zeta}_q^h(t)\right] , \tag{4.38a}$$

$$f_q^{1\mathrm{D}} = -\left(\kappa_m^{1\mathrm{D}}\, q^4 + \sigma_m^{1\mathrm{D}}\, q^2\right)\tilde{h}_q(t) + \rho_0^{\mathrm{B}}\, k\xi_0^2\chi_0 \left(q^2 + \frac{\xi_0^2}{4}q^4\right) \tilde{h}_q(t) \tag{4.38b}$$

Discussion

The first effect of the spectrin network is to renormalize the lipid bilayer mechanics. The force on the membrane (4.38b) can indeed be rewritten as if we had only a lipid bilayer with the following effective membrane tension and bending modulus

$$\sigma_{\text{eff}}^{1\text{D}} = \sigma_m^{1\text{D}} + \rho_0^{\text{B}}\, k\, \xi_0^2 \chi_0\,, \tag{4.39a}$$

$$\kappa_{\text{eff}}^{1\text{D}} = \kappa_m^{1\text{D}} + \rho_0^{\text{B}}\, k \frac{\xi_0^4}{4} \chi_0\,. \tag{4.39b}$$

The spectrin contribution to the tension and bending modulus are formally similar to the ones calculated in [Fournier 2004] and later in [Dubus 2006] where they considered a fully connected network ($\rho_0^{\text{B}} = \rho_0$) in 2 dimensions. The contribution to the bending modulus is however found here of opposite sign than [Dubus 2006]. The sign of the bending modulus renormalization is generally tedious to predict, and we propose that our opposite sign may come from the fact that we have neglected the translational degree of freedom of the junctions within the membrane. This effect is anyway expected to be small, as we discussed in fig. 3.10 A.

We see in eq. (4.37) and eq. (4.38) that for a flat membrane there is no first-order coupling between the membrane mechanics and the chemical reaction. A first-order coupling can be reintroduced remarking that the spectrin network is not embedded in the lipid bilayer but lies at a finite distance $d > 0$. This would make the membrane asymmetric, and we can recalculate the spectrin energy (4.15) taking into account this finite distance d. It leads to a spontaneous curvature-like term of the form $\delta\rho_q^{\text{B}}\, k\xi_0^2\chi_0\, d\, q^2$ in the force on the membrane (4.38b). The thickness d of the junction complexes being only a few nanometers long, the contribution of this effect on the fluctuation spectrum is however negligible numerically.

Another alternative is to choose a naturally curved reference state of the composite membrane as we propose in the next section.

4.2.1.2 Nearly circular 1D membrane

We repeat here essentially the same calculations as in the previous section, but in a circular geometry. We show in the following that imposing a naturally curved reference state to the system {membrane+spectrin} introduces a non-zero contribution of local attachment variations to the membrane height fluctuation spectrum.

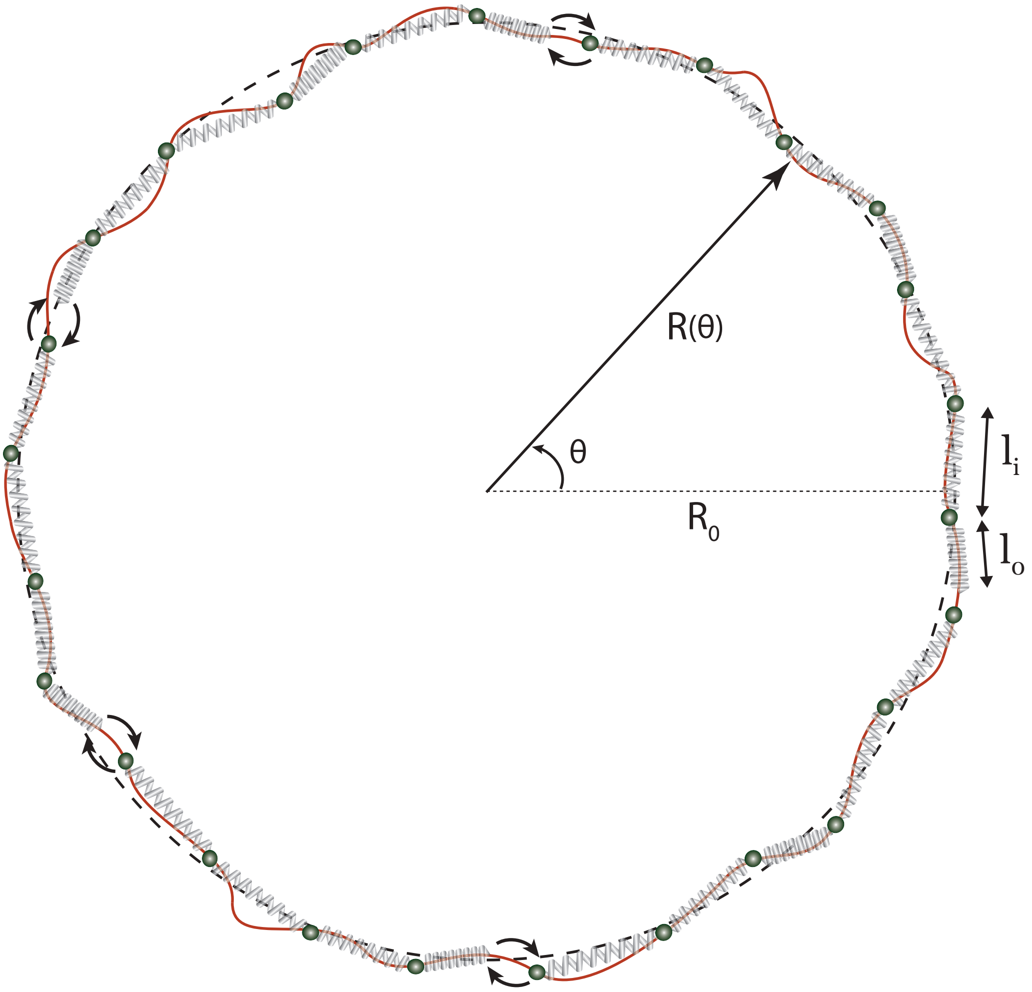

Figure 4.3: Sketch of the circular 1D membrane and embedded spectrin network. The membrane shape is described by the radius $R(\theta) = R_0 + h(\theta)$. The springs ends can reversibly attach and detach to complex junctions represented by green dots. We assume that these junctions do not slide within the membrane: their polar position $\bar{\theta}_i = \theta_{i+1}$ is kept fixed.

Discrete and continuous spectrin elongation

We limit ourselves here to first-order in $|\bar{\mathbf{r}}_i - \mathbf{r}_i|$ in the Taylor expansion of $h(\bar{\mathbf{r}}_i) - h(\mathbf{r}_i)$. For the nearly flat membrane we have done the calculation up to second order (see eq. (4.9)) in order to calculate the renormalization of the bending modulus by the spectrin network. Here we consider only the renormalization of the membrane tension. The spectrin effect on the bending modulus is indeed very weak, in comparison to the renormalization of the tension. For the wavelengths of interest ($q^{-1} \gg \xi_0$), the ratio of the two effects for the flat membrane (4.39) is indeed $\frac{\rho_0^{\mathrm{B}}\, k\, \xi_0^4/4\chi_0\, q^4}{\rho_0^{\mathrm{B}}\, k\, \xi_0^2 \chi_0\, q^2} = \left(\frac{q\xi_0}{2}\right)^2 \ll 1$.

The 1-dimensional nearly circular membrane shape is described in polar coordinates $\Big(\theta, R(\theta)\Big)$ as illustrated on fig. 4.3.

We define the dimensionless membrane height deflection $u(\theta)$ as follows $R(\theta) = R_0 + h(\theta) = R_0\Big(1 + u(\theta)\Big)$. R_0 is defined by the area conservation $A = 4\pi R_0^2$. The fluctuating shape is therefore not expanded around the corresponding stationary shape but rather around a disk with the same total area.

We first evaluate the vectorial position difference between the two ends of the ith spring

$$\bar{\mathbf{r}}_i - \mathbf{r}_i = R(\theta_{i+1})\mathbf{e}_r(\theta_{i+1}) - R(\theta_i)\mathbf{e}_r(\theta_i) \approx R_0 \Delta\theta_i \left\{ \frac{\partial u}{\partial \theta}\mathbf{e}_r + \Big[1 + u(\theta)\Big]\mathbf{e}_\theta \right\} . \tag{4.40}$$

We evaluate the ith spectrin filament length up to order 2 in $u(\theta)$ and its first derivative

$$l_i = \sqrt{(\bar{\mathbf{r}}_{i+1} - \mathbf{r}_i)^2} \approx R_0 \Delta\theta_i \left\{ 1 + u(\theta) + \frac{1}{2}\left(\frac{\partial u}{\partial \theta}\right)^2 \right\} . \tag{4.41}$$

From here on, we suppose that the junctions have a fixed polar coordinate θ_i and are uniformly distributed along the membrane $R_0 \Delta_i \equiv \xi_0$.

Spectrin network energy

We calculate the elastic energy stored in one spring up to 2nd order in u and its successive polar derivatives, denoted u', u", $u^{(3)}$ ...

$$e_i^{\mathrm{circ}} = \frac{k}{2}\left\{l_i - l_0\right\}^2 \approx \frac{k}{2}\xi_0^2 \left\{\chi_0^2 + 2\chi_0\, u + u^2 + \chi_0\, u'^2\right\} , \tag{4.42}$$

where we have defined the prestress parameter $\chi_0 = 1 - l_0/\xi_0$, as previously for the nearly flat membrane.

The continuous spectrin energy for a 1D circular membrane is deduced from its general definition (4.7) as a function of $u(\theta)$

$$\Delta\mathcal{U}_s^{\mathrm{circ}}\big[u(\theta), \rho^{\mathrm{B}}(\theta)\big] = R_0 \int d\theta\, \rho^{\mathrm{B}} \left\{ \frac{k\xi_0^2}{2}\left[\chi_0^2 + 2\chi_0\, u + u^2 + \chi_0\, u'^2\right] - E_B \right\} . \tag{4.43}$$

Membrane energy

The energy associated with the 1-dimensional circular membrane tension and curvature reads formally

$$\Delta\mathcal{U}_m^{\mathrm{circ}} = \int ds \left\{ \sigma_m^{\mathrm{1D}} + \frac{\kappa_m^{\mathrm{1D}}}{2}\, C(s)^2 \right\} , \tag{4.44}$$

where s is the curvilinear length along the membrane and $C(s)$ it the local curvature.

The small variation of curvilinear length ds is given by Pythagore's theorem $ds \approx R_0 d\theta \left[1 + u(\theta) + \frac{1}{2}\left(\frac{\partial u}{\partial \theta}\right)^2\right]$.

In polar coordinates, the curvature is given by

$$C(\theta) = \frac{R^2 + 2R'^2 - RR''}{(R^2 + R'^2)^{3/2}} =\approx \frac{1}{R_0}\left(1 - u - u'' + 2uu'' + u^2 + \frac{1}{2}u'^2\right) . \tag{4.45}$$

Up to order 2 in u and its derivatives, the membrane energy reads therefore

$$\begin{aligned} \Delta\mathcal{U}_m^{\text{circ}}[u(\theta)] \;\approx\; & R_0 \int_0^{2\pi} d\theta \left\{ \sigma_m^{\text{1D}} \left[1 + u + \frac{1}{2}u'^2\right] \right. \\ & \left. + \frac{\kappa_m^{\text{1D}}}{2R_0^2}\left[1 - u - 2u'' + 4uu'' + u^2 + \frac{3}{2}u'^2 + u''^2\right] \right\} . \end{aligned} \tag{4.46}$$

Decomposition in Fourier series

We note $s_0 = R_0\theta$ the curvilinear coordinate and $L_0 = 2\pi R_0$ the membrane length, and decompose any function $g(R_0\theta) \equiv g(s_0)$ in a Fourier series as follows

$$g(s_0) = \frac{1}{L_0}\sum_{q=-\infty}^{\infty} g_q\, e^{iqs_0} = \frac{1}{L_0}\left[g_0 + \sum_{|q|\geq 1} g_q\, e^{iqs_0}\right] , \tag{4.47}$$

where the Fourier coefficients can be calculated as $g_q = \int_0^{L_0} ds_0\, g(s_0)\, e^{-iqs_0}$.

Note that the previous derivatives of order d with respect to θ can be translated into derivatives in s_0 according to the following rule

$$g^{(d)} = \frac{\partial^d g}{\partial \theta^d} = R_0^d \frac{\partial g^d}{\partial s_0^d} = \sum_{q=-\infty}^{\infty} (qR_0)^d\, g_q\, e^{iqs_0} . \tag{4.48}$$

Area conservation The area A delimited by the membrane can be written

$$A = \int_0^{R(\theta)} dr \int_0^{2\pi} r d\theta = \int_0^{2\pi} \frac{R^2(\theta)}{2} \approx \pi R_0^2 + R_0^2\left[u_0 + \frac{1}{L_0}\sum_{q\geq 0}\frac{u_q^2}{2}\right] . \tag{4.49}$$

The area conservation equation $A - \pi R_0^2 = 0$ leads therefore to the following relation between the zeroth order component and the $q \geq 1$ order components of $u(s_0)$:

$$u_0 = -\frac{1}{L_0}\sum_{|q|\geq 1}\frac{u_q^2}{2} , \tag{4.50}$$

where we truncated the expansion at second order in u_q.

Note that, instead of imposing area conservation via the previous condition (4.50), we can alternatively use a (1-dimensional) pressure p_0 as a Lagrange multiplier for the area. The work $\mathcal{W} = -p_0 A$ of the pressure has to be added in the energy $\Delta\mathcal{U}^{\mathrm{circ}}$, and reads[3]

$$\Delta\mathcal{W} \approx -\frac{p_0 R_0^2}{2}\int_{L_0} ds_0 \, \left[1 + 2u + u^2\right] \,, \tag{4.51}$$

in real space up to second order in u.

The force on the membrane $f_0 = -\frac{\delta\Delta U^{\mathrm{circ}}}{\delta h}\Big|_{h=0}$ in the reference state ($h \to 0$, $\rho^{\mathrm{B}} \to \rho_0^{\mathrm{B}}$) must then vanish by force balance (the pressure compensates exactly the membrane tension and curvature). One can deduce the following pressure

$$p_0 = \rho_0^{\mathrm{B}} \frac{k\xi_0^2\chi_0}{R_0} + \frac{\sigma_m^{\mathrm{1D}}}{R_0} - \frac{\kappa_m^{\mathrm{1D}}}{2R_0^3} \,. \tag{4.52}$$

This expression is re-inserted the pressure work $\Delta\mathcal{W}$ to calculate the energy.

The resulting energy $\Delta\mathcal{U}^{\mathrm{circ}}$ is exactly the same as the one that we obtain further with the area conservation condition eq. (4.50).

Spectrin energy The density of bound filaments can be decomposed as

$$\rho^{\mathrm{B}}(s_0) = \rho_0^{\mathrm{B}} + \frac{1}{L_0}\sum_{|q|\geq 1} \delta\rho_q^{\mathrm{B}} \, e^{iqs_0} \,. \tag{4.53}$$

Note that the zeroth-order in $\delta\rho^{\mathrm{B}}(s_0)$ has been included in ρ_0^{B}.

We suppose that $\delta\rho_q^{\mathrm{B}}/\rho_0$ and u_q are of same order. By injecting the Fourier decomposition of $u(s_0)$ and $\rho^{\mathrm{B}}(s_0)$ (4.53) we express the spectrin energy (4.43) in Fourier space up to order two in u_q

$$\begin{aligned}\Delta\mathcal{U}_s^{\mathrm{circ}}[\{u_q, \delta\rho_q^{\mathrm{B}}\}] \;=\; & \rho_0^{\mathrm{B}}\frac{k\xi_0^2}{2}\left\{L_0\chi_0^2 + 2\chi_0 u_0 + \frac{1}{L_0}\sum_{|q|\geq 1} u_q^2 + \frac{\chi_0}{L_0}\sum_{|q|\geq 1}(qR_0)^2 u_q^2\right\} \\ & -\rho_0^{\mathrm{B}} L_0 \, E_{\mathrm{B}} + k\xi_0^2\chi_0 \frac{1}{L_0}\sum_{q\geq 1}\delta\rho_q^{\mathrm{B}} \, u_q \,.\end{aligned}$$

Note that u_0^2 is of order 4 in u_q (for $q \geq 1$) from the area conservation equation (4.50). It is therefore negligible.

Inserting the expression of u_0 leads to the following expression of the spectrin energy

$$\begin{aligned}\Delta\mathcal{U}_s^{\mathrm{circ}}\left[\{u_q, \delta\rho_q^{\mathrm{B}}\}_{|q|\geq 1}\right] = \rho_0^{\mathrm{B}}\frac{k\xi_0^2}{2}&\left\{\chi_0^2 L_0 + \frac{1}{L_0}\sum_{|q|\geq 1}\left[(1-\chi_0) + \chi_0 (qR_0)^2\right] u_q^2\right\} \\ & - \rho_0^{\mathrm{B}} L_0 \, E_{\mathrm{B}} + k\xi_0^2\chi_0 \frac{1}{L_0}\sum_{q\geq 1}\delta\rho_q^{\mathrm{B}} \, u_q\end{aligned}$$

---

[3] This is the method that we have adopted for the quasi-planar membrane by introducing the work $\Delta\mathcal{W}_0^{\mathrm{1D\,flat}}$ of the force f_0 to prestress the membrane.

(4.54)

Lipid-bilayer energy Similarly we can express the lipid bilayer energy as a function of $\{u_q\}_{|q|\geq 1}$ only:

$$\begin{aligned}\Delta\mathcal{U}_m^{\mathrm{circ}}\Big[\{u_q\}_{|q|\geq 1}\Big] &= \sigma_m^{\mathrm{1D}}\left\{L_0+\frac{1}{L_0}\sum_{|q|\geq 1}\Big[(qR_0)^2-1\Big]\frac{u_q^2}{2}\right\}\\ &+\frac{\kappa_m^{\mathrm{1D}}}{2R_0^2}\left\{L_0+\frac{1}{L_0}\sum_{|q|\geq 1}\left[\frac{3}{2}-\frac{5}{2}(qR_0)^2+(qR_0)^4\right]u_q^2\right\}.\end{aligned} \tag{4.55}$$

Composite membrane energy The energy of the composite membrane is the sum of the lipid bilayer energy (4.55) and the spectrin network energy (4.54)

$$\Delta\mathcal{U}^{\mathrm{circ}}=\Delta\mathcal{U}_m^{\mathrm{circ}}+\Delta\mathcal{U}_s^{\mathrm{circ}}. \tag{4.56}$$

Langevin equations

We describe the dynamics of the membrane deflection $h(s_0)$ and bound density variation $\delta\rho^{\mathrm{B}}(s_0)$ by overdamped Langevin equations in real space, as we have done previously for the nearly flat membrane

$$\frac{\partial h}{\partial t}(s_0,t)=\int_{L_0}ds_0'\,\Lambda^{\mathrm{1D}}(s_0-s_0')\left\{-\frac{\delta\Delta\mathcal{U}^{\mathrm{circ}}}{\delta h(s_0',t)}+\zeta^h(s_0',t)\right\}, \tag{4.57a}$$

$$\frac{\partial\delta\rho^B(s_0,t)}{\partial t}=-\left(k_{\mathrm{on}0}+k_{\mathrm{off}}\right)\delta\rho^{\mathrm{B}}(s_0,t)+(\rho_0-\rho_0^{\mathrm{B}})\delta k_{\mathrm{on}}(s_0,t)+\zeta^{\mathrm{B}}(s_0,t). \tag{4.57b}$$

We deduce the Langevin equation for the Fourier component[4] h_q of $h(s_0,t)=u(s_0,t)R_0$ for $|q|\geq 1$

$$\frac{dh_q}{dt}=\Lambda_q^{\mathrm{1D}}\left\{f_q^{\mathrm{circ}}+\zeta_q^h(t)\right\}, \tag{4.58}$$

where we have defined

$$\Lambda_q^{\mathrm{1D}}=\int_{L_0}ds_0\,\Lambda(s_0)\,e^{-iqs_0}, \qquad \zeta_q^h(t)=\int_{L_0}ds_0\,\zeta^h(s_0,t)\,e^{-iqs_0}.$$

The mechanical thermal noise is white and has the following correlations in spatial Fourier space, according to the fluctuation-dissipation theorem

$$\left\langle\zeta_q^h(t)\zeta_{q'}^h(t')\right\rangle=2k_{\mathrm{B}}T\,L_0\Lambda_q^{-1}\delta(q+q')\delta(t-t'). \tag{4.59}$$

---

[4] Note that the zeroth order $h_0=0$.

We calculate the force on the membrane in Fourier space

$$
\begin{aligned}
f_q^{\mathrm{circ}} &= -\frac{1}{R_0}\frac{\delta \Delta U^{\mathrm{circ}}}{\delta u_q} \\
&= -\frac{\sigma_m^{\mathrm{1D}}}{R_0}\left[(qR_0)^2 - 1\right] u_q - \frac{\kappa_m^{1D}}{R_0^3}\left[\frac{3}{2} - \frac{5}{2}(qR_0)^2 + (qR_0)^4\right] u_q \\
&\quad -\frac{\rho_0^{\mathrm{B}}\, k\xi_0^2}{R_0}\left[1 - \chi_0 + \chi_0 (qR_0)^2\right] u_q - \frac{k\xi_0^2\chi_0}{R_0}\,\delta\rho_q^{\mathrm{B}}\,. \qquad (4.60)
\end{aligned}
$$

The above expression for the force can be rewritten in a compact form

$$
f_q^{\mathrm{circ}} = -\Lambda_q^{\mathrm{1D}}\left(\gamma_{\mathrm{eff}}^{\mathrm{1D}} + \sigma_{\mathrm{eff}}^{\mathrm{1D}}\, q^2 + \kappa_m^{\mathrm{1D}}\, q^4\right) h_q - \Lambda_q^{\mathrm{1D}}\frac{W_s}{R_0}\,\delta\rho_q^{\mathrm{B}} \qquad (4.61)
$$

where we define an effective confinement parameter [Gov 2003] and an effective membrane tension

$$
\gamma_{\mathrm{eff}}^{\mathrm{1D}} = \frac{3}{2}\frac{\kappa_m^{\mathrm{1D}}}{R_0^4} - \frac{\sigma_m^{\mathrm{1D}}}{R_0^2} + \rho_0^{\mathrm{B}}\frac{k\xi_0^2}{R_0^2}(1-\chi_0) \qquad (4.62\text{a})
$$

$$
\sigma_{\mathrm{eff}}^{\mathrm{1D}} = \sigma_m^{\mathrm{1D}} - \frac{5}{2}\frac{\kappa_m^{\mathrm{1D}}}{R_0^2} + \rho_0^{\mathrm{B}}\, k\xi_0^2\chi_0 \qquad (4.62\text{b})
$$

We have also introduced a typical spectrin energy

$$
W_s = k\xi_0^2\chi_0\,, \qquad (4.63)
$$

that is non-zero if, and only if the network is prestressed $|W_s| > 0 \iff |\chi_0| > 0 \iff |\xi_0| > 0$. It is positive for a tensed spectrin network $\xi_0 > l_0$ in reference state.

We now write the Langevin equation for the Fourier components $|q| > 1$ of the bound density variation $\delta\rho^{\mathrm{B}}(s_0)$

$$
\frac{d\delta\rho_q^{\mathrm{B}}}{dt} = -\left(k_{\mathrm{on}} + k_{\mathrm{off}}\right)_0 \delta\rho_q^{\mathrm{B}} + \left(\rho_0 - \rho_0^{\mathrm{B}}\right)\delta k_{\mathrm{on}\,q}(t) + \zeta_q^{\mathrm{B}}(t)\,, \qquad (4.64)
$$

where the Fourier components of the chemical white noise have the following correlation at equilibrium

$$
\left\langle \zeta_q^{\mathrm{B}}(t)\zeta_{q'}^{\mathrm{B}}(t')\right\rangle = 2\rho_0\Gamma_0^{\mathrm{B}}\delta(q+q')\delta(t-t')\,, \qquad (4.65\text{a})
$$

$$
\Gamma_0^{\mathrm{B}} = \frac{k_{\mathrm{on}\,0}\, k_{\mathrm{off}}}{k_{\mathrm{on}\,0} + k_{\mathrm{off}}}\,. \qquad (4.65\text{b})
$$

We justify the expression of Γ_0^{B} at equilibrium in the next section section 4.2.2.

We extrapolate the formal formula of k_{on} derived in previous section (4.30a) to circular membranes[5]

$$\begin{aligned} k_{\text{on}} &= k^o \exp\left[-\frac{k\Big(l(s_0)-l_0\Big)^2}{2k_{\text{B}}T}\right] \\ &\approx k^o \exp\left[-\frac{k\xi_0^2}{2k_{\text{B}}T}\left(\chi_0^2 + 2\chi_0\frac{h(s_0)}{R_0} + \frac{h(s_0)}{R_0}^2 + \chi_0\left(\frac{\partial h}{\partial s_0}\right)^2\right)\right] \end{aligned}$$

to calculate the variation δk_{on} at first order in h/R_0

$$\delta k_{\text{on}}(s_0,t) = \left.\frac{\partial k_{\text{on}}}{\partial h}\right|_{h=0} h(s_0) = -k_{\text{on}\,0}\frac{W_s}{k_{\text{B}}T}\frac{h(s_0)}{R_0}\,,$$

where we have defined the zeroth-order on-rate $k_{\text{on}\,0} = k^o \exp\left[-\frac{k\xi_0^2\chi_0^2}{2k_{\text{B}}T}\right] = k_{\text{on}}(h=0)$

We deduce immediately that in Fourier space, $\delta k_{\text{on}\,\text{q}} = -k_{\text{on}\,0}\frac{W_s}{k_{\text{B}}T}\frac{h_q}{R_0}$

The chemical Langevin equation for the bound density deviation Fourier components $\delta\rho_q^{\text{B}}$ $(q \geq 1)$ becomes

$$\frac{d\delta\rho_q^{\text{B}}}{dt} = -\big(k_{\text{on}} + k_{\text{off}}\big)_0 \delta\rho_q^{\text{B}} - \big(\rho_0 - \rho_0^{\text{B}}\big)\,k_{\text{on}\,0}\frac{W_s}{k_{\text{B}}T}\frac{h_q}{R_0} + \zeta_q^{\text{B}}(t)\,. \tag{4.66}$$

Note that the zeroth-order ρ_0^{B} at steady-state is given by

$$0 = k_{\text{on}\,0}\left(\rho_0 - \rho_0^{\text{B}}\right) - k_{\text{off}}\rho_0^{\text{B}}\,. \tag{4.67}$$

We have therefore $\left(\rho_0 - \rho_0^{\text{B}}\right) k_{\text{on}\,0} = \rho_0\frac{k_{\text{on}\,0}k_{\text{off}}}{k_{\text{on}\,0}+k_{\text{off}}} = \rho_0\Gamma_0^{\text{B}}$

---

[5] Note that we could equivalently derive the on-rate again from a Kramer's approach as shown in section 4.A

We sum up below the two coupled linearized Langevin equations in spatial Fourier space[6], governing the dynamics of the composite membrane:

$$\frac{dh_q}{dt} = -\omega_q^{\text{eff}}\, h_q - \Lambda_q \frac{W_s}{R_0}\,\delta\rho_q^{\text{B}} + \Lambda_q \zeta_q^h\,, \qquad \textit{Langevin eq. for } h_q(t) \tag{4.64}$$

$$\frac{d\delta\rho_q^{\text{B}}}{dt} = -\omega_0^{\text{B}}\delta\rho_q^{\text{B}} - \rho_0\Gamma_0^{\text{B}}\frac{W_s}{k_{\text{B}}T}\frac{h_q}{R_0} + \zeta_q^{\text{B}}\,, \qquad \textit{Langevin eq. for } \delta\rho_q^{\text{B}}(t) \tag{4.66}$$

$$\omega_q^{\text{eff}} = \Lambda_q\left(\gamma_{\text{eff}} + \sigma_{\text{eff}}\, q^2 + \kappa_m\, q^4\right), \ \textit{Mechanical relaxation time} \tag{4.68a}$$

$$\omega_0^{\text{B}} = k_{\text{on}\,0} + k_{\text{off}}\,, \qquad \textit{Chemical relaxation time} \tag{4.68b}$$

$$\gamma_{\text{eff}} = \frac{3}{2}\frac{\kappa_m}{R_0^4} - \frac{\sigma_m}{R_0^2} + \rho_0^{\text{B}}\frac{k\xi_0 l_0}{R_0^2}\,, \qquad \textit{Effective confinement param.} \tag{4.62a}$$

$$\sigma_{\text{eff}} = \sigma_m - \frac{5}{2}\frac{\kappa_m}{R_0^2} + \rho_0^{\text{B}} W_s\,, \qquad \textit{Effective tension} \tag{4.62b}$$

$$W_s = k\xi_0^2\chi_0\,, \tag{4.63}$$

$$\Gamma_0^{\text{B}} = \frac{k_{\text{on}\,0}\, k_{\text{off}}}{k_{\text{on}\,0} + k_{\text{off}}}\,, \tag{4.65b}$$

$$\left\langle \zeta_q^h(t)\zeta_{q'}^h(t')\right\rangle = 2k_{\text{B}}TL_0\Lambda_q^{-1}\delta(q+q')\delta(t-t')\,, \ \textit{Thermal noise} \tag{4.59}$$

$$\left\langle \zeta_q^{\text{B}}(t)\zeta_{q'}^{\text{B}}(t')\right\rangle = 2\rho_0\Gamma_0^{\text{B}}\delta(q+q')\delta(t-t')\,. \ \textbf{\textit{Equil.}}\ \textit{chem. noise} \tag{4.65a}$$

Summary 4.1: Summary of the Langevin equations governing the dynamics of the system {membrane+spectrin}. Imposing a nearly circular geometry to the membrane reintroduces a first-order coupling between the membrane height deflection h_q dynamics and the deviation of attachment spectrin density $\delta\rho_q^{\text{B}}$, providing that the spectrin network is prestressed ($|\chi_0| > 0$). Local fluctuations in the attachment density are therefore transduced in the membrane as a direct force, and local membrane shape fluctuations locally disturb the chemical steady-state. Similarly to the 1-dimensional nearly flat membrane, we see that the effective tension is renormalized by a prestressed spectrin network at zeroth-order. Here we neglected its higher-order effect on the bending modulus. The circular geometry leads furthermore to a contribution of the bending modulus to the effective tension σ_{eff} and to an effective confinement parameter γ_{eff} depending on the membrane bending, membrane tension and on the spectrin mechanics.

---

[6] Note that we dropped the $^{\text{1D}}$ superscript for the sake of readability

4.2.2 Fluctuations in a phosphorylation- dephosphorylation cycle

The process of attachment and detachment has been described so far by a two-state mechanism involving simply an on-rate k_{on} and an off-rate k_{off}:

$$\mathrm{Sp} \underset{k_{\mathrm{on}}}{\overset{k_{\mathrm{off}}}{\rightleftharpoons}} \mathrm{Sp}^* \,. \tag{4.69}$$

Sp represents a spectrin filament bound to the network, whereas Sp* is unbound. If this reaction (4.69) is an elementary reaction, i.e. involves only a single reaction step, its steady-state is equivalent to the detailed balance, or Wegsheider's relation, defining equilibrium [Wegscheider 1901] and characterized by zero flux in the system

$$\frac{[\mathrm{Sp}]}{[\mathrm{Sp}^*]} = \frac{k_{\mathrm{on}}}{k_{\mathrm{off}}} \iff \frac{k_{\mathrm{off}}[\mathrm{Sp}]}{k_{\mathrm{on}}[\mathrm{Sp}^*]} = 1 \tag{4.70}$$

To sustain the system in a non-equilibrium steady-state (NESS), one needs at least two different reaction paths for detaching and (re)attaching a spectrin filament. We propose to describe the process of attachment/detachment of spectrin filaments to the junction complex 4.1 R by two reversible chemical reactions: the first one involves the consumption of one molecule of ATP (easily generalizable to n ATP molecules) provided by a reservoir, whereas the second one does not need ATP molecule. These two reactions form a phosphorylation-dephosphorylation cycle (PdPC) represented in fig. 4.4. We neglect here the kinase and phosphatase intermediate enzymatic reactions: those molecules are supposed in very large excess, and do not limit the cycle kinetics. We calculate in the following the fluctuations and response of this chemical cycle at steady-state, at equilibrium and in a non-equilibrium steady-state (NESS).

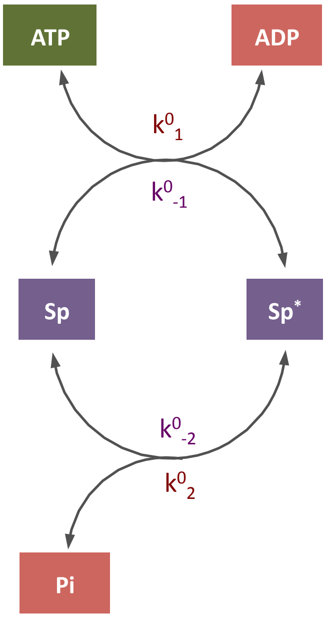

Figure 4.4: Two-state phosphorylation-dephosphorylation cycle

4.2.2.1 Description of the phosphorylation-dephosphorylation cycle at steady-state

Chemical cycle

The two elementary reversible reactions of the cycle read

$$\mathrm{Sp} + \mathrm{ATP} \underset{k^o_{-1}}{\overset{k^o_1}{\rightleftharpoons}} \mathrm{Sp}^* + \mathrm{ADP} \tag{4.71a}$$

$$\mathrm{Sp}^* \underset{k^o_{-2}}{\overset{k^o_2}{\rightleftharpoons}} \mathrm{Sp} + \mathrm{P_i} \tag{4.71b}$$

We define the chemical potential of the chemical species classically as

$$\mu_{\mathrm{Sp}} = \mu^o_{\mathrm{Sp}} + k_{\mathrm{B}}T \log [\mathrm{Sp}] \tag{4.72a}$$

$$\mu_{\mathrm{Sp}^*} = \mu^o_{\mathrm{Sp}^*} + k_{\mathrm{B}}T \log [\mathrm{Sp}^*] \tag{4.72b}$$

$$\mu_{\mathrm{ATP}} = \mu^o_{\mathrm{ATP}} + k_{\mathrm{B}}T \log [\mathrm{ATP}] \tag{4.72c}$$

$$\mu_{\mathrm{ADP}} = \mu^o_{\mathrm{ADP}} + k_{\mathrm{B}}T \log [\mathrm{ADP}] \tag{4.72d}$$

$$\mu_{\mathrm{Pi}} = \mu^o_{\mathrm{Pi}} + k_{\mathrm{B}}T \log [\mathrm{Pi}] \tag{4.72e}$$

The chemical potential difference for reactions (4.71a) and (4.71b) read

$$\Delta\mu_1 \equiv \mu_{\mathrm{ADP}} + \mu_{\mathrm{Sp}^*} - \mu_{\mathrm{ATP}} - \mu_{\mathrm{Sp}} = k_{\mathrm{B}}T \log \left(\frac{\mathcal{J}_1^-}{\mathcal{J}_1^+} \right) \tag{4.73a}$$

$$\Delta\mu_2 \equiv \mu_{\mathrm{Pi}} + \mu_{\mathrm{Sp}} - \mu_{\mathrm{Sp}^*} = k_{\mathrm{B}}T \log \left(\frac{\mathcal{J}_2^-}{\mathcal{J}_2^+} \right) \tag{4.73b}$$

where we defined the following fluxes

$$\mathcal{J}_1^- = k^o_{-1}\,[\mathrm{Sp}^*][\mathrm{ADP}]\,, \qquad \mathcal{J}_1^+ = k^o_1\,[\mathrm{Sp}][\mathrm{ATP}]\,, \tag{4.74a}$$

$$\mathcal{J}_2^- = k^o_{-2}\,[\mathrm{Sp}][\mathrm{P}_i]\,, \qquad \mathcal{J}_2^+ = k^o_2\,[\mathrm{Sp}^*] \tag{4.74b}$$

We remark that the chemical potential difference for a full cycle corresponds exactly to the chemical potential difference of one ATP hydrolysis:

$$\Delta\mu^c_{\mathrm{ATP}} = \Delta\mu_1 + \Delta\mu_2 = \mu_{\mathrm{ADP}} + \mu_{\mathrm{Pi}} - \mu_{\mathrm{ATP}} = k_{\mathrm{B}}T \log \left(\frac{k^o_{-1}k^o_{-2}}{k^o_1 k^o_2} \frac{[\mathrm{ADP}][\mathrm{Pi}]}{[\mathrm{ATP}]} \right) \tag{4.75}$$

We write the deterministic rate of change of bound spectrin concentration [Sp]

$$\begin{aligned} \frac{d[\mathrm{Sp}]}{dt} &= -\left(\mathcal{J}_1^+ - \mathcal{J}_1^-\right) + \left(\mathcal{J}_2^+ - \mathcal{J}_2^-\right) = \frac{d[\mathrm{ATP}]}{dt} + \frac{d[\mathrm{P}_i]}{dt} \\ &= -\left(k_1 + k^o_{-2}\right)[\mathrm{Sp}] + \left(k_{-1} + k_2\right)[\mathrm{Sp}^*] \end{aligned} \tag{4.76}$$

where we define the following pseudo first-order rates as in [Qian 2006]

$$k_1 \equiv k^o_1[\mathrm{ATP}]^{\mathrm{ss}}\,, \qquad k_{-1} \equiv k^o_{-1}[\mathrm{ADP}]^{\mathrm{ss}}\,, \qquad k_{-2} \equiv k^o_{-2}[\mathrm{P}_i]^{\mathrm{ss}} \tag{4.77}$$

The total number of spectrin filaments within the red-blood cell cytoskeleton being conserved, we have furthermore $[\mathrm{Sp}]_0 = [\mathrm{Sp}^*] + [\mathrm{Sp}]$

We are looking for a steady-state, characterized by the superscript $.^{\mathrm{ss}}$, as in $[\mathrm{Sp}]^{\mathrm{ss}}$

$$0 = \frac{d[\mathrm{Sp}]^{\mathrm{ss}}}{dt} = -\frac{d[\mathrm{Sp}^*]^{\mathrm{ss}}}{dt} = -\left(\mathcal{J}_1^+ - \mathcal{J}_1^-\right)^{\mathrm{ss}} + \left(\mathcal{J}_2^+ - \mathcal{J}_2^-\right)^{\mathrm{ss}} . \tag{4.78}$$

It imposes $\left(\mathcal{J}_1^+ - \mathcal{J}_1^-\right)^{\mathrm{ss}} = \left(\mathcal{J}_2^+ - \mathcal{J}_2^-\right)^{\mathrm{ss}} \equiv \mathcal{J}^{\mathrm{ss}}$ which defines a steady-state flux $\mathcal{J}^{\mathrm{ss}}$ in the cycle. If $\mathcal{J}^{\mathrm{ss}} > 0$ the system goes around the cycle in clock-wise direction, and conversely. If $\mathcal{J}^{\mathrm{ss}} = 0$ there is not net flux in the cycle.

We calculate the concentration of bound and unbound spectrin and the cycle flux at steady-state

$$[\mathrm{Sp}]^{\mathrm{ss}} = [\mathrm{Sp}]_0 \, \frac{k_{-1} + k_2^o}{k^{\mathrm{ss}}} , \qquad [\mathrm{Sp}^*]^{\mathrm{ss}} = [\mathrm{Sp}]_0 \, \frac{k_1 + k_{-2}}{k^{\mathrm{ss}}} , \qquad \frac{[\mathrm{Sp}]^{\mathrm{ss}}}{[\mathrm{Sp}^*]^{\mathrm{ss}}} = \frac{k_{-1} + k_2^o}{k_1 + k_{-2}} , \tag{4.79a}$$

$$k^{\mathrm{ss}} = k_1 + k_2^o + k_{-1} + k_{-2} , \tag{4.79b}$$

$$\mathcal{J}^{\mathrm{ss}} = [\mathrm{Sp}]_0 \, \frac{k_1 k_2^o - k_{-1} k_{-2}}{k^{\mathrm{ss}}} = [\mathrm{Sp}]_0 \, \frac{k_1 k_2^o}{k^{\mathrm{ss}}} \left[1 - e^{\frac{\Delta\mu^c_{\mathrm{ATP}}}{k_{\mathrm{B}} T}} \right] . \tag{4.79c}$$

Equilibrium chemical cycle The cycle at steady-state is at chemical equilibrium if, and only if

$$\begin{cases} \Delta\mu_1 = 0 \\ \Delta\mu_2 = 0 \end{cases} \Leftrightarrow \begin{cases} \mathcal{J}_1^+ = \mathcal{J}_1^- \\ \mathcal{J}_2^+ = \mathcal{J}_2^- \end{cases} \Longleftrightarrow \mathcal{J}^{\mathrm{ss}} = 0 \Longleftrightarrow \Delta\mu_{\mathrm{ATP}} = 0 \Longleftrightarrow \frac{k_{-1} k_{-2}}{k_1 k_2^o} = 1 \tag{4.80}$$

The equilibrium is therefore characterized by a vanishing cycle flux $\mathcal{J}^{\mathrm{ss}} = 0$. The equation for $\mathcal{J}^{\mathrm{ss}}$ (4.79c) give us the two ways of reaching equilibrium: either there is no ATP at all in the system, which leads to $k_1 = k_{-1} = 0$ and we are left with the single elementary reaction (4.71b); or the system does contain a certain amount of ATP at initial state but is closed: it therefore relaxes toward the equilibrium concentrations corresponding to $\Delta\mu_{\mathrm{ATP}} = 0$ at steady-state.

Cycle in a non-equilibrium steady-state Imposing a strictly negative $\Delta\mu_{\mathrm{ATP}} < 0$ drives a non-zero cycle flux $\mathcal{J}^{\mathrm{ss}} > 0$, which is exactly the turnover rate of ATP consumption in the system (see section 4.2.2.1). Imposing a constant non-zero $\Delta\mu_{\mathrm{ATP}}$ requires to maintain [ATP], [ADP] and [Pi] at constant values different from their equilibrium values, by maintaining the system in contact with reservoirs of molecules, called *chemiostats.* The cell has indeed an ATP regenerating system that works like a *chemiostat* for ATP and ADP as sketched in fig. 4.5. We assume here that this machinery buffers the concentration of ATP, ADP and Pi that are thus maintained constant.

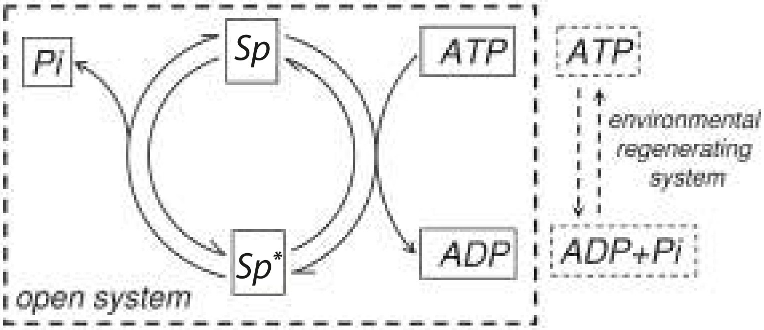

Figure 4.5: ATP hydrolysis and related ATP regenerating process. The entire cycle has a $-\Delta\mu_{\mathrm{ATP}} > 0$ amount of net free-energy input and the same amount of energy dissipated. (Adapted from [Ge 2013])

Using the terminology introduced by Onsager [Onsager 1931] $\Delta\mu_{\mathrm{ATP}}$ is the chemical driving force for the flux $\mathcal{J}^{\mathrm{ss}}$. One can prove that at steady-state, their product

$$-\Delta\mu_{\mathrm{ATP}} \times \mathcal{J}^{\mathrm{ss}} \geq 0 \tag{4.81}$$

corresponds to the amount of work per unit time necessary to constantly supply ATP and remove ADP and Pi from the open system, thereby sustaining the system in NESS [Heuett 2006]. It also corresponds to the dissipated power in the chemical cycle [Qian 2006, Ge 2013].

4.2.2.2 Fluctuations and response at equilibrium

The deviation of bound spectrin concentration from steady-state $\delta[\mathrm{Sp}] = [\mathrm{Sp}] - [\mathrm{Sp}]^{\mathrm{ss}}$ has a stochastic evolution given by the chemical Langevin equation

$$\begin{aligned} \frac{d\delta[\mathrm{Sp}]}{dt} &= -\Big\{k_1^o\,[\mathrm{ATP}]^{\mathrm{ss}} + k_{-1}^o\,[\mathrm{ADP}]^{\mathrm{ss}} + k_2^o + k_{-2}^o[\mathrm{P}_i]^{\mathrm{ss}}\Big\}\delta[\mathrm{Sp}] + \zeta_{\mathrm{Sp}}(t) \\ &= -k^{\mathrm{ss}}\,\delta[\mathrm{Sp}] + \zeta^{\mathrm{Sp}}(t) \end{aligned} \tag{4.82}$$

Response function

We first look at the response of the system to a small variation of the chemical potential imposed externally

$$\delta\mu^{\mathrm{ext}} \equiv \delta\left(\mu_{\mathrm{Sp}^*} - \mu_{\mathrm{Sp}}\right) = -k_{\mathrm{B}}T\frac{\delta[\mathrm{Sp}]}{[\mathrm{Sp}]^{\mathrm{ss}}}\left(1 + \frac{[\mathrm{Sp}]^{\mathrm{ss}}}{[\mathrm{Sp}^*]^{\mathrm{ss}}}\right) = -k_{\mathrm{B}}T\frac{\delta[\mathrm{Sp}]}{[\mathrm{Sp}]^{\mathrm{ss}}}\frac{k^{\mathrm{ss}}}{k_1 + k_{-2}} \tag{4.83}$$

Adding the external driving chemical potential to the Langevin equation (4.82) yields

$$\frac{d\delta[\mathrm{Sp}]}{dt} = -k^{\mathrm{ss}}\,\delta[\mathrm{Sp}] + [\mathrm{Sp}]^{\mathrm{ss}}\,(k_1 + k_{-2})\,\frac{\delta\mu^{\mathrm{ext}}}{k_{\mathrm{B}}T} + \zeta_{\mathrm{Sp}}(t)\,. \tag{4.84}$$

In temporal Fourier Space we have therefore the following response function

$$\tilde{\chi}(\omega) \equiv \frac{\tilde{\delta}[\mathrm{Sp}]}{\delta \tilde{\mu}^{\mathrm{ext}}} = \frac{1}{k_{\mathrm{B}}T} \frac{[\mathrm{Sp}]^{\mathrm{ss}}\,(k_1 + k_{-2})}{k^{\mathrm{ss}} - i\omega}\,, \tag{4.85}$$

the dissipative part of which reads

$$\tilde{\chi}''(\omega) \equiv \mathrm{Im}\,[\tilde{\chi}(\omega)] = \frac{\omega}{k_{\mathrm{B}}T} \frac{[\mathrm{Sp}]^{\mathrm{ss}}\,(k_1 + k_{-2})}{k^{s\,2} + \omega^2} \tag{4.86}$$

Fluctuations

We now look at the fluctuations of $\delta[\mathrm{Sp}]$ using the chemical Langevin equation without any external driving

$$\frac{d\delta[\mathrm{Sp}]}{dt} = -k^{\mathrm{ss}}\,\delta[\mathrm{Sp}] + \zeta_{\mathrm{Sp}}(t)\,. \tag{4.87}$$

At equilibrium, the noise is white and its amplitude is given by the sum of the elementary fluxes in the system [Keizer 1975, Keizer 1987, Gillespie 2000] (for a minimal proof see section 4.D.2.1).

$$\left\langle \zeta^{\mathrm{Sp}}(t) \right\rangle = 0 \tag{4.88a}$$

$$\begin{aligned}\left\langle \zeta^{\mathrm{Sp}}(t)\,\zeta^{\mathrm{Sp}}(t') \right\rangle &= \left(\mathcal{J}_1^+ + \mathcal{J}_1^- + \mathcal{J}_2^+ + \mathcal{J}_2^-\right)^{\mathrm{ss}} \delta(t-t') \\ &= 2[\mathrm{Sp}]^{\mathrm{ss}}\,(k_1 + k_{-2})\,\delta(t-t')\end{aligned} \tag{4.88b}$$

where we have used the fact that $\mathcal{J}_1^+ = \mathcal{J}_1^-$ and $\mathcal{J}_2^+ = \mathcal{J}_2^-$ at equilibrium.

In temporal Fourier space we obtain the following fluctuation correlation function

$$\left\langle \tilde{\delta}[\mathrm{Sp}](\omega)\,\tilde{\delta}[\mathrm{Sp}](\omega') \right\rangle = 2[\mathrm{Sp}]^{\mathrm{ss}} \frac{k_1 + k_{-2}}{k^{\mathrm{ss}\,2} + \omega^2}\,\delta(\omega + \omega') \tag{4.89}$$

Fluctuation-dissipation theorem At equilibrium, the auto-correlation function in temporal Fourier space reads

$$\tilde{C}^{\mathrm{eq}}_{\mathrm{Sp}}(\omega) = \left\langle \tilde{\delta}[\mathrm{Sp}](\omega)^2 \right\rangle = 2[\mathrm{Sp}]^{\mathrm{ss}} \frac{k_1 + k_{-2}}{k^{\mathrm{ss}\,2} + \omega^2} \tag{4.90}$$

and verifies therefore the fluctuation-dissipation theorem

$$\tilde{C}^{\mathrm{eq}}_{\mathrm{Sp}}(\omega) = \frac{2\,k_{\mathrm{B}}T\,\tilde{\chi}''(\omega)}{\omega} \tag{4.91}$$

The fluctuation-dissipation expressed in temporal Fourier space relates the dissipative part of the response function $\tilde{\chi}''(\omega)$ to the correlations of the fluctuations $\left\langle \tilde{\delta}[\mathrm{Sp}](\omega)^2 \right\rangle$ at equilibrium (see section 4.A.3).

Measuring the fluctuations of a system at equilibrium is equivalent to measuring its response to a perturbation. It is not the case out-of-equilibrium, where the fluctuations spectrum and the response function do not coincide.

4.2.2.3 Fluctuations and response in NESS

In non-equilibrium steady-state (NESS), there is a permanent cycle flux $\mathcal{J}^{\mathrm{ss}} > 0$ driven by a strictly negative ATP chemical potential difference[7] $\Delta\mu_{\mathrm{ATP}} < 0$.

We follow here the approach of Harada and Sasa for molecular motors [Harada 2005], which relates the rate of energy dissipation $\left\langle \dot{S} \right\rangle_0$ with the extent of violation of the fluctuation-dissipation.

For a chemical cycle in a NESS, the amount of energy maintaining the system out-of-equilibrium, or chemical motive force, $-\mathcal{J}^{\mathrm{ss}}\Delta\mu_{\mathrm{ATP}}$ is exactly the rate of energy dissipation and the entropy production rate [Qian 2006, Ge 2013]. We propose therefore that in our chemical cycle, the extent of violation of the fluctuation-dissipation is directly related to the steady flux $\mathcal{J}^{\mathrm{ss}} > 0$ that sustains the NESS.

Specifically we write that

$$\int_0^\infty \left[\tilde{C}^{\mathrm{ness}}_{\mathrm{Sp}}(\omega) - \frac{2\, k_{\mathrm{B}}T\, \tilde{\chi}''(\omega)}{\omega} \right] \frac{d\omega}{2\pi} = \frac{\mathcal{J}^{\mathrm{ss}}}{k^{\mathrm{ss}}} \,. \tag{4.92}$$

Note that at equilibrium $\mathcal{J}^{\mathrm{ss}} = 0$ and we recover the fluctuation-dissipation theorem.

We denote A the amplitude of the non-equilibrium contribution to the noise correlations

$$\left\langle \zeta_{\mathrm{Sp}}(t)\, \zeta_{\mathrm{Sp}}(t') \right\rangle^{\mathrm{ness}} = \left[A + \left(\mathcal{J}_1^+ + \mathcal{J}_1^- + \mathcal{J}_2^+ + \mathcal{J}_2^- \right)^{\mathrm{ss}} \right] \delta(t-t') \,. \tag{4.93}$$

Using a calculation similar to that done at equilibrium, we deduce

$$\tilde{C}^{\mathrm{ness}}_{\mathrm{Sp}}(\omega) - \frac{2\, k_{\mathrm{B}}T\, \tilde{\chi}''(\omega)}{\omega} = \frac{A}{{k^{\mathrm{ss}}}^2 + \omega^2} \,. \tag{4.94}$$

eq. (4.92) can therefore be integrated

$$\frac{\mathcal{J}^{\mathrm{ss}}}{k^{\mathrm{ss}}} = \int_0^\infty \frac{A}{{k^{\mathrm{ss}}}^2 + \omega^2} \frac{d\omega}{2\pi} = \frac{1}{4} \frac{A}{k^{\mathrm{ss}}} \,. \tag{4.95}$$

We deduce therefore $A = 4\mathcal{J}^{\mathrm{ss}}$ and the chemical noise correlation at NESS reads

$$\left\langle \zeta_{\mathrm{Sp}}(t)\, \zeta_{\mathrm{Sp}}(t') \right\rangle^{\mathrm{ness}} = 2 \left[\mathcal{J}_1^+ + \mathcal{J}_2^- + 2\mathcal{J}^{\mathrm{ss}} \right] \delta(t-t') \,. \tag{4.96}$$

We recalculate the autocorrelation function using this correlation of the chemical noise in a NESS (4.96) and obtain

$$\tilde{C}^{\mathrm{ness}}_{\mathrm{Sp}}(\omega) = \left\langle \tilde{\delta}[\mathrm{Sp}](\omega)^2 \right\rangle^{\mathrm{ness}} = \frac{2\, k_{\mathrm{B}}T\, \tilde{\chi}''(\omega)}{\omega} + \frac{4\mathcal{J}^{\mathrm{ss}}}{k^{\mathrm{ss}\,2} + \omega^2} \,. \tag{4.97}$$

The chemical cycle therefore violates the fluctuation-dissipation theorem, as expected for a non-equilibrium system.

---

[7] We could also suppose the ATP chemical potential difference positive, which would trigger a negative flux $\mathcal{J}^{\mathrm{ss}}$. $\Delta\mu_{\mathrm{ATP}}$ is however always negative in physiological conditions.

4.2.2.4 Fluctuations and response for the spectrin attachment fraction

The previous results can directly be applied to the surface density of bound filaments $\rho^{\mathrm{B}} = [\mathrm{Sp}]$. However in the next section we prefer working with fractions. We therefore define the fraction of bound and unbound filaments n^{B} and n^{U} We define the following fractions of attached and detached spectrin:

$$n^{\mathrm{B}} = \frac{[\mathrm{Sp}]}{[\mathrm{Sp}]_0}\,, \qquad n^{\mathrm{U}} = \frac{[\mathrm{Sp}^*]}{[\mathrm{Sp}]_0} = 1 - n^{\mathrm{B}}\,. \tag{4.98}$$

Their average values at steady-state are denoted with the subscript 0 and are given by eq. (4.79)

$$n_0^{\mathrm{B}} = \left\langle n^{\mathrm{B}} \right\rangle = \frac{k_{-1} + k_2}{k^{\mathrm{ss}}}\,, \qquad n_0^{\mathrm{U}} = \left\langle n^{\mathrm{U}} \right\rangle = \frac{k_1 + k_{-2}}{k^{\mathrm{ss}}}. \tag{4.99}$$

The time evolution of n_0^{B} is given by the deterministic kinetic equation

$$\frac{dn_0^{\mathrm{B}}}{dt} = -k_{\mathrm{off}}\, n_0^{\mathrm{B}} + k_{\mathrm{on}} \left(1 - n_0^{\mathrm{B}}\right)\,, \tag{4.100}$$

where we have defined the following effective on- and off-rates

$$k_{\mathrm{on}} \equiv k_{-1} + k_2^o = k_{-1}^o\, [\mathrm{ADP}]^{\mathrm{ss}} + k_2^o \tag{4.101a}$$

$$k_{\mathrm{off}} \equiv k_1 + k_{-2} = k_1^o\, [\mathrm{ATP}]^{\mathrm{ss}} + k_{-2}^o\, [\mathrm{P}_i]^{\mathrm{ss}} \tag{4.101b}$$

The steady-state value of the fractions of bound and detached spectrin filaments can be rewritten as

$$n_0^{\mathrm{B}} = \frac{k_{\mathrm{on}}}{k_{\mathrm{on}} + k_{\mathrm{off}}}\,, \qquad n_0^{\mathrm{U}} = \frac{k_{\mathrm{off}}}{k_{\mathrm{on}} + k_{\mathrm{off}}}\,. \tag{4.102}$$

The time evolution of the deviation $\delta n^{\mathrm{B}} = n^{\mathrm{B}} - n_0^{\mathrm{B}}$ of the fraction of attached spectrin is given by the chemical Langevin equation

$$\frac{d\delta n^{\mathrm{B}}}{dt} = -\left[k_{\mathrm{off}} + k_{\mathrm{on}}\right] \delta n^{\mathrm{B}} + \zeta^{\mathrm{B}}(t) \tag{4.103}$$

which allows us to identify $k^{\mathrm{ss}} = k_{\mathrm{off}} + k_{\mathrm{on}} = \omega_0^{\mathrm{B}}$ the relaxation time associated with a perturbation of the chemical cycle at steady-state.
The chemical noise is characterized as

$$\left\langle \zeta^{\mathrm{B}}(t) \right\rangle = 0\,, \qquad \left\langle \zeta^{\mathrm{B}}(t)\, \zeta^{\mathrm{B}}(t') \right\rangle = 2\left(\Gamma_0^{\mathrm{B}} + \Gamma_a\right) \delta(t - t') \tag{4.104}$$

with

$$\Gamma_0^{\mathrm{B}} = \frac{\mathcal{J}_1^+ + \mathcal{J}_2^-}{[\mathrm{Sp}]_0} = \frac{k_{\mathrm{on}} k_{\mathrm{off}}}{k_{\mathrm{on}} + k_{\mathrm{off}}} = \omega_0^{\mathrm{B}}\, n_0^{\mathrm{B}} \left(1 - n_0^{\mathrm{B}}\right) \tag{4.105a}$$

$$\Gamma_a = \frac{2\mathcal{J}^{\mathrm{ss}}}{[\mathrm{Sp}]_0} = \frac{2 k_1 k_2^o}{k_{\mathrm{on}} + k_{\mathrm{off}}} \left[1 - e^{\frac{\Delta\mu_{\mathrm{ATP}}^c}{k_{\mathrm{B}} T}}\right] \tag{4.105b}$$

Expression of k_{on} and k_{off} at $\Delta\mu_{\mathrm{ATP}} = \mathrm{cte}$

To determine the on- and off-rates, one need to know the four constant rates k_1^o, k_{-1}^o, k_2^o, k_{-2}^o, and the average concentration of ATP, ADP and Pi. To simplify the problem we first adimensionalize the pseudo first-order rates k_1, k_{-1} and k_{-2} by k_2^o

$$\theta \equiv k_1^o[\mathrm{ATP}]/k_2^o\,, \qquad \lambda \equiv k_{-1}^o[\mathrm{ATP}]/k_2^o\,, \qquad \exp\left(\frac{-E_{\mathrm{B}}}{k_{\mathrm{B}}T}\right) \equiv k_{-2}^o[\mathrm{Pi}]/k_2^o\,. \tag{4.106}$$

where we have defined the spectrin binding affinity E_{B}.

The chemical potential of ATP hydrolysis can be expressed as a function of the parameters θ, λ, and E_{B}

$$\exp\left(\frac{\Delta\mu_{\mathrm{ATP}}}{k_{\mathrm{B}}T}\right) = \frac{k_{-1}k_{-2}}{k_1 k_2^o} = \frac{\lambda}{\theta}\exp\left(\frac{-E_{\mathrm{B}}}{k_{\mathrm{B}}T}\right). \tag{4.107}$$

We suppose that the cell maintains a constant incoming flux of ATP and constant outcoming fluxes of ADP and Pi so that the chemical potential for the hydrolysis of ATP remains strictly negative and constant. The dimensionless ADP concentration λ becomes therefore directly proportionnal to the dimensionless concentration θ of ATP

$$\lambda = \theta\,\exp\left(\frac{\Delta\mu_{\mathrm{ATP}} + E_{\mathrm{B}}}{k_{\mathrm{B}}T}\right), \tag{4.108}$$

Considering the binding affinity E_{B}, the chemical potential $\Delta\mu_{\mathrm{ATP}}$ and the typical reattachment rate k_2^o known and constant, the on- and off-rates can finally be written as a function on the dimensionless ATP concentration θ only

$$k_{\mathrm{on}} = k_2^o\left\{1 + \theta\,\exp\left(\frac{E_{\mathrm{B}} + \Delta\mu_{\mathrm{ATP}}}{k_{\mathrm{B}}T}\right)\right\}\exp\left(\frac{-E(l)}{k_{\mathrm{B}}T}\right), \tag{4.109a}$$

$$k_{\mathrm{off}}^c = k_2^o\left\{\theta + \exp\left(\frac{-E_{\mathrm{B}}}{k_{\mathrm{B}}T}\right)\right\}. \tag{4.109b}$$

Note that we have added an exponential dependence of the on-rate on $E(l) \equiv \frac{1}{2}k\left(l - l_0^2\right)$ to take into account the mechanical energy of a spectrin filament elongation l into the kinetic scheme. This relation can be simply recovered at equilibrium by writing the detailed balance (see eq. (4.30))

$$\frac{k_{\mathrm{on}}(l)}{k_{\mathrm{off}}} = \exp\left[-\frac{k/2\left(\langle l\rangle - l_0\right)^2 - E_{\mathrm{B}}}{k_{\mathrm{B}}T}\right] \tag{4.110}$$

We can alternatively derive this exponential dependence on $E(l)$ following a Kramers approach (see section 4.C), which allows furthermore to evaluate the constant k_2^o

$$k_2^o = \frac{8\pi^{3/2}\eta\,R_{\mathrm{g}}}{k_s}\sqrt{\frac{2k_{\mathrm{B}}T}{k\left(\langle l\rangle - l_0\right)^2}} \tag{4.111}$$

where η is the viscosity of the surrounding fluid, and R_{g} the radius of gyration of a spectrin filament (see eq. (4.202)).

4.3 A 2-dimensional model of active RBC fluctuations

4.3.1 Quasi-spherical composite membrane

The instantaneous quasi-spherical shape is parametrized in spherical coordinates (r, θ, ϕ) by

$$r(\theta, \phi) = R_0\Big[1 + u(\theta, \phi)\Big] , \tag{4.112}$$

as shown on fig. 4.1. R_0 is the radius from which the small displacement $u(\theta, \phi) \ll 1$ is defined.

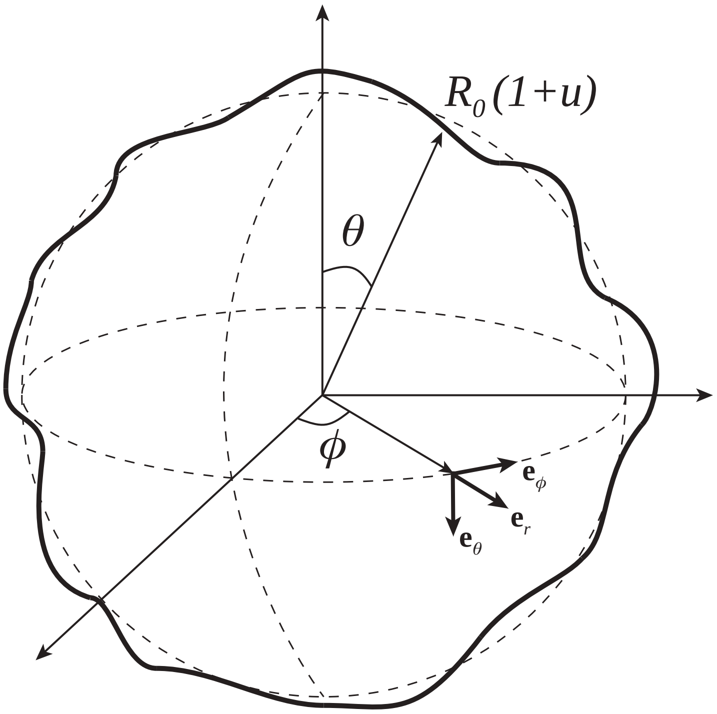

Figure 4.1: Parametrization in spherical coordinates of a membrane (bold line) fluctuating around a reference sphere (dashed line).

Similarly to the previous section we calculate the Helfrich energy and spectrin energy, but for a 2-dimensional quasi-spherical membrane and as an expansion in spherical harmonics.

4.3.1.1 Spherical geometry

Curvature
We first calculate the curvature, which is easily obtained by introducing the normal $\mathbf{n} = (n_r, n_\theta, n_\varphi)$ to the surface. The surface is defined implicitly by the equation

$$0 = F(r, \theta, \phi) = r - R_0\Big[1 + u(\theta, \phi)\Big] , \tag{4.113}$$

which allows to calculate the normal pointing out the quasi-spherical shape as $\mathbf{n} = \frac{\boldsymbol{\nabla} F}{\|\boldsymbol{\nabla} F\|}$. The gradient in spherical coordinates is given by $\boldsymbol{\nabla} \equiv \mathbf{e}_r \frac{\partial}{\partial r} + \frac{\mathbf{e}_\theta}{r} \frac{\partial}{\partial \theta} + \frac{\mathbf{e}_\varphi}{r \sin\theta} \frac{\partial}{\partial \varphi}$, which leads to

$$\boldsymbol{\nabla} F = \left(1, -\frac{1}{r}\frac{\partial u}{\partial \theta}, -\frac{1}{r\sin\theta}\frac{\partial u}{\partial \varphi}\right), \qquad \| \boldsymbol{\nabla} F \| \sim 1 + \frac{1}{2}\left(\boldsymbol{\nabla}_\perp u\right)^2 + \mathcal{O}(u^3). \tag{4.114}$$

where we have truncated the expansion to the second order in u. The operator $\boldsymbol{\nabla}_\perp$ is the gradient in spherical coordinates, restricted to the variables (θ, φ): $\boldsymbol{\nabla}_\perp \equiv \mathbf{e}_\theta \frac{\partial}{\partial \theta} + \frac{\mathbf{e}_\varphi}{\sin\theta}\frac{\partial}{\partial \varphi}$. We deduce the radial component of the normal $n_r \sim 1 - \frac{1}{2}\left(\boldsymbol{\nabla}_\perp u\right)^2$.

The total curvature $C = 1/R_1 + 1/R_2$ is given by the divergence of the surface normal

$$C = \boldsymbol{\nabla} \cdot \mathbf{n} = \frac{2}{R_0}\left[1 - u - \frac{1}{2}\boldsymbol{\nabla}_\perp^2 u + u^2 + u\boldsymbol{\nabla}_\perp^2 u\right] + \mathcal{O}(u^3)\,. \tag{4.115}$$

Membrane area element

The membrane area dA per solid angle $d\Omega = \sin\theta\, d\varphi\, d\theta$ is given by $dA = \frac{r^2}{n_r} d\Omega$, where n_r is the cosine of the angle the normal $\mathbf{n}$ makes with $\mathbf{e}_r$.

Inserting the above formula of n_r, we obtain the expression of dA up to 2nd order in u

$$dA = R_0^2 d\Omega \left[(1+u)^2 + \frac{1}{2}\left(\boldsymbol{\nabla}_\perp u\right)^2\right] + \mathcal{O}(u^3)\,. \tag{4.116}$$

4.3.1.2 Spherical Harmonics expansion

General properties

We expand the small displacement $u(\theta, \phi)$ in spherical harmonics

$$u(\theta,\phi) = \sum_{l\geq 0}\sum_{m=-l}^{l} u_{lm}\mathcal{Y}_{lm} = \frac{u_{00}}{\sqrt{4\pi}} + \sum_{l\geq 2}\sum_{m=-l}^{l} u_{lm}\mathcal{Y}_{lm}\,, \tag{4.117}$$

where $\mathcal{Y}_{lm} = a_{lm}\mathcal{P}_l^m(\cos\theta)\, e^{im\varphi}$ is the spherical harmonic of degrees l and m, with $\mathcal{P}_l^m$ an associated Legendre polynomial and a_{lm} a normalization factor (see section 2.D.1). Note that $u_{lm}^* = u_{l,-m}$ since u is real. The mode $l = 1$ can be ignored as it corresponds to sphere translations without shape changes. In the following we denote $\sum_{l,m} = \sum_{l\geq 1}\sum_{m=-l}^{m}$ to simplify the writing.

We recall three important properties of spherical harmonics, described in more details in section 2.D.1

- Orthogonality $\int d\Omega\, \mathcal{Y}_{lm}\mathcal{Y}_{l'm'}^* = \delta_{mm'}\,\delta_{ll'}$.
- Closure relation $\int d\Omega\, |u(\Omega)|^2 = \sum_{l\geq 0}\sum_{m=-l}^{l} |u_{lm}|^2$.
- Eigenvalue equation $\boldsymbol{\nabla}_\perp^2 \mathcal{Y}_{lm} = -l(l+1)\,\mathcal{Y}_{lm}$.

Volume expansion

The volume V enclosed by the membrane is expanded up to order 2 in u_{lm}

$$\begin{aligned} V &= \int d\Omega \int dr\, r^2 = \int d\Omega \frac{r^3(\Omega)}{3} = \frac{R_0^3}{3} \int d\Omega \Big[1 + u(\Omega)\Big]^3 \\ &= R_0^3 \left\{ \frac{4\pi}{3} \left(1 + \frac{u_{00}}{\sqrt{4\pi}}\right)^3 + \left(1 + \frac{u_{00}}{\sqrt{4\pi}}\right) \sum_{l,m} |u_{lm}|^2 + \mathcal{O}(u_{lm}^3) \right\} \end{aligned} \tag{4.118}$$

Volume conservation reads $V - \frac{4\pi}{3} R_0^3 = 0$ which leads to the following expression for u_{00} up to 2nd order in u_{lm}

$$u_{00} \sim -\frac{1}{\sqrt{4\pi}} \sum_{l,m} |u_{lm}|^2 . \tag{4.119}$$

u_{00} is therefore of second order and we can rewrite (4.118) as in [Milner 1987]

$$V \sim R_0^3 \left\{ \frac{4\pi}{3} \left(1 + \frac{u_{00}}{\sqrt{4\pi}}\right)^3 + \sum_{l,m} |u_{lm}|^2 \right\} . \tag{4.120}$$

Membrane area and area excess

Using eq. (4.116) we expand the total membrane surface up to second order in u_{lm} as in [Milner 1987]

$$\begin{aligned} A &= \int dA = R_0^2 \int d\Omega \left[(1+u)^2 + \frac{1}{2} \left(\boldsymbol{\nabla}_\perp u\right)^2 + + \mathcal{O}(u^3) \right] \\ &= R_0^2 \left\{ 4\pi \left(1 + \frac{u_{00}}{\sqrt{4\pi}}\right)^2 + \sum_{l,m} \left[1 + \frac{l(l+1)}{2}\right] |u_{lm}|^2 + \mathcal{O}\left(u_{lm}^3\right) \right\} . \end{aligned} \tag{4.121}$$

Inserting the previous equation (4.119) for u_{00} originating from volume conservation, we obtain

$$A \sim R_0^2 \left\{ 4\pi + \frac{1}{2} \sum_{l,m} (l-1)(l+2) |u_{lm}|^2 \right\} . \tag{4.122}$$

We can therefore express the adimensionalized excess area Δ as

$$\Delta \equiv \frac{A - 4\pi R_0^2}{R_0^2} \sim \frac{1}{2} \sum_{l,m} (l-1)(l+2) |u_{lm}|^2 , \tag{4.123}$$

4.3.1.3 Helfrich and spectrin energies

Helfrich energy

The Canham-Helfrich energy[8] with 2-dimensional bending modulus κ and 2-dimensional tension σ is classically defined as

$$\Delta\mathcal{U}_m = \int dA \left\{\frac{\kappa}{2}C^2 + \sigma\right\} . \tag{4.124}$$

σ acts as a Lagrange multiplier which ensures that the mean excess area of the fluctuating membrane is equal to some prescribed value Δ such as

$$A = (4\pi + \Delta)\, R_0^2 . \tag{4.125}$$

Using eq. (4.116) we evaluate $C^2\, dA$ in quadratic approximation

$$C^2\, dA \sim 4\left[1 - \boldsymbol{\nabla}_\perp^2 u + \frac{1}{4}\left(\boldsymbol{\nabla}_\perp^2 u\right)^2 + u\boldsymbol{\nabla}_\perp^2 u + \frac{1}{2}\left(\boldsymbol{\nabla}_\perp u\right)^2\right] . \tag{4.126}$$

We insert the spherical harmonics decomposition of $u(\Omega)$ (4.117) and integrate over the membrane surface, replacing u_{00} by its expression (4.119), which yields

$$\frac{\kappa}{2}\int dA\, C^2 = \kappa\left\{8\pi + \frac{1}{2}\sum_{l,m}(l+2)(l+1)l(l-1)\,|u_{lm}|^2 + \mathcal{O}(u_{lm}^3)\right\} . \tag{4.127}$$

The tension term is simply deduced from the area decomposition (4.122)

$$\sigma\int dA = \sigma A \sim \sigma R_0^2\left\{4\pi + \frac{1}{2}\sum_{l,m}(l-1)(l+2)\,|u_{lm}|^2\right\} . \tag{4.128}$$

We define a dimensionless reduced tension $\bar{\sigma} = \frac{R_0^2\sigma}{\kappa}$ which allows us to rewrite the lipid-bilayer energy (4.124) as

$$\Delta\mathcal{U}_m \sim \frac{\kappa}{2}\sum_{l,m}|u_{lm}|^2\,(l+2)(l-1)\Big[(l+1)l + \bar{\sigma}\Big] , \tag{4.129}$$

where we omitted the constant part of the energy $\kappa\,[8\pi + 4\pi\bar{\sigma}]$.

Spectrin energy

We now calculate the spectrin energy, following the same approach as for the previous 1-dimensional case (see section 4.2.1.2).

We recall the definition of the spectrin energy

$$\Delta\mathcal{U}_s\big[\,\{l_i, b_i\}\,\big] = \sum_{i=1}^{N} b_i\left\{\frac{k}{2}\,[l_i - l_0]^2 - E_B\right\} . \tag{4.2}$$

---

[8] We do not consider here a spontaneous curvature C_0

We consider the i-th filament, which makes an angle ψ_i with $\mathbf{e}_\theta$ in the membrane plane. The spectrin vector $\mathbf{l}_i = \mathbf{r}_{i+1} - \mathbf{r}_i$ can be projected on $(\mathbf{e}_\theta, \mathbf{e}_\varphi)$ as

$$\mathbf{l}_i = l_{\theta\, i}\, \mathbf{e}_\theta(\theta_i, \varphi_i) + l_{\varphi\, i}\, \mathbf{e}_\varphi(\theta_i, \varphi_i)\,. \tag{4.130}$$

The membrane length being given by $l_i = \sqrt{l_{i\,\theta}^2 + l_{i\,\varphi}^2}$, we evaluate these two components in the following.

Using Pythagore's theorem, we can express $l_{i\,\theta}$ and $l_{i\,\varphi}$ as a function of the elongation ξ_0 at reference state ($u = 0$), the membrane deviation $u(\theta, \varphi)$ and the angle ψ_i

$$l_{\theta\, i}^2 = \xi_0^2 \cos^2\psi_i \left[(1+u)^2 + \left(\frac{\partial u}{\partial\theta}\right)^2\right], \quad l_{\varphi\, i}^2 = \xi_0^2 \sin^2\psi_i \left[(1+u)^2 + \left(\frac{1}{\sin\theta}\frac{\partial u}{\partial\varphi}\right)^2\right]. \tag{4.131}$$

We deduce the expression of l_i up to second order in u and its derivatives

$$l_i \sim \xi_0 \left\{1 + u + \frac{1}{2}\left[\cos^2\psi \left(\frac{\partial u}{\partial\theta}\right)^2 + \sin^2\psi \left(\frac{1}{\sin\theta}\frac{\partial u}{\partial\varphi}\right)^2\right]\right\}. \tag{4.132}$$

Here, we ignore the underlying triangular topology of the spectrin network since we are working at a length scale very large compared to the mesh size ξ_0. We therefore suppose that filaments have an isotropic orientation in average, which leads to $\langle\cos^2\psi_i\rangle = \langle\sin^2\psi_i\rangle = \frac{1}{2}$. We deduce the local spectrin length

$$l(\theta, \varphi) = \langle l_i\rangle \sim \xi_0 \left\{1 + u + \frac{1}{4}(\boldsymbol{\nabla}_\perp u)^2 + \mathcal{O}(u^3)\right\}. \tag{4.133}$$

We can evaluate the local spectrin energy up to 2nd order in u as

$$\frac{k}{2}(l - l_0)^2 \sim \frac{k}{2}\xi_0^2 \left\{\chi_0^2 + 2\chi_0\left[u + \frac{1}{4}(\boldsymbol{\nabla}_\perp u)^2\right] + u^2 + \mathcal{O}(u^3)\right\}, \tag{4.134}$$

where we defined $\chi_0 = 1 - l_0/\xi_0$ similarly as for 1-dimensional membranes.

We deduce the total spectrin energy

$$\Delta\mathcal{U}_s \sim R_0^2 \int d\Omega\, \rho^{\mathrm{B}}(\Omega) \left\{\frac{k}{2}\xi_0^2\left(\chi_0^2 + 2\chi_0\left[u + \frac{1}{4}(\boldsymbol{\nabla}_\perp u)^2\right] + u^2\right) - E_{\mathrm{B}}\right\} \tag{4.135}$$

where $\rho^{\mathrm{B}}(\Omega) = \rho_0^{\mathrm{B}} + \delta\rho^{\mathrm{B}}(\Omega)$ is the local surface density of bound filaments.

The underlying triangular network topology reappears via the parameter $g \equiv 2\sqrt{3}$ in total spectrin surface density ρ_0, that can be calculated as

$$\rho_0 \equiv \frac{\mathrm{Nb[springs/triangle]}}{\mathrm{Area[triangle]}} = \frac{3/2}{\xi_0^2\sqrt{3}/4} = \frac{2\sqrt{3}}{\xi_0^2} = \frac{g}{\xi_0^2}\,. \tag{4.136}$$

We define the fraction of attachment $n^{\mathrm{B}}(\theta,\varphi) = \frac{\rho^{\mathrm{B}}(\theta,\varphi)}{\rho_0} = \rho^{\mathrm{B}}(\theta,\varphi)\frac{\xi_0^2}{g}$, that we expand in spherical harmonics as

$$n^{\mathrm{B}}(\theta,\varphi) = n_0^{\mathrm{B}}\left[1 + \frac{n_{00}}{\sqrt{4\pi}} + \sum_{l,m} n_{lm}\,\mathcal{Y}_{lm}\right] = n_0^{\mathrm{B}}\left[1 + \sum_{l,m} n_{lm}\,\mathcal{Y}_{lm}\right], \tag{4.137}$$

where the zeroth order n_{00} is included in n_0^{B} and therefore chosen to be zero.

By expanding the spectrin energy (4.135) up to 2nd order and omitting the constant terms we find

$$\Delta\mathcal{U}_s \sim g\,kR_0^2\left\{\sum_{l,m}\frac{|u_{lm}|^2}{2}\,n_0^{\mathrm{B}}\left[(1-\chi_0) + \frac{\chi_0}{2}\,(l-1)(l+2)\right] + \chi_0\sum_{l,m}|n_{lm}u_{lm}|\right\}. \tag{4.138}$$

RBC composite membrane energy

The dimensionless energy of the RBC composite membrane, composed by the lipid-bilayer and the cytoskeleton, can be written up to second order in fluctuations as

$$\frac{\Delta\mathcal{U}}{\kappa} \sim \frac{1}{2}\sum_{l,m}|u_{lm}|^2\left\{\bar{\gamma}^{\mathrm{eff}} + (l+2)(l-1)\left[(l+1)l + \bar{\sigma}^{\mathrm{eff}}\right]\right\} + \bar{e}^{s}\sum_{l,m}|n_{lm}u_{lm}|, \tag{4.139}$$

where we defined the following dimensionless membrane effective parameters

$$\bar{\sigma}^{\mathrm{eff}} = \bar{\sigma} + \frac{gn_0^{\mathrm{B}}\,kR_0^2\chi_0}{2\kappa} = \frac{R_0^2}{\kappa}\left[\sigma + \frac{1}{2}gn_0^{\mathrm{B}}\,k\chi_0\right], \tag{4.140a}$$

$$\bar{\gamma}^{\mathrm{eff}} = \frac{R_0^2}{\kappa}\,gn_0^{\mathrm{B}}\,k(1-\chi_0), \tag{4.140b}$$

$$\bar{e}^{s} = \frac{\rho_0R_0^2\,k\xi_0^2\chi_0}{\kappa} = \frac{g\,kR_0^2\,\chi_0}{\kappa}. \tag{4.140c}$$

From eq. (4.140a) we can define a tension jump at the spectrin network mesh size $\Delta\sigma = \frac{1}{2}gn_0^{\mathrm{B}}\,k\chi_0$ as in [Fournier 2004]. When we take $n_0^{\mathrm{B}} \to 1$ (fully connected network), we recover exactly the same results as [Fournier 2004, Dubus 2006] (see eq. (3.32a) and eq. (3.36a)).

4.3.2 Thermal and chemical fluctuations

4.3.2.1 Langevin dynamics

Langevin equation for the membrane

The equation of motion for $u_{lm}(t)$ $(l \geq 2)$ is the normal force balance equation of the membrane. One has to solve the hydrodynamics problem inside and outside the quasi-spherical membrane and match the solutions at the sphere of radius R_0 for small deformations. The derivation, detailed for example in [Seifert 1999], is tedious and we only state the result here, presented in the same form as in [Abreu 2013]

$$\frac{\partial u_{lm}}{\partial t} = -\mu_l \, \frac{\partial \Delta \mathcal{U}}{\partial u^*_{lm}} + \zeta^u_{lm}(t) \, , \tag{4.141}$$

where

$$\mu_l = \frac{\Gamma_l}{\eta R_0^3} \, , \qquad \Gamma_l = \frac{l(l+1)}{4l^3+6l^2-1} = \frac{l(l+1)}{(2l+1)(2l^2+2l-1)} \, . \tag{4.142}$$

and the thermal noise $\zeta_{lm}(t)$ is white and its correlations

$$\left\langle \zeta^u_{lm}(t) \zeta^u_{l'm'}(t') \right\rangle = 2\mu_l \, k_\mathrm{B}T \, \delta_{l,l'} \delta_{m,m'} \delta(t-t') \, , \tag{4.143}$$

are given by the fluctuation-dissipation theorem at equilibrium.

The normal "force" on the membrane is calculated as

$$-\frac{\partial \Delta \mathcal{U}}{\partial u^*_{lm}} = -\kappa \Big\{ \bar{E}^\mathrm{eff}_l \, u_{lm} - \bar{e}^s \, n_{lm} \Big\} \, , \tag{4.144}$$

where the dimensionless composite membrane energy $\bar{E}^\mathrm{eff}_l$ for the mode l is given by

$$\bar{E}^\mathrm{eff}_l = \bar{\gamma}^\mathrm{eff} + (l+2)(l-1) \Big[l(l+1) + \bar{\sigma}^\mathrm{eff} \Big] \tag{4.145}$$

The Langevin equation for the mode u_{lm} can finally be rewritten as

$$\frac{\partial u_{lm}}{\partial t} = -\omega^\mathrm{eff}_l \, u_{lm} - \omega^s_l \, n_{lm} + \zeta^u_{lm}(t) \tag{4.146}$$

where we defined a composite membrane relaxation frequency ω^eff_l and spectrin-associated frequency ω^s_l, both depending on the mode l

$$\omega^\mathrm{eff}_l = \mu_l \kappa \bar{E}^\mathrm{eff}_l = \frac{\kappa}{\eta R_0^3} \, \bar{E}^\mathrm{eff}_l \Gamma_l \qquad \omega^s_l = \mu_l \kappa \bar{e}^s = \mu_l \, \rho_0 R_0^2 \, k \xi_0^2 \chi_0 \, . \tag{4.147}$$

Langevin equation for the chemical reaction

The Langevin equation for the mode $l \geq 2$, m of the fraction of attachment n_{lm} is calculated as for the 1-dimensional membrane and reads

$$\frac{\partial n_{lm}}{\partial t} = -\omega^\mathrm{B}_0 \, n_{lm} - \Gamma^\mathrm{B}_0 \lambda^s_0 \, u_{lm} + \zeta^\mathrm{B}_{lm}(t) \tag{4.148}$$

where we defined the following parameters

$$\omega^\mathrm{B}_0 = k_\mathrm{on0} + k_\mathrm{off} \tag{4.149a}$$

$$\lambda^s_0 = \frac{g k R_0^2 \chi_0}{k_\mathrm{B}T} = \frac{\kappa \bar{e}_s}{k_\mathrm{B}T} \tag{4.149b}$$

$$\Gamma^\mathrm{B}_0 = \omega^\mathrm{B}_0 \, n^\mathrm{B}_0 (1 - n^\mathrm{B}_0) = \frac{k_\mathrm{on0} \, k_\mathrm{off}}{k_\mathrm{on0} + k_\mathrm{off}} \tag{4.149c}$$

with $k_{\mathrm{on}0} = k^o \exp\left(-\frac{k\xi_0^2\chi_0^2}{2k_{\mathrm{B}}T}\right)$ as in 1-dimensional case.

Note the useful following relation $\omega_l^s = \mu_l\,\lambda_0^s\,k_{\mathrm{B}}T$.

The chemical noise is white and its correlations are given by

$$\left\langle \zeta_{lm}^{\mathrm{B}}(t)\zeta_{l'm'}^{\mathrm{B}}(t')\right\rangle = 2\left(\Gamma_0^{\mathrm{B}} + \Gamma_a^{\mathrm{B}}\right)\,\delta_{l,l'}\delta_{m,m'}\delta(t-t') \tag{4.150}$$

where Γ_a^{B} is the active (non-equilibrium) part of the chemical noise and $N = 4\pi R_0^2\rho_0$ is the total number of springs.

4.3.2.2 Fluctuations and response of the coupled system

The coupled system of Langevin equations for the mode $l \geq 2$, $-l \leq m \leq l$ reads

$$\begin{aligned}
\frac{\partial u_{lm}}{\partial t} &= -\omega_l^{\mathrm{eff}}\,u_{lm} - \omega_l^s\,n_{lm} + z_{lm}^u(t)\\
\frac{\partial n_{lm}}{\partial t} &= -\omega_0^{\mathrm{B}}\,n_{lm} - \Gamma_0^{\mathrm{B}}\lambda_0^s\,u_{lm} + z_{lm}^{\mathrm{B}}(t)
\end{aligned}$$

In Fourier space, i can be condensed in a matrix form

$$\mathbf{M}_{lm}(\omega)\cdot\mathbf{X}_{lm}(\omega) = \boldsymbol{Z}_{lm}(\omega)\,, \tag{4.152}$$

where we have defined

$$\mathbf{M}_{lm}(\omega) = \begin{pmatrix} -i\omega + \omega_l^{\mathrm{eff}} & \omega_l^s \\ \Gamma_0^{\mathrm{B}}\lambda_0^s & -i\omega + \omega_0^{\mathrm{B}} \end{pmatrix} \tag{4.153a}$$

$$\mathbf{X}_{lm}(\omega) = \begin{pmatrix} u_{lm} \\ n_{lm} \end{pmatrix} \tag{4.153b}$$

and the vector $\mathbb{Z}_{lm}(\omega)$ is chosen either as the noise or as an external driving, whether the correlation function or the response function is calculated:

$$\boldsymbol{Z}_{lm}^{\mathrm{noise}}(\omega) = \begin{pmatrix} \zeta_{lm}^{\mathrm{u}} \\ \zeta_{lm}^{\mathrm{B}} \end{pmatrix}\,, \qquad \boldsymbol{Z}_{lm}^{\mathrm{driving}}(\omega) = \begin{pmatrix} \mu_l\,f_{lm}^{\mathrm{ext}} \\ \Gamma_0^{\mathrm{B}}\,\frac{\Delta\mu_{lm}^{\mathrm{ext}}}{k_{\mathrm{B}}T} \end{pmatrix}\,. \tag{4.154}$$

In temporal Fourier space, the correlation of the two noise sources are given by

$$\left\langle \zeta_{lm}^u(\omega)\zeta_{l'm'}^u(\omega')\right\rangle = 2\mu_l\,k_{\mathrm{B}}T\,\delta_{l,l'}\delta_{m,m'}\delta(\omega+\omega')\,, \tag{4.155a}$$

$$\left\langle \zeta_{lm}^{\mathrm{B}}(\omega)\zeta_{l'm'}^{\mathrm{B}}(\omega')\right\rangle = 2\left(\Gamma_0^{\mathrm{B}} + \Gamma_a\right)\,\delta_{l,l'}\delta_{m,m'}\delta(\omega+\omega') \tag{4.155b}$$

The determinant of the matrix $\mathbf{M}_{lm}(\omega)$ reads

$$\det\left[\mathbf{M}_{lm}(\omega)\right] = \omega_0^{\mathrm{B}}\omega_l^{\mathrm{eff}} - \omega^2 - \omega_l^s\Gamma_0^{\mathrm{B}}\lambda_0^s - i\omega\left(\omega_l^{\mathrm{eff}} + \omega_0^{\mathrm{B}}\right)\,. \tag{4.156}$$

It vanishes if, and only if $\omega = 0$ and $\omega_0^{\mathrm{B}}\omega_l^{\mathrm{eff}} = \omega_l^s\Gamma_0^{\mathrm{B}}\lambda_0^s$.

For $\omega > 0$, we can therefore define the inverse matrix $\mathbf{M}_{lm}^{-1}(\omega)$

We remark that the matrix $\mathbf{M}_{lm}(\omega)$ does not depend on m, which implies that its complex conjugate is obtained as $\mathbf{M}_{lm}^{*}(\omega) = \mathbf{M}_{lm}(-\omega)$. To simplify, we omit in the following the index m: $\mathbf{M}_{lm}(\omega) = \mathbf{M}_{l}(\omega)$

The square modulus of the determinant can be calculated as

$$\begin{aligned} \left|\det\left[\mathbf{M}_l(\omega)\right]\right|^2 &= \det\left[\mathbf{M}_l(\omega)\right]\det\left[\mathbf{M}_l(-\omega)\right] \\ &= \left[\omega^2 + (\omega_0^{\mathrm{B}})^2\right]\left[\omega^2 + (\omega_l^{\mathrm{eff}})^2\right] + \omega_l^s\Gamma_0^{\mathrm{B}}\lambda_0^s\left[2\left(\omega^2 - \omega_0^{\mathrm{B}}\omega_l^{\mathrm{eff}}\right) + \omega_l^s\Gamma_0^{\mathrm{B}}\lambda_0^s\right]. \end{aligned}$$

Response function

The response $\mathbf{X}_{lm}(\omega)$ of the system to an external driving $\mathbf{Z}_{lm}^{\mathrm{driving}}(\omega)$ is given by $\mathbf{X}_{lm}(\omega) = \mathbf{M}_l^{-1}(\omega)\cdot \boldsymbol{Z}_{lm}^{\mathrm{driving}}(\omega)$.

The response function in Fourier Space $\tilde{\boldsymbol{\chi}}_{lm}(\omega)$ and is defined as (see section 4.A.1)

$$\mathbf{X}_{lm}(\omega) = \tilde{\boldsymbol{\chi}}_{lm}(\omega)\cdot\begin{pmatrix}\tilde{f}_{lm}^{\mathrm{ext}}\\ \delta\tilde{\Delta\mu}_{lm}^{\mathrm{ext}}\end{pmatrix} \tag{4.157}$$

It depends only on l and ω and we obtain

$$\tilde{\boldsymbol{\chi}}_l(\omega) = \frac{\det\left[\mathbf{M}_l(-\omega)\right]}{\left|\det\left[\mathbf{M}_l(\omega)\right]\right|^2}\begin{pmatrix}\mu_l\left(-i\omega + \omega_0^{\mathrm{B}}\right) & -\mu_l\Gamma_0^{\mathrm{B}}\lambda_0^s\\ -\mu_l\Gamma_0^{\mathrm{B}}\lambda_0^s & \left(-i\omega + \omega_l^{\mathrm{eff}}\right)\Gamma_0^{\mathrm{B}}/k_{\mathrm{B}}T\end{pmatrix}, \tag{4.158}$$

using the relation $\omega_l^s = \mu_l\,\lambda_0^s\,k_{\mathrm{B}}T$.

We now calculate the dissipative part of the response function. We multiply it by $\frac{2k_{\mathrm{B}}T}{\omega}$ to compare it directly to the fluctuations correlation function

$$\frac{2k_{\mathrm{B}}T}{\omega}\,\tilde{\boldsymbol{\chi}}_l''(\omega) = \frac{1}{\left|\det\left[\mathbf{M}_l(\omega)\right]\right|^2}\begin{pmatrix}\tilde{\chi}_l^{\mathrm{uu}}(\omega) & \tilde{\chi}_l^{\mathrm{Bu}}(\omega)\\ \tilde{\chi}_l^{\mathrm{uB}}(\omega) & \tilde{\chi}_l^{\mathrm{BB}}(\omega)\end{pmatrix} \tag{4.159}$$

with

$$\tilde{\chi}_l^{\mathrm{uu}}(\omega) = 2\,k_{\mathrm{B}}T\,\mu_l\left[(\omega_0^{\mathrm{B}})^2 + \omega^2\right] + 2\,\Gamma_0^{\mathrm{B}}\,(\omega_l^s)^2 \tag{4.160a}$$

$$\tilde{\chi}_l^{\mathrm{Bu}}(\omega) = \tilde{\chi}_l^{\mathrm{uB}}(\omega) = -2\,\omega_l^s\,\Gamma_0^{\mathrm{B}}\left(\omega_l^{\mathrm{eff}} + \omega_0^{\mathrm{B}}\right) \tag{4.160b}$$

$$\tilde{\chi}_l^{\mathrm{uu}}(\omega) = 2\,\Gamma_0^{\mathrm{B}}\left[(\omega_l^{\mathrm{eff}})^2 + \omega^2\right] + 2\,(\Gamma_0^{\mathrm{B}})^2\,\omega_l^s\lambda_0^s \tag{4.160c}$$

Autocorrelation function

The autocorrelation function in Fourier Space is defined by

$$\begin{aligned} \tilde{\boldsymbol{\mathcal{C}}}_{lm}(\omega) &= \begin{pmatrix} u_{lm}(\omega)u_{lm}(-\omega) & u_{lm}(\omega)n_{lm}(-\omega) \\ n_{lm}(\omega)u_{lm}(-\omega) & n_{lm}(\omega)n_{lm}(-\omega) \end{pmatrix} \\ &\equiv \frac{1}{\left|\det\left[\mathbf{M}_l(\omega)\right]\right|^2} \begin{pmatrix} \tilde{\mathcal{C}}^{\mathrm{uu}}_{lm}(\omega) & \tilde{\mathcal{C}}^{\mathrm{Bu}}_{lm}(\omega) \\ \tilde{\mathcal{C}}^{\mathrm{uB}}_{lm}(\omega) & \tilde{\mathcal{C}}^{\mathrm{BB}}_{lm}(\omega) \end{pmatrix}, \end{aligned} \tag{4.161}$$

where $\begin{pmatrix} u_{lm} \\ n_{lm} \end{pmatrix} = \mathbf{X}_{lm}(\omega) = \mathbf{M}_l^{-1}(\omega) \cdot \boldsymbol{Z}^{\mathrm{noise}}_{lm}(\omega)$.

The thermal noise on the membrane and the chemical noise are uncorrelated, therefore, the previous autocorrelation matrix can be decomposed into two contributions

$$\tilde{\boldsymbol{\mathcal{C}}}_{lm}(\omega) = \frac{\left\langle \left|\zeta^u_{lm}(\omega)\right|^2 \right\rangle}{\left|\det\left[\mathbf{M}_l(\omega)\right]\right|^2} \boldsymbol{\mathcal{L}}_{\mathrm{u}}(l,\omega) + \frac{\left\langle \left|\zeta^B_{lm}(\omega)\right|^2 \right\rangle}{\left|\det\left[\mathbf{M}_l(\omega)\right]\right|^2} \boldsymbol{\mathcal{L}}_{\mathrm{B}}(l,\omega), \tag{4.162}$$

with $\boldsymbol{\mathcal{L}}_{\mathrm{u}}(l,\omega)$ and $\boldsymbol{\mathcal{L}}_{\mathrm{n}}(l,\omega)$ are hermitian matrices

$$\boldsymbol{\mathcal{L}}_{\mathrm{u}}(l,\omega) = \begin{pmatrix} \omega^2 + (\omega_0^{\mathrm{B}})^2 & -\Gamma_0^{\mathrm{B}}\lambda_0^s\left(\omega_0^{\mathrm{B}} - i\omega\right) \\ -\Gamma_0^{\mathrm{B}}\lambda_0^s\left(\omega_0^{\mathrm{B}} + i\omega\right) & \left(\Gamma_0^{\mathrm{B}}\lambda_0^s\right)^2 \end{pmatrix} \tag{4.163a}$$

$$\boldsymbol{\mathcal{L}}_{\mathrm{B}}(l,\omega) = \begin{pmatrix} (\omega_l^{\mathrm{s}})^2 & -\omega_l^{\mathrm{s}}\left(\omega_l^{\mathrm{eff}} + i\omega\right) \\ -\omega_l^{\mathrm{s}}\left(\omega_l^{\mathrm{eff}} - i\omega\right) & \omega^2 + (\omega_l^{\mathrm{eff}})^2 \end{pmatrix} \tag{4.163b}$$

The correlations of the noise are deduced from eq. (4.164)

$$\left\langle \left|\zeta^u_{lm}(\omega)\right|^2 \right\rangle = 2\mu_l\, k_{\mathrm{B}}T\,, \qquad \left\langle \left|\zeta^{\mathrm{B}}_{lm}(\omega)\right|^2 \right\rangle = 2\left(\Gamma_0^{\mathrm{B}} + \Gamma_a\right) \tag{4.164}$$

And we can calculate the coefficients of the autocorrelation matrix (4.165)

$$\mathcal{C}_l^{\mathrm{uu}}(\omega) = 2\, k_{\mathrm{B}}T\, \mu_l\left[(\omega_0^{\mathrm{B}})^2 + \omega^2\right] + 2\,(\omega_l^{\mathrm{s}})^2\,\left(\Gamma_0^{\mathrm{B}} + \Gamma_a\right) \tag{4.165a}$$

$$\mathcal{C}_l^{\mathrm{uB}}(\omega) = -2\,\Gamma_0^{\mathrm{B}}\,\omega_l^s(\omega_0^{\mathrm{B}} + \omega_l^s) - 2\,\Gamma_a\,\omega_l^s\left(i\omega + \omega_l^{\mathrm{eff}}\right) \tag{4.165b}$$

$$\mathcal{C}_l^{\mathrm{Bu}}(\omega) = -2\,\Gamma_0^{\mathrm{B}}\,\omega_l^s(\omega_0^{\mathrm{B}} + \omega_l^s) - 2\,\Gamma_a\,\omega_l^s\left(-i\omega + \omega_l^{\mathrm{eff}}\right) \tag{4.165c}$$

$$\mathcal{C}_l^{\mathrm{BB}}(\omega) = 2\,\left(\Gamma_0^{\mathrm{B}} + \Gamma_a\right)\left[\omega^2 + (\omega_l^{\mathrm{eff}})^2\right] - 2\,(\Gamma_0^{\mathrm{B}})^2\omega_l^s\lambda_0^s \tag{4.165d}$$

Fluctuation-dissipation theorem at equilibrium

Taking the difference between fluctuations and dissipation matrices we get

$$\tilde{\boldsymbol{\mathcal{C}}}_l(\omega) - \frac{2k_{\mathrm{B}}T}{\omega}\,\tilde{\boldsymbol{\chi}}_l''(\omega) = \frac{2\Gamma_a}{\left|\det\left(\mathbf{M}_l(\omega)\right)\right|^2} \begin{pmatrix} (\omega_l^s)^2 & -\omega_l^s\left(i\omega + \omega_l^{\mathrm{eff}}\right) \\ -\omega_l^s\left(-i\omega + \omega_l^{\mathrm{eff}}\right) & \omega^2 + (\omega_l^{\mathrm{eff}})^2 \end{pmatrix}$$

(4.166)

At chemical equilibrium, $\Gamma_a = 0$ (see eq. (4.105)) and the fluctuation-dissipation theorem is verified

$$\tilde{\boldsymbol{\mathcal{C}}}_l(\omega) = \frac{2k_{\mathrm{B}}T}{\omega}\,\tilde{\boldsymbol{\chi}}_l''(\omega) \tag{4.167}$$

4.3.2.3 Fluctuations and response of the composite membrane

Experimentally, a mechanical driving f^{ext} can be applied with an optical tweezer (active microrheology, see section 4.4) whereas the chemical driving $\Delta\mu^{\mathrm{ext}}$ is hardly possible to apply. Similarly one can measure the membrane fluctuations by careful shape recording or passive microrheology (see section 4.4), whereas the chemical fluctuations are difficult to access.

In the following we therefore restrict ourselves to the case where $\Delta\mu^{\mathrm{ext}} = 0$ and where we can only measure the response function $\chi(\omega) \equiv \sum_{l,m}\chi_{lm}(\omega)$ and the fluctuation spectrum on one single point of the membrane $\left\langle \left|u(\omega)\right|^2\right\rangle \equiv \sum_{l,m}\left\langle \left|u_{lm}(\omega)\right|^2\right\rangle$.

The membrane autocorrelation function for the mode l, m is given by eqs. (4.165) and (4.165a)

$$\left\langle \left|u_{lm}(\omega)\right|^2\right\rangle = \frac{2\,k_{\mathrm{B}}T\,\mu_l\left[(\omega_0^{\mathrm{B}})^2+\omega^2\right]+2\,\left(\Gamma_0^{\mathrm{B}}+\Gamma_a\right)(\omega_l^{\mathrm{s}})^2}{\left|\,\det\left(\mathbf{M}_l(\omega)\right)\right|^2} \tag{4.168}$$

Membrane at equilibrium

We recall that $\Gamma_0^{\mathrm{B}} = \omega_0^{\mathrm{B}}\,n_0^{\mathrm{B}}\left(1-n_0^{\mathrm{B}}\right)$ (see eq. (4.149c)) and that at equilibrium $\Gamma_a = 0$. We can study two limit cases: a spectrin network fully attached $n_0^{\mathrm{B}} \to 1$, and no spectrin network $n_0^{\mathrm{B}} \to 0$. Both cases lead immediately to $\Gamma_0^{\mathrm{B}} \to 0$ and $\left|\,\det\left[M_l(\omega)\right]\right|^2 \to \left[\omega^2+(\omega_0^{\mathrm{B}})^2\right]\left[\omega^2+(\omega_l^{\mathrm{eff}})^2\right]$ (section 4.3.2.2), which leads to the following membrane autocorrelation at equilibrium

$$\left\langle \left|u_{lm}(\omega)\right|^2\right\rangle^{\mathrm{eq}} \xrightarrow[n_0^{\mathrm{B}}\to 0,\,1]{} \frac{2\,\mu_l\,k_{\mathrm{B}}T}{\omega^2+(\omega_l^{\mathrm{eff}})^2}\,, \tag{4.169}$$

which is the classical form of the fluctuation spectrum for the mode l, m for a simple quasi-spherical membrane, with effective mechanical parameters if $n_0^{\mathrm{B}} \to 1$ and pure lipid-bilayer properties if $n_0^{\mathrm{B}} \to 0$.

Hence, if the depletion of ATP leads to a perfectly connected spectrin network ($n_0^{\mathrm{B}} \to 1$), as we expect from the biochemical studies, the fluctuation spectrum should be of the form (4.169), with the following mechanical parameters[9]

$$\bar{\sigma}^{\mathrm{eff}} = \bar{\sigma} + \frac{g\,k R_0^2 \chi_0}{2\kappa} = \frac{R_0^2}{\kappa}\left[\sigma + \frac{1}{2} g\,k\chi_0\right], \tag{4.170a}$$

$$\bar{\gamma}^{\mathrm{eff}} = \frac{R_0^2}{\kappa}\, g\,k(\chi_0 - 1)\,. \tag{4.170b}$$

Membrane response function

In the general case (no ATP depletion), the dissipative part of the response function $\tilde{\chi}_l''(\omega)$ for the membrane only ($\Delta\mu^{\mathrm{ext}} = 0$) is the same as in eq. (4.160)

$$\frac{2k_{\mathrm{B}}T}{\omega}\,\tilde{\chi}_l''(\omega) = \frac{2\,k_{\mathrm{B}}T\,\mu_l\left[(\omega_0^{\mathrm{B}})^2 + \omega^2\right] + 2\,\Gamma_0^{\mathrm{B}}\,(\omega_l^s)^2}{\left|\det\left[\mathbf{M}_l(\omega)\right]\right|^2} \tag{4.171}$$

4.3.3 Numerical application

4.3.3.1 Composite membrane at equilibrium

We first consider a membrane depleted of ATP. We suppose therefore that $\Delta\mu_{\mathrm{ATP}} = 0$ and $\theta = 0$, which implies the active part of the chemical noise correlation $\Gamma_a = 0$.

Reference state

We recall the expression of the on- and off-rates and of the attachment fraction of at equilibrium and with $\theta = 0$ from eq. (4.109)

$$k_{\mathrm{on}} = k_2^o \exp\left(-\frac{k\xi_0^2\chi_0^2}{2k_{\mathrm{B}}T}\right), \qquad k_{\mathrm{off}} = k_2^o \exp\left(-\frac{E_{\mathrm{B}}}{k_{\mathrm{B}}T}\right), \qquad n_0^{\mathrm{B}} = \frac{k_{\mathrm{on}}}{k_{\mathrm{on}} + k_{\mathrm{off}}}.$$

According to biochemical studies,the binding affinity of the spectrin filament to the complex 4.1 R is high $\frac{E_{\mathrm{B}}}{k_{\mathrm{B}}T} \gg 1$. Taking typical values from the literature for the spectrin mechanical parameters table 4.E.1. The spectrin filament elongation energy $\frac{1}{2}k\xi_0^2\chi_0^2$ for a prestress $\chi_0 = 1$ is of the order of $k_{\mathrm{B}}T$. Therefore, at equilibrium $k_{\mathrm{off}} \ll k_{\mathrm{on}}$, which leads to $n_0^{\mathrm{B}} \sim 1$: there is no spontaneous detachment of spectrin filaments. The fraction of attachment does not depend on the prestress as we check on fig. 4.2.

---

[9] Note that we neglected here the renormalization of the bending modulus by the spectrin network.

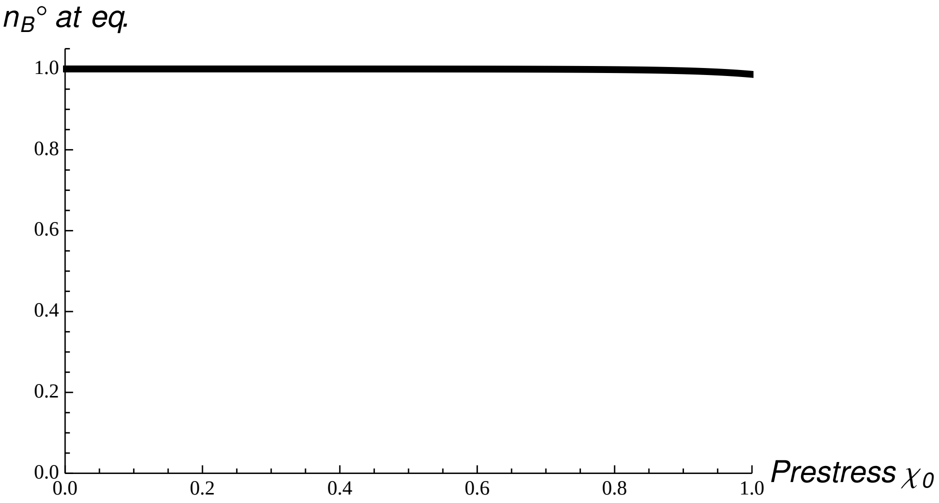

Figure 4.2: Fraction of attachment n_0^{B} at equilibrium, as a function of the prestress χ_0 for a realistic value of the binding affinity $E_{\mathrm{B}} \sim 20\, k_{\mathrm{B}}T$.

On the contrary the spectrin contribution to the membrane tension $\Delta\sigma = \frac{1}{2} g n_0^{\mathrm{B}}\, k\, \chi_0$ is directly proportional the prestress as shown on fig. 4.3

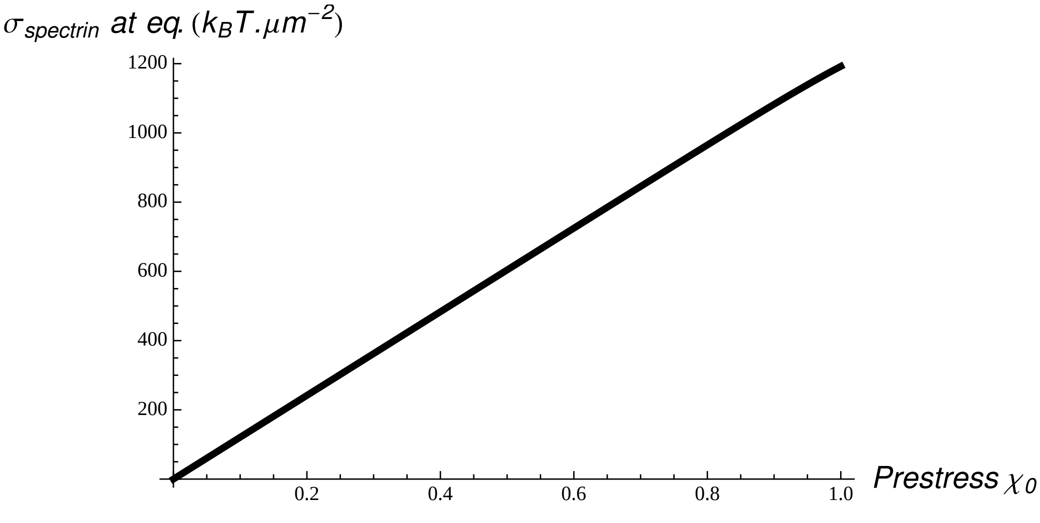

Figure 4.3: Spectrin tension $\sigma_{\mathrm{spectrin}}$ at equilibrium, as a function of the prestress χ_0 at for a realistic value of the binding affinity $E_{\mathrm{B}} \sim 20\, k_{\mathrm{B}}T$.

This behavior changes radically, if the binding energy is decreased to lower values, close to $k_{\mathrm{B}}T$: spontaneous spectrin filament detachment becomes possible for non-zero prestress, thereby decreasing the fraction of attachment and lowering or compensating the increase of spectrin tension as a function of the prestress, as shown on fig. 4.4

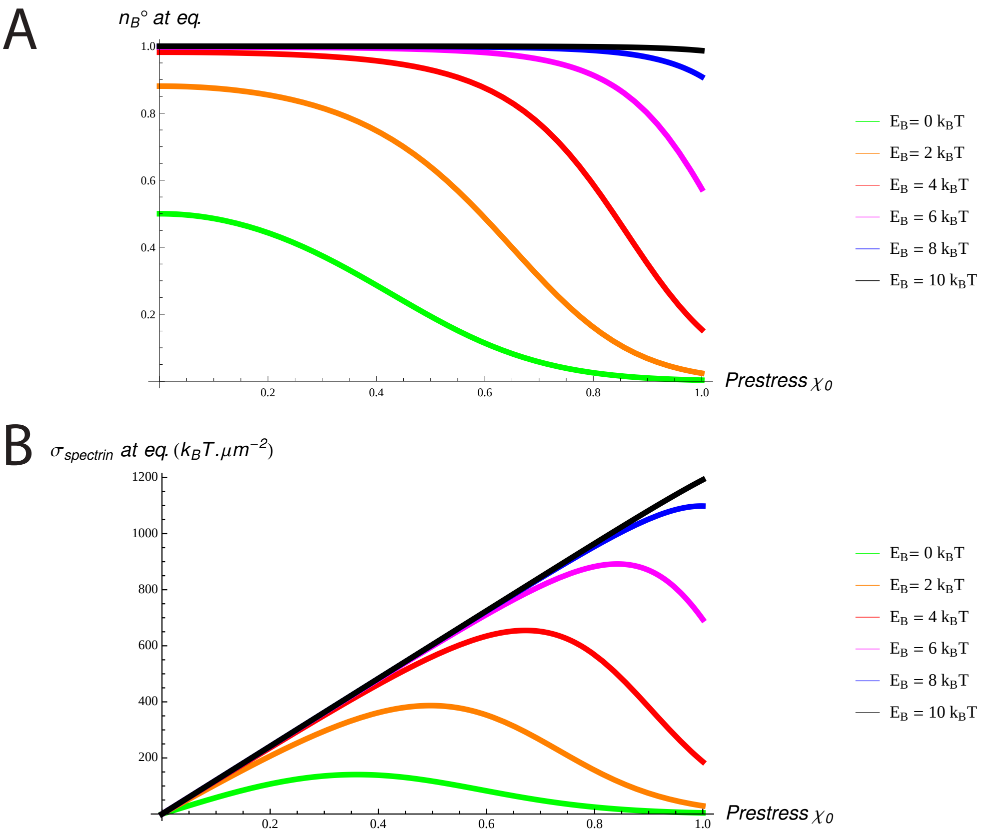

Figure 4.4: Fraction of attachment n_0^{B} and spectrin tension $\sigma_{\mathrm{spectrin}}$ at equilibrium, as a function of the prestress χ_0 for various values of the binding affinity $0 \leq E_{\mathrm{B}} \leq 20$.

Membrane fluctuations at equilibrium (high binding affinity)

We plot the fluctuation amplitude $\left\langle u_{lm}^2 \right\rangle = \int_0^\infty \frac{d\omega}{2\pi} \left\langle u_{lm}^2(\omega) \right\rangle$, as a function of the mode l in fig. 4.5. The lower modes have the highest amplitude, which is expected

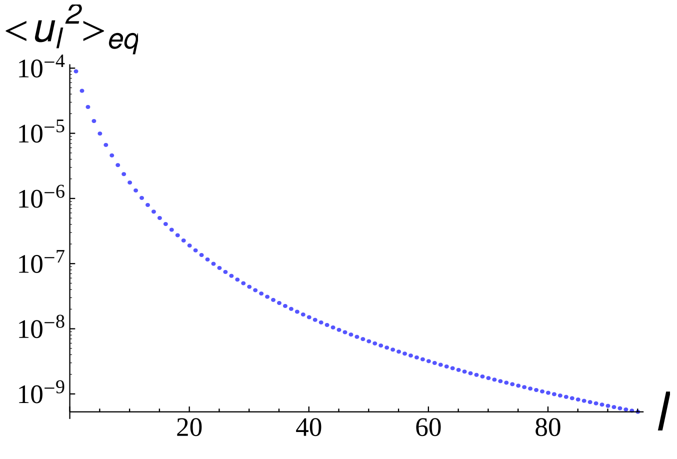

Figure 4.5: Fluctuation autocorrelation function $\left\langle u_{lm}^2 \right\rangle$ as a function of the mode l ($n_0^{\mathrm{B}} = 1$).

from the equilibrium expression of the fluctuation spectrum (4.169), that, in the limit $\omega \to 0$, becomes

$$\left\langle \left| u_{lm}(\omega) \right|^2 \right\rangle^{\mathrm{eq}} \xrightarrow[\omega\to 0]{} \frac{2\,\mu_l\, k_{\mathrm{B}}T}{(\omega_l^{\mathrm{eff}})^2} \sim \frac{2k_{\mathrm{B}}T}{\kappa \bar{E}_l^{\mathrm{eff}}}\,, \tag{4.172}$$

where $\bar{E}_l^{\mathrm{eff}}$ is a increasing function of l.

We plot in fig. 4.6 the fluctuation spectrum $\langle u^2(\omega)\rangle = \sum_{lm} \langle u_{lm}^2(\omega)\rangle$ for a binding affinity $E_{\mathrm{B}}/k_{\mathrm{B}}T \gg 1$ and various spectrin network prestress values χ_0 between 0 and 1. When the prestress increases, the spectrin contribution to the membrane tension increases, thereby lowering the amplitude of low frequency fluctuations.

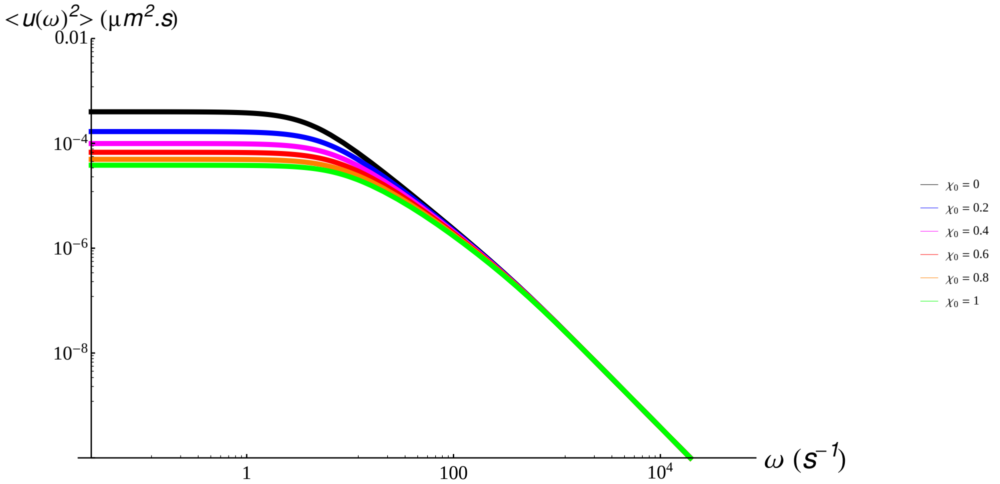

Figure 4.6: Fluctuation spectrum $\langle u^2(\omega)\rangle$ at equilibrium for high binding affinity $E_{\mathrm{B}}/k_{\mathrm{B}}T \gg 1$ and various prestress of spectrin filaments χ_0.

We compare now in fig. 4.7 the fluctuation spectrum obtained from the general formula that includes chemistry (eq. (4.168) at equilibrium ($\Gamma_a = 0$), and the fluctuation spectrum obtained in the limit $n_{\mathrm{B}} \to 1$ eq. (4.169) that neglects chemistry. We show the curves for three binding affinities $E_{\mathrm{B}}/k_{\mathrm{B}}T = 0$, 10, 20 at fixed prestress $\chi_0 = 0.4$. For $E_{\mathrm{B}}/k_{\mathrm{B}}T = 0$ and 10, there is a notable difference at low frequencies, indicating that allowing for the attachment and detachment of spectrin, even at equilibrium, not only renormalizes the membrane tension but can drastically affect the fluctuation spectrum. Note that for a higher binding affinity $E_{\mathrm{B}}/k_{\mathrm{B}}T = 20$, the two fluctuation spectra coincide, as expected in the strict limit $n_{\mathrm{B}} \xrightarrow[E_{\mathrm{B}} \gg k_{\mathrm{B}}T]{} 1$.

Instability at $\omega = 0$

At $\omega = 0$ the determinant of the matrix $\mathbf{M}_l(\omega)$ can cancel out if $\omega_0^{\mathrm{B}} \omega_l^{\mathrm{eff}} = \omega_l^s \Gamma_0^{\mathrm{B}} \lambda_0^s$ (see eq. (4.156)). This condition can be rewritten as $n_0^{\mathrm{B}}\big(1 - n_0^{\mathrm{B}}\big)\lambda_o^{s2} = \frac{E_l^{\mathrm{eff}}}{k_{\mathrm{B}}T}$, where the membrane energy E_l^{eff} for the mode l never vanishes. Therefore, for $n_0^{\mathrm{B}} = 0$ or 1 (no spectrin, or fully attached network), the membrane is stable for any mode of deformation.

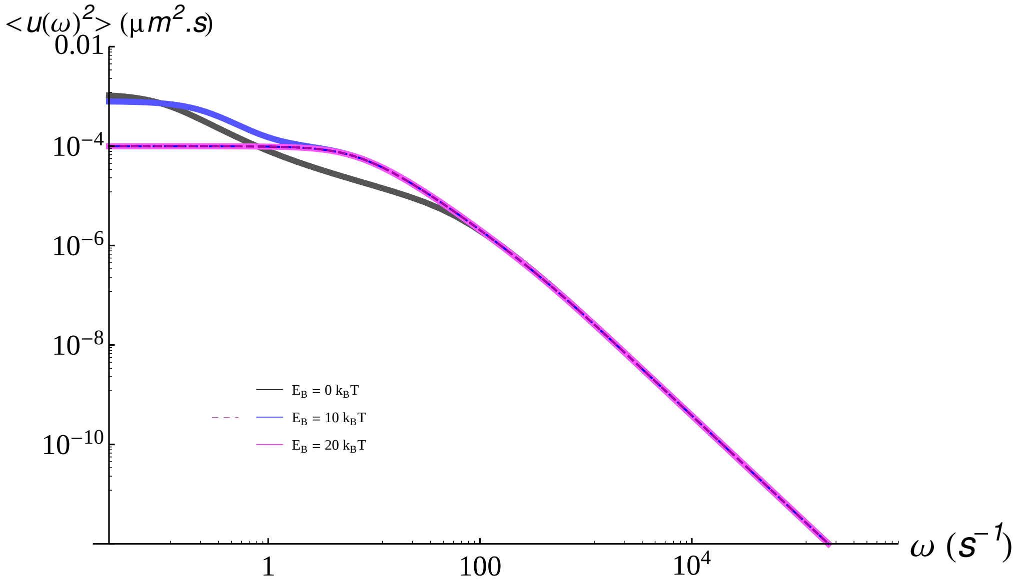

Figure 4.7: Fluctuation spectrum $\langle u^2(\omega)\rangle$ at equilibrium for three binding affinities $E_{\mathrm{B}}/k_{\mathrm{B}}T \gg 0$, 10, 20 and fixed prestress $\chi_0 = 0.4$. Plain lines include chemical noise at equilibrium ($k_2^o = 1\,s^{-1}$); dashed lines include only thermal fluctuations of the membrane.

For any value $0 < n_0^{\mathrm{B}} < 1$, we can solve numerically the previous condition considering l as the unknown, using realistic numerical values of the membrane parameters (see table 4.E.1). We find that there is generally an integer l_c between 2 and 30 that approaches the real solution, depending on the exact value of the attachment fraction n_0^{B}. As a consequence, the fluctuations are maximal for this mode. The plot of the fluctuation amplitude as a function of the mode l displays a sharp peak around the mode l_c, as shown on fig. 4.8.

This instability can be understood as follows: fluctuations enhance locally the filament elongation, thereby decreasing the attachment rate; the spectrin network being less attached, the fluctuations are locally favored as a consequence. This phenomenon may be partially buffered by imposing the value of the membrane excess area, thereby imposing the strict conservation of total membrane surface. We have not applied this constraint here. The fluctuation amplitude at fixed volume is indeed naturally limited by excess area available to deform. Here, we sketch only the procedure, that we plan to develop further in the future. We recall that the membrane excess area can be expressed as a function of the square amplitude of the fluctuations

$$\Delta \sim \frac{1}{2}\sum_{l,m}(l-1)(l+2)\left|u_{lm}\right|^2 . \tag{4.123}$$

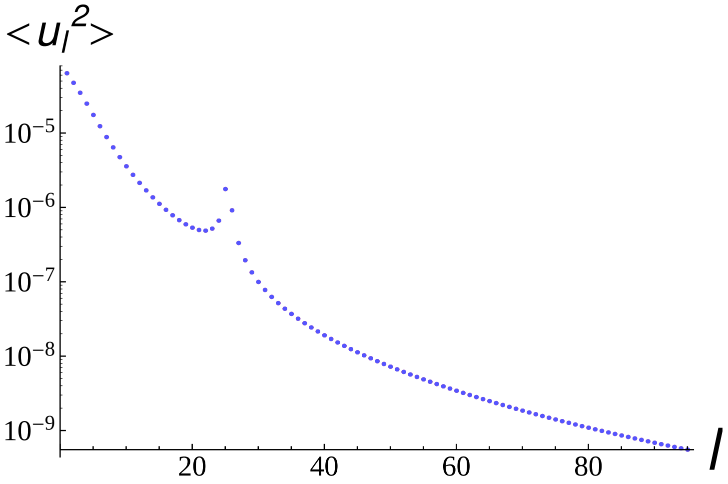

Figure 4.8: Fluctuation autocorrelation function $\langle u_{lm}^2 \rangle$ at equilibrium, as a function of the mode l for $n_0^{\mathrm{B}} \sim 0.75$, displaying a characteristic peak around a mode l_c, where $\det\left[\mathbf{M}_l(\omega)\right]$ approaches zero for $\omega = 0$.

Following the method proposed in [Seifert 1995], and extended by [Loubet 2012] to active membranes (see section 3.3.3.4), one can inject the expression for the membrane $|u_{lm}|^2$ that depends on the lipid bilayer tension $\bar{\sigma}$. This gives a self-consistent equation for the lipid-bilayer tension as a function of the excess area. We expect the resulting effective tension to buffer the amplitude of the fluctuations.

4.3.3.2 Violation of the fluctuation-dissipation theorem

We bypass in this part the complication arising from the instability, to study numerically the effect of the non-equilibrium chemical noise on the membrane fluctuations.

In fig. 4.9 we compare the fluctuation amplitudes and the dissipative part of the response function (multiplied by a factor $\frac{2k_{\mathrm{B}}T}{\omega}$) as a function of the mode l in non-equilibrium steady-state ($\Gamma_a > 0$). The mean square amplitude of the fluctuations (red) is clearly higher than the response function for low modes $l \lesssim 30$, indicating a violation of the fluctuation-dissipation theorem. We confirm the strong violation of the fluctuation-dissipation theorem in a chemical NESS, by plotting in fig. 4.10 A the total fluctuations mean-square amplitude[10] $\left\langle u^2 \right\rangle = \int_1^\infty \frac{d\omega}{2\pi} \sum_{l,m} \left\langle u_{lm}^2(\omega) \right\rangle$ as a function of the dimensionless concentration θ of ATP. For $\theta = 0$ (no ATP), the fluctuations (red) and the dissipative part of the response (blue) coincide, but start to strongly diverge for $\theta > 0$. We observe that the mean-square fluctuation amplitude first increases rapidly, before decreasing slowly, thereby displaying a maximum, which reminds the experimental results of [Tuvia 1998] in RBC ghosts, that we plot in fig. 4.10 B.

---

[10] Note that our integration in angular frequency ω starts at 1 and not 0 in order to bypass the instability previously mentioned, that arises for angular frequencies lower than 1.

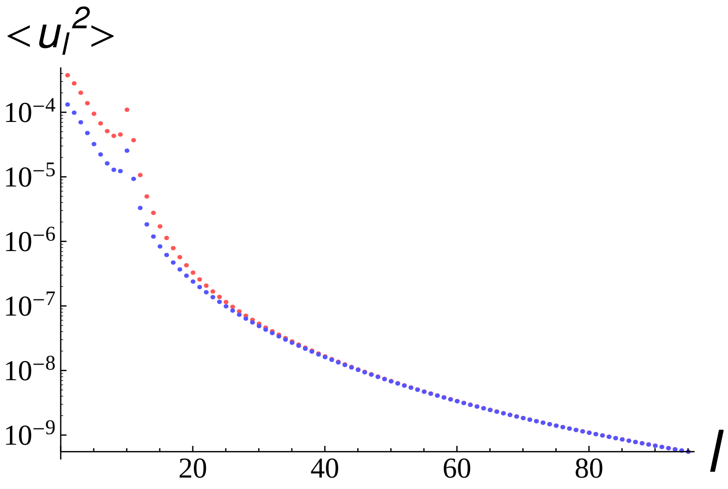

Figure 4.9: Membrane autocorrelation function (red) $\langle u_{lm}^2 \rangle$ and dissipative part of the response function (blue), as a function of the mode l in a NESS. ($E_\mathrm{B} = 20\,k_\mathrm{B}T$, $\chi_0 = 0.12$, $k_2^o = 0.1\,s^{-1}$, $\Delta\mu_\mathrm{ATP} = -20\,k_\mathrm{B}T$, and $\theta = 0.1$).

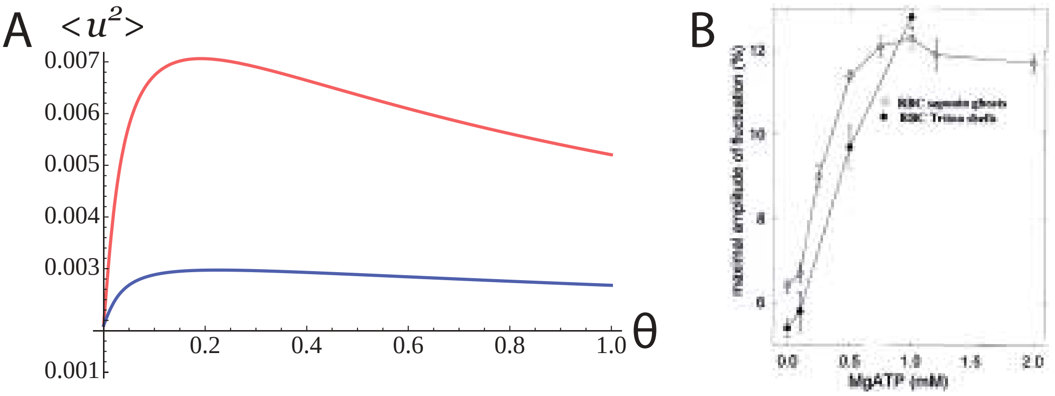

Figure 4.10: (A) Mean-square amplitude $\langle u^2 \rangle$ of the fluctuations and the dissipative part of the response function as a function of the concentration θ of ATP. ($E_\mathrm{B} = 20\,k_\mathrm{B}T$, $\chi_0 = 0.12$, $k_2^o = 0.1\,s^{-1}$, $\Delta\mu_\mathrm{ATP} = -20\,k_\mathrm{B}T$). (B) Effect of the ATP concentration on the cell-membrane fluctuations in RBC ghosts (open circle) and in Triton RBC shells (closed circle). (Reproduced from [Tuvia 1998]).

4.4 Experimental violation of the fluctuation-dissipation relation in RBCs

4.4.1 Experimental setup

T. Betz has performed experiments on human red-blood cells to measure the membrane fluctuation spectrum and response function (unpublished work). An optical trap coupled to quadrant photodiode detector allows to achieve passive or active microrheology on a polystyrene bead attached to the red-cell membrane. Using a very weak trap stiffness, passive microrheology consists in recording the free movement of a bead, thereby measuring the temporal fluctuations of one point of the

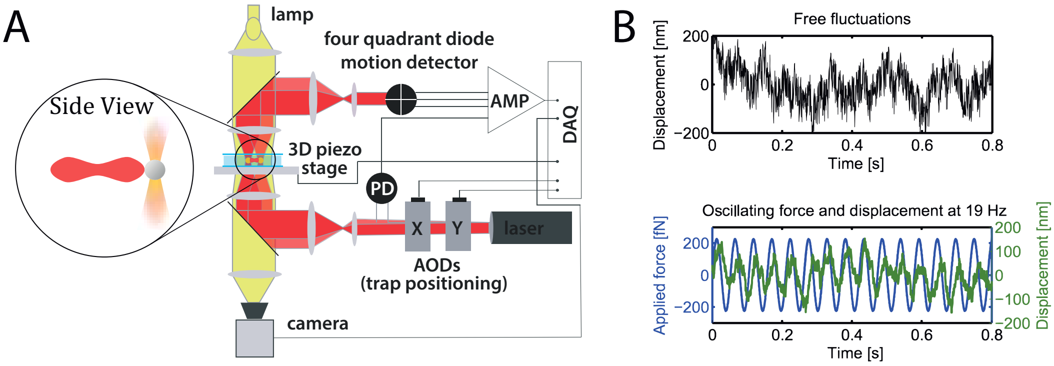

Figure 4.1: Experimental passive and active microrheology setup. (A) Sketch of the experimental setup: a bead, adhering to one point of the red-blood cell membrane, is trapped in an optical tweezer and its position is recorded by a four quadrant photodiode. (B) The free fluctuations of the membrane are recorded via the bead displacement for a low trap stiffness (passive microrheology). To measure the response of the membrane, a sinusoidal force is applied to the bead and its displacement is recorded simultaneously (active microrheology). (Credits T. Betz).

membrane. Active microrheology consists on the contrary in applying a sinusoidal force on the bead, and thus on the membrane, using a stronger trap stiffness, and to concomitantly measure de bead displacement to infer the response function. A schematic representation of the setup is shown on fig. 4.1.

The experimental approach, very similar to [Mizuno 2007], is therefore to measure in the same system both the fluctuation spectrum and Fourier transform of the dissipative part of the response functions, and to compare them to test the equilibrium or non-equilibrium nature of the system, as illustrated on fig. 4.3.

4.4.2 Comparison to theoretical results

We use typical numerical values for the red-blood cell lipid-bilayer and cytoskeleton mechanics, taken from the literature (see table 4.E.1). The exact values of E_{B} and $|\Delta\mu_{\mathrm{ATP}}|$ have no influence on the dynamics, as long as they are very large compared to $k_{\mathrm{B}}T$ and that $|\Delta\mu_{\mathrm{ATP}}| \geq E_{\mathrm{B}}$. The typical chemical rate k_2^o and typical dimensionless ATP concentration θ are adjusted to fit the experimental data at best. Note that the sum on the modes is calculated for l between 2 and $l_{\mathrm{max}} \sim \frac{2\pi R_0}{a} \sim 10$, where a is the typical size of the adhesion region of the bead on the membrane. The larger modes are indeed strongly damped by the bead.

We plot in fig. 4.3 the response $\chi"(\omega)$ and the fluctuations, as derived from the fluctuation-dissipation theorem $\langle u^2(\omega)\rangle \frac{\omega}{2k_{\mathrm{B}}T}$. The theoretical prediction fits reasonnably well the fluctuations, but less satisfactorily the response function. We attribute this discrepancy to the instability of our model at low frequency. The dashed lines represent the contribution of the chemical noise only $2(\Gamma_0^{\mathrm{B}} + \Gamma_a)$ (red) or the thermal mechanical noise only $(2k_{\mathrm{B}}T\,\mu_l)$ (blue) to the fluctuations. We see that the non-equilibrium chemical noise contributes mainly to the low frequency fluctuations.

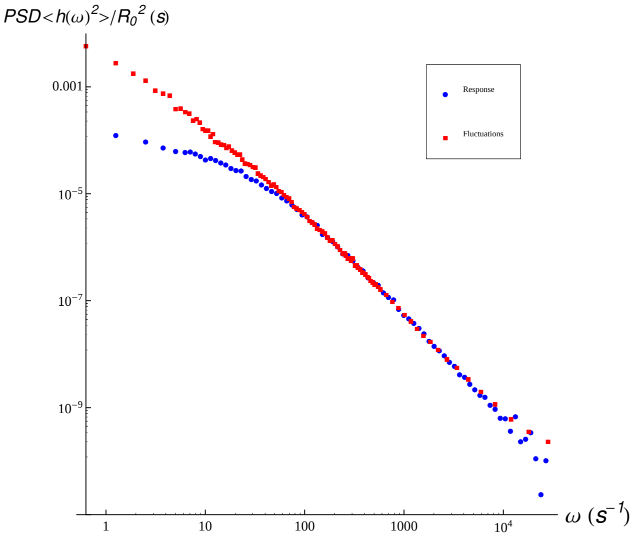

Figure 4.2: Comparison of the dimensionless fluctuation spectrum (red) and the dissipative part of the response function (blue), measured in living human red-blood cells. The fluctuations and response differ significantly, starting from an angular frequency of $100\,s^{-1}$ (Credits: T. Betz, unpublished work).

4.4.3 Discussion

We propose a model to account for the active fluctuations of the red-blood cell membrane. Experimental measurements of the fluctuation spectrum and the response function show a clear violation of the fluctuation-dissipation theorem. This non-equilibrium feature of living matter is generally associated to the steady consumption of ATP, however the comparison between the fluctuations in ATP-depleted cells (dead cells) and normal (living) cells [Betz 2009, Park 2010], cannot be considered as absolutely conclusive and they have been a source of controversy. The experimental results of Betz close this debate, and imply necessarily a source of non-thermal noise in the system.

The spectrin cytoskeleton and the lipid-bilayer do not associate to molecular motors in red-blood cells, to the best of our knowledge. However some of its components can be phosphorylated. We therefore conjecture that the active noise could be of chemical nature directly. Therefore we prove that a direct force on the membrane can emerge from the detachment kinetics of spectrin filaments, as suggested by previous studies [Gov 2007]. But we show that this direct force emerges for a curved membrane only, and if the spectrin cytoskeleton is naturally under tension (or compression) in the red-cell. Then we state that the detachment kinetics must involve at least two different reversible reaction paths to display non-equilibrium features at steady-state. The detachment of filaments is supposed to be driven mainly by ATP, whereas the re-attachment

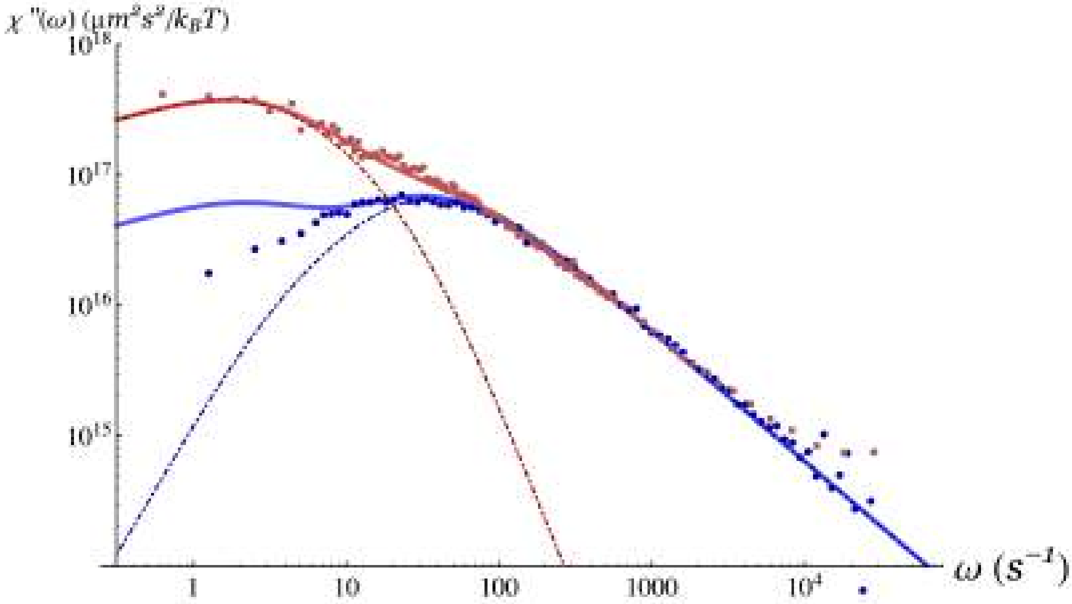

Figure 4.3: Comparison of experimental data and theoretical prediction for the response function (blue) and the response as derived from the fluctuation spectrum (red), using the FDT. Experimental data are dots, theoretical predictions are plane lines. Dashed lines represent the response derived from the fluctuation spectrum, keeping only the thermal mechanical noise contribution (blue) or only the chemical noise contribution (red).

step is supposed essentially spontaneous. In contact to a reservoir of ATP, the filament cycles between the attached and detached states and displays active noise. We finally couple this phoshorylation-dephosphorylation cycle to the membrane to show that the chemical noise can be transduced mechanically. Therefore it breaks the thermal equilibrium of the membrane, when the cell continuously produces ATP.

This work is still ongoing and results are preliminary. We have shown that the system generally displays an instability, using realistic values for the red-blood cell mechanical parameters. This unstable behavior does not seem compatible with experimental observations. We suggest that the limited excess area of lipid-bilayer may limit the amplitude of the instability, but another more profound mechanism may prevent the system to get unstable. Ankyrins may form more stable anchoring points for spectrin in the membrane than the $4.1R$ complex. It may therefore stabilize the network and prevent unstable modes from appearing. This is yet speculative and this possibility should be looked into more closely. We should also point out here that our model approximates the discocyte shape of the red-blood cell membrane by a quasi-spherical membrane. This is a non-negligible approximation, which may lead to quantitative differences. We expect however the fundamental behavior of the membrane to remain qualitatively similar. The study of fluctuations around a discocyte shape with spherical harmonics is out of the scope of this thesis, and may involve terms of higher order.

A second point deserves attention. To calculate the chemical active noise correlation, we have made an analogy with the approach of Harada and Sasa for molecular motors [Harada 2005]. This is a conjecture, but not a concluding proof, and we are investigating the origin of noise in a chemical cycle in a NESS. This point is an active subject of research, but it has not been studied closely within the framework of Langevin equations. An analysis on a simpler system than the phosphorylation-dephosphorylation cycle presented in this thesis tends to indicate that the active noise comes from the explicit contact to the reservoirs. Although the reservoirs are considered as perfect, the contact with the system implies necessarily fluxes of molecules with the open-system, and these fluxes may fluctuate, exactly like the fluxes within the cycle. We pursue therefore also this route, in relation to the main subject of red-blood cell membrane fluctuations.

Appendix

Contents

4.A Fluctuation and response, fluctuation-dissipation theorem

4.A.1 Correlation functions

We first introduce time-dependent correlation functions.

$\langle . \rangle$ denotes an average with respect to an ensemble. In the canonical ensemble we will write the average of an observable ϕ as

$$\langle \phi \rangle = \frac{1}{\mathcal{Z}} \int \phi \, e^{-\mathcal{H}/k_{\mathrm{B}}T} d\mathbf{r} d\mathbf{p} \, , \tag{4.173}$$

where $\mathcal{H}(\mathbf{r}, \mathbf{p})$ is the Hamiltonian of the system that depends on position $\mathbf{r}$ and momentum $\mathbf{p}$, $\mathcal{Z} \equiv \int e^{-\mathcal{H}/k_{\mathrm{B}}T} d\mathbf{r} d\mathbf{p}$ is the partition function of the system.

The two correlation functions for the field $\phi(\mathbf{r}, t)$ is defined as

$$C_\phi(\mathbf{r}, \mathbf{r}', t, t') \equiv \left\langle \phi(\mathbf{r}, t) \phi(\mathbf{r}', t') \right\rangle \, , \tag{4.174a}$$

$$S_\phi(\mathbf{r}, \mathbf{r}', t, t') \equiv \left\langle \Big(\phi(\mathbf{r}, t) - \langle \phi(\mathbf{r}, t) \rangle \Big) \Big(\phi(\mathbf{r}', t') - \left\langle \phi(\mathbf{r}', t') \right\rangle \Big) \right\rangle \tag{4.174b}$$

$$= C_\phi(\mathbf{r}, \mathbf{r}', t, t') - \langle \phi(\mathbf{r}, t) \rangle \left\langle \phi(\mathbf{r}', t') \right\rangle \, . \tag{4.174c}$$

For Hamiltonian independent of time, all thermodynamic averages are invariant under time translation, which implies $\langle \phi(\mathbf{r}, t) \rangle = \langle \phi(\mathbf{r}) \rangle$ and $C(\mathbf{r}, \mathbf{r}', t, t') = C_\phi(\mathbf{r}, \mathbf{r}', t - t')$. It is therefore more convenient to work in temporal Fourier space defining the angular frequency $\omega = 2\pi/(t - t')$:

$$\tilde{\phi}(\mathbf{r}, \omega) = \int_{-\infty}^{\infty} dt e^{i\omega t} \phi(\mathbf{r}, t) \, , \tag{4.175a}$$

$$\phi(\mathbf{r}, t) = \int_{-\infty}^{\infty} \frac{d\omega}{2\pi} e^{-i\omega t} \tilde{\phi}(\mathbf{r}, \omega) \, . \tag{4.175b}$$

The Fourier transform of $S_\phi(\mathbf{r}, \mathbf{r}', t - t'$ is called the power spectrum of $\phi(\mathbf{r}, t)$.

4.A.2 Response functions

The response function $\chi(\mathbf{r}, \mathbf{r}', t - t')$ relates the changes $\delta \langle \phi(\mathbf{r}, t) \rangle$ to time-dependent changes $\delta h(\mathbf{r}, t)$ of an external field h acting on the system as

$$\delta \langle \phi(\mathbf{r}, t) \rangle = \int d\mathbf{r}' dt' \, \chi(\mathbf{r}, \mathbf{r}', t - t') \, \delta h(\mathbf{r}, t) \, . \tag{4.176}$$

The causality principle implies that $\chi(\mathbf{r}, \mathbf{r}', t - t') = 0$ for $t < t'$.

For simplicity we restrict ourselves to the study of one single point $\mathbf{r}$: the perturbation and the response are applied on the same point. One can easily show that the Fourier transform of χ verifies

$$\left\langle \delta \tilde{\phi} \right\rangle = \chi(\omega) \delta h(\omega) \tag{4.177}$$

4.A.3 Fluctuation-dissipation theorem

We propose in the following a classical demonstration of the fluctuation-dissipation theorem (FDT). We denote $\mathcal{H}_0$ the unperturbed Hamiltonian and the associated average $\langle . \rangle_0$, defined as $\langle \phi \rangle = \frac{1}{\mathcal{Z}} \int \phi \, e^{-\mathcal{H}_0/k_\mathrm{B}T} d\mathbf{r} d\mathbf{p}$.

We start from an initial state out-of-equilibrium: for $t < 0$ the system is governed by a perturbed Hamiltonian $\mathcal{H}_0 + \delta\mathcal{H}$, where $\delta\mathcal{H} \sim -\delta h \, \phi(0)$ at first order. δh is the constant perturbation that we suppose small. We use a different notation to denote the mean value of ϕ with respect to this perturbed Hamiltonian for $t < 0$

$$\bar{\phi}(t < 0) = \langle \phi \rangle_0 + \delta\bar{\phi} \,.$$

At $t = 0$ we shut off the perturbation $h(t \geq 0) = 0$ and we look at the system relaxation from its perturbed state, under the Hamiltonian $\mathcal{H}_0$ as sketched on fig. 4.A.1

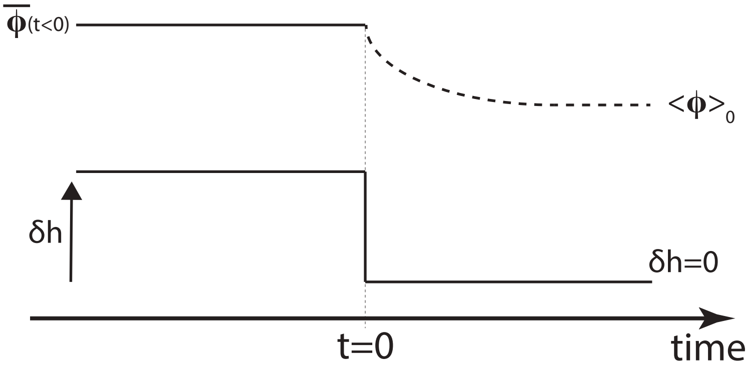

Figure 4.A.1: Sketch of the relaxation of mean value of the field ϕ upon perturbation shut-off $h = 0$ at time $t = 0$.

The correlation function is defined as

$$C_\phi(t, t') = \langle \phi(t)\phi(t') \rangle_0 = \frac{1}{\mathcal{Z}_0} \int d\mathbf{r} d\mathbf{p} \, e^{-\mathcal{H}_0/k_\mathrm{B}T} \, \phi(t, \mathbf{r}, \mathbf{p})\phi(t', \mathbf{r}, \mathbf{p}) \,,$$

We suppose $\mathcal{H}_0$ independent of time and therefore $C_\phi(t, t') = C_\phi(t - t')$.

Let evaluate $\delta\bar{\phi}$:

$$\delta\bar{\phi}(t) = \bar{\phi}(t) - \langle \phi \rangle_0 = \frac{\int d\mathbf{r} d\mathbf{p} \, e^{-(\mathcal{H}_0 + \delta\mathcal{H})/k_\mathrm{B}T} \, \phi(t)}{\int d\mathbf{r} d\mathbf{p} \, e^{-(\mathcal{H}_0 + \delta\mathcal{H})/k_\mathrm{B}T}} - \frac{\int d\mathbf{r} d\mathbf{p} \, e^{-\mathcal{H}_0/k_\mathrm{B}T} \, \phi(t)}{\int d\mathbf{r} d\mathbf{p} \, e^{-\mathcal{H}_0/k_\mathrm{B}T}} \,. \quad (4.178)$$

Since δh is small we develop the previous expression up to first order

$$\int d\mathbf{r} d\mathbf{p} \, e^{-(\mathcal{H}_0 + \delta\mathcal{H})/k_\mathrm{B}T} \, \phi(t) \sim \int d\mathbf{r} d\mathbf{p} \, e^{-\mathcal{H}_0/k_\mathrm{B}T} \, \phi(t) \left[1 + \phi(0) \frac{\delta h}{k_\mathrm{B}T} \right] ,$$

$$\left(\int d\mathbf{r} d\mathbf{p} \, e^{-(\mathcal{H}_0 + \delta\mathcal{H})/k_\mathrm{B}T} \right)^{-1} \sim \left(\int d\mathbf{r} d\mathbf{p} \, e^{-\mathcal{H}_0/k_\mathrm{B}T} \right)^{-1} \left[1 - \frac{\delta h}{k_\mathrm{B}T} \int d\mathbf{r} d\mathbf{p} \, e^{-\mathcal{H}_0/k_\mathrm{B}T} \right] .$$

We can therefore rewrite eq. (4.178) as

$$\begin{aligned}
\delta\bar{\phi}(t) &\sim \left[\langle\phi(t)\rangle_0 + \frac{\delta h}{k_{\mathrm{BT}}}\langle\phi(0)\phi(t)\rangle_0\right]\left[1 - \frac{\delta h}{k_{\mathrm{BT}}}\langle\phi(0)\rangle_0\right] \\
&\sim \frac{\delta h}{k_{\mathrm{BT}}}\left[C_\phi(t) - \langle\phi(t)\rangle_0\langle\phi(0)\rangle_0\right] \\
&\sim \frac{\delta h}{k_{\mathrm{BT}}}\left[C_\phi(t) - \langle\phi(0)\rangle_0^2\right], \qquad (4.180) \\
&\sim \frac{\delta h}{k_{\mathrm{BT}}} S_\phi(t)\,, \qquad (4.181)
\end{aligned}$$

where $\langle\phi(t)\rangle_0 = \langle\phi(0)\rangle_0$ because $\mathcal{H}_0$ is independent on time.

In the frame of linear response theory, the response function χ to the perturbation δh reads

$$\begin{aligned}
\delta\bar{\phi}(t) &\equiv \int_{-\infty}^{\infty} dt'\chi(t-t')\,\delta h(t') \\
&= \int_{-\infty}^{0} \chi(t-t')\,\delta h(t') \qquad \text{by causality} \\
&= \delta h \int_t^{\infty} \chi(t')\,dt'\,, \qquad (4.182)
\end{aligned}$$

because $\delta h = \text{cte}$ for $t < 0$.

From section 4.A.3 we can conclude that $\frac{\delta h}{k_{\mathrm{BT}}} S_\phi(t) = \delta h \int_t^\infty \chi(t')\,dt'$ which implies directly the temporal formulation of the fluctuation-dissipation theorem (FDT)

$$\chi(t) = -\frac{1}{k_{\mathrm{B}}T}\frac{dS_\phi}{dt} \qquad (4.183)$$

The Fourier transform of $\frac{dS_\phi}{dt}$ can be written $-i\omega\,\tilde{S}_\phi(\omega)$, which leads to

$$\begin{aligned}
i\omega\,\tilde{S}_\phi(\omega) &= -\int_{-\infty}^{\infty} dt\,\frac{dS_\phi}{dt}\,e^{i\omega t} \\
&= -2i\int_0^{\infty} dt\,\sin\omega t\,\frac{dS_\phi}{dt} \\
&= 2i\int_0^{\infty} dt\,\sin\omega t\chi(t) \\
&= 2i\,k_{\mathrm{B}}T\,\tilde{\chi}''(\omega)\,, \qquad (4.184)
\end{aligned}$$

which gives immediatly the Fourier formulation of the fluctuation-dissipation theorem

$$\tilde{S}_\phi(\omega) = \frac{2k_{\mathrm{B}}T\tilde{\chi}''(\omega)}{\omega}\,. \qquad (4.185)$$

4.B Oseen tensor

We sketch below a derivation of the Oseen-tensor as proposed in [Doi 1988]. The Oseen-tensor is an hydrodynamics Green's function for the Stokes flow solution due to a point-like force.

We consider a force $\mathbf{F}$ applied to a point particle $\mathbf{r}$ immersed in space filled with viscous liquid. In the case of incompressible and low Reynolds flow, this problem takes the form

$$-\boldsymbol{\nabla} p(\mathbf{r}) + \eta \boldsymbol{\nabla}^2 \mathbf{v}(\mathbf{r}) = -F\delta(\mathbf{r})\,, \tag{4.186a}$$

$$\boldsymbol{\nabla} \cdot \mathbf{v} = 0\,, \tag{4.186b}$$

where the flow fluid is supposed to vanish at infinity $|\mathbf{v}(\mathbf{r})| \underset{r\to\infty}{\rightarrow} 0$.

As the Stokes equations are linear in the pressure p and velocity $\mathbf{v}$, the unique fundamental solution to this problem, also known as *stokeslet*, can be formally written as follows

$$p(\mathbf{r}) = \mathbf{P}(\mathbf{r}) \cdot \mathbf{F}\,, \tag{4.187a}$$

$$\mathbf{v}(\mathbf{r}) = \mathbb{\Lambda}(\mathbf{r}) \cdot \mathbf{F}\,. \tag{4.187b}$$

The second-rank tensor $\mathbb{\Lambda}(\mathbf{r})$ is called the Oseen-tensor.

We first turn the previous motion equations (4.186) in spatial Fourier space

$$i\mathbf{q}\,p + \eta q^2 \mathbf{v} = \mathbf{F}\,, \tag{4.188a}$$

$$i\mathbf{q} \cdot \mathbf{v} = 0\,. \tag{4.188b}$$

We multiply the first equation (4.188a) by $-i\mathbf{q}$ and insert the second equation (4.188b) to obtain the pressure

$$p = -\frac{i\mathbf{q} : \mathbf{F}}{q^2}\,, \tag{4.189}$$

where the symbol : designs the dyadic product $(\mathbf{q} : \mathbf{F})_{ij} = q_i F_j$.

Inserting this equation in (4.188a) we can solve for the velocity

$$\mathbf{v} = \frac{1}{\eta q^2}\left(1 - \frac{\mathbf{q} : \mathbf{q}}{q^2}\right)\mathbf{F}\,. \tag{4.190}$$

In real space this relation becomes

$$\mathbf{v}(\mathbf{r}) = \int \mathbb{\Lambda}(\mathbf{r} - \mathbf{r}')\mathbf{F}(\mathbf{r}')d^3r'\,, \tag{4.191}$$

where the Oseen-tensor in 3-dimensional real space is given by

$$\mathbb{\Lambda}(\mathbf{r} - \mathbf{r}') \equiv \frac{1}{\eta}\int \frac{d^3q}{(2\pi)^3}\frac{1}{q^2}\left(1 - \frac{\mathbf{q} : \mathbf{q}}{q^2}\right) e^{-i\mathbf{q}\cdot(\mathbf{r}-\mathbf{r}')}\,. \tag{4.192}$$

The Oseen tensor depends only on $\rho = \mathbf{r} - \mathbf{r}'$ and by analogy to electrostatics, it has the following form

$$\mathbb{\Lambda}(\rho) = A\delta_{ij} + B\frac{\rho_i \rho_j}{\rho^2}\,, \tag{4.193}$$

where the scalars A and B are determined by the following two equations

$$3A + B = \sum_i \mathbb{\Lambda}_{ii} = \frac{1}{(2\pi)^3}\int d^3q \frac{2}{\eta q^2}\, e^{-i\mathbf{q}\cdot\rho} = \frac{1}{2\pi\eta\rho} \tag{4.194a}$$

$$A + B = \mathbb{\Lambda}_{ij}\frac{\rho_i \rho_j}{\rho^2} = \frac{1}{(2\pi)^3}\int d^3q \frac{1}{\eta q^2}\left(1 - \frac{(\mathbf{q}\rho)^2}{q^2\rho^2}\right) e^{-i\mathbf{q}\cdot\rho} = \frac{1}{4\pi\eta\rho} \tag{4.194b}$$

It leads immediately to

$$A = B = \frac{1}{8\pi\eta\rho}\,. \tag{4.195}$$

We deduce the form of the Oseen tensor in real space

$$\mathbb{\Lambda}_{ij}(\mathbf{r}, \mathbf{r}') = \frac{1}{8\pi\eta|\mathbf{r} - \mathbf{r}'|}\left[\delta_{ij} + \frac{(r_i - r_i')(r_j - r_j')}{|\mathbf{r} - \mathbf{r}'|^2}\right]. \tag{4.196}$$

Its diagonal part is simply

$$\mathbb{\Lambda}_{ii}(\mathbf{r}, \mathbf{r}') = \frac{1}{8\pi\eta|\mathbf{r} - \mathbf{r}'|}\,, \tag{4.197}$$

in real space, or

$$\mathbb{\Lambda}_{ii}(\mathbf{q}) = \frac{1}{4\eta|\mathbf{q}|}\,, \tag{4.198}$$

in Fourier space.

4.C Kramers approach to calculate the on-and off-rates

We show below that the dependence of the on-rate on the local state of the network can be calculated exactly by a Kramer's approach, and therefore does not need to be approximated by a Bell model. We assume a 1-dimensonal energy landscape for the reattachment for the i-th spectrin filamentis as represented schematically in fig. 4.C.1

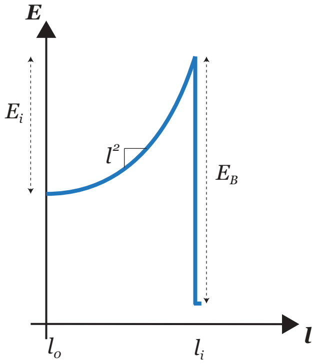

Figure 4.C.1: Schematical representation of the energy landscape for a spectrin filament as a function of its length l. $_i$ is the current elongation of the i-th spring considered.

Following Kramer, the (re-)attachment rate k_{on} is defined as the inverse of the mean escape time from the point $l = l_0$ to the point $l = l_i$ in the energy landscape (fig. 4.C.1).

The formula for escape time over a barrier by diffusion, originating from the Smoluchowski equation in high friction regime (Formula (5.2.166), pp. 139–141 in [Gardiner 2004]) reads

$$\tau_{\mathrm{on}} = D \int_{-\infty}^{\xi_0} dl \, \exp\left(-\frac{E(l)}{k_{\mathrm{B}}T}\right) \int_{l_0}^{\xi_0} dl' \, \exp\left(\frac{E(l)}{k_{\mathrm{B}}T}\right) \tag{4.199}$$

with D the diffusion constant over the (re-)attachment energy barrier $E_i = \frac{1}{2} k_s \left(l_i - l_0\right)^2$.

The sharp cut-off in fig. 4.C.1 leads to a slightly different calculation than the classical Kramer's formula: Near $l \sim l_0$, $E(l) \approx E(l_0) + \frac{1}{2}\left(l - l_0\right)^2 \frac{d^2E}{dl^2}(l_0)$ whereas for $l \sim \xi_0$, $E(l) \approx E(\xi_0) + \left(l - l_0\right) \frac{dE}{dl}(\xi_0)$.

Furthermore $\frac{d^2E}{dl^2}(l_0) = k_s$ and $\frac{dE}{dl}(\xi_0) = k_s\left(\xi_0 - l_0\right)$.

Consistently with the Formula 7.73 in the review [Hänggi 1990], the calculation of the escape mean time leads to

$$\tau_{\mathrm{on}} = D \frac{\omega_s^2}{2\pi} \sqrt{\pi \frac{E_i}{k_{\mathrm{B}}T}} \exp\left(\frac{E_i}{k_{\mathrm{B}}T}\right) \tag{4.200}$$

with here $\omega_s = \sqrt{\frac{k_s}{k_{\mathrm{B}}T}}$.

We need finally to evaluate the diffusion coefficient D. We adopt a Zimm model for the spectrin polymer chain, since it describes well the dynamics of unentangled dilute polymer, and write the Einstein relation

$$D = \frac{k_{\mathrm{B}}T}{4\pi\eta\, R_{\mathrm{g}}} \tag{4.201}$$

with R_{g} the gyration radius of the spectrin filament.

We get finally the following formula for the rate of attachment

$$k_{\mathrm{on}} = \frac{8\pi^{3/2}\eta\, R_{\mathrm{g}}}{k_s}\sqrt{\frac{2k_{\mathrm{B}}T}{k_s\left(l_i - l_0\right)^2}}\exp\left(-\frac{k_s\left(\xi_i - l_0\right)^2}{2k_{\mathrm{B}}T}\right) \tag{4.202}$$

The radius of gyration of a spectrin filament is easily accessible experimentally by light scattering and gives values around a few tenths of nanometers [Elgsaeter 1978], [Bø e 1979].

4.D Equivalence between Langevin and master equation approaches for an unimolecular reversible reaction

We consider an unimolecular reversible reaction of activation of a molecule A into A*.

$$\mathrm{A} \underset{k_+}{\overset{k_-}{\rightleftharpoons}} \mathrm{A}^* \tag{4.203}$$

We consider a total number of molecules n_0 and define $n = n_{\mathrm{A}}$ and $n^* = n_{\mathrm{A}^*}$ the number of desactivated and activated molecules A and A*. The system is supposed closed (no molecule reservoir or *chemiostats*), which imposes $n + n^* = n_0$.

4.D.1 Master equation approach

We first describe the problem with a master equation.

We define $\mathcal{P}(n,t)$ the probability of having n molecules A in the system at time t. By definition of a probability, $\sum_{n=0}^{n_0} \mathcal{P}(n,t) = 1$. The time evolution for this probability is given by the master equation

$$\begin{aligned} \frac{d\mathcal{P}(n,t)}{dt} &= k_-(n+1)\mathcal{P}(n+1,t) - k_- n\,\mathcal{P}(n,t) && (4.204) \\ &\quad + k_+\left[n_0 - (n-1)\right]\mathcal{P}(n-1,t) - k_+(n_0 - n)\mathcal{P}(n,t)\,. && (4.205) \end{aligned}$$

We want to calculate the correlation function of the fluctuations in number of molecules A around its mean $\langle \Delta n^2 \rangle \equiv \left\langle \left(n - \langle n \rangle\right)^2 \right\rangle = \langle n^2 \rangle - \langle n \rangle^2$.

We define a generating function

$$f(\theta,t) \equiv \sum_{n=0}^{n_0} \theta^n \mathcal{P}(n,t)\,. \tag{4.206}$$

The successive cumulants are given by

$$\langle n(n-1)...(n-k)\rangle = \left.\frac{\partial^k f}{\partial \theta^k}\right|_{\theta=1} \tag{4.207}$$

The first moment and second moment are therefore given by

$$\langle n \rangle = \left.\frac{\partial f}{\partial \theta}\right|_{\theta=1}\,, \tag{4.208a}$$

and

$$\langle n^2 \rangle = \langle n(n-1)\rangle + \langle n \rangle = \left.\frac{\partial^2 f}{\partial \theta^2}\right|_{\theta=1} + \left.\frac{\partial f}{\partial \theta}\right|_{\theta=1}\,. \tag{4.208b}$$

The equation of evolution for the mean number $\langle n \rangle \equiv \sum_{n=0}^{n_0} n\,\mathcal{P}(n,t)$ of molecules A can also be simply calculated by multiplying (4.204) by n and summing over $n \in [0, n_0]$. It leads to the deterministic equation

$$\frac{d\,\langle n \rangle}{dt} = -k_- \langle n \rangle + k_+ \langle n_0 - n \rangle \ , \tag{4.209}$$

which can be solved directly with the initial condition $\langle n \rangle (0) = n_0$:

$$\langle n \rangle (t) = n_0 \frac{k_+}{k_- + k_+} \left[1 + \frac{k_-}{k_+} e^{-(k_+ + k_-)t} \right] \tag{4.210}$$

We use the generating function to calculate the second moment. Inserting (4.206) in the master equation leads to the following partial differential equation (p.d.e.) for $f(\theta, t)$

$$\frac{\partial f}{\partial t} + (\theta - 1)(k_- + k_+ \theta) \frac{\partial f}{\partial \theta} = n_0 k_+ (\theta - 1) f(\theta) \, . \tag{4.211}$$

We use the method of characteristics to solve this p.d.e.. The characteristic lines in the space (t, θ, f) are defined by the following relations

$$\frac{dt}{1} = \frac{d\theta}{(\theta - 1)(k_- + k_+ \theta)} = \frac{df}{n_0 k_+ (\theta - 1) f} \tag{4.212}$$

We look for two functions $\Phi(t, \theta, f)$ and $\Psi(t, \theta, f)$, such that $d\Phi = d\Psi = 0$ according to the previous relations. We define the rates sum and ratio

$$k = k_- + k_+ \, , \qquad \alpha = \frac{k_-}{k_+} \, . \tag{4.213}$$

By choosing

$$\Phi(t, \theta, f) = \log\left(\frac{\theta - 1}{\alpha + \theta} \right) - kt \, , \tag{4.214a}$$

and

$$\Psi(t, \theta, f) = \frac{f}{(\alpha + \theta)^{n_0}} \tag{4.214b}$$

We find that $d\Phi = d\Psi = 0$ is equivalent to (4.212).

The general solution of the pde (4.211) reads $\mathcal{F}(\Phi, \Psi) = 0$. There exists therefore a function $\mathcal{H}$ so that

$$\frac{f(\theta, t)}{(\alpha + \theta)^{n_0}} = \mathcal{H}\left(\log\left(\frac{\theta - 1}{\alpha + \theta} \right) - kt \right) \, . \tag{4.215}$$

The initial condition $n(0) = n_0$ yields $f(\theta, 0) = \mathcal{P}(n_0, 0)\,\theta^{n_0} = \theta^{n_0}$. We insert this equation in (4.215) and find finally $\mathcal{H}(x) = \frac{1}{(\alpha+1)^{n_0}}\,(1 + \alpha\, e^{x})^{n_0}$.

The solution of the pde (4.211) with the initial condition $n(0) = n_0$ follows

$$f(\theta, t) = \left(\frac{\alpha + \theta + \alpha(\theta - 1)e^{-kt}}{1 + \alpha}\right)^{n_0} . \tag{4.216}$$

We deduce after some calculation the first and second moments from (4.208)

$$\langle n \rangle\,(t) = n_0 \frac{1}{1+\alpha}\left[1 + \alpha\, e^{-kt}\right] , \tag{4.217a}$$

equivalent to (4.210) and

$$\left\langle n^2 \right\rangle(t) = \frac{n_0}{(1+\alpha)^2}\left(1 + \alpha\, e^{-kt}\right)\left(\alpha + n_0 + \alpha(n_0 - 1)e^{-kt}\right) . \tag{4.217b}$$

They both have correct limit values: $\langle n \rangle \underset{t\to 0}{\longrightarrow} n_0$, $\langle n \rangle \underset{t\to\infty}{\longrightarrow} n_0$, $\left\langle n^2 \right\rangle \underset{t\to 0}{\longrightarrow} n_0^2$.

The autocorrelation function follows

$$\left\langle \Delta n^2 \right\rangle(t) = \frac{\alpha n_0}{(1+\alpha)^2}\left(1 + \alpha e^{-kt}\right)\left(1 - e^{-kt}\right) . \tag{4.218}$$

Its steady-state value is $\left\langle \Delta n^2 \right\rangle^{\infty} = n_0 \frac{k_- k_+}{(k_- + k_+)^2}$.

4.D.2 Chemical Langevin equation approach

We propose the following chemical Langevin equation for the evolution of the instantaneous number of molecules A

$$\frac{dn}{dt} = k_+\,(n_0 - n) - k_- n + \zeta(t)\,, \tag{4.219}$$

where $\zeta(t)$ is the chemical noise in the reaction.

4.D.2.1 Variance of the chemical noise

According to [Keizer 1975, Keizer 1987] or [Gillespie 2000], the noise $\zeta(t)$ in a Langevin approach of chemical reactions is a Gaussian white noise ($\langle \zeta(t) \rangle = 0$) and its variance is the sum of the average elementary fluxes in the system

$$\left\langle \zeta(t)\zeta(t') \right\rangle = \sum_i \langle j_i \rangle\, \delta(t - t') = \left[k_- \langle n \rangle + k_+\,(n_0 - \langle n \rangle)\right]\, \delta(t - t')\,. \tag{4.220}$$

We give below a pedestrian proof for this expression of the chemical noise variance. We consider the instantaneous fluxes in the system

$$j_+ = k_+\,(n_0 - n) \tag{4.221a}$$

$$j_- = k_-\, n \tag{4.221b}$$

Since n fluctuates, the two fluxes fluctuate as well.

We know define the number of molecules δn_+ of molecules A^* that become A and δn_- the number of molecules A that become A^* during a time Δt

$$\mathrm{A} \underset{\delta n_+}{\overset{\delta n_-}{\rightleftharpoons}} \mathrm{A}^* \tag{4.222}$$

They can be simply expressed as a function of the instantaneous fluxes j_+ and j_-

$$\delta n_+ = j_+ \Delta t\,, \tag{4.223a}$$

$$\delta n_- = j_- \Delta t\,. \tag{4.223b}$$

If we assume Δt small enough and the number of reactants n and $n_0 - n$ high enough, the two variables δn_+ and δn_- can be considered as statistically independent Poisson random variables, following [Gillespie 2000]. It follows immediately that

$$\left\langle \delta n_+^2 \right\rangle = \langle \delta n_+ \rangle\ , \tag{4.224a}$$

$$\left\langle \delta n_-^2 \right\rangle = \langle \delta n_- \rangle\ . \tag{4.224b}$$

Using eq. (4.223), we deduce immmediately

$$\begin{matrix} \left\langle \delta n_+^2 \right\rangle = \langle j_+ \rangle \Delta t \\ \left\langle \delta n_-^2 \right\rangle = \langle j_- \rangle \Delta t \end{matrix} \quad \xrightarrow[\Delta t \to 0]{} \quad \begin{matrix} \left\langle \delta n_+^2 \right\rangle = \langle j_+ \rangle \delta(t) \\ \left\langle \delta n_-^2 \right\rangle = \langle j_- \rangle \delta(t) \end{matrix} \tag{4.225}$$

The total variation of molecules A during Δt is simply $\delta n = \delta n_+ - \delta n_-$, and therefore

$$\left\langle (\delta n_+ - \delta n_-)^2 \right\rangle = \left\langle \delta n_+^2 \right\rangle + \left\langle \delta n_-^2 \right\rangle - 2\,\langle \delta n_+ \delta n_- \rangle = \left\langle \delta n_+^2 \right\rangle + \left\langle \delta n_-^2 \right\rangle \tag{4.226}$$

because δn_+ and δn_- are independent random variables and therefore are uncorrelated.

We deduce

$$\langle \zeta(t)\zeta(0) \rangle \equiv \left\langle \delta n^2 \right\rangle = \Big(\langle j_+ \rangle + \langle j_- \rangle \Big) \delta(t) = \Big(k_+\ (n_0 - \langle n \rangle) + k_- \langle n \rangle \Big) \delta(t) \tag{4.227}$$

4.D.2.2 Correlations of the fluctuations

Taking the average of the Langevin dynamics (4.219) leads to the same deterministic evolution equation (4.209) for the mean number $\langle n \rangle$ of A molecules as in the master equation approach. As pointed out in the previous section, we can integrate directly (4.209) which leads to $\langle n \rangle (t) = \frac{n_0}{1+\alpha} \left(1 + \alpha\, e^{-kt}\right)$.

We deduce the variance of the noise from eq. (4.227)

$$\left\langle \zeta(t)\zeta(t') \right\rangle = n_0 \frac{k_-}{1+\alpha} \left[2 + e^{-kt} (\alpha - 1) \right] \delta(t - t')\,. \tag{4.228}$$

Then, we calculate the correlation function $\left\langle \Delta n^2 \right\rangle = \left\langle (n - n_0)^2 \right\rangle$. From the Langevin dynamics (4.219) we deduce

$$\frac{d\Delta n}{dt} = -k\, \Delta n + \zeta(t)\,. \tag{4.229}$$

and therefore

$$\frac{d\Delta n^2}{dt} = 2\Delta n \, \frac{d\Delta n}{dt} = -2k \, \Delta n^2 + 2\Delta n \, \zeta(t) \, . \tag{4.230}$$

The homogeneous equation can be integrated into $\Delta n^2 = A(t)e^{-2kt}$, and we then apply the constant variation technique to determine $A(t)$. We obtain $\sqrt{A(t)} = \int_0^t dt_1 \, e^{kt_1}\zeta(t_1) + B$, and the initial condition $\Delta n^2 \xrightarrow[t\to 0]{0}$ results in $B = 0$.

We can now calculate the autocorrelation function $\left\langle \Delta n^2 \right\rangle (t)$

$$\begin{aligned}
\left\langle \Delta n^2 \right\rangle (t) &= \left\langle \left(\sqrt{A(t)}\right)^2 e^{-2kt} \right\rangle \\
&= \left\langle e^{-2kt} \int_0^t dt_1 \, e^{kt_1}\zeta(t_1) \int_0^t dt_2 \, e^{kt_2}\zeta(t_2) \right\rangle \\
&= e^{-2kt} \int_0^t dt_2 \int_0^t dt_1 \, e^{k(t_1+t_2)} \left\langle \zeta(t_1)\zeta(t_2) \right\rangle \\
&= e^{-2kt} \int_0^t dt_2 \int_0^t dt' \, e^{k(2t_2+T)} \delta(T) \frac{n_0 k_-}{1+\alpha} \left[2 + e^{-kt_2}(\alpha - 1) \right] \\
&\quad \text{using (4.228) and inserting } T = t_1 - t_2 \\
&= e^{-2kt} \, \frac{n_0 k_-}{1+\alpha} \int_0^t dt_2 \, e^{2kt_2} \left[2 + e^{-kt_2}(\alpha - 1) \right] \\
&= e^{-2kt} \, \frac{n_0 k_-}{1+\alpha} \left\{ \frac{2}{2k}\left(e^{2kt} - 1\right) + \frac{\alpha - 1}{k}\left(e^{kt} - 1\right) \right\} \\
&= \frac{n_0 \alpha}{(1+\alpha)^2} \left\{ 1 - \alpha e^{-2kt} + \alpha e^{-kt} - e^{-kt} \right\} \\
&= \frac{n_0 \alpha}{(1+\alpha)^2} \left(1 + \alpha e^{-kt}\right) \left(1 - e^{-kt}\right)
\end{aligned} \tag{4.231}$$

which is equivalent to the formula (4.218) found in the master equation approach.

We have therefore proven that the chemical Langevin equation approach is equivalent to the master equation approach up to the second moment of fluctuations for a unimolecular reversible chemical reaction at equilibrium.

4.E Numerical values for the red-blood cell membrane

Parameter	**Value**	**Signification**	**Reference(s)**
N	~ 27000	Number of spectrin filaments	[Fedosov 2010]
R_0	$\sim 3.5\,\mu m$	RBC typical radius	/
$\rho_0 = \frac{N}{4\pi R_0^2}$	$\sim 146.9\,\mu m^{-2}$	Surface density of filaments	/
$\xi_0 = \sqrt{g/\rho_0}$	$\sim 154\,nm$	Filament extension	/
χ_0	~ 0.12	Spectrin prestress	/
$l_0 = \xi_0(1-\chi_0)$	$\sim 135\,nm$	Spectrin resting length	/
k	$\sim 698\,k_{\mathrm{B}}T.\mu m^{-2}$	Spectrin stiffness	[Fedosov 2010]
$\frac{1}{2}k\,(\xi_0 - l_0)^2$	$\sim 0.1\,k_{\mathrm{B}}T$	Spectrin elongation energy	/
η	$\sim 19\,k_{\mathrm{B}}T.\mu m^{-3}$	Cytoplasm viscosity	[Betz 2009]
σ	$\sim -19\,k_{\mathrm{B}}T.\mu m^{-2}$	Compressed lipid bilayer tension	[Fournier 2004]
κ	$\sim 64.5\,k_{\mathrm{B}}T$	Lipid bilayer bending modulus	[Betz 2009]

Table 4.E.1: Table of the numerical parameters used for the red-blood cell membrane.

General conclusion

In this thesis, we have proposed two theories of active cell membranes.

In the first part, we have derived equations for an active-viscous membrane theory of the cell cortex. Motivated by experiments, we have shown that our model can reproduce qualitatively and quantitatively many aspects of two essential processes in biology: cell polarization and cytokinesis. Cortical flows are predicted to be the basis for cell cortex polarization in a suspended fibroblast cell. In the modelisation of cytokinesis, we reproduce the formation and ingression of a cleavage furrow and predict constriction completion above a well-defined threshold of equatorial contractility. Our model gives a physical explanation of the independence of cytokinesis duration on cell size in embryos, and predicts a critical role of turnover on the rate of constriction. We propose simple scaling arguments to interpret the numerical results. A key mechanism of cytokinesis is unveiled: cytoplasmic incompressibility results in a competition between the furrow line tension and the cell poles surface tension. Future work needs to adress the coupling of cortical flows with filaments orientation, the regulation of volume on long time-scales and the role of blebs in cytokinesis.

In the second part, we have considered the composite membrane of the red-blood cell. Focusing on non-equilibrium fluctuations in this system, we formulate an active fluctuations theory of the red-blood cell membrane. In agreement with former studies, we show that the spectrin cytoskeleton renormalizes the membrane tension. Coupling the thermal fluctuations of the membrane with a phosphorylation-dephosphorylation cycle, we show that maintaining the system in contact with a reservoir of ATP sustains the membrane in non-equilibrium steady-state. We calculate the response and the fluctuation spectrum of the coupled system and propose that active chemical fluctuations, driven by ATP, break the fluctuation-dissipation relation. The numerical results are compared to experimental measurements of the violation of the fluctuation-dissipation relation in human red-blood cell membranes. Our model, however, displays an intrinsic instability for realistic values of the parameters. It suggests that a – yet uncharacterized – mechanism should prevent the red-blood cell membrane to destabilize. Future work needs to adress this point.

Bibliography

[Abreu 2013] David Abreu and Udo Seifert. *Noisy Nonlinear Dynamics of Vesicles in Flow.* Physical Review Letters, vol. 110, no. 23, page 238103, June 2013. (Cited on page 197.)

[Akkas 1980] Nuri Akkas. *On the biomechanics of cytokinesis in animal cells.* Journal of Biomechanics, vol. 13, no. 12, pages 977–988, January 1980. (Cited on pages 33 and 36.)

[Alberts 2007] Bruce Alberts, Alexander Johnson, Julian Lewis, Martin Raff, Keith Roberts and Peter Walter. Molecular Biology of the Cell. Garland Publishing Inc, 5th. édition, 2007. (Cited on pages 7, 8, 9, 11, 13 and 19.)

[Argiros 2012] Haroula Argiros, Lauren Henson, Christiana Holguin, Victoria Foe and Charles Bradley Shuster. *Centralspindlin and chromosomal passenger complex behavior during normal and Rappaport furrow specification in echinoderm embryos.* Cytoskeleton (Hoboken, N.J.), vol. 000, August 2012. (Cited on page 104.)

[Atilgan 2012] Erdinc Atilgan, David Burgess and Fred Chang. *Localization of cytokinesis factors to the future cell division site by microtubule-dependent transport.* Cytoskeleton (Hoboken, N.J.), vol. 69, no. 11, pages 973–82, November 2012. (Cited on page 29.)

[Audoly 2013] Basile Audoly, Nicolas Clauvelin, Pierre-Thomas Brun, Miklós Bergou, Eitan Grinspun and Max Wardetzky. *A discrete geometric approach for simulating the dynamics of thin viscous threads.* Journal of Computational Physics, vol. 253, pages 18–49, November 2013. (Cited on pages 77, 82, 84 and 90.)

[Batty 2008] Christopher Batty and Robert Bridson. *Accurate Viscous Free Surfaces for Buckling , Coiling , and Rotating Liquids.* In SCA '08 Proceedings of the 2008 ACM SIGGRAPH/Eurographics Symposium on Computer Animation, pages 219–228, 2008. (Cited on page 85.)

[Bement 2005] William M Bement, Hélène A Benink and George von Dassow. *A microtubule-dependent zone of active RhoA during cleavage plane specification.* The Journal of cell biology, vol. 170, no. 1, pages 91–101, July 2005. (Cited on pages 27, 28, 29, 95 and 106.)

[Bergou 2010] Miklós Bergou, Basile Audoly, Etienne Vouga, Max Wardetzky and Eitan Grinspun. *Discrete viscous threads.* ACM Transactions on Graphics, vol. 29, no. 4, page 1, July 2010. (Cited on pages 77 and 84.)

[Berk 1991] David Berk and Evan Evans. *Detachment of agglutinin-bonded red blood cells. III. Mechanical analysis for large contact areas.* Biophysical journal, vol. 59, no. 4, pages 861–72, April 1991. (Cited on page 127.)

[Bertin 2010] Aurélie Bertin, Michael A McMurray, Luong Thai, Galo Garcia, Violet Votin, Patricia Grob, Theresa Allyn, Jeremy Thorner and Eva Nogales. *Phosphatidylinositol-4,5-bisphosphate promotes budding yeast septin filament assembly and organization.* Journal of molecular biology, vol. 404, no. 4, pages 711–31, December 2010. (Cited on page 15.)

[Betz 2009] Timo Betz, Martin Lenz, Jean-François Joanny and Cécile Sykes. *ATP-dependent mechanics of red blood cells.* Proceedings of the National Academy of Sciences of the United States of America, vol. 106, no. 36, pages 15320–5, September 2009. (Cited on pages 159, 160, 210 and 226.)

[Biro 2013] Maté Biro, Yves Romeo, Sonja Kroschwald, Miia Bovellan, Annett Boden, Joseph Tcherkezian, Philippe P. Roux, Guillaume Charras and Ewa K. Paluch. *Cell cortex composition and homeostasis resolved by integrating proteomics and quantitative imaging.* Cytoskeleton, vol. 00, pages n/a–n/a, October 2013. (Cited on page 16.)

[Biron 2005] David Biron, Enrique Alvarez-Lacalle, Tsvi Tlusty and Elisha Moses. *Molecular Model of the Contractile Ring.* Physical Review Letters, vol. 95, no. 9, page 098102, August 2005. (Cited on pages 33 and 42.)

[Bø e 1979] Arild Bø e, Arnljot Elgsaeter, Gunnhild Oftedal, Knut A. Strand, Eberhard Hoyer, V. P. Spiridonov and T. G. Strand. *Human Spectrin. III. A Study Based on Dynamic and Static Light Scattering.* Acta Chemica Scandinavica, vol. 33a, pages 245–249, 1979. (Cited on page 220.)

[Boal 2012] David H Boal. Mechanics of the cell. Cambridge University Press, 2nd édition, 2012. (Cited on page 145.)

[Boivin 1988] Pierre Boivin. *Role of the phosphorylation of red blood cell membrane proteins.* The Biochemical journal, vol. 256, no. 3, pages 689–95, December 1988. (Cited on page 137.)

[Borghi 2007] Nicolas Borghi and Françoise Brochard-Wyart. *Tether extrusion from red blood cells: integral proteins unbinding from cytoskeleton.* Biophysical journal, vol. 93, no. 4, pages 1369–79, August 2007. (Cited on page 159.)

[Boss 2012] Daniel Boss, Annick Hoffmann, Benjamin Rappaz, Christian Depeursinge, Pierre J Magistretti, Dimitri Van de Ville and Pierre Marquet. *Spatially-resolved eigenmode decomposition of red blood cells membrane fluctuations questions the role of ATP in flickering.* PloS one, vol. 7, no. 8, page e40667, January 2012. (Cited on page 161.)

[Bowen 2011] Jonathan R Bowen, Daniel Hwang, Xiaobo Bai, Dheeraj Roy and Elias T Spiliotis. *Septin GTPases spatially guide microtubule organization and plus end dynamics in polarizing epithelia.* The Journal of cell biology, vol. 194, no. 2, pages 187–97, July 2011. (Cited on page 15.)

[Bray 1988] Dennis Bray and John G. White. *Cortical flow in animal cells.* Science, vol. 239, no. 4842, pages 883–888, February 1988. (Cited on pages 19, 20 and 112.)

[Bringmann 2005] Henrik Bringmann and Anthony A Hyman. *A cytokinesis furrow is positioned by two consecutive signals.* Nature, vol. 436, no. 7051, pages 731–4, 2005. (Cited on page 28.)

[Brochard 1975] Françoise Brochard and Jean-François Lennon. *Frequency spectrum of the flicker phenomenon in erythrocytes.* Journal de Physique, vol. 36, no. 11, pages 1035–1047, 1975. (Cited on pages 144 and 145.)

[Broedersz 2010] Chase P Broedersz, Martin Depken, Norman Y Yao, Martin R Pollak, David A Weitz and Frederick C. MacKintosh. *Cross-Link-Governed Dynamics of Biopolymer Networks.* Physical Review Letters, vol. 105, no. 23, page 238101, November 2010. (Cited on page 18.)

[Callan-Jones 2011] A Callan-Jones and F Jülicher. *Hydrodynamics of active permeating gels.* New Journal of Physics, vol. 13, no. 9, page 093027, September 2011. (Cited on pages 24 and 40.)

[Calvert 2011] Meredith E K Calvert, Graham D Wright, Fong Yew Leong, Keng-Hwee Chiam, Yinxiao Chen, Gregory Jedd and Mohan K Balasubramanian. *Myosin concentration underlies cell size-dependent scalability of actomyosin ring constriction.* The Journal of cell biology, vol. 195, no. 5, pages 799–813, November 2011. (Cited on page 32.)

[Canham 1970] P.B. Canham. *The minimum energy of bending as a possible explanation of the biconcave shape of the human red blood cell.* Journal of Theoretical Biology, vol. 26, no. 1, pages 61–81, January 1970. (Cited on page 140.)

[Cao 1990a] L G Cao. *Mechanism of the formation of contractile ring in dividing cultured animal cells. II. Cortical movement of microinjected actin filaments.* The Journal of Cell Biology, vol. 111, no. 5, pages 1905–1911, November 1990. (Cited on page 30.)

[Cao 1990b] L G Cao and Y L Wang. *Mechanism of the formation of contractile ring in dividing cultured animal cells. I. Recruitment of preexisting actin filaments into the cleavage furrow.* The Journal of cell biology, vol. 110, no. 4, pages 1089–95, April 1990. (Cited on page 30.)

[Cao 1990c] L G Cao and Y L Wang. *Mechanism of the formation of contractile ring in dividing cultured animal cells. I. Recruitment of preexisting actin filaments into the cleavage furrow.* The Journal of cell biology, vol. 110, no. 4, pages 1089–95, April 1990. (Cited on page 97.)

[Carvalho 2009] Ana Carvalho, Arshad Desai and Karen Oegema. *Structural memory in the contractile ring makes the duration of cytokinesis independent of cell size.* Cell, vol. 137, no. 5, pages 926–37, 2009. (Cited on pages 31, 32, 106 and 113.)

[Chaikin 2000] P. M. Chaikin and T. C. Lubensky. Principles of Condensed Matter Physics. Cambridge University Press, 2000. (Cited on page 22.)

[Chang 2004] Lynne Chang and Robert D Goldman. *Intermediate filaments mediate cytoskeletal crosstalk.* Nature reviews. Molecular cell biology, vol. 5, no. 8, pages 601–13, August 2004. (Cited on page 14.)

[Charras 2006] Guillaume T Charras, Chi-Kuo Hu, Margaret Coughlin and Timothy J Mitchison. *Reassembly of contractile actin cortex in cell blebs.* The Journal of cell biology, vol. 175, no. 3, pages 477–90, November 2006. (Cited on page 17.)

[Charras 2008] Guillaume T Charras, Margaret Coughlin, Timothy J Mitchison and L Mahadevan. *Life and times of a cellular bleb.* Biophysical journal, vol. 94, no. 5, pages 1836–53, March 2008. (Cited on page 45.)

[Charras 2009] Guillaume T Charras, Timothy J Mitchison and L Mahadevan. *Animal cell hydraulics.* Journal of cell science, vol. 122, no. Pt 18, pages 3233–41, September 2009. (Cited on page 80.)

[Chen 2004] Hsuan-Yi Chen. *Internal States of Active Inclusions and the Dynamics of an Active Membrane.* Physical Review Letters, vol. 92, no. 16, page 168101, April 2004. (Cited on page 158.)

[Chen 2008] Wei Chen, Margit Foss, Kuo-Fu Tseng and Dahong Zhang. *Redundant mechanisms recruit actin into the contractile ring in silkworm spermatocytes.* PLoS biology, vol. 6, no. 9, page e209, 2008. (Cited on page 28.)

[Chen 2010] Hsuan-Yi Chen and Alexander S. Mikhailov. *Dynamics of biomembranes with active multiple-state inclusions.* Physical Review E, vol. 81, no. 3, page 031901, March 2010. (Cited on page 158.)

[Cingolani 2008] Lorenzo A Cingolani and Yukiko Goda. *Actin in action: the interplay between the actin cytoskeleton and synaptic efficacy.* Nature reviews. Neuroscience, vol. 9, no. 5, pages 344–56, May 2008. (Cited on page 9.)

[Clark 2013] Andrew G. Clark, Kai Dierkes and Ewa K. Paluch. *Monitoring actin cortex thickness in live cells.* Biophysical journal, vol. 105, no. 3, pages 570–80, August 2013. (Cited on pages 16, 17 and 95.)

[Cyron 2013] C. J. Cyron, K. W. Müller, K. M. Schmoller, a. R. Bausch, W. a. Wall and R. F. Bruinsma. *Equilibrium phase diagram of semi-flexible polymer networks with linkers.* EPL (Europhysics Letters), vol. 102, no. 3, page 38003, May 2013. (Cited on page 10.)

[Dan 1938] Katsuma Dan and Toshio Yanagida. *Behaviour of the cell surface during cleavage. II.* Cytologia, vol. 8, no. 3-4, pages 521–531, 1938. (Cited on page 34.)

[Dan 1940] Katsuma Dan and Jean Clark Dan. *Behavior of the cell surface during cleavage III. On the formation of new surface in the eggs of Strongylocentrotus pulcherrimus.* The Biological Bulletin, vol. 78, no. 3, pages 486–501, 1940. (Cited on page 34.)

[Daniels 2006] Brian R Daniels, Byron C Masi and Denis Wirtz. *Probing single-cell micromechanics in vivo: the microrheology of C. elegans developing embryos.* Biophysical journal, vol. 90, no. 12, pages 4712–9, June 2006. (Cited on page 80.)

[Danilov 1990] Y N Danilov, R Fennell, E Ling and C M Cohen. *Selective modulation of band 4.1 binding to erythrocyte membranes by protein kinase C.* The Journal of biological chemistry, vol. 265, no. 5, pages 2556–62, February 1990. (Cited on page 137.)

[de Gennes 1995] Pierre-Gilles de Gennes and Jacques Prost. The physics of liquid crystals. Oxford University Press, 1995. (Cited on pages 23 and 24.)

[de Gennes 2004] Pierre-Gilles de Gennes, Françoise Brochard-Wyart and David Quere. Capillarity and Wetting Phenomena. Springer-Verlag, New York, 2004. (Cited on page 44.)

[De Groot 1962] S.R. De Groot and Peter Mazur. Non-equilibrium thermodynamics. Dover Publications, 1962. (Cited on page 22.)

[Dean 2005] Sara O Dean, Stephen L Rogers, Nico Stuurman, Ronald D Vale and James A Spudich. *Distinct pathways control recruitment and maintenance of myosin II at the cleavage furrow during cytokinesis.* Proceedings of the National Academy of Sciences of the United States of America, vol. 102, no. 38, pages 13473–8, September 2005. (Cited on page 113.)

[Döbereiner 2000] Hans-Günther Döbereiner. *Properties of giant vesicles.* Current Opinion in Colloid & Interface Science, vol. 5, no. 3-4, pages 256–263, July 2000. (Cited on page 142.)

[Doi 1988] Masao Doi and S.F. Edwards. The Theory of Polymer Dynamics. Oxford Science Publications, 1st édition, 1988. (Cited on page 217.)

[Drubin 1996] David G Drubin and W.James Nelson. *Origins of Cell Polarity.* Cell, vol. 84, no. 3, pages 335–344, February 1996. (Cited on page 64.)

[Dubus 2006] C Dubus and J.-B Fournier. *A Gaussian model for the membrane of red blood cells with cytoskeletal defects.* Europhysics Letters (EPL), vol. 75, no. 1, pages 181–187, July 2006. (Cited on pages 151, 152, 153, 154, 155, 164, 165, 174 and 196.)

[Dubus 2007] Cyril Dubus. *Etude théorique de l'élasticité et des fluctuations de la membrane du globule rouge.* PhD thesis, Université Paris 7, 2007. (Cited on page 149.)

[Echard 2004] Arnaud Echard, Gilles R X Hickson, Edan Foley and Patrick H O'Farrell. *Terminal cytokinesis events uncovered after an RNAi screen.* Current biology : CB, vol. 14, no. 18, pages 1685–93, September 2004. (Cited on page 27.)

[Echard 2012] Arnaud Echard. *Phosphoinositides and cytokinesis: the "PIP" of the iceberg.* Cytoskeleton (Hoboken, N.J.), vol. 69, no. 11, pages 893–912, November 2012. (Cited on page 31.)

[Eder 1986] P S Eder, C J Soong and M Tao. *Phosphorylation reduces the affinity of protein 4.1 for spectrin.* Biochemistry, vol. 25, no. 7, pages 1764–70, April 1986. (Cited on page 137.)

[Elgsaeter 1978] A Elgsaeter. *Human spectrin. I. A classical light scattering study.* Biochimica et biophysica acta, vol. 536, no. 1, pages 235–44, September 1978. (Cited on page 220.)

[Elia 2012] Natalie Elia, Gur Fabrikant, Michael M Kozlov and Jennifer Lippincott-Schwartz. *Computational model of cytokinetic abscission driven by ESCRT-III polymerization and remodeling.* Biophysical journal, vol. 102, no. 10, pages 2309–20, May 2012. (Cited on page 27.)

[Emoto 2005] Kazuo Emoto, Hironori Inadome, Yasunori Kanaho, Shuh Narumiya and Masato Umeda. *Local change in phospholipid composition at the cleavage furrow is essential for completion of cytokinesis.* The Journal of biological chemistry, vol. 280, no. 45, pages 37901–7, November 2005. (Cited on page 31.)

[Euteneuer 1980] Ursula Euteneuer and J R McIntosh. *Polarity of midbody and phragmoplast microtubules.* The Journal of cell biology, vol. 87, no. 2 Pt 1, pages 509–15, November 1980. (Cited on page 25.)

[Evans 1972] Evan Evans and Yuan-Cheng Fung. *Improved measurements of the erythrocyte geometry.* Microvascular Research, vol. 4, no. 4, pages 335–347, October 1972. (Cited on page 134.)

[Evans 1987] Evan Evans and David Needham. *Physical properties of surfactant bilayer membranes: thermal transitions, elasticity, rigidity, cohesion and colloidal interactions.* The Journal of Physical Chemistry, vol. 91, no. 16, pages 4219–4228, July 1987. (Cited on page 139.)

[Evans 1989] E Evans and a Yeung. *Apparent viscosity and cortical tension of blood granulocytes determined by micropipet aspiration.* Biophysical journal, vol. 56, no. 1, pages 151–60, July 1989. (Cited on page 20.)

[Evans 1990] E. Evans and W Rawicz. *Entropy-driven tension and bending elasticity in condensed-fluid membranes.* Physical Review Letters, vol. 64, no. 17, pages 2094–2097, April 1990. (Cited on page 148.)

[Fabrikant 2009] Gur Fabrikant, Suman Lata, James D Riches, John A G Briggs, Winfried Weissenhorn and Michael M Kozlov. *Computational model of membrane fission catalyzed by ESCRT-III.* PLoS computational biology, vol. 5, no. 11, page e1000575, November 2009. (Cited on page 27.)

[Fededa 2012] Juan Pablo Fededa and Daniel W Gerlich. *Molecular control of animal cell cytokinesis.* Nature cell biology, vol. 14, no. 5, pages 440–7, May 2012. (Cited on page 25.)

[Fedosov 2010] Dmitry a. Fedosov, Bruce Caswell and George Em Karniadakis. *Systematic coarse-graining of spectrin-level red blood cell models.* Computer Methods in Applied Mechanics and Engineering, vol. 199, no. 29-32, pages 1937–1948, June 2010. (Cited on page 226.)

[Fehon 2010] Richard G Fehon, Andrea I McClatchey and Anthony Bretscher. *Organizing the cell cortex: the role of ERM proteins.* Nature reviews. Molecular cell biology, vol. 11, no. 4, pages 276–87, April 2010. (Cited on page 31.)

[Field 2005] Seth J Field, Nikki Madson, Monica L Kerr, Kenneth a a Galbraith, Caitlin E Kennedy, Mamta Tahiliani, Andrew Wilkins and Lewis C Cantley. *PtdIns(4,5)P2 functions at the cleavage furrow during cytokinesis.* Current biology : CB, vol. 15, no. 15, pages 1407–12, August 2005. (Cited on page 31.)

[Fishkind 1993] D J Fishkind and Y L Wang. *Orientation and three-dimensional organization of actin filaments in dividing cultured cells.* The Journal of cell biology, vol. 123, no. 4, pages 837–48, November 1993. (Cited on pages 30 and 115.)

[Fletcher 2010] Daniel a Fletcher and R Dyche Mullins. *Cell mechanics and the cytoskeleton.* Nature, vol. 463, no. 7280, pages 485–92, January 2010. (Cited on page 6.)

[Foe 2008] Victoria E Foe and George von Dassow. *Stable and dynamic microtubules coordinately shape the myosin activation zone during cytokinetic furrow formation.* The Journal of cell biology, vol. 183, no. 3, pages 457–70, November 2008. (Cited on page 28.)

[Founounou 2013] Nabila Founounou, Nicolas Loyer and Roland Le Borgne. *Septins Regulate the Contractility of the Actomyosin Ring to Enable Adherens Junction Remodeling during Cytokinesis of Epithelial Cells.* Developmental cell, vol. 24, no. 3, pages 242–55, February 2013. (Cited on page 15.)

[Fournier 2001] J.-B. Fournier, A Ajdari and L Peliti. *Effective-Area Elasticity and Tension of Micromanipulated Membranes.* Physical Review Letters, vol. 86, no. 21, pages 4970–4973, May 2001. (Cited on page 147.)

[Fournier 2004] Jean-Baptiste Fournier, David Lacoste and Elie Raphaël. *Fluctuation Spectrum of Fluid Membranes Coupled to an Elastic Meshwork: Jump of the Effective Surface Tension at the Mesh Size.* Physical Review Letters, vol. 92, no. 1, pages 1–4, January 2004. (Cited on pages 149, 151, 152, 164, 165, 174, 196 and 226.)

[Frank 1958] F C Frank. *I. Liquid crystals. On the theory of liquid crystals.* Discussions of the Faraday Society, vol. 25, no. I, page 19, 1958. (Cited on pages 24 and 141.)

[Fritzsche 2013] Marco Fritzsche, Alexandre Lewalle, Tom Duke, Karsten Kruse and Guillaume Charras. *Analysis of turnover dynamics of the submembranous actin cortex.* Molecular biology of the cell, vol. 24, pages 757–767, January 2013. (Cited on pages 18, 95 and 113.)

[Gallagher 2005] Patrick G Gallagher. *Red cell membrane disorders.* Hematology / the Education Program of the American Society of Hematology. American Society of Hematology. Education Program, no. 203, pages 13–8, January 2005. (Cited on page 135.)

[Gardel 2004] M L Gardel, J H Shin, F C MacKintosh, L Mahadevan, P Matsudaira and D A Weitz. *Elastic behavior of cross-linked and bundled actin networks.* Science (New York, N.Y.), vol. 304, no. 5675, pages 1301–5, May 2004. (Cited on page 10.)

[Gardiner 2004] C W Gardiner. Handbook Of Stochastic Methods(Gardiner).pdf. 3rd édition, 2004. (Cited on page 219.)

[Gauthier 2011] Emilie Gauthier, Xinhua Guo, Narla Mohandas and Xiuli An. *Phosphorylation-dependent perturbations of the 4.1R-associated multiprotein complex of the erythrocyte membrane.* Biochemistry, vol. 50, no. 21, pages 4561–7, May 2011. (Cited on page 137.)

[Ge 2013] Hao Ge and Hong Qian. *Dissipation, generalized free energy, and a self-consistent nonequilibrium thermodynamics of chemically driven open subsystems.* Physical Review E, vol. 87, no. 6, page 062125, June 2013. (Cited on pages 186 and 188.)

[Gillespie 2000] Daniel T Gillespie. *The chemical Langevin equation.* The Journal of Chemical Physics, vol. 113, no. 1, page 297, 2000. (Cited on pages 187, 223 and 224.)

[Gittes 1993] F Gittes, B Mickey, J Nettleton and J Howard. *Flexural rigidity of microtubules and actin filaments measured from thermal fluctuations in shape.*

The Journal of cell biology, vol. 120, no. 4, pages 923–34, February 1993. (Cited on page 13.)

[Glotzer 2009] Michael Glotzer. *Cytokinesis: GAP gap.* Current biology : CB, vol. 19, no. 4, pages R162–5, 2009. (Cited on page 26.)

[Goehring 2010] Nathan W Goehring, Debanjan Chowdhury, Anthony a Hyman and Stephan W Grill. *FRAP analysis of membrane-associated proteins: lateral diffusion and membrane-cytoplasmic exchange.* Biophysical journal, vol. 99, no. 8, pages 2443–52, October 2010. (Cited on page 20.)

[Goehring 2011] Nathan W Goehring, Philipp Khuc Trong, Justin S Bois, Debanjan Chowdhury, Ernesto M Nicola, Anthony a Hyman and Stephan W Grill. *Polarization of PAR proteins by advective triggering of a pattern-forming system.* Science (New York, N.Y.), vol. 334, no. 6059, pages 1137–41, November 2011. (Cited on page 75.)

[Goehring 2013] Nathan W Goehring and Stephan W Grill. *Cell polarity: mechanochemical patterning.* Trends in cell biology, vol. 23, no. 2, pages 72–80, February 2013. (Cited on page 75.)

[Goldenveizer 1961] A. L. Goldenveizer. Theory of elastic thin shells. Pergamon Press, New York, NY, USA, 1st édition, 1961. (Cited on page 49.)

[Goldman 1971] R D Goldman. *The role of three cytoplasmic fibers in BHK-21 cell motility. I. Microtubules and the effects of colchicine.* The Journal of cell biology, vol. 51, no. 3, pages 752–62, December 1971. (Cited on page 14.)

[Gouliaev 1998] Nikolai Gouliaev and John Nagle. *Simulations of a single membrane between two walls using a Monte Carlo method.* Physical Review E, vol. 58, no. 1, pages 881–888, July 1998. (Cited on page 155.)

[Gov 2003] N Gov, A. Zilman and S Safran. *Cytoskeleton Confinement and Tension of Red Blood Cell Membranes.* Physical Review Letters, vol. 90, no. 22, page 228101, June 2003. (Cited on pages 148 and 180.)

[Gov 2004] N. Gov. *Membrane Undulations Driven by Force Fluctuations of Active Proteins.* Physical Review Letters, vol. 93, no. 26, page 268104, December 2004. (Cited on pages 158 and 159.)

[Gov 2005] N S Gov and S a Safran. *Red blood cell membrane fluctuations and shape controlled by ATP-induced cytoskeletal defects.* Biophysical journal, vol. 88, no. 3, pages 1859–74, March 2005. (Cited on pages 158, 159 and 164.)

[Gov 2007] Nir Gov. *Active elastic network: Cytoskeleton of the red blood cell.* Physical Review E, vol. 75, no. 1, pages 1–6, January 2007. (Cited on pages 159 and 210.)

[Green 1987] K J Green, B Geiger, J C Jones, J C Talian and R D Goldman. *The relationship between intermediate filaments and microfilaments before and during the formation of desmosomes and adherens-type junctions in mouse epidermal keratinocytes.* The Journal of cell biology, vol. 104, no. 5, pages 1389–402, May 1987. (Cited on page 14.)

[Green 2012] Rebecca A Green, Ewa Paluch and Karen Oegema. *Cytokinesis in Animal Cells.* Annual review of cell and developmental biology, no. June, pages 1–30, July 2012. (Cited on pages 26, 27 and 32.)

[Greenspan 1977] H.P. Greenspan. *On the dynamics of cell cleavage.* Journal of Theoretical Biology, vol. 65, no. 1, pages 79–99, March 1977. (Cited on pages 33, 35, 37, 38 and 49.)

[Greenspan 1978] H.P. Greenspan. *On fluid-mechanical simulations of cell division and movement.* Journal of Theoretical Biology, vol. 70, no. 1, pages 125–134, January 1978. (Cited on pages 35 and 36.)

[Guha 2005] Minakshi Guha, Mian Zhou and Yu-Li Wang. *Cortical actin turnover during cytokinesis requires myosin II.* Current biology : CB, vol. 15, no. 8, pages 732–6, 2005. (Cited on pages 17, 18, 95 and 113.)

[Guizetti 2010] Julien Guizetti and Daniel W Gerlich. *Cytokinetic abscission in animal cells.* Seminars in cell & developmental biology, vol. 21, no. 9, pages 909–16, December 2010. (Cited on page 27.)

[Guo 2013] Ming Guo, Allen J Ehrlicher, Saleemulla Mahammad, Hilary Fabich, Mikkel H Jensen, Jeffrey R Moore, Jeffrey J Fredberg, Robert D Goldman and David A Weitz. *The role of vimentin intermediate filaments in cortical and cytoplasmic mechanics.* Biophysical journal, vol. 105, no. 7, pages 1562–8, October 2013. (Cited on page 14.)

[Hänggi 1990] Peter Hänggi and Michal Borkovec. *Reaction-rate theory: fifty years after Kramers.* Reviews of Modern Physics, vol. 62, no. 2, pages 251–341, April 1990. (Cited on page 219.)

[Happel 1983] John Happel and Howard Brenner. Low Reynolds Number Hydrodynamics. T. hague édition, 1983. (Cited on page 54.)

[Harada 2005] Takahiro Harada and Shin-ichi Sasa. *Equality Connecting Energy Dissipation with a Violation of the Fluctuation-Response Relation.* Physical Review Letters, vol. 95, no. 13, page 130602, September 2005. (Cited on pages 188 and 212.)

[Harris 1990] Albert K. Harris. *Testing Cleavage Mechanisms by Comparing Computer Simulations to Actual Experimental Results.* Annals of the New York Academy of Sciences, vol. 582, no. 1 Cytokinesis, pages 60–77, April 1990. (Cited on page 39.)

[Haviv 2008] Lior Haviv, David Gillo, Frederic Backouche and Anne Bernheim-Groswasser. *A cytoskeletal demolition worker: myosin II acts as an actin depolymerization agent.* Journal of molecular biology, vol. 375, no. 2, pages 325–30, January 2008. (Cited on page 18.)

[Hawkins 2011] Rhoda J Hawkins, Renaud Poincloux, Olivier Bénichou, Matthieu Piel, Philippe Chavrier and Raphaël Voituriez. *Spontaneous contractility-mediated cortical flow generates cell migration in three-dimensional environments.* Biophysical journal, vol. 101, no. 5, pages 1041–5, September 2011. (Cited on pages 22 and 75.)

[He 1997] X He and M Dembo. *On the mechanics of the first cleavage division of the sea urchin egg.* Experimental cell research, vol. 233, no. 2, pages 252–73, June 1997. (Cited on pages 33, 39, 40 and 49.)

[Helfrich 1973] Wolfgang Helfrich. *Elastic properties of lipid bilayers: theory and possible experiments.* Zeitschrift für Naturforschung. Teil C: Biochemie, Biophysik, Biologie, Virologie, vol. 28, no. 11, pages 693–703, 1973. (Cited on page 140.)

[Helfrich 1984] W. Helfrich and R.-M Servuss. *Undulations, steric interaction and cohesion of fluid membranes.* Il Nuovo Cimento D, vol. 3, no. 1, pages 137–151, January 1984. (Cited on page 147.)

[Henne 2012] William Mike Henne, Nicholas J Buchkovich, Yingying Zhao and Scott D Emr. *The Endosomal Sorting Complex ESCRT-II Mediates the Assembly and Architecture of ESCRT-III Helices.* Cell, vol. 151, no. 2, pages 356–71, October 2012. (Cited on page 27.)

[Heuett 2006] William J Heuett and Hong Qian. *Grand canonical Markov model: a stochastic theory for open nonequilibrium biochemical networks.* The Journal of chemical physics, vol. 124, no. 4, page 044110, January 2006. (Cited on page 186.)

[Heussinger 2012] C Heussinger. *Stress relaxation through crosslink unbinding in cytoskeletal networks.* New Journal of Physics, vol. 14, no. 9, page 095029, September 2012. (Cited on page 18.)

[Hickson 2006] Gilles R X Hickson, Arnaud Echard and Patrick H O'Farrell. *Rho-kinase controls cell shape changes during cytokinesis.* Current biology : CB, vol. 16, no. 4, pages 359–70, February 2006. (Cited on page 98.)

[Hiramoto 1958] Y. Hiramoto. *A quantitative description of protoplasmic sea-urchin egg.* The Journal of Experimental Biology, vol. 35, no. 2, pages 407–424, 1958. (Cited on pages 33, 34, 38, 75 and 80.)

[Hiramoto 1963] Y. Hiramoto. *Mechanical properties of sea urchin eggs.* Experimental Cell Research, vol. 32, no. 1, pages 59–75, October 1963. (Cited on pages 36, 39 and 40.)

[Hiramoto 1971] Yukio Hiramoto. *A Photographic Analysis of protoplasmic movement during cleavage in the sea urchin egg.* Development, Growth and Differentiation, vol. 13, no. 3, pages 191–200, October 1971. (Cited on pages 33 and 40.)

[Howard 1997] J Howard. *Molecular motors: structural adaptations to cellular functions.* Nature, vol. 389, no. 6651, pages 561–7, October 1997. (Cited on page 11.)

[Howell 1994] P D Howell. *Extensional Thin Layer Flows.* PhD thesis, University of Oxford, 1994. (Cited on page 56.)

[Howell 1996] P D Howell. *Models for thin viscous sheets.* European Journal of Applied Mathematics, vol. 7, no. 04, pages 24–29, September 1996. (Cited on pages 49 and 56.)

[Hu 2012] Chi-Kuo Hu, Margaret Coughlin and Timothy J Mitchison. *Midbody assembly and its regulation during cytokinesis.* Molecular biology of the cell, vol. 23, no. 6, pages 1024–34, March 2012. (Cited on page 26.)

[Inoue 2004] Yoshihiro H Inoue, Matthew S Savoian, Takao Suzuki, Endre Máthé, Masa-Toshi Yamamoto and David M Glover. *Mutations in orbit/mast reveal that the central spindle is comprised of two microtubule populations, those that initiate cleavage and those that propagate furrow ingression.* The Journal of cell biology, vol. 166, no. 1, pages 49–60, July 2004. (Cited on page 29.)

[Ishizaka 1957] Shozo Ishizaka. *Surface characters of dividing cells I. Stationary surface rings.* Journal of Experimental Biology, vol. 35, no. 2, pages 396–399, 1957. (Cited on pages 33 and 34.)

[Ishizaka 1966] Shozo Ishizaka. *Surface characters of dividing cells II. Isotropy and uniformity of surface membrane.* Journal of Experimental Biology, vol. 44, no. 2, pages 225–232, 1966. (Cited on pages 34 and 35.)

[Jiang 2013] Hongyuan Jiang and Sean X. Sun. *Cellular pressure and volume regulation and implications for cell mechanics.* Biophysical journal, vol. 105, no. 3, pages 609–19, August 2013. (Cited on page 21.)

[Joanny 2007] J F Joanny, F Jülicher, K Kruse and J Prost. *Hydrodynamic theory for multi-component active polar gels.* New Journal of Physics, vol. 9, no. 11, pages 422–422, November 2007. (Cited on page 24.)

[Joanny 2013] J-F Joanny, K Kruse, J Prost and S Ramaswamy. *The actin cortex as an active wetting layer.* The European physical journal. E, Soft matter, vol. 36, no. 5, page 52, May 2013. (Cited on page 24.)

[Joo 2007] Emily Joo, Mark C Surka and William S Trimble. *Mammalian SEPT2 is required for scaffolding nonmuscle myosin II and its kinases.* Developmental cell, vol. 13, no. 5, pages 677–90, November 2007. (Cited on page 15.)

[Kalwarczyk 2011] Tomasz Kalwarczyk, Natalia Ziebacz, Anna Bielejewska, Ewa Zaboklicka, Kaloian Koynov, Jedrzej Szymanski, Agnieszka Wilk, Adam Patkowski, Jacek Gapinski, Hans-Jürgen Butt and Robert Hoyst. *Comparative analysis of viscosity of complex liquids and cytoplasm of mammalian cells at the nanoscale.* Nano letters, vol. 11, no. 5, pages 2157–63, May 2011. (Cited on page 80.)

[Kamijo 2006] Keiju Kamijo, Naoya Ohara, Mitsuhiro Abe, Takashi Uchimura, Hiroshi Hosoya, Jae-seon Lee and Toru Miki. *Dissecting the role of Rho-mediated signaling in contractile ring formation.* Molecular biology of the cell, vol. 17, no. 1, pages 43–55, January 2006. (Cited on page 29.)

[Kantor 1987] Yacov Kantor and David Nelson. *Crumpling transition in polymerized membranes.* Physical Review Letters, vol. 58, no. 26, pages 2774–2777, June 1987. (Cited on page 139.)

[Karlsson 2013] Thommie Karlsson, Anastasia Bolshakova, Marco A O Magalhães, Vesa M Loitto and Karl-Eric Magnusson. *Fluxes of water through aquaporin 9 weaken membrane-cytoskeleton anchorage and promote formation of membrane protrusions.* PloS one, vol. 8, no. 4, page e59901, January 2013. (Cited on page 21.)

[Keizer 1975] Joel Keizer. *Concentration fluctuations in chemical reactions.* The Journal of Chemical Physics, vol. 63, no. 11, page 5037, 1975. (Cited on pages 187 and 223.)

[Keizer 1987] Joel Keizer. No Title. Springer Verlag, 1987. (Cited on pages 187 and 223.)

[Kimura 1996] Kazushi Kimura, Masaaki Ito, Mutsuki Amano, Kazuyasu Chihara, Yuko Fukata, Masato Nakafuku, Bunpei Yamamori, Jianhua Feng, Takeshi Nakano, Katsuya Okawa, Akihiro Iwamatsu and Kozo Kaibuchi. *Regulation of Myosin Phosphatase by Rho and Rho-Associated Kinase (Rho-Kinase).* Science, vol. 273, no. 5272, pages 245–248, July 1996. (Cited on page 12.)

[Kinoshita 2002] Makoto Kinoshita, Christine M Field, Margaret L Coughlin, Aaron F Straight and Timothy J Mitchison. *Self- and actin-templated assembly of Mammalian septins.* Developmental cell, vol. 3, no. 6, pages 791–802, December 2002. (Cited on page 15.)

[Kirchhoff 1859] G. Kirchhoff. *Ueber das Gleichgewicht und die Bewegung eines unendlich dünnen elastischen Stabes.* Journal für die reine und angewandte Mathematik (Crelles Journal), vol. 1859, no. 56, pages 285–313, January 1859. (Cited on page 49.)

[Koyama 2012] Hiroshi Koyama, Tamiki Umeda, Kazuyuki Nakamura, Tomoyuki Higuchi and Akatsuki Kimura. *A high-resolution shape fitting and simulation demonstrated equatorial cell surface softening during cytokinesis and its promotive role in cytokinesis.* PloS one, vol. 7, no. 2, page e31607, January 2012. (Cited on page 33.)

[Kruse 2005] K Kruse, J F Joanny, F Jülicher, J Prost and K Sekimoto. *Generic theory of active polar gels: a paradigm for cytoskeletal dynamics.* The European physical journal. E, Soft matter, vol. 16, no. 1, pages 5–16, 2005. (Cited on pages 22, 23, 37, 42, 49 and 114.)

[Kunda 2008] Patricia Kunda, Andrew E Pelling, Tao Liu and Buzz Baum. *Moesin controls cortical rigidity, cell rounding, and spindle morphogenesis during mitosis.* Current biology : CB, vol. 18, no. 2, pages 91–101, January 2008. (Cited on page 31.)

[Lacoste 2005] D Lacoste and a. W. C Lau. *Dynamics of active membranes with internal noise.* Europhysics Letters (EPL), vol. 70, no. 3, pages 418–424, May 2005. (Cited on page 158.)

[Lafaurie-Janvore 2013] Julie Lafaurie-Janvore, Paolo Maiuri, Irène Wang, Mathieu Pinot, Jean-Baptiste Manneville, Timo Betz, Martial Balland and Matthieu Piel. *ESCRT-III assembly and cytokinetic abscission are induced by tension release in the intercellular bridge.* Science (New York, N.Y.), vol. 339, no. 6127, pages 1625–9, March 2013. (Cited on page 27.)

[Lekomtsev 2012] Sergey Lekomtsev, Kuan-Chung Su, Valerie E Pye, Ken Blight, Sriramkumar Sundaramoorthy, Tohru Takaki, Lucy M Collinson, Peter Cherepanov, Nullin Divecha and Mark Petronczki. *Centralspindlin links the mitotic spindle to the plasma membrane during cytokinesis.* Nature, vol. 492, no. 7428, pages 276–9, December 2012. (Cited on pages 29 and 103.)

[Lenormand 2001] G Lenormand, S Hénon, a Richert, J Siméon and F Gallet. *Direct measurement of the area expansion and shear moduli of the human red blood cell membrane skeleton.* Biophysical journal, vol. 81, no. 1, pages 43–56, July 2001. (Cited on page 151.)

[Lenz 2012a] Martin Lenz, Margaret L Gardel and Aaron R Dinner. *Requirements for contractility in disordered cytoskeletal bundles.* New journal of physics, vol. 14, March 2012. (Cited on page 18.)

[Lenz 2012b] Martin Lenz, Todd Thoresen, Margaret L. Gardel and Aaron R. Dinner. *Contractile Units in Disordered Actomyosin Bundles Arise from F-Actin Buckling.* Physical Review Letters, vol. 108, no. 23, page 238107, June 2012. (Cited on page 19.)

[Levayer 2012] Romain Levayer and Thomas Lecuit. *Biomechanical regulation of contractility: spatial control and dynamics.* Trends in cell biology, vol. 22, no. 2, pages 61–81, February 2012. (Cited on pages 12 and 19.)

[Libai 1998] A. Libai and J.G. Simmonds. The nonlinear theory of elastic shells. Cambridge University Press, 2nd édition, 1998. (Cited on page 81.)

[Lieleg 2008] O. Lieleg, M. Claessens, Y. Luan and a. Bausch. *Transient Binding and Dissipation in Cross-Linked Actin Networks.* Physical Review Letters, vol. 101, no. 10, page 108101, September 2008. (Cited on page 10.)

[Lieleg 2010] Oliver Lieleg, Mireille M. A. E. Claessens and Andreas R. Bausch. *Structure and dynamics of cross-linked actin networks.* Soft Matter, vol. 6, no. 2, page 218, 2010. (Cited on page 10.)

[Lim H. W. 2002] Gerald Lim H. W., Michael Wortis and Ranjan Mukhopadhyay. *Stomatocyte-discocyte-echinocyte sequence of the human red blood cell: evidence for the bilayer- couple hypothesis from membrane mechanics.* Proceedings of the National Academy of Sciences of the United States of America, vol. 99, no. 26, pages 16766–9, December 2002. (Cited on page 143.)

[Lin 2004] Lawrence Lin and Frank Brown. *Brownian Dynamics in Fourier Space: Membrane Simulations over Long Length and Time Scales.* Physical Review Letters, vol. 93, no. 25, page 256001, December 2004. (Cited on page 155.)

[Lin 2005] Lawrence Lin and Frank Brown. *Dynamic simulations of membranes with cytoskeletal interactions.* Physical Review E, vol. 72, no. 1, page 011910, July 2005. (Cited on page 155.)

[Liu 1987] S. C. Liu, L. H. Derick and J. Palek. *Visualization of the hexagonal lattice in the erythrocyte membrane skeleton.* The Journal of cell biology, vol. 104, no. 3, pages 527–36, March 1987. (Cited on page 136.)

[Lo 2000] C. M. Lo, H. B. Wang, M. Dembo and Y. L. Wang. *Cell movement is guided by the rigidity of the substrate.* Biophysical journal, vol. 79, no. 1, pages 144–52, July 2000. (Cited on page 64.)

[Lomakina 2004] E. B. Lomakina, C. M. Spillmann, M. R. King and R .E. Waugh. *Rheological analysis and measurement of neutrophil indentation.* Biophysical journal, vol. 87, no. 6, pages 4246–58, December 2004. (Cited on page 20.)

[Lomholt 2006] Michael Lomholt. *Fluctuation spectrum of quasispherical membranes with force-dipole activity.* Physical Review E, vol. 73, no. 6, page 061914, June 2006. (Cited on page 158.)

[Loria 2012] Andy Loria, Katrina M. Longhini and Michael Glotzer. *The RhoGAP domain of CYK-4 has an essential role in RhoA activation.* Current biology : CB, vol. 22, no. 3, pages 213–9, February 2012. (Cited on page 102.)

[Loubet 2012] Bastien Loubet, Udo Seifert and Michael Andersen Lomholt. *Effective tension and fluctuations in active membranes.* Physical Review E, vol. 85, no. 3, page 031913, March 2012. (Cited on pages 159 and 207.)

[Love 1927] A.E.H. Love. A Treatise on the Mathematical Theory of Elasticity. (Reprinted by Dover, New York, 1944). Cambridge University Press, 2nd édition, 1927. (Cited on page 49.)

[Ma 2012] Xuefei Ma, Mihály Kovács, Mary Anne Conti, Aibing Wang, Yingfan Zhang, James R Sellers and Robert S Adelstein. *Nonmuscle myosin II exerts tension but does not translocate actin in vertebrate cytokinesis.* Proceedings of the National Academy of Sciences of the United States of America, vol. 109, no. 12, pages 4509–14, March 2012. (Cited on page 32.)

[Manneville 1999] J.-B. Manneville, P. Bassereau, D. Lévy and J. Prost. *Activity of Transmembrane Proteins Induces Magnification of Shape Fluctuations of Lipid Membranes.* Physical Review Letters, vol. 82, no. 21, pages 4356–4359, May 1999. (Cited on page 157.)

[Manneville 2001] J.-B. Manneville, P. Bassereau, S. Ramaswamy and J. Prost. *Active membrane fluctuations studied by micropipet aspiration.* Physical Review E, vol. 64, no. 2, page 021908, July 2001. (Cited on page 157.)

[Manno 2005] Sumie Manno, Yuichi Takakuwa and Narla Mohandas. *Modulation of erythrocyte membrane mechanical function by protein 4.1 phosphorylation.* The Journal of biological chemistry, vol. 280, no. 9, pages 7581–7, March 2005. (Cited on page 137.)

[Martin 1972] P. C. Martin, O. Parodi and P. S. Pershan. *Unified Hydrodynamic Theory for Crystals, Liquid Crystals, and Normal Fluids.* Physical Review A, vol. 6, no. 6, pages 2401–2420, December 1972. (Cited on page 22.)

[Mastronarde 1993] D. N. Mastronarde, K. L. McDonald, R. Ding and J. R. McIntosh. *Interpolar spindle microtubules in PTK cells.* The Journal of cell biology, vol. 123, no. 6 Pt 1, pages 1475–89, December 1993. (Cited on page 26.)

[Matzke 2001] R. Matzke, K. Jacobson and M. Radmacher. *Direct, high-resolution measurement of furrow stiffening during division of adherent cells.* Nature cell biology, vol. 3, no. 6, pages 607–10, June 2001. (Cited on page 32.)

[Mayer 2010] Mirjam Mayer, Martin Depken, Justin S. Bois, Frank Jülicher and Stephan W. Grill. *Anisotropies in cortical tension reveal the physical basis of polarizing cortical flows.* Nature, vol. 467, no. 7315, pages 617–21, September 2010. (Cited on pages 20, 22 and 113.)

[Medalia 2002] Ohad Medalia, Igor Weber, Achilleas S. Frangakis, Daniela Nicastro, Gunther Gerisch and Wolfgang Baumeister. *Macromolecular architecture in* *eukaryotic cells visualized by cryoelectron tomography.* Science (New York, N.Y.), vol. 298, no. 5596, pages 1209–13, November 2002. (Cited on pages 16 and 17.)

[Mendes Pinto 2012] Inês Mendes Pinto, Boris Rubinstein, Andrei Kucharavy, Jay R. Unruh and Rong Li. *Actin depolymerization drives actomyosin ring contraction during budding yeast cytokinesis.* Developmental cell, vol. 22, no. 6, pages 1247–60, June 2012. (Cited on page 33.)

[Miao 1994] Ling Miao, Udo Seifert, Michael Wortis and Hans-Günther Döbereiner. *Budding transitions of fluid-bilayer vesicles: The effect of area-difference elasticity.* Physical Review E, vol. 49, no. 6, pages 5389–5407, June 1994. (Cited on page 141.)

[Miller 2011] Ann L. Miller. *The contractile ring.* Current biology : CB, vol. 21, no. 24, pages R976–8, December 2011. (Cited on page 26.)

[Milner 1987] Scott T. Milner and S. A. Safran. *Dynamical fluctuations of droplet microemulsions and vesicles.* Physical Review A, vol. 36, no. 9, pages 4371–4379, November 1987. (Cited on page 193.)

[Mishra 2013] Mithilesh Mishra, Jun Kashiwazaki, Tomoko Takagi, Ramanujam Srinivasan, Yinyi Huang, Mohan K. Balasubramanian and Issei Mabuchi. *In vitro contraction of cytokinetic ring depends on myosin II but not on actin dynamics.* Nature Cell Biology, vol. 15, no. 7, pages 853–859, June 2013. (Cited on page 112.)

[Mizuno 2007] Daisuke Mizuno, Catherine Tardin, C. F. Schmidt and Frederick C. MacKintosh. *Nonequilibrium mechanics of active cytoskeletal networks.* Science (New York, N.Y.), vol. 315, no. 5810, pages 370–3, January 2007. (Cited on page 209.)

[Mohandas 1994] Narla Mohandas and Evan Evans. *Mechanical properties of the red cell membrane in relation to molecular structure and genetic defects.* Annual review of biophysics and biomolecular structure, vol. 23, pages 787–818, January 1994. (Cited on page 138.)

[Mohandas 2008] Narla Mohandas and Patrick G. Gallagher. *Red cell membrane: past, present, and future.* Blood, vol. 112, no. 10, pages 3939–48, November 2008. (Cited on page 135.)

[Morita 2007] Eiji Morita, Virginie Sandrin, Hyo-Young Chung, Scott G. Morham, Steven P. Gygi, Christopher K. Rodesch and Wesley I. Sundquist. *Human ESCRT and ALIX proteins interact with proteins of the midbody and function in cytokinesis.* The EMBO journal, vol. 26, no. 19, pages 4215–27, October 2007. (Cited on page 27.)

[Morone 2006] Nobuhiro Morone, Takahiro Fujiwara, Kotono Murase, Rinshi S. Kasai, Hiroshi Ike, Shigeki Yuasa, Jiro Usukura and Akihiro Kusumi. *Three-dimensional reconstruction of the membrane skeleton at the plasma membrane interface by electron tomography.* The Journal of cell biology, vol. 174, no. 6, pages 851–62, September 2006. (Cited on pages 16 and 17.)

[Mostowy 2012] Serge Mostowy and Pascale Cossart. *Septins: the fourth component of the cytoskeleton.* Nature reviews. Molecular cell biology, vol. 13, no. 3, pages 183–94, March 2012. (Cited on page 15.)

[Mukhina 2007] Svetlana Mukhina, Yu-Li Wang and Maki Murata-Hori. *Alpha-actinin is required for tightly regulated remodeling of the actin cortical network during cytokinesis.* Developmental cell, vol. 13, no. 4, pages 554–65, 2007. (Cited on pages 16 and 17.)

[Munro 2004] Edwin Munro, Jeremy Nance and James R. Priess. *Cortical flows powered by asymmetrical contraction transport PAR proteins to establish and maintain anterior-posterior polarity in the early C. elegans embryo.* Developmental cell, vol. 7, no. 3, pages 413–24, September 2004. (Cited on pages 20 and 64.)

[Murrell 2012] Michael P. Murrell and Margaret L. Gardel. *F-actin buckling coordinates contractility and severing in a biomimetic actomyosin cortex.* Proceedings of the National Academy of Sciences of the United States of America, vol. 109, no. 51, pages 20820–5, December 2012. (Cited on pages 18, 19 and 113.)

[Murthy 2005] Kausalya Murthy and Patricia Wadsworth. *Myosin-II-dependent localization and dynamics of F-actin during cytokinesis.* Current biology : CB, vol. 15, no. 8, pages 724–31, 2005. (Cited on pages 17, 95 and 113.)

[Nishimura 2006] Yukako Nishimura and Shigenobu Yonemura. *Centralspindlin regulates ECT2 and RhoA accumulation at the equatorial cortex during cytokinesis.* Journal of cell science, vol. 119, no. Pt 1, pages 104–14, January 2006. (Cited on page 29.)

[Novozhilov 1964] Valentin Valentinovich Novozhilov. The theory of thin shells. Groningen, 2nd édition, 1964. (Cited on page 49.)

[Oegema 1997] Karen Oegema and Timothy J. Mitchison. *Rappaport rules: cleavage furrow induction in animal cells.* Proceedings of the National Academy of Sciences of the United States of America, vol. 94, no. 10, pages 4817–20, May 1997. (Cited on page 28.)

[Onsager 1931] Lars Onsager. *Reciprocal Relations in Irreversible Processes. I.* Physical Review, vol. 37, no. 4, pages 405–426, February 1931. (Cited on pages 22 and 186.)

[Paramore 2006] Sterling Paramore, Gary S. Ayton, Dina T. Mirijanian and Gregory A. Voth. *Extending a spectrin repeat unit. I: linear force-extension response.* Biophysical journal, vol. 90, no. 1, pages 92–100, January 2006. (Cited on page 136.)

[Park 2010] YongKeun Park, Catherine A. Best, Thorsten Auth, Nir S. Gov, Samuel A. Safran, Gabriel Popescu, Subra Suresh and Michael S. Feld. *Metabolic remodeling of the human red blood cell membrane.* Proceedings of the National Academy of Sciences of the United States of America, vol. 107, no. 4, pages 1289–94, January 2010. (Cited on pages 137, 160, 161 and 210.)

[Peterson 1992] Mark A. Peterson, Helmut Strey and Erich Sackmann. *Theoretical and phase contrast microscopic eigenmode analysis of erythrocyte flicker : amplitudes.* Journal de Physique II, vol. 2, no. 5, pages 1273–1285, May 1992. (Cited on page 169.)

[Phillips 2008] Robert Brooks Phillips, Jane Kondev, Julie Theriot, Nigel Orme and Hernan G. Garcia. Physical Biology of the Cell. New York, New York, USA, 2008. (Cited on page 135.)

[Piekny 2005] Alisa Piekny, Michael Werner and Michael Glotzer. *Cytokinesis: welcome to the Rho zone.* Trends in cell biology, vol. 15, no. 12, pages 651–8, December 2005. (Cited on page 30.)

[Piekny 2008] Alisa J. Piekny and Michael Glotzer. *Anillin is a scaffold protein that links RhoA, actin, and myosin during cytokinesis.* Current biology : CB, vol. 18, no. 1, pages 30–6, January 2008. (Cited on page 32.)

[Pollard 1982] T. D. Pollard. *Structure and polymerization of Acanthamoeba myosin-II filaments.* The Journal of cell biology, vol. 95, no. 3, pages 816–25, December 1982. (Cited on page 11.)

[Pozrikidis 1992] C. Pozrikidis. Boundary Integral and Singularity Methods for Linearized Viscous Flow. Cambridge University Press, 1st édition, 1992. (Cited on page 37.)

[Prost 1996] Jacques Prost and Robin Bruinsma. *Shape fluctuations of active membranes.* Europhysics Letters (EPL), vol. 33, no. 4, pages 321–326, February 1996. (Cited on pages 156, 157 and 158.)

[Prothero 1967] J. W. Prothero and R. T. Rockafeller. *A model of cell cleavage.* Biophysical journal, vol. 7, no. 6, pages 659–73, November 1967. (Cited on pages 33 and 34.)

[Pujara 1979] P. Pujara and T.J. Lardner. *A model for cell division.* Journal of Biomechanics, vol. 12, no. 4, pages 293–299, January 1979. (Cited on page 36.)

[Qian 2006] Hong Qian. *Open-system nonequilibrium steady state: statistical thermodynamics, fluctuations, and chemical oscillations.* The journal of physical chemistry. B, vol. 110, no. 31, pages 15063–74, August 2006. (Cited on pages 184, 186 and 188.)

[Ramaswamy 2000] Sriram Ramaswamy, John Toner and Jacques Prost. *Nonequilibrium Fluctuations, Traveling Waves, and Instabilities in Active Membranes.* Physical Review Letters, vol. 84, no. 15, pages 3494–3497, 2000. (Cited on pages 157 and 158.)

[Rappaport 1985] R. Rappaport. *Repeated furrow formation from a single mitotic apparatus in cylindrical sand dollar eggs.* The Journal of experimental zoology, vol. 234, no. 1, pages 167–71, April 1985. (Cited on page 27.)

[Rappaport 1996] R. Rappaport. Cytokinesis in Animal Cells. Cambridge University Press, Cambridge, 1996. (Cited on pages 27 and 28.)

[Rawicz 2000] W. Rawicz, K. C. Olbrich, T. McIntosh, D. Needham and E. Evans. *Effect of chain length and unsaturation on elasticity of lipid bilayers.* Biophysical journal, vol. 79, no. 1, pages 328–39, July 2000. (Cited on page 148.)

[Rayleigh 1976] J.W.S Rayleigh. The Theory of Sound. 2nd editio édition, 1976. (Cited on page 49.)

[Reichl 2008] Elizabeth M. Reichl, Yixin Ren, Mary K. Morphew, Michael Delannoy, Janet C. Effler, Kristine D. Girard, Srikanth Divi, Pablo A. Iglesias, Scot C Kuo and Douglas N Robinson. *Interactions between myosin and actin crosslinkers control cytokinesis contractility dynamics and mechanics.* Current biology : CB, vol. 18, no. 7, pages 471–80, 2008. (Cited on page 17.)

[Reymann 2012] Anne-Cécile Reymann, Rajaa Boujemaa-Paterski, Jean-Louis Martiel, Christophe Guérin, Wenxiang Cao, Harvey F Chin, Enrique M. De La Cruz, Manuel Théry and Laurent Blanchoin. *Actin network architecture can determine myosin motor activity.* Science (New York, N.Y.), vol. 336, no. 6086, pages 1310–4, June 2012. (Cited on page 112.)

[Ribe 2002] N. M. Ribe. *A general theory for the dynamics of thin viscous sheets.* Journal of Fluid Mechanics, vol. 457, pages 255–283, April 2002. (Cited on page 49.)

[Ridley 2003] Anne J. Ridley, Martin A. Schwartz, Keith Burridge, Richard A. Firtel, Mark H. Ginsberg, Gary Borisy, J. Thomas Parsons and Alan Rick Horwitz. *Cell migration: integrating signals from front to back.* Science (New York, N.Y.), vol. 302, no. 5651, pages 1704–9, December 2003. (Cited on page 64.)

[Rivlin 1948] R. S. Rivlin. *Large Elastic Deformations of Isotropic Materials. IV. Further Developments of the General Theory.* Philosophical Transactions of the Royal Society A: Mathematical, Physical and Engineering Sciences, vol. 241, no. 835, pages 379–397, October 1948. (Cited on page 36.)

[Roubinet 2011] Chantal Roubinet. *Rôles et régulation du PI(4,5)P2 dans le remodelage cortical et la morphogénèse cellulaire en mitose.* PhD thesis, Université Paul Sabatier, Toulouse, 2011. (Cited on page 31.)

[Salbreux 2007] Guillaume Salbreux, Jean-François Joanny, Jacques Prost and Pramod Pullarkat. *Shape oscillations of non-adhering fibroblast cells.* Physical biology, vol. 4, no. 4, pages 268–84, December 2007. (Cited on pages 20 and 65.)

[Salbreux 2008] Guillaume Salbreux. *Modélisation des instabilités du cortex d'actine.* PhD thesis, Université Pierre et Marie Curie - Paris 6, 2008. (Cited on pages 41, 42, 53 and 115.)

[Salbreux 2009] G. Salbreux, J. Prost and J. Joanny. *Hydrodynamics of Cellular Cortical Flows and the Formation of Contractile Rings.* Physical Review Letters, vol. 103, no. 5, pages 1–4, July 2009. (Cited on pages 20, 22, 30, 33, 38, 41, 42, 53, 114 and 115.)

[Salbreux 2012] Guillaume Salbreux, Guillaume Charras and Ewa Paluch. *Actin cortex mechanics and cellular morphogenesis.* Trends in cell biology, vol. 22, no. 10, pages 536–45, October 2012. (Cited on pages 19, 20 and 95.)

[Salmon 1990] E. D. Salmon and S. M. Wolniak. *Role of microtubules in stimulating cytokinesis in animal cells.* Annals of the New York Academy of Sciences, vol. 582, pages 88–98, January 1990. (Cited on page 29.)

[Sapir 1985] T. Sapir and A. Nir. *A hydrodynamic study of the furrowing stage during cleavage.* Physicochemical hydrodynamics, vol. 6, no. 803, 1985. (Cited on page 37.)

[Saxton 1990] Michael J. Saxton. *The membrane skeleton of erythrocytes. A percolation model.* Biophysical journal, vol. 57, no. 6, pages 1167–77, June 1990. (Cited on pages 152, 153 and 156.)

[Schmoller 2011] Kurt M. Schmoller, Christine Semmrich and Andreas R. Bausch. *Slow down of actin depolymerization by cross-linking molecules.* Journal of Structural Biology, vol. 173, no. 2, pages 350–357, 2011. (Cited on page 18.)

[Schroeder 1972] Thomas E. Schroeder. *The contractile ring II Determining its Brief Existence, Volumetric Changes, and Vital Role in Cleaving Arbacia Eggs.* The Journal of Cell Biology, vol. 53, 1972. (Cited on page 32.)

[Sedzinski 2011] Jakub Sedzinski, Maté Biro, Annelie Oswald, Jean-Yves Tinevez, Guillaume Salbreux and Ewa Paluch. *Polar actomyosin contractility destabilizes the position of the cytokinetic furrow.* Nature, vol. 476, no. 7361, pages 462–6, August 2011. (Cited on pages 16, 32, 33, 44, 45, 80 and 116.)

[Seifert 1995] Udo Seifert. *The concept of effective tension for fluctuating vesicles.* Zeitschrift für Physik B Condensed Matter, vol. 97, no. 2, pages 299–309, June 1995. (Cited on pages 159 and 207.)

[Seifert 1999] Udo Seifert. *Fluid membranes in hydrodynamic flow fields: Formalism and an application to fluctuating quasispherical vesicles in shear flow.* The European Physical Journal B, vol. 8, no. 3, pages 405–415, April 1999. (Cited on page 197.)

[Sheetz 1974] Michael P. Sheetz and S. J. Singer. *Biological membranes as bilayer couples. A molecular mechanism of drug-erythrocyte interactions.* Proceedings of the National Academy of Sciences of the United States of America, vol. 71, no. 11, pages 4457–61, November 1974. (Cited on page 141.)

[Sheetz 1977] M P Sheetz. *On the mechanism of ATP-induced shape changes in human erythrocyte membranes. I. The role of the spectrin complex.* The Journal of Cell Biology, vol. 73, no. 3, pages 638–646, June 1977. (Cited on page 143.)

[Skalak 1973] R. Skalak, A. Tozeren, R. P. Zarda and S. Chien. *Strain energy function of red blood cell membranes.* Biophysical journal, vol. 13, no. 3, pages 245–64, March 1973. (Cited on page 36.)

[Soares E Silva 2011] Marina Soares E Silva, Martin Depken, Björn Stuhrmann, Marijn Korsten, Frederick C. MacKintosh and Gijsje H. Koenderink. *Active multistage coarsening of actin networks driven by myosin motors.* Proceedings of the National Academy of Sciences of the United States of America, vol. 108, no. 23, pages 9408–13, June 2011. (Cited on page 19.)

[Stewart 2011] Martin P. Stewart, Jonne Helenius, Yusuke Toyoda, Subramanian P. Ramanathan, Daniel J. Muller and Anthony A. Hyman. *Hydrostatic pressure and the actomyosin cortex drive mitotic cell rounding.* Nature, vol. 469, no. 7329, pages 226–30, January 2011. (Cited on page 22.)

[Straight 2003] Aaron F. Straight, Amy Cheung, John Limouze, Irene Chen, Nick J. Westwood, James R. Sellers and Timothy J. Mitchison. *Dissecting temporal and spatial control of cytokinesis with a myosin II Inhibitor.* Science (New York, N.Y.), vol. 299, no. 5613, pages 1743–7, 2003. (Cited on page 12.)

[Subrahmanyam 1991] G. Subrahmanyam, P. J. Bertics and R. A. Anderson. *Phosphorylation of protein 4.1 on tyrosine-418 modulates its function in vitro.* Proceedings of the National Academy of Sciences of the United States of America, vol. 88, no. 12, pages 5222–6, June 1991. (Cited on page 137.)

[Szollosi 1970] D. Szollosi. *Cortical cytoplasmic filaments of cleaving eggs: a structural element corresponding to the contractile ring.* The Journal of cell biology, vol. 44, no. 1, pages 192–209, January 1970. (Cited on page 114.)

[Tharmann 2007] R. Tharmann, M. Claessens and a. Bausch. *Viscoelasticity of Isotropically Cross-Linked Actin Networks.* Physical Review Letters, vol. 98, no. 8, page 088103, February 2007. (Cited on page 10.)

[Timoshenko 1959] S. Timoshenko and S. Woinowsky-Krieger. Theory of plates and shells. McGraw-Hill (New York), 2nd editio édition, 1959. (Cited on page 49.)

[Tinevez 2009] Jean-Yves Tinevez, Ulrike Schulze, Guillaume Salbreux, Julia Roensch, Jean-François Joanny and Ewa Paluch. *Role of cortical tension in bleb growth.* Proceedings of the National Academy of Sciences of the United States of America, vol. 106, no. 44, pages 18581–6, November 2009. (Cited on pages 20 and 95.)

[Tuvia 1998] S. Tuvia, S. Levin, A. Bitler and R. Korenstein. *Mechanical fluctuations of the membrane-skeleton are dependent on F-actin ATPase in human erythrocytes.* The Journal of cell biology, vol. 141, no. 7, pages 1551–61, June 1998. (Cited on pages 159, 160, 207 and 208.)

[Uehara 2010] Ryota Uehara, Gohta Goshima, Issei Mabuchi, Ronald D. Vale, James A. Spudich and Eric R. Griffis. *Determinants of myosin II cortical localization during cytokinesis.* Current biology : CB, vol. 20, no. 12, pages 1080–5, June 2010. (Cited on page 17.)

[van Leeuwen 1999] F. N. van Leeuwen, S. van Delft, H. E. Kain, R. A. van der Kammen and J. G. Collard. *Rac regulates phosphorylation of the myosin-II heavy chain, actinomyosin disassembly and cell spreading.* Nature cell biology, vol. 1, no. 4, pages 242–8, August 1999. (Cited on page 12.)

[Vogel 2013] Sven K Vogel, Zdenek Petrasek, Fabian Heinemann and Petra Schwille. *Myosin motors fragment and compact membrane-bound actin filaments.* eLife, vol. 2, page e00116, January 2013. (Cited on pages 18 and 113.)

[von Dassow 2009a] George von Dassow. *Concurrent cues for cytokinetic furrow induction in animal cells.* Trends in cell biology, vol. 19, no. 4, pages 165–73, 2009. (Cited on page 95.)

[von Dassow 2009b] George von Dassow, Koen J. C. Verbrugghe, Ann L. Miller, Jenny R. Sider and William M. Bement. *Action at a distance during cytokinesis.* The Journal of cell biology, vol. 187, no. 6, pages 831–45, December 2009. (Cited on pages 27, 28 and 29.)

[Wegscheider 1901] Rud Wegscheider. *Über simultane Gleichgewichte und die Beziehungen zwischen Thermodynamik und Reactionskinetik homogener Systeme.* Monatshefte für Chemie, vol. 22, no. 8, pages 849–906, August 1901. (Cited on page 183.)

[Wen 2011] Qi Wen and Paul A. Janmey. *Polymer physics of the cytoskeleton.* Current opinion in solid state & materials science, vol. 15, no. 5, pages 177–182, October 2011. (Cited on page 18.)

[White 1983] J. G. White and G. G. Borisy. *On the mechanisms of cytokinesis in animal cells.* Journal of theoretical biology, vol. 101, no. 2, pages 289–316, March 1983. (Cited on pages 33, 38, 39 and 112.)

[Wolpert 1960] L. Wolpert. *The mechanics and mechanism of cleavage.* International review of cytology, vol. 10, pages 163–216, 1960. (Cited on pages 33 and 34.)

[Yam 2007] Patricia T Yam, Cyrus a Wilson, Lin Ji, Benedict Hebert, Erin L Barnhart, Natalie a Dye, Paul W Wiseman, Gaudenz Danuser and Julie a Theriot. *Actin-myosin network reorganization breaks symmetry at the cell rear to spontaneously initiate polarized cell motility.* The Journal of cell biology, vol. 178, no. 7, pages 1207–21, September 2007. (Cited on page 64.)

[Yao 2013] Norman Y. Yao, Chase P. Broedersz, Martin Depken, Daniel J. Becker, Martin R. Pollak, Frederick C. MacKintosh and David A. Weitz. *Stress-Enhanced Gelation: A Dynamic Nonlinearity of Elasticity.* Physical Review Letters, vol. 110, no. 1, page 018103, January 2013. (Cited on page 10.)

[Yeung 1989] A. Yeung and E. Evans. *Cortical shell-liquid core model for passive flow of liquid-like spherical cells into micropipets.* Biophysical journal, vol. 56, no. 1, pages 139–49, July 1989. (Cited on page 80.)

[Yoneda 1972] Mitsuki Yoneda and Katsuma Dan. *Tension at the surface of the dividing sea-urchin egg.* Journal of Experimental Biology, vol. 57, no. 3, pages 575–587, 1972. (Cited on pages 20, 32, 33, 34, 35, 45, 49 and 107.)

[Yüce 2005] Ozlem Yüce, Alisa J. Piekny and Michael Glotzer. *An ECT2-centralspindlin complex regulates the localization and function of RhoA.* The Journal of cell biology, vol. 170, no. 4, pages 571–82, August 2005. (Cited on page 28.)

[Zhang 2005] Wendy Zhang and Douglas N. Robinson. *Balance of actively generated contractile and resistive forces controls cytokinesis dynamics.* Proceedings of the National Academy of Sciences of the United States of America, vol. 102, no. 20, pages 7186–91, May 2005. (Cited on pages 33, 42, 43 and 80.)

[Zhang 2008] Rui Zhang and Frank L H Brown. *Cytoskeleton mediated effective elastic properties of model red blood cell membranes.* The Journal of chemical physics, vol. 129, no. 6, page 065101, August 2008. (Cited on pages 153, 154, 155 and 164.)

[Zilker 1987] A. Zilker, H. Engelhardt and E. Sackmann. *Dynamic reflection interference contrast (RIC-) microscopy : a new method to study surface excitations of cells and to measure membrane bending elastic moduli.* Journal de Physique, vol. 48, no. 12, pages 2139–2151, 1987. (Cited on pages 149 and 151.)

[Zinemanas 1987] Daniel Zinemanas and Avinoam Nir. *On the viscous deformation of biological cells under anisotropic surface tension.* Journal of Fluid Mechanics, vol. 193, pages 217–241, April 1987. (Cited on pages 33, 37, 38, 39, 42 and 49.)

[Zinemanas 1990] Daniel Zinemanas and Avinoam Nir. *Surface viscoelastic effects in cell cleavage.* Journal of biomechanics, vol. 23, no. 5, pages 417–24, January 1990. (Cited on page 33.)

[Zumdieck 2005] Alexander Zumdieck, Marco Lagomarsino, Catalin Tanase, Karsten Kruse, Bela Mulder, Marileen Dogterom and Frank Jülicher. *Continuum Description of the Cytoskeleton: Ring Formation in the Cell Cortex.* Physical Review Letters, vol. 95, no. 25, pages 1–4, 2005. (Cited on pages 33 and 41.)

[Zumdieck 2007] Alexander Zumdieck, Karsten Kruse, Henrik Bringmann, Anthony a Hyman and Frank Jülicher. *Stress generation and filament turnover during actin ring constriction.* PloS one, vol. 2, no. 1, page e696, 2007. (Cited on pages 33, 43 and 49.)

Hervé TURLIER

Shaping the cell:
Theories of active membranes

Résumé

La surface des cellules animales est composée d'une bicouche lipidique et d'un cytosquelette. Les cellules contrôlent leur forme en remodelant leur cytosquelette par des processus actifs. Nous considérons tout d'abord le cortex d'actomyosine et son rôle lors la cytocinèse, dernière étape de la division cellulaire. Nous formulons une théorie mécanique de membrane de la couche corticale active et visqueuse. La formulation Lagrangienne de la théorie est implémentée numériquement pour étudier la cytocinèse en régime de larges déformations. Nous montrons qu'une bande d'hyperactivité de la myosine à l'équateur de la cellule suffit à reproduire la formation et la contraction du sillon de division. Nous prédisons le succès de la cytocinèse au delà d'un certain seuil de contractilité équatoriale et proposons une explication physique de l'indépendance de la durée de contraction avec la taille d'un embryon. Des arguments d'échelle permettent d'interpréter les résultats numériques et révèlent un mécanisme clé: l'incompressibilité du cytoplasme induit une compétition entre la tension de ligne du sillon et la tension de surface aux pôles. Nous étudions ensuite la membrane du globule rouge et proposons un modèle pour ses fluctuations actives. Nous considérons à la fois les fluctuations thermiques de la membrane et les fluctuations chimiques de l'ancrage des filaments de spectrine dans la membrane. Un apport constant d'ATP, en affaiblissant cet ancrage, est la source de fluctuations supplémentaires dans la membrane. Ces fluctuations hors-équilibre violent le théorème de fluctuation-dissipation, en accord avec les résultats expérimentaux, signe que les globules rouges sont vivants.

Mots clés : membrane active, forme cellulaire, cortex d'actomyosine, cytocinèse, globule rouge, fluctuation-dissipation

Abstract

The surface of animal cells is a thin layer composed of a lipid bilayer and a cytoskeleton. Cells control their shape dynamically by remodeling their cytoskeleton via active processes. In a first part, we consider the actomyosin cortex and its role in cytokinesis, the last stage of cell division. We formulate a viscous-active membrane mechanical theory of the cortical layer. The Lagrangian formulation of the theory is implemented numerically to study large cortical deformations during cytokinesis. We show that an equatorial band of myosin overactivity is sufficient to reproduce the formation and ingression of a cleavage furrow. We predict cytokinesis above a well-defined threshold of equatorial contractility and propose a physical explanation of the independence of cytokinesis duration on cell size in embryos. Scaling arguments are proposed as a simple interpretation of the numerical results and unveil a key mechanism: cytoplasmic incompressibility results in a competition between the furrow line tension and the cell poles surface tension. In the second part, we study the red-blood cell membrane and propose a model for its active fluctuations. We consider both the thermal fluctuations of the lipid bilayer and the chemical fluctuations of the spectrin skeleton anchoring to the lipid bilayer. The constant supply of ATP, by weakening this anchoring, is proposed to give rise to extra-fluctuations of the membrane. These non-equilibrium fluctuations violate the fluctuation-dissipation theorem, in agreement with experimental measurements, thereby exhibiting the living nature of the red-blood cell.

Keywords: active membrane, cell shape, actomyosin cortex, cytokinesis, red-blood cell, fluctuation-dissipation.